Carnegie Mellon University
MELLON COLLEGE OF SCIENCE

THESIS

SUBMITTED IN PARTIAL FULFILLMENT OF THE REQUIREMENTS
FOR THE DEGREE OF

DOCTOR OF PHILOSOPHY IN THE FIELD OF PHYSICS

TITLE: "Astrophysical systematics in weak gravitational lensing."

PRESENTED BY: Hung-Jin Huang

ACCEPTED BY THE DEPARTMENT OF PHYSICS

Rachel Mandelbaum	8/27/19
RACHEL MANDELBAUM, CHAIR PROFESSOR	DATE
Scott Dodelson	8/28/19
SCOTT DODELSON, DEPT HEAD	DATE

APPROVED BY THE COLLEGE COUNCIL

Rebecca Doerge	9/04/19
REBECCA DOERGE, DEAN	DATE

Astrophysical Systematics in Weak Gravitational Lensing

Hung-Jin Huang

Department of Physics
Carnegie Mellon University

Thesis Committee:
Rachel Mandelbaum (Chair)
Tim Eifler
Tiziana Di Matteo
Hy Trac

August 28, 2019

Submitted in partial fulfillment of the requirements
for the degree of Doctor of Philosophy.

Abstract

Large-scale structure surveys allow us to constrain cosmology through the growth of structure and the expansion history. Together with Cosmic Microwave Background (CMB) measurements from the early Universe, the standard ΛCDM with general relativity has become a concordance model that explains the origin and evolution of our Universe for over thirteen billion years. However, recent analyses reveal hints of tension between the early and late time Universe observables. The tension could point to new physics beyond ΛCDM, but could also be due to unknown systematic biases. Improving the precision and accuracy of cosmological measurements could be the key to a revolutionary new discovery about gravity on cosmological scales or about the nature dark energy. The challenges of cosmology in this era is to broadly explore and control possible systematics that could limit science from on going Stage III and future Stage IV surveys.

In this thesis, we investigate astrophysical systematics of intrinsic alignment (IA) and the baryonic physics that would contaminate the weak lensing observables.

Intrinsic alignment of galaxies arise under the effect of their local gravitational field. This effect mimics the shear correlation and introduces a systematic bias in the measured weak lensing signal. We carried out IA analyses using ~ 8000 redMaPPer clusters. There are two types of alignment within the one-halo scale: the alignment of the central galaxy with respect to the host halo shape and the radial alignment of satellite galaxies toward the halo center. For the central galaxy alignment, the mean misalignment angle between the central and cluster major axes is measured to be $\sim 35°$ (random alignments give 45°). The satellite galaxy alignment is a more subtle effect. We concluded that no net radial alignment signal is detected across the entire sample based on the re-Gaussianization shapes (the most conservative measurements). We also studied the dependence of IA signal on a total of 17 cluster and galaxy related properties in a concordant framework to properly account for parameter degeneracies. With several predictors identified for central and satellite alignments inside galaxy clusters, our results suggest that small-scale IA is a complicated phenomenon potentially involving multiple relevant physical processes during galaxy and cluster formation and evolution history.

The modification of the matter distribution due to baryonic physics is a non-negligible source of uncertainty for precision cosmology. Using various sets of hydrodynamical simulations, we investigated the effect of baryons on the matter power spectrum as functions of wavenumber frequency and redshift. We developed methodology to model the effect of baryons on weak lensing cosmic shear observables through the principal component analysis (PCA). We constructed mock cosmic shear observables with contamination from different hydrodynamical scenarios, and then performed PCA on the contaminated mock observable vectors. The resulting principal component (PC) modes are then form a set of efficient bases to span uncertainties of baryons in the observable data vector space. Overall, our results suggest that the effects of baryonic physics on cosmic shear power spectra can be efficiently captured and mitigated using a few linear combinations of PC modes.

Small-scale information in galaxy surveys has substantial statistical power to improve cosmological constraints, but conventional cosmological analyses discard this information to avoid biased inference on parameters due to lack of good astrophysical models for it. The continued developments on astrophysical modeling techniques in advance with better statistical quality of data will be essential in the new era of precision cosmology.

Acknowledgements

In completing this dissertation, I have received a great deal of support and assistance from many.

First and foremost, I would like to express my deepest appreciation to my advisor, Rachel Mandelbaum, for being a very supportive advisor and my role model as a great scientist. I have learned a lot from her keen insight behind plots and her persistence of pursuing high quality research until any scientific difficulty could be fully addressed to the limit. I feel really excited working together with her to explore the unknown and to make breakthroughs in the scientific front. I appreciate her encouragements when I was depressed, the freedom and resources she provided for me to explore things I am curious, her assistance on working with me to define research projects that maximally match my interests, and her guidance in shaping me into an independent researcher. I feel really happy to have Rachel as my advisor.

I would also like to thank my committee members for their constructive suggestions and comments in the progress of this thesis research. I would especially like to thank Tim Eifler for helping me understand the details of cosmological analyses, and for friendly sharing his experiences and little stories about the developments of the field along with our conversations. I anticipate continuing working with you in Tucson. I appreciate Hy Trac for kindly chatting with me when I need help, both scientifically and mentally. His encouragements have boosted my confidence for several times. I thank Tiziana Di Matteo for nicely discussing with me about hydrodynamical simulations for my baryon paper.

I must also thank my collaborators for their help and guidance in various projects. I am grateful to Scott Dodelson for many stimulating discussions with me. I benefited a lot from your unique vision behind equations and from your gravitational lensing course. I would also like to thank Peter Freeman for his contribution on statistical analyses in my intrinsic alignment papers and Yen-Chi Chen for answering many of my statistical questions when having lunch together. I thank Eduardo Rozo and Eli Rykoff for their assistance when I had questions about redMaPPer clusters and their comments on my paper. I deeply thank Yen-Ting Lin for involving me in several research projects, for teaching me many of the astrophysical knowledge which equipped me as a solid foundation on later studies, and for always nicely chatting with me and encouraging me while I came back to Taiwan.

I benefited a lot from the advices and discussions with researchers in Pittsburgh area. In particular, I would like to thank Yao-Yuan Mao for organizing many coding discussions for students, and for several constructive conversions during my job search, which helps me firmly moving forward. I also thank Simon Samuroff, Danielle Leonard, Francois Lanusse, Qirong Zhu, Arya Farahi, Markus Rau, Duncan Campbell, Mei-Yu Wang, Shadab Alam, Ying Zu, Alex Geringer-Sameth, Melanie Simet, Brett Andrews for always willing to listen to my questions and generously sharing their point of views. I have also received many helpful suggestions in my job season from friends I met when attending conferences, with special thanks to Hao-Yi Wu, Chieh-An Lin and Paulo Montero for sharing their experiences with me. I would also like to thank Alexie Leauthaud for inviting me to give a talk, providing guidance on my proposal and sharing the big picture development of the future field.

The department of physics of Carnegie Mellon University has provided a great environment for me to pursue my PhD. I had a wonderful time with my friends here. I thank the company of Siyu He, Hsiu-Hsien Lin, Yueying Ni, Tassia Ferreira, Aklant Bhowmick, Kuan-Wei Huang, Amy Stetten,

Evan Tucker, Zhonghao Luo, Hongyu Zhu, Mao-Sheng Liu, Husni Almoubayyed, Chien-Hao Lin, Abel Sun, Bai-Cian Ke, Larisa Thorne, Michael Sinko, Siddharth Satpathy, Yizhou He, Matthew Ho, Olga Navros, Shashin Pavaskar, I-Hsuan Kao, Nianyi Chen, Andresa Rodrigues de Campos, Tianqing Zhang, Diane Turnshek and many more for all the enjoyable conversations during working hours, lunches and dinners, and outdoor activities. I thank Manfred Paulini for being a really nice graduate program head and his help in providing solutions for the issues I had encountered. I also want to thank the efficient administrative staffs at the department for their assistance in many of my needs.

I feel so lucky to be able to extend the great memories from Taiwan to Unite States with my astronomy friends Wei-Ting Liao, Yu-Cian Hong, Yun-Hsin Huang, Jennifer Li, Joshua Yao-Yu Lin, Chun-Hao To, and Thomas Lai. I enjoyed several great trips we had arranged together to explore this continent, your visits to Pittsburgh playing with me, and for your entertainments durning my stays at your cities. I would like to thank my dear friends Jing-Hua Lin, Yen-Chu Ko, Kuan-Yu Chi, and Ji-Jia Tang for their continuous warm greetings during my PhD.

I am very grateful to my family for their endless support and for providing me with the opportunity to be where I am today. Their optimistic nature makes me feel reassuring when pursuing my PhD at several thousands of miles away from home. Last but not least, I would like to thank my dearest husband Sukhdeep Singh. Thank you for always patiently explaining and discussing scientific questions I came up with, for holding my hands passing through emotional ups and downs, for being so considerate and can always surprisingly make me laugh. I feel so fortunate to have your accompany in my life.

Contents

1 Introduction

Modern Cosmology

1.1 Modern Cosmology

The modern picture of cosmology is established from several milestones in the past century. After the completion of General Relativity (GR), Einstein derived the first mathematical model for the Universe from the field equations, based upon the cosmological principle stating that the Universe is spatially homogeneous and isotropic. He introduced the cosmological constant Λ, which provides repulsive gravity in opposition to the attractive matter gravity, in order to create a static Universe solution pivoted on his believe at that time. In 1922, Friedmann constructed GR-based cosmological models, now known as Friedmann equations, exploring both static and expanding solutions. In 1929, Hubble discovered that the recession velocities of galaxies are linearly related to their distances, providing a direct evidence on the expanding Universe. This tremendous discovery made Einstein declared that the idea of cosmological constant is the biggest blunder of his life, and proposed the Einstein–de Sitter Universe model with a vanishing cosmological constant (Einstein & de Sitter, 1932). The begin and continuous expansion of the Universe to the present day implies it must have been driven by some tremendous event in the past. This Hot Big Bang Theory was proven through the discovery of the cosmic microwave background (CMB; Penzias & Wilson 1965) in 1965. In the mid-1970s, the concept of dark matter caught people's attention in order to explain the motions of satellite galaxies (rotation curve) in our Milky Way and for other nearby spiral galaxies (Ostriker et al., 1974; Einasto et al., 1974). Actually, the origin on the idea of dark matter can be traced back to 1933. Zwicky studied the velocity dispersion of galaxies in the Coma cluster and proposed that ~400 times more mass compared with the ordinary matter in stars and gas (Zwicky, 1933) is necessary in order to hold this giant cluster together. In 1981, Alan Guth invented the theory of cosmic inflation which elegantly explain the two major problems in the standard cosmology at that time: the flatness (fine-tuning) problem and the homogeneity (horizon) problem. After that, the Einstein–de Sitter universe became particularly popular in the 1980s, with its zero spatial curvature assumption ($\Omega_\kappa = 0, \Omega_\mathrm{m} = 1, \Omega_\Lambda = 0$) being supported not only observationally from data, but also theoretically via inflation. From the distance-redshift relation of Type Ia Supernovae, in 1988, with the original goal of measuring the deceleration parameter predicted from a matter-dominated universe model, two independent research teams surprisingly find that the expansion rate of our Universe is accelerating (Riess et al., 1998; Perlmutter et al., 1999), revolutionized our understanding of the Universe. The concept of cosmological constant Λ was then taken back as a mysterious *dark energy* to drive the cosmic acceleration. The flat Λ–Cold Dark Matter (ΛCDM) model has become a widely accepted model in modern cosmology.

Since the 2000s, the field of cosmology entered the precision era with the launch of several cosmological experiments. Various cosmological probes from the larger sample size of supernova, higher resolution CMB data from the Wilkinson Microwave Anisotropy Probe (WMAP), baryon

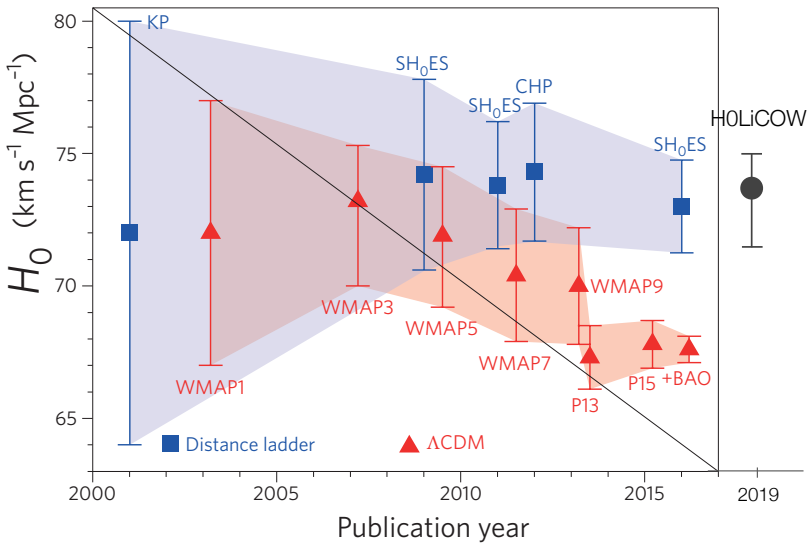

Figure 1.1: The current tension in the determination of H_0. The H_0 constraints as a function of publication date. The blue squires represent values of H_0 determined in the nearby Universe with a calibration based on the Cepheid distance scale. The red triangles show the derived values of H_0 based on CMB. The gray circle is a recent constraint from the H0LiCOW quasar time delay measurement. According to Wong et al. (2019), a combination of quasar time delay and the distance ladder constraints is in 5.3σ tension with the Planck CMB determinations of H_0 in flat ΛCDM. [Figure credit: Freedman 2017.]

acoustic oscillation (BAO), galaxy clustering and weak lensing from the CFHT Legacy Survey and the Sloan Digital Sky Survey (SDSS), and massive clusters in X-ray surveys, have shown concordance results within the ΛCDM framework, and have been pushing cosmological constraints to higher precision.

Despite the success of ΛCDM, the recent highest-resolution CMB measurements from the Planck satellite (Planck Collaboration et al., 2014, 2016, 2018) has revealed a tendency of tension with other low redshift cosmological probes. The largest deviation to date is the H_0 constraints between local estimates from Type Ia Supernovae and Planck CMB, revealing a $\sim 3\sigma$ tension, as shown in Fig. 1.1. Moreover, if combining the latest quasar time delay measurement with the local distance ladder constraints, the H_0 tension is reaching to 5.3σ (Wong et al., 2019) between late and early Universe.

Besides the tendency of tension in the expansion rate, there is also a mild ($< 3\sigma$) tension for the amplitudes of matter fluctuation (usually quantified as $S_8 = \sigma_8(\Omega_m/0.3)^\alpha$, $\alpha \approx 0.5$) between the Planck CMB and several on-going Stage III weak lensing cosmic shear constraints. As shown in Fig. 1.2, although within 3σ error bar the constraint from each cosmic shear experiment is in agreement with the Planck CMB, the S_8 constraints from all of the cosmic shear experiments are all appearing lower.

The potential tension between early and late-time Universe has arisen broad discussions and debates among different collaboration teams in the field of cosmology. Dose this imply new physics

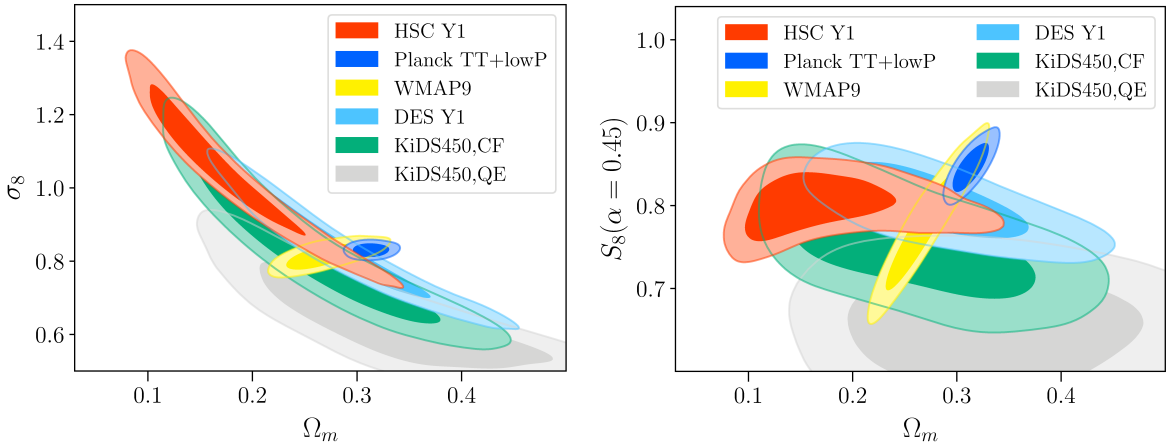

Figure 1.2: Marginalized posterior distributions for Ω_m, σ_8, and S_8 from several current Stage III cosmic shear constraints, overplotted with CMB results from the Planck2015 and WMAP9. HSC Y1 result is from Hikage et al. (2019), DES Y1 from Troxel et al. (2018), KiDS450 real space correlation function (CF) result from Hildebrandt et al. (2017), and KiDS450 Fourier space quadratic estimators (QE) from Köhlinger et al. (2017). [Figure credit: Hikage et al. 2019.]

beyond ΛCDM or purely be due to unrecognized systematic effects? So far, no general consensus could be reached given the statistical errors of current cosmological measurements. The next generation Stage IV cosmological experiments, e.g. CMB–S4 (Abazajian et al., 2016), LSST (The LSST Dark Energy Science Collaboration et al., 2018), DESI (DESI Collaboration et al., 2016), WFIRST (Doré et al., 2018), will lower the statistical uncertainty to sub-percent level, potentially deliver a factor of 2∼4 improvement in the dark energy figure of merit compared to the current Stage III surveys (Weinberg et al., 2013). The science output will become limited by our confidence on modeling systematic effects. Exploring the impact of systematics and developing mitigation strategics is becoming ever more important in preparation for future data sets.

In this dissertation, I focus on investigating astrophysical systematic effects associated with weak gravitational lensing, one of the primary cosmological probes to understand the effects of dark matter and dark energy through the growth of structure and global geometry of the Universe.

1.2 Weak Gravitational Lensing

Gravitational lensing is a fundamental phenomenon predicted from Einstein's theory of general relativity. The gravity from massive objects distorts the curvature of spacetime and causes light rays to bend and refocus at somewhere else, just as common glass lenses do. Gravitational lensing thus can be viewed as a "natural" telescope for us to observe dark masses in the Universe through their gravitational field as revealed from amount of light bending.

In the strong lensing regime, when light rays are distorted intensely to form multiple images, arcs, or Einstein rings, we can infer the lens mass, identify the existence of subhalos, or even reconstruct detailed mass map of the whole lens structure from the observed image. In the microlensing regime,

from the short-term magnification in the light curve of a distant star, we are capable of detecting the star's associated exoplanets. In the weak lensing regime, though with only tiny effect on the distortion of passing light rays, we can statistically extract the overall coherence of shape distortions from an ensemble source galaxies (or from the CMB map) to infer the global matter distribution in our Universe. Here I provide a brief overview on the theoretical framework of gravitational lensing with a special focus on weak lensing cosmic shear, the coherent galaxy shape distortions caused by large-scale structure of Universe. For a broader scope of gravitation lensing, we refer readers to Dodelson (2017) for detail.

1.2.1 The deflection of particles in General Relativity

Consider a particle passing by a compact object with mass M. The change of space-time geometry induced by M can be described by the perturbed metric $g_{\mu\nu}$:

$$\begin{aligned} g_{00} &= c^2(1 - \frac{2MG}{rc^2}) \\ g_{ij} &= -\delta_{ij}(1 + \frac{2MG}{rc^2}) \qquad \text{for } i, j = [1, 2, 3] \,. \end{aligned} \tag{1.1}$$

The geodesic equation that governs the motion of particles in coordinate x^i is:

$$\frac{\mathrm{d}^2 x^i}{\mathrm{d}\lambda^2} = -\Gamma^i_{\alpha\beta}\frac{\mathrm{d}x^\alpha}{\mathrm{d}\lambda}\frac{\mathrm{d}x^\beta}{\mathrm{d}\lambda} \,, \tag{1.2}$$

where $\Gamma^i_{\alpha\beta}$ is the Christoffel symbol related to the metric as:

$$\Gamma^i_{\alpha\beta} = \frac{g^{ij}}{2}\left[\frac{\partial g_{j\alpha}}{\partial x^\beta} + \frac{\partial g_{j\beta}}{\partial x^\alpha} - \frac{\partial g_{\alpha\beta}}{\partial x^j}\right] \,.^{1} \tag{1.3}$$

The $\frac{\mathrm{d}x^\alpha}{\mathrm{d}\lambda}$ is the four-momentum vector:

$$p^\alpha = \frac{\mathrm{d}x^\alpha}{\mathrm{d}\lambda} = (\frac{E}{c}, \mathbf{p}) \,. \tag{1.4}$$

Transforming the derivative to be with respect to time t, with some algebra ($\frac{\mathrm{d}x^i}{\mathrm{d}\lambda} = \frac{\mathrm{d}t}{\mathrm{d}\lambda}\frac{\mathrm{d}x^i}{\mathrm{d}\lambda} = \frac{E}{c}\frac{\mathrm{d}x^i}{\mathrm{d}t}$), we have:

$$\begin{aligned} \frac{\mathrm{d}^2 x^i}{\mathrm{d}t^2} &= -(\frac{c}{E})^2\,\Gamma^i_{\alpha\beta}p^\alpha p^\beta \\ &= -(\frac{c}{E})^2\left[\Gamma^i_{00}p^0p^0 + \Gamma^i_{jk}p^j p^k\right] \,. \end{aligned} \tag{1.5}$$

Under the Newtonian limit, for a non-relativistic particle ($\frac{E}{c} >> |\mathbf{p}|$), the first term in Eq. (1.5) would be way dominant, so

$$\frac{\mathrm{d}^2 x^i}{\mathrm{d}t^2} = -\frac{GMx^i}{r^3} \,. \tag{1.6}$$

For a photon, ($\frac{E}{c} = |\mathbf{p}|$), the first and the second terms of Eq. (1.5) have equal contributions, leading to a factor of 2 difference. The deflection equation of light from a point mass is:

$$\frac{\mathrm{d}^2 x^i}{\mathrm{d}t^2} = -2\frac{GMx^i}{r^3} \,. \tag{1.7}$$

[1] Since $g^{ij}g_{jk} = \delta^i_k$, we have $g^{ij} = (g_{ij})^{-1}$ here.

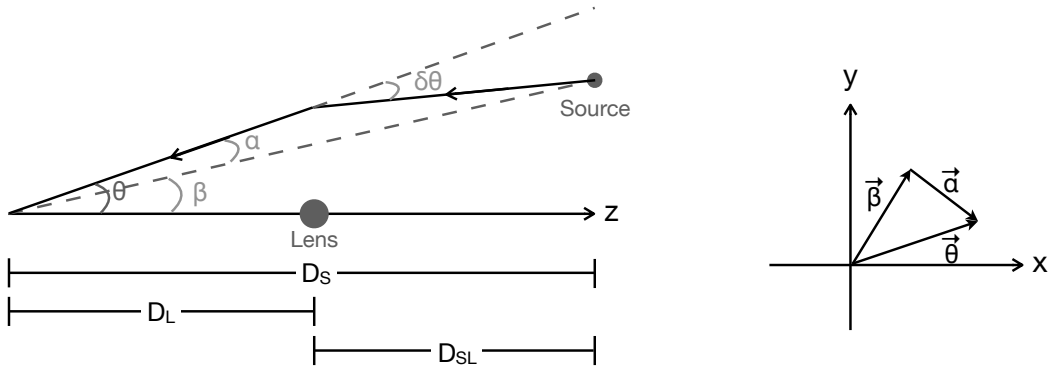

Figure 1.3: Gravitational lens system. [Left] Light from a source at distance D_S would be observed at θ, under the effect of lensing. The source would appear at angle β if not being deflected. The difference between the two angles is α. [Right] Angular vectors in the x–y plane perpendicular to the line of sight. The lens equation describes the relationship of angular positions: $\boldsymbol{\beta} = \boldsymbol{\theta} - \boldsymbol{\alpha}$. Under the choice of our convention, the distances D_L, D_S and $D_{SL} = D_S - D_L$ are the *comoving* angular-diameter distances from the observer to the lens, from the observer to the source, and from the lens to the source, respectively.

More generally, we can extend the format of Eq. (1.7) to a more complicated mass configuration, under the description of gravitational potential $\phi(\mathbf{x})$:

$$\begin{aligned} \phi(\mathbf{x}) &= -G \int \mathrm{d}^3 x' \frac{\rho(\mathbf{x}')}{|\mathbf{x} - \mathbf{x}'|} \,. \\ \phi(r) &= -\frac{MG}{r} \qquad \text{(for point mass)} \,. \end{aligned} \tag{1.8}$$

The deflection of light under the effect of gravitational potential ϕ is:

$$\frac{\mathrm{d}^2 x^i}{\mathrm{d}t^2} = -2 \frac{\partial \phi}{\partial x^i} \,. \tag{1.9}$$

1.2.2 The Lens Equation

The lens equation relates the true position of the source ($\boldsymbol{\beta}$) to its observed position ($\boldsymbol{\theta}$) on the sky, as demonstrated in Fig. 1.3 for a sketch of gravitational lens system. From simple geometry, we have:

$$\boldsymbol{\beta} = \boldsymbol{\theta} - \boldsymbol{\alpha}(\boldsymbol{\theta}) \,, \tag{1.10}$$

where $\boldsymbol{\alpha}$ is the deflection angle. Below we will try to derive $\boldsymbol{\alpha}$, for a given mass distribution along the line of sight (LOS).

Setting z-axis to be the LOS direction, as shown in Fig. 1.3, and assuming a small deflection angle, we can use the z position to label the photon trajectory with its relation with time t via $z = c(t_0 - t)$, with t_0 being the time we observed the light particle at our position $z = 0$. After the change of variable, Eq. (1.9) becomes:

$$\frac{\mathrm{d}^2 x^i(z)}{\mathrm{d}z^2} = -\frac{2}{c^2} \frac{\partial \phi(x^i, z)}{\partial x^i} \quad \text{for } i = [1,2], \text{ and } x^3 = z \,. \tag{1.11}$$

To derive the cumulated shift in the transverse direction ($x^i (i = 1, 2)$) of a photon during its travel history from $z = D_S$ to $z = 0$, we perform integration twice on Eq. (1.9):

$$\frac{\mathrm{d}x^i(z')}{\mathrm{d}z'} = C^i - \frac{2}{c^2}\int_0^{z'} \mathrm{d}z \frac{\partial\phi(x^i, z)}{\partial x^i} \quad \text{(first integration from } z = 0 \text{ to } z'), \tag{1.12}$$

where C^i is an integration constant. Integrate Eq. (1.12) to derive x^i:

$$x^i(z')\Big|_{z'=0}^{z'=D_S} = C'^i - \frac{2}{c^2}\int_0^{D_S} \mathrm{d}z' \int_0^{z'} \mathrm{d}z \frac{\partial\phi(x^i, z)}{\partial x^i} \quad \text{(Second integration from } z' = 0 \text{ to } D_S). \tag{1.13}$$

Here C'^i is another integration constant. The integrals on the RHS can be switched from $\int_0^{D_S} \mathrm{d}z' \int_0^{z'} \mathrm{d}z \rightarrow \int_0^{D_S} \mathrm{d}z \int_z^{D_S} \mathrm{d}z'$. For the LHS, use the fact that the true position of x^i at D_S is $D_S\beta^i$. Finally we get:

$$D_S\beta^i = D_S\theta^i - \frac{2}{c^2}\int_0^{D_S} \mathrm{d}z\, (D_S - z)\frac{\partial\phi(x^i, z)}{\partial x^i} \tag{1.14}$$

where C'^i is set to be $D_S\theta^i$ using the fact that if there is no gravitational effect along LOS ($\phi(x^i, z) = 0$), we expect $\boldsymbol{\beta} = \boldsymbol{\theta}$. Matching Eq. (1.10) with Eq. (1.14), the 2D deflection angle $\boldsymbol{\alpha}$ is:

$$\begin{aligned} \alpha^i &= \frac{2}{c^2 D_S}\int_0^{D_S} \mathrm{d}z\, (D_S - z)\frac{\partial\phi(x^i, z)}{\partial x^i} \\ &\rightarrow \frac{2}{c^2 D_S}\int_0^{D_S} \mathrm{d}z\, (D_S - z)\frac{\partial\phi(z\theta^i, z)}{\partial x^i} \quad \text{(Born Approximation)}. \end{aligned} \tag{1.15}$$

Ideally, we should evaluate $\phi(x^i, z)$ at position $x^i(z) = z\tilde{\theta}^i(z)$, with $\tilde{\theta}^i(z)$ being the actual fluctuated angular position along the photon trajectory reflecting the matter fluctuations along the LOS. But with the expectation of small perturbations on the deflection angle for most of cases, we can apply Born approximation, i.e. $\tilde{\theta}^i(z) \approx \theta^i$, and integrate along the LOS defined by this constant angular position. The deflection vector $\boldsymbol{\alpha}(\boldsymbol{\theta})$ is then purely a function of $\boldsymbol{\theta}$. Since the derivative with respect to $\frac{\partial}{\partial x^i}$ in Eq. (1.15) can be written as $\frac{1}{z}\frac{\partial}{\partial\theta^i}$, people also write $\boldsymbol{\alpha}$ as:

$$\alpha^i(\boldsymbol{\theta}) = \frac{1}{c^2}\frac{\partial\Phi(\boldsymbol{\theta})}{\partial\theta^i}, \tag{1.16}$$

with Φ being defined as the projected gravitational potential:

$$\Phi(\boldsymbol{\theta}) = 2\int_0^{D_S} \mathrm{d}D_L \frac{D_{SL}}{D_S D_L}\phi(D_L\boldsymbol{\theta}, D_L; t = t_0 - D_L/c). \tag{1.17}$$

Here we change the variable z to be D_L in Eq. (1.15), and $D_{SL} = D_S - D_L$. Under the choice of our convention, the distances D_L, D_S and D_{SL} are the *comoving* angular-diameter distances from the observer to the lens, from the observer to the source, and from the lens to the source, respectively.

1.2.3 Magnification (Convergence) and Distortion (Shear)

The lens equation ($\boldsymbol{\beta} = \boldsymbol{\theta} - \boldsymbol{\alpha}$) describes a mapping from the source position ($\boldsymbol{\beta}$) to the observed image position ($\boldsymbol{\theta}$). In the case of an extend source, each photon from the source plane travels through

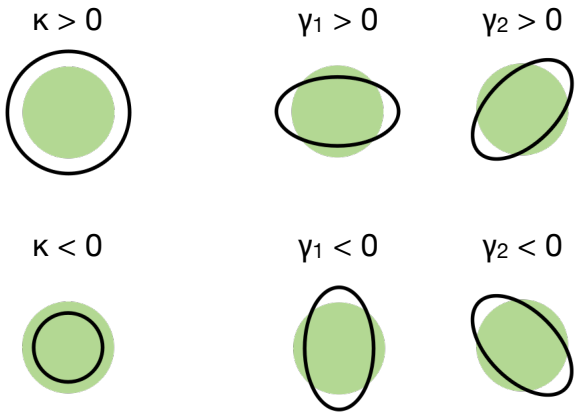

Figure 1.4: The effects of convergence and shear on an initially circular background object (green).

slightly different light path, ending up with a deformed shape on the image plane. The transformation can be characterized in a Jacobian matrix:

$$\begin{aligned}\frac{\partial\beta_i}{\partial\theta_j} &= \begin{pmatrix} 1-\frac{\partial\alpha_x}{\partial\theta_x} & -\frac{\partial\alpha_x}{\partial\theta_y} \\ -\frac{\partial\alpha_y}{\partial\theta_x} & 1-\frac{\partial\alpha_y}{\partial\theta_y}\end{pmatrix} = \delta_{ij} - \frac{\partial\alpha_i}{\partial\theta_j} = \delta_{ij} - \frac{1}{c^2}\frac{\partial^2\Phi}{\partial\theta_i\partial\theta_j} \text{ (using Eq. (1.16))} \\ &\equiv \begin{pmatrix} 1-\kappa-\gamma_1 & -\gamma_2 \\ -\gamma_2 & 1-\kappa+\gamma_1\end{pmatrix} = (1-\kappa)\begin{pmatrix} 1-g_1 & -g_2 \\ -g_2 & 1-g_1\end{pmatrix} .\end{aligned} \tag{1.18}$$

Here we relate the convergence κ and the shear components γ_1, γ_2 to the projected gravitational potential Φ as:

$$\begin{aligned}\kappa &\equiv \frac{1}{2c^2}\left(\frac{\partial^2\Phi}{\partial\theta_x^2} + \frac{\partial^2\Phi}{\partial\theta_y^2}\right) \\ \gamma_1 &\equiv \frac{1}{2c^2}\left(\frac{\partial^2\Phi}{\partial\theta_x^2} - \frac{\partial^2\Phi}{\partial\theta_y^2}\right) \\ \gamma_2 &\equiv \frac{1}{c^2}\frac{\partial^2\Phi}{\partial\theta_x\partial\theta_y} \\ g_i &\equiv \frac{\gamma_i}{1-\kappa} \to\approx \gamma_i \text{ (when } \kappa << 1, \text{ in the weak lensing regime)} .\end{aligned} \tag{1.19}$$

The convergence leads to a change in the angular size of an object, while the shear causes a distortion on the source shape, as demonstrated in Fig. 1.4. Observationally, since the intrinsic size of a galaxy is unknown, the only quantity we can measure is the *reduced shear*, g_i. In the weak lensing regime, when $|\kappa| << 1$, we have $|g_i| \approx \gamma_i$.

Substituting the projected gravitational potential in Eq. (1.17) into the κ shown in Eq. (1.19), we

obtain:

$$\begin{aligned}
\kappa(\boldsymbol{\theta}) &= \frac{1}{c^2 D_{\rm S}} \nabla_\theta^2 \int_0^{D_{\rm S}} {\rm d}D_{\rm L} \frac{D_{\rm SL}}{D_{\rm L}} \phi(x^i = D_{\rm L}\theta^i, D_{\rm L}) \\
\left(\nabla_\theta^2 = D_{\rm L}^2 \nabla_x^2\right) &\rightarrow \kappa(\boldsymbol{\theta}) = \frac{1}{c^2} \int_0^{D_{\rm S}} {\rm d} \frac{D_{\rm SL} D_{\rm L}}{D_{\rm S}} \nabla_x^2 \phi(x^i = D_{\rm L}\theta^i, D_{\rm L}) \\
\left(\nabla_x^2 \phi(\mathbf{x}, t) = 4\pi G \overline{\rho}_{\rm m}(t) a^2(t) \delta(\mathbf{x}, t) \quad ; \quad \overline{\rho}_{\rm m}(t) = \overline{\rho}_{\rm m}(t_0) a^{-3} = \Omega_{\rm m} \frac{3H_0^2}{8\pi G} a^{-3}\right) &\rightarrow \\
\kappa(\boldsymbol{\theta}) &= \int_0^{D_{\rm S}} {\rm d}D_{\rm L} \Big[\frac{3H_0^2}{2c^2} \frac{\Omega_{\rm m}}{a(D_{\rm L})} \frac{D_{\rm SL} D_{\rm L}}{D_{\rm S}}\Big] \delta(D_{\rm L}\boldsymbol{\theta}, D_{\rm L}) \, .
\end{aligned} \tag{1.20}$$

From the final format of Eq. (1.20), κ reflected as a measure of the over-density field integrated along the LOS with the weighting of some combination of distance ratios. People term this weighting factor as lensing kernel:

$$q(D_{\rm L}, D_{\rm S}) = \frac{3H_0^2}{2c^2} \frac{\Omega_{\rm m}}{a(D_{\rm L})} \frac{D_{\rm SL} D_{\rm L}}{D_{\rm S}} \, . \tag{1.21}$$

1.2.4 Two Point Statistics for Cosmic Shear

To extract the mass distribution of foreground LSS from the coherence of background galaxy shapes, two types of two point statistics are usually used to quantify the level of coherence: the cosmic shear power spectrum, or its real-space equivalent, the cosmic shear correlation function.

Cosmic Shear Power Spectrum

To construct the power spectrum, we take the Fourier transform of the shear components:

$$\tilde{\gamma}_{1,2}(\boldsymbol{\ell}) = \int {\rm d}^2\theta \gamma_{1,2}(\boldsymbol{\theta}) e^{-i\boldsymbol{\ell}\cdot\boldsymbol{\theta}} \quad \leftrightarrow \quad \gamma_{1,2}(\boldsymbol{\theta}) = \int \frac{{\rm d}^2\ell}{(2\pi)^2} \tilde{\gamma}_{1,2}(\boldsymbol{\ell}) e^{i\boldsymbol{\ell}\cdot\boldsymbol{\theta}} \, . \tag{1.22}$$

Using the replacement $\frac{\partial}{\partial\theta_i} \rightarrow i\ell_i$ in Eq. 1.19, in Fourier space we have:

$$\begin{aligned}
\tilde{\kappa}(\boldsymbol{\ell}) &= -\frac{\ell^2}{2c^2} \tilde{\Phi}(\boldsymbol{\ell}) \\
\tilde{\gamma}_1(\boldsymbol{\ell}) &= -\frac{\ell_x^2 - \ell_y^2}{2c^2} \tilde{\Phi}(\boldsymbol{\ell}) = -\frac{\ell^2}{2c^2} \tilde{\Phi}(\boldsymbol{\ell}) [\cos^2(\phi_\ell) - \sin^2(\phi_\ell)] = -\frac{\ell^2}{2c^2} \tilde{\Phi}(\boldsymbol{\ell}) \cos(2\phi_\ell) \\
\tilde{\gamma}_2(\boldsymbol{\ell}) &= -\frac{\ell_x \ell_y}{c^2} \tilde{\Phi}(\boldsymbol{\ell}) = -\frac{\ell^2}{2c^2} \tilde{\Phi}(\boldsymbol{\ell}) [2\sin(\phi_\ell)\cos(\phi_\ell)] = -\frac{\ell^2}{2c^2} \tilde{\Phi}(\boldsymbol{\ell}) \sin(2\phi_\ell) \, .
\end{aligned} \tag{1.23}$$

with the angle ϕ_ℓ being defined such that $\tan(\phi_\ell) = \ell_y/\ell_x$.

It is convenient to rotate the Fourier-space components to a basis aligned with the direction of the wave vector $\boldsymbol{\ell}$. The rotated components are called the E-mode and B-mode:

$$\begin{pmatrix} \tilde{\gamma}_E(\boldsymbol{\ell}) \\ \tilde{\gamma}_B(\boldsymbol{\ell}) \end{pmatrix} = \begin{pmatrix} \cos(2\phi_\ell) & \sin(2\phi_\ell) \\ -\sin(2\phi_\ell) & \cos(2\phi_\ell) \end{pmatrix} \begin{pmatrix} \tilde{\gamma}_1(\boldsymbol{\ell}) \\ \tilde{\gamma}_2(\boldsymbol{\ell}) \end{pmatrix} = \begin{pmatrix} \tilde{\kappa}(\boldsymbol{\ell}) \\ 0 \end{pmatrix} \, . \tag{1.24}$$

After rotation, the E-mode is equal to $\tilde{\kappa}(\boldsymbol{\ell})$, and therefore carries the main information of lensing. The B-mode should vanish, and therefore can be used to check for residual systematic errors.

To derive the full expression of $\tilde{\kappa}(\boldsymbol{\ell})$, we take Fourier transform of Eq. (1.20) as defined in Eq. (1.22):

$$\begin{aligned}
&\tilde{\kappa}(\boldsymbol{\ell}) = \int \mathrm{d}^2\theta e^{-i\boldsymbol{\ell}\cdot\boldsymbol{\theta}} \int_0^{D_\mathrm{S}} \mathrm{d}D_\mathrm{L} q(D_\mathrm{L}, D_\mathrm{S}) \delta(D_\mathrm{L}\boldsymbol{\theta}, D_\mathrm{L}) \\
&\left(\delta(D_\mathrm{L}\boldsymbol{\theta}, D_\mathrm{L}) = \int \frac{\mathrm{d}^3k}{(2\pi)^3} e^{i\mathbf{k}\cdot(D_\mathrm{L}\theta_x, D_\mathrm{L}\theta_y, D_\mathrm{L})} \tilde{\delta}(\mathbf{k}) = \int \frac{\mathrm{d}k_z}{2\pi} e^{ik_z D_\mathrm{L}} \int \frac{\mathrm{d}^2k_\perp}{(2\pi)^2} e^{i\mathbf{k}_\perp\cdot D_\mathrm{L}\boldsymbol{\theta}} \tilde{\delta}(\mathbf{k}_\perp, k_z) \right) \rightarrow \\
&\tilde{\kappa}(\boldsymbol{\ell}) = \int_0^{D_\mathrm{S}} \mathrm{d}D_\mathrm{L} q(D_\mathrm{L}, D_\mathrm{S}) \int \frac{\mathrm{d}k_z}{2\pi} e^{ik_z D_\mathrm{L}} \int \mathrm{d}^2k_\perp \Big[\int \frac{\mathrm{d}^2\theta}{(2\pi)^2} e^{-i(\boldsymbol{\ell} - D_\mathrm{L}\mathbf{k}_\perp)\cdot\boldsymbol{\theta}} \Big] \tilde{\delta}(\mathbf{k}_\perp, k_z) \\
&\left(\int \frac{\mathrm{d}^2\theta}{(2\pi)^2} e^{-i(\boldsymbol{\ell} - D_\mathrm{L}\mathbf{k}_\perp)\cdot\boldsymbol{\theta}} = \delta_\mathrm{D}^2(D_\mathrm{L}\mathbf{k}_\perp - \boldsymbol{\ell}) = \frac{1}{D_\mathrm{L}^2} \delta_\mathrm{D}^2(\mathbf{k}_\perp - \frac{\boldsymbol{\ell}}{D_\mathrm{L}}) \right) \rightarrow \\
&\tilde{\kappa}(\boldsymbol{\ell}) = \int_0^{D_\mathrm{S}} \mathrm{d}D_\mathrm{L} \frac{q(D_\mathrm{L}, D_\mathrm{S})}{D_\mathrm{L}^2} \int \frac{\mathrm{d}k_z}{2\pi} e^{ik_z D_\mathrm{L}} \tilde{\delta}(\frac{\boldsymbol{\ell}}{D_\mathrm{L}}, k_z)
\end{aligned} \tag{1.25}$$

The 2D cosmic shear (convergence) power spectrum is defined as:

$$\left\langle \tilde{\gamma}_E(\boldsymbol{\ell}) \tilde{\gamma}_E(\boldsymbol{\ell}') \right\rangle = \left\langle \tilde{\kappa}(\boldsymbol{\ell}) \tilde{\kappa}(\boldsymbol{\ell}') \right\rangle = (2\pi)^2 \delta_\mathrm{D}^2(\boldsymbol{\ell} + \boldsymbol{\ell}') C_{\kappa\kappa}(\boldsymbol{\ell}) \,, \tag{1.26}$$

and can be equivalently derived starting from

$$\begin{aligned}
C_{\kappa\kappa}(\boldsymbol{\ell}) &= \int \frac{\mathrm{d}^2\ell'}{(2\pi)^2} \left\langle \tilde{\kappa}(\boldsymbol{\ell}) \tilde{\kappa}(\boldsymbol{\ell}') \right\rangle \\
&= \int \frac{\mathrm{d}^2\ell'}{(2\pi)^2} \int_0^{D_\mathrm{S}} \mathrm{d}D_\mathrm{L} \frac{q(D_\mathrm{L}, D_\mathrm{S})}{D_\mathrm{L}^2} \int \frac{\mathrm{d}k_z}{2\pi} e^{ik_z D_\mathrm{L}} \int_0^{D_\mathrm{S}} \mathrm{d}D'_\mathrm{L} \frac{q(D'_\mathrm{L}, D_\mathrm{S})}{D'^2_\mathrm{L}} \int \frac{\mathrm{d}k'_z}{2\pi} e^{ik'_z D'_\mathrm{L}} \left\langle \tilde{\delta}(\frac{\boldsymbol{\ell}}{D_\mathrm{L}}, k_z) \tilde{\delta}(\frac{\boldsymbol{\ell}'}{D'_\mathrm{L}}, k'_z) \right\rangle \,.
\end{aligned} \tag{1.27}$$

Based on the definition of 3D matter power spectrum:

$$\left\langle \tilde{\delta}(\mathbf{k}) \tilde{\delta}(\mathbf{k}') \right\rangle = (2\pi)^3 \delta_\mathrm{D}^3(\mathbf{k} + \mathbf{k}') P(\mathbf{k}) \tag{1.28}$$

we can replace the $\left\langle \tilde{\delta}\tilde{\delta} \right\rangle$ term in Eq. (1.27) as:

$$\begin{aligned}
\left\langle \tilde{\delta}(\frac{\boldsymbol{\ell}}{D_\mathrm{L}}, k_z) \tilde{\delta}(\frac{\boldsymbol{\ell}'}{D'_\mathrm{L}}, k'_z) \right\rangle &= (2\pi)^3 \delta_\mathrm{D}(k_z + k'_z) \delta_\mathrm{D}^2(\frac{\boldsymbol{\ell}}{D_\mathrm{L}} + \frac{\boldsymbol{\ell}'}{D'_\mathrm{L}}) P(\frac{\boldsymbol{\ell}}{D_\mathrm{L}}, k_z) \\
&= (2\pi)^3 \delta_\mathrm{D}(k_z + k'_z) D'^2_\mathrm{L} \delta_\mathrm{D}^2(\boldsymbol{\ell}' + \frac{D'_\mathrm{L}}{D_\mathrm{L}} \boldsymbol{\ell}) P(\frac{\boldsymbol{\ell}}{D_\mathrm{L}}, k_z) \,.
\end{aligned} \tag{1.29}$$

Putting it back to continue Eq. (1.27), and with $\int \frac{\mathrm{d}k_z}{2\pi} e^{ik_z(D_\mathrm{L} - D'_\mathrm{L})} = \delta_\mathrm{D}(D_\mathrm{L} - D'_\mathrm{L})$, we have:

$$C_{\kappa\kappa}(\boldsymbol{\ell}) = \int_0^{D_\mathrm{S}} \mathrm{d}D_\mathrm{L} \frac{q^2(D_\mathrm{L}, D_\mathrm{S})}{D_\mathrm{L}^2} P(\frac{\boldsymbol{\ell}}{D_\mathrm{L}}, k_z; a(D_\mathrm{L})) \,. \tag{1.30}$$

Finally, for smaller angular power scales $\ell > 50$, we usually apply Limber's approximation (Limber, 1953) to relate the physical scale ($\mathbf{k}$) of the 3D matter power spectrum to the angular scale ($\boldsymbol{\ell}$) of the projected 2D convergence power spectrum when taking integration in Eq. (1.30):

$$P(\frac{\boldsymbol{\ell}}{D_\mathrm{L}}, k_z; a(D_\mathrm{L})) \approx P(\frac{\ell}{D_\mathrm{L}}; a(D_\mathrm{L})) \,. \tag{1.31}$$

As revealed from Limber approximation, the (smaller scale) LOS modes (i.e. $k_z D_\mathrm{L} \gg 1$) do not contribute to the integral; for the transverse direction, the dominant contribution comes from wavenumbers that satisfy $k_\perp D_\mathrm{L} \sim \ell$. This is because for perturbation scales that vary rapidly along the LOS or along the transverse direction, we expect the fluctuations between under- and over-dense regions end up cancelling their contributions with the integral. Also from the basic cosmological principal of isotropy, we can change the vector $\boldsymbol{\ell}$ to simply a scale ℓ in Eq. (1.30). The lensing kernel term, as defined in Eq. (1.21) for a single source galaxy at certain distance D_S can be generalized to for an ensemble of source galaxies given their redshift distribution $n_\mathrm{S}(z)$:

$$q(D_\mathrm{L}) = \frac{3H_0^2}{2c^2}\frac{\Omega_\mathrm{m}}{a(D_\mathrm{L})}\int_0^{\chi_\mathrm{h}} \mathrm{d}z\, n_\mathrm{S}(z)\frac{D_\mathrm{SL}(z)D_\mathrm{L}}{D_\mathrm{S}(z)}\,\Theta(D_\mathrm{S}(z) - D_\mathrm{L})\,, \tag{1.32}$$

where Θ is a step function with value of 1 if $D_\mathrm{S}(z) > D_\mathrm{L}$, and 0 otherwise. The upper integration limit χ_h is the comoving horizon distance which represents the observable boundary of our Universe.

To gain more information from cosmological evolution at different epochs, we can split the source galaxies into few redshift slices, and conduct tomographic analysis (Hu, 1999) by taking auto- and cross correlations between two redshift slices of source samples:

$$C^{ij}_{\kappa\kappa}(\ell) = \int_0^{\chi_\mathrm{h}} \mathrm{d}D_\mathrm{L}\frac{q^i(D_\mathrm{L})q^j(D_\mathrm{L})}{D_\mathrm{L}^2}P(\frac{\ell}{D_\mathrm{L}}; a(D_\mathrm{L}))\,, \tag{1.33}$$

where i, j are indices for tomographic bins. The redshift evolution can then be extracted via different weightings as absorbed in the lensing kernels. The tomographic technique also helps break parameter degeneracies in some level through their different dependencies with redshift.

Cosmic Shear Correlation Function

The real space correlation function of cosmic shear is defined as:

$$\begin{aligned}\xi_\pm(\boldsymbol{\theta}) &= \langle\gamma_1(\boldsymbol{\theta}_0)\gamma_1(\boldsymbol{\theta}_0+\boldsymbol{\theta})\rangle_{\boldsymbol{\theta}_0} \pm \langle\gamma_2(\boldsymbol{\theta}_0)\gamma_2(\boldsymbol{\theta}_0+\boldsymbol{\theta})\rangle_{\boldsymbol{\theta}_0} \\ &\to = \langle\gamma_1(\mathbf{0})\gamma_1(\boldsymbol{\theta})\rangle \pm \langle\gamma_2(\mathbf{0})\gamma_2(\boldsymbol{\theta})\rangle\ ,\end{aligned} \tag{1.34}$$

where the average is taken over every pair of shears considered as coordinated in $\boldsymbol{\theta}_0$. Alternatively, we can view $\boldsymbol{\theta}$ as the pair separation vector, and simply set the reference point $\boldsymbol{\theta}_0 = \mathbf{0}$ for every pair. Using the Fourier expression of $\gamma_{1,2}$ as defined in Eq. (1.22), we have:

$$\xi_\pm(\boldsymbol{\theta}) = \int\frac{\mathrm{d}\ell^2}{(2\pi)^2}\int\frac{\mathrm{d}\ell'^2}{(2\pi)^2}\left\langle\tilde{\gamma}_1(\boldsymbol{\ell})\tilde{\gamma}_1(\boldsymbol{\ell'}) \pm \tilde{\gamma}_2(\boldsymbol{\ell})\tilde{\gamma}_2(\boldsymbol{\ell'})\right\rangle e^{i\boldsymbol{\ell}\cdot\boldsymbol{\theta}}\,. \tag{1.35}$$

We can use the 2D plane wave expansion to expand the $e^{i\boldsymbol{\ell}\cdot\boldsymbol{\theta}}$ term in Eq. (1.35):

$$e^{i\boldsymbol{\ell}\cdot\boldsymbol{\theta}} = e^{i\ell\theta\,\cos(\phi_\ell-\phi_\theta)} = \sum_{\mathrm{n}=-\infty}^{\infty} i^\mathrm{n} J_\mathrm{n}(\ell\theta)e^{i\mathrm{n}(\phi_\ell-\phi_\theta)}\,, \tag{1.36}$$

with the angle ϕ_ℓ and ϕ_θ being defined such that $\tan(\phi_\ell) = \ell_y/\ell_x$ and $\tan(\phi_\theta) = \theta_y/\theta_x$. J_n are spherical Bessel functions.

Based on Eq. (1.24), with the coordinate rotation, we can express $\tilde{\gamma}_{1,2}$ in terms of $\tilde{\gamma}_{E,B}$:

$$\begin{aligned}\tilde{\gamma}_1^2 + \tilde{\gamma}_2^2 &= \tilde{\gamma}_E^2 + \tilde{\gamma}_B^2 = \tilde{\gamma}_E^2 \\ \tilde{\gamma}_1^2 - \tilde{\gamma}_2^2 &= \cos 4\phi_\ell\ \tilde{\gamma}_E^2 - \cos 4\phi_\ell\ \tilde{\gamma}_B^2 - 2\sin 4\phi_\ell\ \tilde{\gamma}_E\tilde{\gamma}_B = \cos 4\phi_\ell\ \tilde{\gamma}_E^2\ .\end{aligned} \tag{1.37}$$

According to Eq. (1.24), we expect $\tilde{\gamma}_B = 0$. Also based on the isotropy cosmological principal, we have $\xi_\pm(\boldsymbol{\theta}) = \xi_\pm(\theta)$; there is no special direction for $\boldsymbol{\theta}$ and thus we can set $\phi_\theta = 0$ without loss of generation. Using the definition of Eq. (1.26), and applied these replacements back to Eq. (1.35), we have:

$$\begin{aligned}\xi_+(\theta) &= \int \frac{\mathrm{d}\ell^2}{(2\pi)^2} C_{\kappa\kappa}(\ell) \sum_{\mathrm{n}=-\infty}^{\infty} i^{\mathrm{n}} J_{\mathrm{n}}(\ell\theta) e^{i\mathrm{n}\phi_\ell} \\ \xi_-(\theta) &= \int \frac{\mathrm{d}\ell^2}{(2\pi)^2} C_{\kappa\kappa}(\ell) \cos 4\phi_\ell \sum_{\mathrm{n}=-\infty}^{\infty} i^{\mathrm{n}} J_{\mathrm{n}}(\ell\theta) e^{i\mathrm{n}\phi_\ell}\ .\end{aligned} \tag{1.38}$$

For ξ_+ (ξ_-), only the n = 0 (n = 4) term would contribute to the integral. With the replacement $\int \mathrm{d}\ell^2 \to \int \mathrm{d}\ell\ 2\pi\ell$, and with the tomographic indices added, we reach the final expression of $\xi_\pm$ as:

$$\xi_{+/-}^{ij}(\theta) = \int \frac{\mathrm{d}\ell}{2\pi} \ell C_{\kappa\kappa}^{ij}(\ell) J_{0/4}(\ell\theta)\ . \tag{1.39}$$

Observationally, it is more straightforward to measure correlation function due to the discreteness of galaxy distribution and the complex survey geometry. While from the modeling perspective, it is easier to make theory prediction, to define scale cuts or to compute covariance matrix in power spectrum, since data points are less correlated in Fourier space. In principal, the cosmic shear power spectrum and correlation function carry the same amount of information when considering full range of scales. In practice, cosmological analyses from correlation function or power spectrum would lead to different parameter constrains (see Köhlinger et al. 2017; Hildebrandt et al. 2017 for KiDS-450 and Hikage et al. 2019; Hamana et al. 2019 for HSC Y1 cosmic shear analyses). This is primary driven by drawing information from different multipole ranges, with the analyses from correlation function usually including more information from small scales.

1.3 Weak Lensing Systematic Effects

A great amount of progress have been accumulated in the past decade to overcome various challenges, pushing weak lensing to be a precision cosmological probe. Here I briefly summarize a few most notable systematic uncertainties for weak lensing, including the shear calibration and the photometric redshift errors, the intrinsic alignment of galaxies, and the uncertainty of baryonic effects on the matter power spectrum. For a more detailed review on the technical developments of weak lensing, from raw images to scientific inferences, one can take Mandelbaum (2018) for reference.

1.3.1 Shape measurement

The success of weak lensing is based on high precision galaxy shape measurement technique, in order to robustly extract the tiny coherent shear signal from the nearly random distribution of galaxy

ellipticity. Measuring galaxy shapes has long been a tough task due to a variety of difficulties to overcome:

- The clumpiness and asymmetric nature of galaxy light profile complicates the parametrization on galaxy morphology.
- The observed images are blurred by perturbations in the atmosphere and instrument. This blurring effect is characterized via the point spread function (PSF).
- Other detecter systematics that cannot be simply treated as a PSF convolution, such as the brighter-fatter effect (Antilogus et al., 2014).
- Blending of light among nearby objects.

To the linear order, the systematic error in shear measurement is commonly parametrized with the multiplicative and the additive components:

$$\hat{\gamma}_i = (1 + m)\gamma_i + c_i \ . \tag{1.40}$$

The multiplicative bias m depends on γ, contributing in making galaxies appear rounder or more elliptical. The addictive bias c_i leads to modifications on the sheared direction. Additive systematics are easier to identify by designing null tests from data itself. For example through the non-zero B mode detection or by cross-correlating the shapes of stars with the PSF-corrected galaxy shapes to help identify modeling errors from PSF (Mandelbaum, 2018). In contrast, multiplicative bias is harder to estimate, as it only causes a constant shift in the lensing shear correlations without special pattern in terms of scale dependence. Typically, image simulations are required to understand the biases from the adopted shear estimation algorithm. It is however challenging to simulate highly realistic images as required for future surveys given our limited knowledge of galaxies. Recent development of the metacalibration technique, a self-calibration method to calibrate shear biases based on manipulations of the real images, would be a promising way to estimate calibration factors from real galaxy populations of the data (Huff & Mandelbaum, 2017; Sheldon & Huff, 2017).

1.3.2 Photometric redshift

Photometric redshift (photo-z) is a technique of approximating a galaxy's distance from the information of its broad-band spectral energy distribution (SED). The cheap time requirement of photo-z allows the weak lensing cosmological experiment possible in compromise with current technology. To derive the weak lensing signal, a lot of source galaxies are required, and it would be too expensive to perform spectroscopy follow up for every single galaxy.

The basic principal of photo-z is that the SED of galaxies are not too diversified, so with a set of templates of galaxy SEDs, we can evolve the galaxy photometry as a function of redshift to match with the observed photometry (Ilbert et al., 2006). There are also machine learning based methods, which uses a representative spectroscopic training sample to learn the relationship between photometries and redshifts (Firth et al., 2003).

Generally, the photo-z technique works specifically well for galaxy types with distinct spectral feature across bands, like the red and dead galaxies with the 4000 Å break. However, with insufficient number of photometric bands available, the photo-z estimation would sometimes yield a completely wrong redshift. The catastrophic outliers would cause biases in cosmology constraints if their fraction

is too large over the entire sample. Also, there is always an issue for our control on the diversity of galaxy SEDs from the available training spectroscopic redshift samples, given the complexity in galaxy formation physics (Newman et al., 2015). Developing other independent methods of photo-z is thus important to increase the reliability of our estimation.

Another popular method of estimating photo-z is by taking cross correlation between the photometric galaxy sample with a given spectroscopic sample (Newman, 2008). The clustering signal would show up only when the two populations of galaxies are physically located in the same redshift interval, because galaxies are only clustered over narrow range of cosmological scales. One major uncertainty of this method is that the clustering signal is degenerate with the redshift evolution of galaxy bias. Also to avoid the modeling challenge on non-linear galaxy bias, one would need to perform clustering over large sky area, which would require large survey of spectroscopic sample. The other systematic effect of clustering signal is the magnification bias originating from the lensing effect. The lensing effect from the foreground (spectroscopic) object increases the brightness of its background sources, leading to some extra clustering signal even when the two samples are not physically located in the same redshift interval (see e.g. Singh et al. 2019).

Obtaining tight constrains on the redshift distribution of source galaxies help driving better cosmological constraints due to the break of degeneracies among cosmology and other systematic effects through the distinction in their redshift evolutions. However, current photo-z pipelines from independent collaboration teams have not yet reached consistent agreements, which places potential tensions on the cosmological constraint. For example, the photo-z constraints from the Dark Energy Survey (DES) year one (Y1) are a combined results from two independent photo-z calibration methods (Hoyle et al., 2018): the template-fitting method calibrated with the high-quality photometric redshift catalog in the COSMOS field (Laigle et al., 2016), and the cross-correlation method with the redMaGiC galaxy sample. Recently, the Kilo Degree Survey (KiDs) survey team applied their photo-z pipeline, which is calibrated based on several available spectroscopic surveys, on the DES-Y1 data, and derived consistently higher mean redshifts across tomographic bins. Adopting the revised redshifts leads to a 0.8σ shift in the S_8 constraint compared with the original DES-Y1 result (Joudaki et al., 2019). This highlights the importance of developing accurate photo-z calibration methods for current and future weak lensing surveys.

1.3.3 Intrinsic alignment

An underlying assumption of gravitational lensing is that in the absence of lensing, galaxies are randomly oriented in the sky with their ellipticity averaged to zero, i.e. $\langle e_i \rangle = 0$; any net anisotropy measured in an ensemble of galaxy shapes then can simply be resorted to the effect of lensing, linking with the density fluctuations in the foreground. The effect of intrinsic alignment (IA) violates this simple assumption. Galaxies are observed showing alignment patterns even in the linear regime (Mandelbaum et al., 2006; Singh et al., 2015), at a significance level of that can not be ignored given the current precision of cosmological survey.

In the presence of IA, the contaminated shear can be expressed as:

$$\gamma = \gamma_{\rm G} + \gamma_{\rm I} \tag{1.41}$$

where $\gamma_{\rm G}$ is the lensing shear, and $\gamma_{\rm I}$ represents for the intrinsic alignment component. Propagating

into the two-point statistics, we have:

$$\begin{aligned}\langle\gamma\gamma\rangle &= \langle\gamma_{\rm G}\gamma_{\rm G} + \gamma_{\rm G}\gamma_{\rm I} + \gamma_{\rm I}\gamma_{\rm G} + \gamma_{\rm I}\gamma_{\rm I}\rangle \\ C^{ij}_{\gamma\gamma}(\ell) &= C^{ij}_{\rm GG}(\ell) + C^{ij}_{\rm GI}(\ell) + C^{ij}_{\rm IG}(\ell) + C^{ij}_{\rm II}(\ell)\ .\end{aligned} \tag{1.42}$$

The GG term is the true cosmic shear signal of interest, with its full expression shown in Eq. (1.33). The GI and II terms are for IA contamination. The II term is the intrinsic-intrinsic shape correlation induced by local gravity on pairs of source galaxies, while the GI term stands for the lensing-intrinsic shape correlations for pairs of galaxies with the foreground one being tidally torqued and the background one being sheared under the effect of the same gravitational field. Mathematically, they can be expressed as:

$$\begin{aligned}C^{ij}_{\rm II}(\ell) &= \int_0^{\chi_{\rm h}} {\rm d}\chi_{\rm s} \frac{n^i_{\rm s}(\chi_{\rm s}) n^j_{\rm s}(\chi_{\rm s})}{\chi^2_{\rm s}} P_{\rm II}(k = \frac{\ell}{\chi_{\rm s}}, \chi_{\rm s}) \\ C^{ij}_{\rm GI}(\ell) + C^{ij}_{\rm IG}(\ell) &= \int_0^{\chi_{\rm h}} {\rm d}\chi \frac{g^i(\chi) n^j_{\rm s}(\chi) + n^i_{\rm s}(\chi) g^j(\chi)}{\chi^2} P_{\rm GI}(k = \frac{\ell}{\chi}, \chi)\ .\end{aligned} \tag{1.43}$$

The $n^i_{\rm s}(\chi_{\rm s})$ in the II term stands for the probability density function (pdf) for the redshift distribution of source galaxies in tomographic bin i, with $\chi_{\rm s}$ being the comoving angular diameter distance to the source galaxy (which is the same as the $D_{\rm S}$ convention in **Chapter** 1.2). As revealed in the equation, $C^{ij}_{\rm II}(\ell)$ would only show values when there is an overlap in the source redshift pdf between tomographic bins i and j. The $g^i(\chi)$ function in the GI term is the lensing kernel for tomographic bin i as defined in Eq. (1.32), below we rewrite it in the format of integration with respect to (comoving) distance χ rather than to redshift:

$$g^i(\chi) = \frac{3}{2}\frac{H_0^2\Omega_{\rm m}}{c^2}\frac{\chi}{a(\chi)}\int_\chi^{\chi_{\rm h}} {\rm d}\chi_{\rm s} n^i_{\rm s}(\chi_{\rm s})\frac{\chi_{\rm s} - \chi}{\chi_{\rm s}}\ , \tag{1.44}$$

with the effect of step function being absorbed in the lower limit of the integral. One can find that $g^i(\chi)$ only has a non-zero value when χ is less than the farthest distance $\chi_{\rm s}$ that $n^i_{\rm s}(\chi_{\rm s})$ can reach. Given this fact, the GI term would be zero when cross correlating lower redshift lensing shear in tomographic bin j ($g^j(\chi)$) with higher redshift intrinsic shape tomographic bin i ($n^i(\chi)$). This can be understood from the fact that the density fluctuations of and below the lower redshift bin j should not be correlated with the local gravitational filed in the higher redshift tomographic bin i. However this statement would not be true if there is an overlap in redshift between tomographic bins i and j, or when there is an error in photometric redshift.

The $P_{\rm II}$ and $P_{\rm GI}$ terms in Eq. (1.43) are the IA power spectra, controlling the overall amplitude and scale dependence of IA. There are several models of IA with varying levels of complexity. Assuming a linear relationship between the strength of IA and the local tidal field, the tidal alignment paradigm has been successfully applied to model the observed IA signal for elliptical galaxies on linear scales with the linear alignment (LA) model (Catelan et al., 2001; Hirata & Seljak, 2004a), and to the quasi-linear regime with the extension of non-linear alignment (NLA) model (Bridle & King, 2007). Under the

tidal alignment paradigm:

$$\begin{aligned} P_{\rm II}(k,z) &= A^2(z)P_\delta(k,z) \\ P_{\rm GI}(k,z) &= A(z)P_\delta(k,z) \\ A(z) &= -A_{\rm IA}C_1\frac{3H_0^2\Omega_{\rm m}}{8\pi G}\frac{1}{D(z)}\left(\frac{1+z}{1+z_0}\right)^{\eta_{\rm IA}} . \end{aligned} \tag{1.45}$$

Here $D(z)$ is the linear growth factor, normalized to unity at $z = 0$; C_1 is the normalization constant being set at 5×10^{-14} $\mathrm{M}_\odot^{-1}h^{-2}\mathrm{Mpc}^3$ (Brown et al., 2002). In the original LA model, $P_\delta(k,z)$ is set to be the linear matter power spectrum. The NLA model replaces this part with the non-linear power spectrum to extend the model coverage to quasi-linear scales. The degrees of freedom for redshift evolution is captured in $\eta_{\rm IA}$, reflecting the combined effects on the evolution of IA amplitude and the evolution of galaxy sample selection effect. The z_0 is the pivot redshift. There are also other variants of IA modeling with different parameterizations on the redshift evolution, or considering the luminosity dependence of galaxy sample (see e.g. Krause et al. 2016).

Beyond the linear order, the quadratic alignment model (Lee & Pen, 2000) is proposed to describe IA for spiral galaxies through tidal torquing. A more elaborate 'mixed' IA model developed by Blazek et al. (2017) includes both linear and quartic orders of tidal effects into a unified prescription. In the one-halo regime, an empirical fitting functional form of IA is provided by Schneider & Bridle (2010), based on a phenomenological halo model assuming that central galaxies are aligned with the halo shapes and the satellite galaxies are radially pointing toward halo centers.

The choices of IA modeling, the variant in ways of parametrizing IA redshift evolution, would shift the cosmological parameter constraints, although currently the amount of shifts are considered small given the size of error bars, as revealed from the DES Y1 results (Troxel et al., 2018; Samuroff et al., 2018). Besides purely affected by tidal field, IA is also potentially depending on other physical mechanisms like baryonic processes and the nonlinear gravitational evolution. The situation is further complicated by the fact that the observed IA signal depends on the properties of tracer galaxies, and is weighted by the galaxy density field (Blazek et al., 2015). Due to these challenges, IA is still an active research area requiring inputs in preparation for future Stage IV survey.

1.3.4 Baryonic effects

To extract cosmological information from observables that are sensitive to the growth of structure, building a precision library of matter power spectra as functions of cosmology, $P_\delta(k, z \mid \text{cosmology})$, is an essential piece of work. In the linear and quasi-linear regime, perturbation theory can be used to predict the matter power spectra (Bernardeau et al., 2002). On smaller scales, N-body simulations are required to capture the non-linear evolution of structure growth. Beyond pure gravity interaction among dark matter particles, complex physical mechanisms involved with baryons, though with their only ~5% occupancy on the energy density of Universe, places non-negligible effect on the distribution of matter.

The two main effects of baryons are cooling and feedback. The cooling mechanisms allows gas to densely accumulate so that galaxies can form at the centers of their dark matter halos. On the contrary, the feedback mechanisms from exploding stars or from the active galactic nuclei (AGN) activities

inject enormous amounts of energy, heating up surrounding gas or even blowing gas out of the galaxy in terms of galactic winds or AGN jets, thereby suppress the effect of cooling. With the occupancy of baryons, halo structure would be modified in the presence of their gravity. The magnitude of this back-reaction effect depends on details of baryonic physics (see e.g. van Daalen et al. 2011, 2019). However, besides knowing their important roles in providing explanations on observational results, we are still far from understanding how exactly they operate in the whole process of galaxy formation and evolution.

Over the past 10 years, several hydrodynamical simulations with varying subgrid modeling prescriptions are run with parameters tuned to roughly reproduce some key observational results of our Universe (e.g. stellar mass function, galaxy color-magnitude diagram, stellar mass–blackhole mass relation...), but the level of uncertainties are far from the precision for cosmology, not to mention the extensive demand on computational resources. Under this situation, developing baryon modeling schemes based on the output of N-body simulation is becoming a promising avenue to account for uncertainties of baryon for future surveys.

There are currently four types of strategies on modeling baryonic uncertainties. The first category is to develop economic strategies on discarding data that are challenging to model. For example, the most straightforward way is to define safe scale cuts on observables such that the cosmological results would not be biased. Instead of applying cuts on summary statistics, the density peak clipping method applies cuts on high density peaks in matter fluctuation maps to make the derived summary statistics being less sensitive to the poorly-modeled non-linear regime, while allowing wider range of scales to extract cosmological information (Simpson et al., 2011, 2013). The second category focuses on modeling the discrepancy between hydrodynamical and N-body simulations. Empirical models are build to model the ratio of power spectra between hydrodynamical and N-body simulations (Chisari et al., 2018; Harnois-Déraps et al., 2015). Eifler et al. (2015) apply principal component analysis (PCA) on the summary statistics of various baryonic scenarios, and use the resulting PC modes as flexible bases to span the uncertainty range of baryonic effects. The third category is to resort on halo model. Since baryonic effects are dominant on small scales, their effects can be modeled through the change of halo density profiles (Mead et al., 2015; Copeland et al., 2018). The final category is to paint baryons on N-body simulations. There is a gradient-based method to shift dark matter particles in N-body simulations along the gradient of estimated thermal pressure to mimic the effect of baryonic feedback (Dai et al., 2018). A more detail method includes adding galaxy stellar and gas profiles as well as accounting for the back-reaction of dark matter particles (Schneider & Teyssier, 2015; Schneider et al., 2019). Machine learning methods may also be a promising tool to perform the mapping between hydrodynamical and N-body simulations (Tröster et al., 2019).

1.4 Thesis Overview

The main result of this dissertation is comprised of four research projects. All together they provide advancing measurements and improve our understanding of astrophysical systematics in the field of weak gravitational lensing. In Chapters 2 and 3, we focus on intrinsic alignment of galaxies. Chapters 4 and 5 concentrates on systematics of baryonic effects. Below I provide a brief summary on what these projects are about.

In **Chapter** 2, we present our investigation on the the alignment of the massive central galaxies with respect to their host halo shapes. From the ∼ 8000 redMaPPer clusters constructed from SDSS, the average misalignment angle between the central and cluster major axes is measured to be ∼ 35°. We conclude that central galaxy alignment is potentially a complicated physical effect with many of the relevant predictors identified. We provide physical explanations on the identified correlations between the alignment signal and parameters related to galaxies and clusters properties there. This work is published in Huang et al. 2016, MNRAS, 463, 222.

Using the same set of redMaPPer cluster sample, in **Chapter** 3, we analyze the radial alignment of satellite galaxies toward their belonging halo centers. We detect satellite alignment signal based on different shape measurement method, and investigate the origin of the measurement discrepancy. For the shape measurement that puts more weight in the inner light profile of galaxies, no net radial alignment signal is detected across the entire sample. However, when limiting to a subsample of satellites with certain threshold, we do observe significant radial alignment signal. We also discuss the dependence of IA signal on several important galaxies properties. This work is originally published in Huang et al. 2018, MNRAS, 474, 4.

Chapter 4 presents our investigation on modeling baryonic physics for weak lensing. Using several hydrodynamical simulations, we investigate the effects of baryons on matter power spectrum and on the cosmic shear observables for various baryonic scenarios. We validate two different baryon mitigation schemes under an LSST-like experiment and discuss the performance and limitations of these models. This work is published in Huang et al. 2019, MNRAS, 488, 1652.

In **Chapter** 5, we implement our baryon modeling scheme in the DES cosmological pipeline, in order to include small scale cosmic shear data in the DES Y1 3×2 points analysis. We validate our pipeline and determine our settings by running likelihood simulations. We also investigate the interplay between our baryonic parameters with cosmology and with other nuisance parameters. We expect to have ∼10% smaller error bar on S_8 constraint by including small scale cosmic shear data into analysis. This is currently an ongoing project which we expect to submit for publication in the future.

Finally we conclude and provide future outlooks of the field in **Chapter** 6.

2 Intrinsic alignments in redMaPPer clusters – I. Central galaxy alignments and angular segregation of satellites

Hung-Jin Huang[1], Rachel Mandelbaum[1], Peter E. Freeman[1,2], Yen-Chi Chen[1,2,3], Eduardo Rozo[4], Eli Rykoff[5], Eric J. Baxter[6]

[1]McWilliams Center for Cosmology, Department of Physics, Carnegie Mellon University, Pittsburgh, PA 15213, USA
[2]Department of Statistics, Carnegie Mellon University, Pittsburgh, PA 15213, USA
[3]Department of Statistics, University of Washington, Seattle, WA 98195, USA
[4]Department of Physics, University of Arizona, 1118 E. Fourth St., Tucson, AZ 85721, USA
[5]SLAC National Accelerator Laboratory, Menlo Park, CA 94025, USA
[6]Center for Particle Cosmology, Department of Physics, University of Pennsylvania, Philadelphia, PA 19104

Abstract

The shapes of cluster central galaxies are not randomly oriented, but rather exhibit coherent alignments with the shapes of their parent clusters as well as with the surrounding large-scale structures. In this work, we aim to identify the galaxy and cluster quantities that most strongly predict the central galaxy alignment phenomenon among a large parameter space with a sample of 8237 clusters and 94817 members within $0.1 < z < 0.35$, based on the redMaPPer cluster catalog constructed from the Sloan Digital Sky Survey. We first quantify the alignment between the projected central galaxy shapes and the distribution of member satellites, to understand what central galaxy and cluster properties most strongly correlate with these alignments. Next, we investigate the angular segregation of satellites with respect to their central galaxy major axis directions, to identify the satellite properties that most strongly predict their angular segregation. We find that central galaxies are more aligned with their member galaxy distributions in clusters that are more elongated and have higher richness, and for central galaxies with larger physical size, higher luminosity and centering probability, and redder color. Satellites with redder color, higher luminosity, located closer to the central galaxy, and with smaller ellipticity show a stronger angular segregation toward their central galaxy major axes. Finally, we provide physical explanations for some of the identified correlations, and discuss the connection to theories of central galaxy alignments, the impact of primordial alignments with tidal fields, and the importance of anisotropic accretion.

2.1 Introduction

In the framework of the standard cold dark matter (CDM)-dominated Universe, cosmic structures grow hierarchically. Small galaxies form first, then merge and group together through channels of the filamentary network to form clusters of galaxies (White & Rees, 1978; Blumenthal et al., 1984). During the process of structure formation, the distribution and orientation of galaxies may be set by the surrounding gravitational tidal fields, or be disturbed by activities such as mergers or feedback processes due to supernova or active galactic nuclei. In this work, we refer to any net preferred orientation toward some reference direction or any existing galaxy shape correlations caused by these physically-induced events as *intrinsic* alignments (in contrast with the coherent alignments induced by gravitational lensing). For recent reviews, see Joachimi et al. (2015), Kiessling et al. (2015) and Kirk et al. (2015).

Intrinsic alignments occur on a variety of scales. On large scales, several Mpc and above, galaxies show a net tendency to align radially towards overdensities (e.g., Mandelbaum et al., 2006; Hirata et al., 2007; Okumura et al., 2009; Joachimi et al., 2011), and more detailed analysis of the cosmic web indicates coherent alignments along the stretching direction of filaments (Tempel et al., 2015; Chen et al., 2015; Rong et al., 2016). One of the leading theoretical models for intrinsic alignments at large scales ($\gtrsim 6$ Mpc) is the linear alignment model, which relates the alignment strength linearly to the smoothed tidal field at the time of galaxy formation (Catelan et al., 2001; Hirata & Seljak, 2004b), or variations of that model that include nonlinear evolution of the density field (Bridle & King, 2007; Blazek et al., 2015). Based on a sample of luminous red galaxies (LRGs), Singh et al. (2015) adopted the above alignment models to quantify the large-scale alignment amplitude as a function of several LRG properties. They found that the alignment amplitude becomes stronger toward more luminous LRGs residing in higher mass halos (see also Hirata et al., 2007; Joachimi et al., 2011).

On small scales, within galaxy clusters, there are two types of alignments. The first type is the alignment of satellite major axes toward the center of their host dark matter (DM) halo, for which the observational proxy usually is the brightest cluster galaxy (BCG). This is often called *satellite* (or *radial*) alignment. Satellite alignment is believed to originate from the tidal torque induced primarily from the gravitational field of the DM halo (Ciotti & Dutta, 1994; Kuhlen et al., 2007; Pereira et al., 2008; Faltenbacher et al., 2008; Tenneti et al., 2015a). Observationally, the existence of satellite alignment is still controversial, with Pereira & Kuhn (2005); Agustsson & Brainerd (2006); Faltenbacher et al. (2007); Singh et al. (2015) reporting detections of the signal, while Hung & Ebeling (2012); Schneider et al. (2013); Chisari et al. (2014); Sifón et al. (2015) found no significant detection. Some of this tension may arise from selection effects, as discussed by Singh et al. (2015). In addition, Hao et al. (2011) cautioned about the possibility of spurious satellite alignment signals due to systematic errors (the contamination from the diffuse light from BCGs). We will report our measurement of satellite alignment in red-sequence Matched-filter Probabilistic Percolation (redMaPPer) clusters and present detailed systemic analysis in the upcoming Paper II. In the current paper, we focus on the second type of alignment, called *central galaxy* alignment.

Central galaxy alignment refers to the tendency of the major axis of the central galaxy to align with that of its host DM halo, for which the observational signature is that satellites (which we use as a tracer of the DM halo shape) preferentially reside along the central's major axis direction. This type

of alignment is also termed "*BCG* alignment" in the literature, as it is often assumed that the brightest galaxy within each cluster is the central galaxy (the central galaxy paradigm, see van den Bosch et al. 2005). However, Skibba et al. (2011) showed that 40%, and Hoshino et al. (2015) that 20-30%, of BCGs are not the galaxies that are located closest to the center of the cluster potential well. The fact that the redMaPPer algorithm identifies centrals not only based on their luminosity but also on their color and local galaxy density enables us to select a more robust set of central galaxies for our intrinsic alignment study. Therefore, through out this work, we will use the term "central galaxy alignment" for our result, and keep the term "BCG alignment" when referring to previous works that utilize the BCG as a proxy for the central galaxy.

Unlike satellite alignment, the observational evidence for central galaxy alignment is strong and uncontroversial (e.g., Sastry, 1968; Binggeli, 1982; Niederste-Ostholt et al., 2010), and it can be explained by two possible physical mechanisms. The first is the filamentary nature of matter accretion (Dubinski, 1998), and the second is primordial alignment with the tidal field set by both the host dark matter halo and large-scale structure (Faltenbacher et al., 2008). Since central galaxy alignment is robustly detected with existing large datasets, many studies have investigated its dependence on physical predictors such as central galaxy luminosity, color, host halo mass, redshift, and so on, in order to better understand the physical origin of the effect (Brainerd, 2005; Yang et al., 2006; Azzaro et al., 2007; Faltenbacher et al., 2007; Wang et al., 2008; Siverd et al., 2009; Agustsson & Brainerd, 2010; Niederste-Ostholt et al., 2010; Hao et al., 2011). There is general agreement that the central galaxy alignment signal is stronger for red and luminous centrals, and shows higher significance when using red satellites as tracers. However, some controversies still remain about the importance of other predictors besides luminosity or color. Furthermore, some of the previous studies started with the assumption that only a few predictors could be important in determining the central galaxy alignments, and therefore performed an analysis based only on those predictors without considering others, ignoring potential degeneracies among predictors when splitting and comparing subsamples.

In Paper I, our goal is to present a comprehensive analysis of the predictors of central galaxy alignments. We include as many physical properties as possible, and properly account for potential correlations among them with the help of a linear regression analysis. We also discuss potential systematic effects based on signals obtained from various shape measurement methods. The two main questions we aim to address are 1) what central and cluster properties are the strongest predictors of the strength of central galaxy alignments? 2) What kinds of satellites are more likely to lie along the major axis direction of their host centrals? We build corresponding linear regression models, use variable selection techniques to select important predictors, and further quantify their significance. Finally, we discuss possible physical origins for these selected predictors and compare our result with the literature.

The paper is organized as follows. In Sec. 2.2, we describe our data and definitions of the physical quantities used in the linear regression analysis. Details of the linear regression process are described in Sec. 2.3. Sec. 2.4 presents our measurement of central galaxy alignment and results of the variable selection process. Sec. 2.5 discusses the detected central galaxy alignment signal for three different shape measurement methods, and the interpretation of those findings. The physical origins of our identified featured predictors for central galaxy alignments with the cluster shape and angular segregation of satellites with respect to the central galaxy major axis are discussed in detail

in Secs. 2.6 and 2.7, respectively. We conclude and summarize our key findings in Sec. 2.8.

Throughout this paper, we adopt the standard flat ΛCDM cosmology with $\Omega_m = 0.3$ and $\Omega_\Lambda = 0.7$. All the length and magnitude units are presented as if the Hubble constant were 100 km s^{-1} Mpc^{-1}. In addition, we use log as shorthand for the 10-based logarithm, and ln for the natural logarithm.

2.2 Data and measurements

In this section, we introduce the data that we analyze in this work, including the definitions of the galaxy cluster and galaxy properties that we use. All data used in this paper came from the Sloan Digital Sky Survey (SDSS) I/II surveys. The SDSS I (York et al., 2000) and II surveys imaged roughly π steradians of the sky, and followed up approximately one million of the detected objects spectroscopically (Eisenstein et al., 2001; Richards et al., 2002; Strauss et al., 2002). The imaging was carried out by drift-scanning the sky in photometric conditions (Hogg et al., 2001; Ivezić et al., 2004), in five bands ($ugriz$) (Fukugita et al., 1996; Smith et al., 2002) using a specially-designed wide-field camera (Gunn et al., 1998). These imaging data were used to create the catalogs that we use in this paper. All of the data were processed by completely automated pipelines that detect and measure photometric properties of objects, and astrometrically calibrate the data (Lupton et al., 2001; Pier et al., 2003; Tucker et al., 2006). The SDSS-I/II imaging surveys were completed with a seventh data release (Abazajian et al., 2009), but we use the processed data from an improved data reduction pipeline that was part of the eighth data release, from SDSS-III (Aihara et al., 2011); and an improved photometric calibration ('ubercalibration', Padmanabhan et al., 2008).

2.2.1 Galaxy cluster catalog

We use member galaxies in the redMaPPer v5.10 cluster catalog[1] to study galaxy alignments in galaxy clusters. The redMaPPer cluster catalog is constructed based on photometric galaxy samples with a magnitude cut $m_i < 21.0$ from the SDSS data release eight (DR8; Aihara et al. 2011) over a total area of ∼10,000 deg^2. Details of the redMaPPer cluster finding algorithm and properties of the SDSS redMaPPer catalogs can be found in Rykoff et al. (2014); Rozo & Rykoff (2014); Rozo et al. (2015a,b). Briefly, the redMaPPer algorithm has two stages: the red-sequence calibration, and the cluster-finding stage. With a set of red spectroscopic galaxies as training sample, redMaPPer first constructs a redshift-dependent evolutionary red-sequence model, including zero-point, tilt, and scatter. The calibrated red-sequence model is then used to group red galaxies at similar redshifts into clusters, assuming certain radial and luminosity filters.

One of the features of the redMaPPer algorithm is that it is probabilistic, which enables users to select suitable samples to do statistics. For each cluster, it provides the central galaxy probability, $P_{\rm cen}$, for the top five potential BCGs, and all potential member galaxies are assigned with a membership probability, $p_{\rm mem}$, according to their color, magnitude, and position information. The photometric redshift z for each cluster is estimated from high-probability members; and the cluster richness, λ, is defined by summing the membership probabilities over all cluster members.

[1] http://risa.stanford.edu/redmapper/

In this work, we restrict our analysis to clusters with richness $\lambda \geq 20$, corresponding to a halo mass threshold of $M_{200\mathrm{m}} \gtrsim 10^{14}\ \mathrm{h}^{-1}\mathrm{M}_{\odot}$ (Rykoff et al., 2012), and photometric redshift in the range $0.1 \leq z \leq 0.35$. The lower redshift limit is selected so as to minimize edge effects from the training sample when doing calibration, while the upper redshift cutoff is set such that the sample of clusters is volume-limited (Rykoff et al., 2014). All in all, there are 10702 clusters within this redshift and richness range. To perform higher quality statistics, we only explore satellite galaxies with membership probability $p_{\mathrm{mem}} \geq 0.8$ when doing linear regression analysis, and restrict to satellites with $p_{\mathrm{mem}} \geq 0.2$ when defining cluster shape (while weighting those satellites appropriately by their values of p_{mem}).

2.2.2 Definitions and measurements of physical parameters

In this subsection, we describe many of the physical parameters that we will use to study central galaxy alignments.

Galaxy ellipticity

The galaxy ellipticity used for the majority of this work is corrected for the effect of the PSF using the re-Gaussianization shape measurement method (see Sec. 2.2.3 for detail). We use the components of the distortion e_1 and e_2 (Bernstein & Jarvis, 2002) provided from the Reyes et al. (2012) (or R12) and Mandelbaum et al. (2005) (or M05) catalogs by fitting the 'atlas images' (Stoughton et al., 2002) in both r and i bands. The distortion can be related to the axis ratio b/a as

$$(e_1,\ e_2) = \frac{1-(b/a)^2}{1+(b/a)^2}(\cos 2\alpha,\ \sin 2\alpha), \tag{2.1}$$

where α is the position angle of the major axis. The total galaxy distortion e is calculated as

$$e = \sqrt{e_1^2 + e_2^2} \tag{2.2}$$

Galaxy alignment angles

Once the galaxy position angle is known, we can assign each satellite its central galaxy alignment angle, θ_{cen}, and satellite alignment angle, ϕ_{sat}.

The central galaxy alignment angle θ_{cen} is defined as the angle between the major axis of the central galaxy and the line connecting the central to the satellite galaxy, as illustrated in the left panel of Fig. 2.1. Calculating θ_{cen} requires a viable shape measurement for the central galaxy (but not the satellites). Within the redshift range $0.1 \leq z \leq 0.35$, there are 8237 centrals with shape measurements in the R12 catalog, resulting in 94817 central-satellite pairs with satellites that have $p_{\mathrm{mem}} \geq 0.8$.

The satellite alignment angle ϕ_{sat} is defined as the angle between the major axis of the satellite galaxy and the line connecting its center to the central, as shown in the right panel of Fig. 2.1. Calculating ϕ_{sat} requires a shape measurement for the satellite galaxy. In this paper, we only consider ϕ_{sat} as a potential predictor of central galaxy alignments; future work will include a detailed analysis of satellite alignments.

We restrict both θ_{cen} and ϕ_{sat} to the range $[0°, 90°]$ due to symmetry. By definition, $\theta_{\mathrm{cen}} = 0°/90°$ indicates a satellite located along the major/minor axis of the central. A satellite is radially/tangentially aligned with the central if $\phi_{\mathrm{sat}} = 0°/90°$.

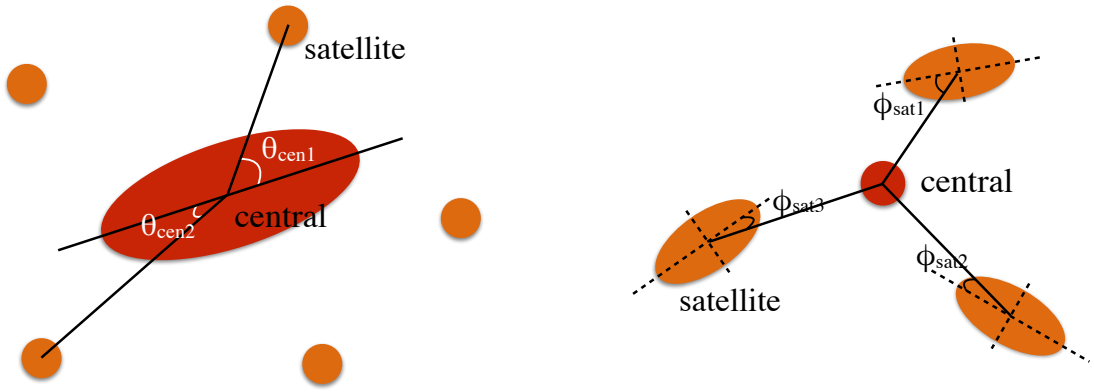

Figure 2.1: Illustration of the galaxy alignment angles. The left panel shows the definition of central alignment angle $\theta_{\rm cen}$, while the right panel shows the definition of satellite alignment angle $\phi_{\rm sat}$.

Cluster position angle and ellipticity

We follow the method used in Niederste-Ostholt et al. (2010) to define the orientation and ellipticity of the redMaPPer clusters from their satellite distributions. In order to have enough member galaxies to trace the shape of each cluster, we use all member galaxies with membership probability $p_{\rm mem} \geq 0.2$. We calculate the reduced second moments from the positions of member galaxies, weighted by $p_{\rm mem}$:

$$M_{\rm xx} \equiv \left\langle \frac{x^2}{r^2} \right\rangle = \frac{\sum_i p_{{\rm mem},i} \frac{x_i^2}{r_i^2}}{\sum_i p_{{\rm mem},i}} \tag{2.3}$$

and likewise for $M_{\rm yy}$ and $M_{\rm xy}$; by definition, $M_{\rm xx} + M_{\rm yy} = 1$. Here x_i is the distance of member galaxy i from the cluster center. We can then define the cluster ellipticity as

$$(Q,\ U) = \frac{1 - b/a}{1 + b/a}(\cos 2\beta,\ \sin 2\beta) = (\mathrm{M_{xx}} - \mathrm{M_{yy}},\ 2\mathrm{M_{xy}}), \tag{2.4}$$

where b/a is the cluster projected minor-to-major axis ratio and β is the cluster position angle (P.A.). The cluster ellipticity can then be calculated via

$$\text{cluster } e = \sqrt{Q^2 + U^2}. \tag{2.5}$$

With the $1/r^2$ weighting (an explicitly spherically-symmetric weight function) in the reduced second moments, the derived cluster ellipticity tends to be underestimated. We show later that this does not change our conclusion regarding how cluster ellipticity affects the central galaxy alignment.

Central galaxy dominance

The central galaxy dominance parameter is defined as the difference in the r-band absolute magnitude of the central galaxy and the mean magnitude of the first and second brightest satellites:

$$\text{Central dominance} \ \equiv\ \text{Central}\ {}^{0.1}M_{\rm r} - \frac{{}^{0.1}M_{\rm r,1st} + {}^{0.1}M_{\rm r,2nd}}{2}. \tag{2.6}$$

We calculate the central galaxy dominance parameter using only $p_{\rm mem} \geq 0.8$ members. For the very few clusters (134 out of 8237) that have only one member satisfying the $p_{\rm mem} \geq 0.8$ criterion, we simply use the difference between the absolute magnitudes of central and that member galaxy to define the central galaxy dominance. Smaller central dominance values correspond to more dominant central galaxies.

Central galaxy probability

For each cluster, the redMaPPer catalog contains the five most likely central galaxy candidates, each with centering probability $P_{\rm cen}$. In this paper, we use the most probable central as our central galaxy, and measure the central galaxy and satellite alignment angles of the associated central-satellite pairs. Over 80% of our centrals have $P_{\rm cen} \geq 0.7$.

Galaxy absolute magnitude

We calculate the absolute magnitude for each galaxy using the luminous red galaxy (LRG) templates in the `kcorrect` package (v4.2) distributed by Blanton & Roweis (2007). The `kcorrect` software determines the best composite fit to the observed galaxy spectral energy distribution (SED) with the Chabrier (2003) initial mass function (IMF) and a variety of Bruzual & Charlot (2003) stellar population synthesis models differing in star formation histories and metallicities. We use extinction-corrected SDSS model magnitudes and the photometric redshift z provided in redMaPPer as input, and k-correct the magnitudes of all galaxies in our sample to $z = 0.1$.

Galaxy effective radius

The effective radius we report in this paper is the circularly-averaged half-light radius, defined as

$$R_{\rm eff} \equiv \sqrt{\frac{b}{a}}\, R_{\rm deV}, \tag{2.7}$$

where b/a is the semi-minor to semi-major axis ratio taken from the SDSS parameter `deVAB_r`, and $R_{\rm deV}$ is the semi-major half-light radius, `deVRad_r`. Both parameters are estimated as part of the SDSS DR8 pipeline by fitting de Vaucouleurs light profiles to galaxy r-band images. Here we convert the value of $R_{\rm deV}$ from the provided angular units to physical units (h^{-1}kpc), using the redshift z of the host cluster.

Member distance from the cluster center

For each satellite galaxy, we compute its projected distance, r, to the central galaxy, to check for radial dependence in the central galaxy alignment signal. To fairly compare among satellite galaxies in clusters with different halo masses, we further normalize r by the estimated halo radius, $R_{\rm 200m}$, corresponding to the radius within which the average density of the enclosed mass is 200 times the mean density, $\overline{\rho}$. We first use the mass-richness relation provided in Eq. B4 of Rykoff et al. (2012),

$$\ln\left(\frac{M_{\rm 200m}}{h_{70}^{-1}\ 10^{14}\ {\rm M}_\odot}\right) = 1.72 + 1.08\ \ln\frac{\lambda}{60}, \tag{2.8}$$

to estimate $M_{200\mathrm{m}}$. Then we compute $R_{200\mathrm{m}}$ via the definition $M_{200\mathrm{m}} = (4\pi/3)\ 200\overline{\rho}\ R^3_{200\mathrm{m}}$. Our conclusions would not change even if applying different mass-richness relations recently calibrated via weak lensing (Simet et al., 2017) or via clustering of clusters (Baxter et al., 2016).

Cluster member concentration Δ_{R}

Recently, Miyatake et al. (2016) found that the average projected distance of member galaxies from the cluster center, defined as

$$\overline{R}_{\mathrm{mem}} = \frac{\sum_i p_{\mathrm{mem},i} R_i}{\sum_i p_{\mathrm{mem},i}}, \tag{2.9}$$

not only describes the concentration of the member galaxy distribution in the cluster, but also plays a role in determining the large-scale clustering of redMaPPer clusters at fixed mass. Here $p_{\mathrm{mem},i}$ is the membership probability of the i-th member galaxy, and R_i is the physical separation between that galaxy and its corresponding cluster central galaxy.

To properly model the richness and redshift dependence in $\overline{R}_{\mathrm{mem}}$, we use another parameter, Δ_{R}, defined in Eq. 22 of Baxter et al. (2016) as an indicator of cluster member concentration at fixed λ and z:

$$\Delta_{\mathrm{R}} = \frac{\overline{R}_{\mathrm{mem}} - \left\langle \overline{R}_{\mathrm{mem}} | \lambda, z \right\rangle}{\left\langle \overline{R}_{\mathrm{mem}} | \lambda, z \right\rangle}. \tag{2.10}$$

Here $\left\langle \overline{R}_{\mathrm{mem}} | \lambda, z \right\rangle$ is the mean $\overline{R}_{\mathrm{mem}}$ value at a particular λ and z bin, estimated by fitting a spline to the average value of $\overline{R}_{\mathrm{mem}}$ in ten bins of λ and five bins of z. By construction, negative Δ_{R} value means the cluster has a more compact member galaxy distribution than the average cluster at that richness and redshift.

2.2.3 Galaxy shape data

In this work, we use 3 different galaxy shape measurement methods from 4 catalogs to determine the galaxy position angle and ellipticity, to investigate systematics in the measured central galaxy alignment signal. This section includes a description of all of these methods.

Re-Gaussianization shape measurement

The first shape measurement method is based on the re-Gaussianization technique (Hirata & Seljak, 2003), which not only corrects the effects of the point spread function (PSF) on the observed galaxy shapes with a standard elliptical Gaussian profile, but also corrects for low-order deviations from Gaussianity in both the galaxy and PSF profiles.

Two shape catalogs generated using the re-Gaussianization technique are used in this work; the primary one is based on the SDSS DR8 photometric pipeline, and was presented in R12; however, for systematics tests we also use the catalog from M05, which was based on the DR4 photometric pipeline. The R12 catalog covers an area of 9432 deg^2, with an average of 1.2 galaxies arcmin^{-2} with shape measurements; the M05 catalog covers an area of 7002 deg^2. Both shape catalogs select

galaxies down to the extinction-corrected r-band model magnitude $m_r < 21.8$, and require galaxies to be well resolved compared to the PSF size in both r and i bands. While there are minor differences in galaxy selection criteria in the catalogs, the main difference is the version of the SDSS photometric pipeline (`photo`) that they used. The M05 catalog relies on `photo` v5.4 (Adelman-McCarthy et al., 2006) while the R12 is based on `photo` v5.6 (Aihara et al., 2011). The new version of `photo` has a more sophisticated sky-subtraction algorithm that improves the photometry of large galaxies and fainter ones near them. By comparing the central galaxy alignment measured using these catalogs, we will estimate the impact of the sky-subtraction quality on the final results.

Isophotal shape measurement

Many previous central galaxy alignment studies used the SDSS isophotal position angle to define the orientation of the BCG (Brainerd, 2005; Yang et al., 2006; Faltenbacher et al., 2007; Azzaro et al., 2007; Wang et al., 2008; Siverd et al., 2009; Agustsson & Brainerd, 2010; Hao et al., 2011). To compare with these studies, we also measure the central galaxy alignment using the isophotal shape measurement. The SDSS pipeline measures the isophotal position angle of galaxies at the isophote corresponding to 25 mag arcsec^{-2}, which is fairly low surface brightness and generally encompasses a much larger part of the galaxy light profile than the centrally-weighted re-Gaussianization shapes.

Isophotal shapes were not released in DR8, so we take the isophotal position angle in r band from DR7 (using the previous version of `photo`) to compute central galaxy alignments.

De Vaucouleurs shape measurement

Some galaxy alignment studies use the shape measurement from the de Vaucouleurs model fit (Niederste-Ostholt et al., 2010; Siverd et al., 2009; Hao et al., 2011), which is a good description of the surface brightness profile for a typical elliptical galaxy, including most galaxies in redMaPPer clusters. Here we use the de Vaucouleurs fit position angle provided in the SDSS DR7, which fits galaxies through a two-dimensional fit to a PSF-convolved de Vaucouleurs profile. For more detail about these SDSS shape measurements, we refer readers to Stoughton et al. (2002).

2.2.4 The central-satellite pair sample

We define three samples of central-satellite pairs for our analysis:

1. After applying the redshift cut and requiring that central galaxies have shape measurements in the R12 catalog, we have 8237 centrals with DR8 re-Gaussianization shape measurement, and 94817 satellites with $p_{\rm mem} \geq 0.8$ in our parent sample. This parent sample is used for the majority of our analysis, while the other subsamples are used primarily for systematics tests.
2. To investigate the effect of the sky-subtraction technique on the measured central galaxy alignment signal, we match our parent centrals with the M05 catalog, and construct another subsample of centrals that have re-Gaussianization shape measurement based on both DR4 and DR8 photometry. This subsample has 4316 centrals and 46370 central-satellite pairs within the DR4 footprint.

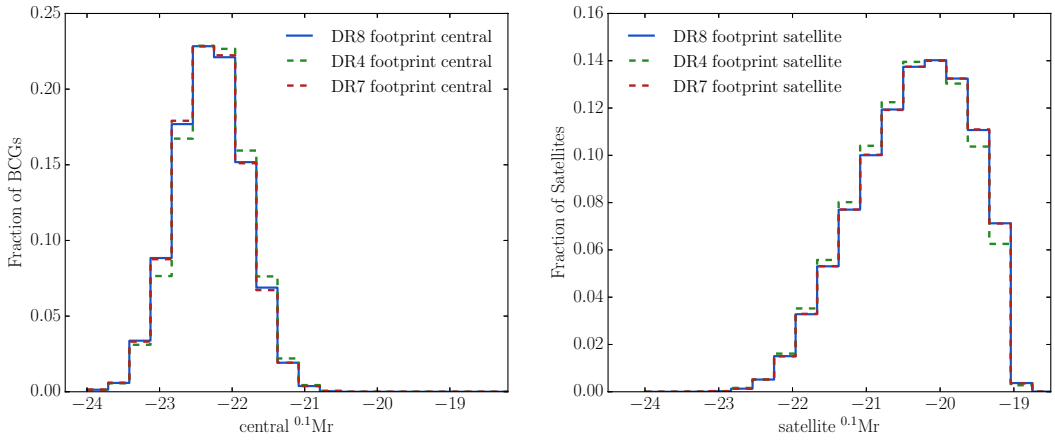

Figure 2.2: Distributions of the central (left panel) and satellite (right panel) $^{0.1}M_r$ for the three sets of central-satellite pairs defined in Sec. 2.2.4.

3. To compare the degree of central galaxy alignment signal using different shape measurement methods, another subsample of central-satellite pairs is constructed. If we require centrals to have a DR8 re-Gaussianization shape, along with both isophotal and de Vaucouleurs shape measurements from DR7, we have 7488 centrals with 86350 satellites within the DR7 footprint.

Fig. 2.2 shows the distributions of the r-band absolute magnitude, $^{0.1}M_r$, of the centrals (left panel) and satellites (right panel) in these three sets of central-satellite pairs. Both the central and satellite $^{0.1}M_r$ distributions for the subsample in the DR7 footprint (iii) are almost the same as for the parent DR8 sample (i), while there are slight shifts for the subsamples in DR4 footprint (ii).

When measuring the central alignment angle, we only require satellite positions and central shape measurements. However, in the linear regression analysis, we require all galaxies to have well-defined physical parameters such as ellipticity, color, effective radius. . . ; these requirements eliminate some satellites, mainly due to the requirement of an ellipticity measurement. Table 2.1 summarizes the three sets of central-satellite pairs defined in this section, and also records the actual number of central-satellite pairs used when doing linear regression analysis.

In Fig. 2.3, we compare the absolute magnitude distributions of the satellite subsamples actually used in the linear regression analysis to that of the original set of satellites from which they were drawn. The selected satellites used in linear regression are biased to brighter magnitudes, since we rely on good quality photometry (higher S/N and/or more resolved light profile) to measure shapes. For the reason, the derived significance levels for potential predictors that could possibly affect the degree of central galaxy alignment in this work are lower limits, especially for predictors that strongly correlate with satellite brightness. If the effect of a predictor on central galaxy alignment is strong enough, then even if some faint satellites are excluded when doing linear regression, we could still select the predictor out as a featured predictor.

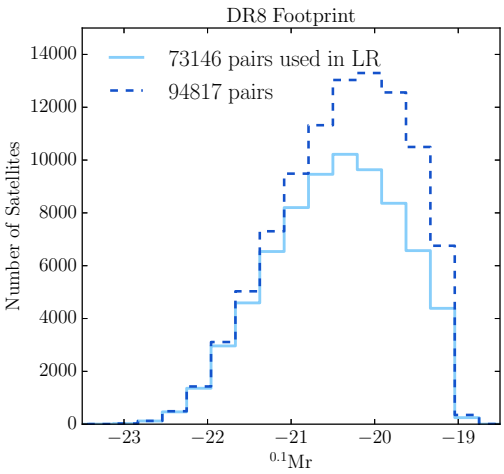

Figure 2.3: Distributions of the $^{0.1}M_r$ for satellites in the DR8 footprint. The dark blue dashed line indicates the total 94817 satellites, while the light blue line shows the selected subsample when doing linear regression analysis.

Table 2.1: Numbers of clusters and central-satellite pairs used in this work. The first three rows are the the three subsamples we used for the overall measurement of the central galaxy alignment angle defined in Sec. 2.2.4. The last row is the subsamples used when doing linear regression analysis.

Sample	$N_{cluster}$	N_{pair}
DR8 Footprint Sample	8237	94817
DR4 Footprint Sample	4316	46370
DR7 Footprint Sample	7488	86350
Linear Regression Sample	8233	73146

2.3 Linear regression analysis

Regression is one of the most commonly used methods to study dependence. It is used to find optimal values of the free parameters in a specified function $Y = f(\mathbf{X}) + \epsilon$. Here Y is the response variable, which quantifies the physical effect one wants to study, $\mathbf{X} = (X_1, ...X_i, ...X_N)$ is a set of potential predictors that may affect the behavior of Y, and ϵ represents random observational error, usually assumed to be drawn from a normal distribution. For the central galaxy alignment effect, as there is no a priori-known functional form relating $\mathbf{X}$ to Y, we apply *multiple linear regression*, which allows one to at least determine if the central galaxy alignment depends on $\mathbf{X}$ to first order.

The multiple linear regression model we apply is

$$Y = f(\mathbf{X}) = \beta_0 + \beta_1 X_1 + \ldots + \beta_i X_i + \ldots + \beta_N X_N, \tag{2.11}$$

where the intercept β_0 and the slopes β_i are the unknown regression coefficients to be estimated via least squares. For each regression coefficient β_i, we perform the two-sided t-value and p-value tests for the dependence of Y on the X_i. These are tests of the hypothesis that $\beta_i = 0$ against the alternative hypothesis that $\beta_i \neq 0$. The t-value is the ratio of β_i to its standard error, which can be positive or negative depending on the sign of β_i. A larger $|t|$ indicates a more significant statement that $\beta_i \neq 0$, which means it is more likely that there is a relationship between Y and X_i. Statistically, the t-value and p-value are inextricably linked. Under the assumption of normally distributed errors, a p-value of 0.05 corresponds to a 95% confidence that β_i is not equal to zero. Thus we select out a regressor X_i as a featured predictor if its p-value < 0.05 (e.g., Weisberg, 2013).

There are reasons not to use our predictors P_i defined in Sec. 2.2.2 (cluster ellipticity, central galaxy dominance, etc.) directly as regressors X_i. Since there is a large variation in the range of each predictor, if we simply regress by $Y = \beta_0 + \sum_i \beta_i{}' P_i$, the fitted magnitude of $\beta_i{}'$ would depend on that range, i.e., for a given level of correlation between the parameters, $\beta_i{}'$ would be small if its P_i tends to be large. To make our results more directly illustrate how the relative change of a physical parameter affects the value of Y, throughout we normalize our predictors P_i to obtain regressors as follows:

$$X_i = \frac{P_i - \langle P \rangle_i}{\sigma_{P_i}}. \tag{2.12}$$

Here σ_{P_i} is the sample standard deviation of the predictor P_i, reflecting the width of the intrinsic distribution and measurement error. We will use the term "predictor" to correspond to the original variables, and "regressor" to refer to variables that are transformed as in Eq. (2.12). We note, however, that using the normalized predictors as our regressors does not affect the result of hypothesis tests to select featured predictors.

In this work, we will build two multiple linear regression models with two different response variables, and use a total of 16 potential predictors to analyze the central galaxy alignment and the angular segregation of satellites. Details on the definitions and measurements of these physical parameters were presented in Sec. 2.2.2.

2.3.1 Response variables

The two response variables used to quantify the level of central alignment are: 1) the position angle difference between the central galaxy and its host cluster

$$\Delta\eta = |P.A._{\rm cen} - P.A._{\rm cluster}|, \tag{2.13}$$

and 2) the central galaxy alignment angle for each central-satellite pair, $\theta_{\rm cen}$. We use these in different ways as described below.

$\Delta\eta$ lies in the range $[0°, 90°]$, where $0°$ indicates that the central galaxy is perfectly aligned with the shape of the projected member galaxy distribution of the cluster. That distribution is believed to trace the underlying DM halo shape with some scatter (Evans & Bridle, 2009; Oguri et al., 2010). The quantity $\Delta\eta$ is thus an observable proxy for the level of central galaxy alignment with its DM halo. We will regress it onto central galaxy- and cluster-related predictors to identify what central galaxy properties and/or cluster properties most strongly predict the alignments of central galaxies with their satellite galaxy distributions.

The definition of $\theta_{\rm cen}$ is illustrated in the left panel of Fig. 2.1. It is a direct observable reflecting a satellite's angular position with respect to the major axis direction of it's central galaxy. With each satellite galaxy having its corresponding $\theta_{\rm cen}$ as the response variable, we will regress it onto individual satellite quantities to understand what kind of satellites are more preferentially located along the major axis of the central galaxy.

2.3.2 Potential predictors

We classify the 16 predictors into three categories: central-related, cluster-related and satellite-related quantities. Table 2.2 lists these predictors under each category.

Central Galaxy Quantities: We use six central galaxy related physical parameters: central galaxy dominance, ${}^{0.1}M_r$, ${}^{0.1}M_g$-${}^{0.1}M_r$ color, ellipticity, effective radius, and central probability. Since there is a tight correlation between the size and luminosity of galaxies (e.g., Bernardi et al., 2014), in order to investigate the effect of galaxy size on central galaxy alignments, we use the offsets in galaxy size from the fitted size-magnitude relation, $\Delta\log(\text{cental } R_{\rm eff}) \equiv$ measured $\log(\text{cental } R_{\rm eff})$ − predicted $\log(\text{cental } R_{\rm eff})$, as our predictor when doing linear regression. The top panel of Fig. 2.4 shows the log(central $\rm R_{eff}$)–central ${}^{0.1}M_r$ correlations for the DR8 central galaxies. In the bottom panel, we present the log(central $\rm R_{eff}$) residuals from the fitted log(central $\rm R_{eff}$)–central ${}^{0.1}M_r$ relation, as a function of central ${}^{0.1}M_r$.

Cluster Quantities: We have four cluster-related physical parameters: log(richness), redshift, cluster ellipticity and cluster member concentration $\Delta_{\rm R}$.

Satellite Quantities: The six satellite-related quantities are the cluster-centric distance of each satellite normalized by its host $R_{\rm 200m}$, ${}^{0.1}M_r$, ${}^{0.1}M_g$-${}^{0.1}M_r$ color, ellipticity, effective radius, and the satellite alignment angle $\phi_{\rm sat}$. As for the central galaxies, we use the residual effective radius, $\Delta\log(R_{\rm eff})$, for satellites as our physical parameter instead of the directly measured $R_{\rm eff}$, in attempt to eliminate the contribution of luminosity on size. We fit the log($\rm R_{eff}$)–${}^{0.1}M_r$ correlations for the the 73146 satellites as shown in the top panel of Fig. 2.5 first, and then use $\Delta\log(R_{\rm eff}) \equiv$ measured $\log(R_{\rm eff})$

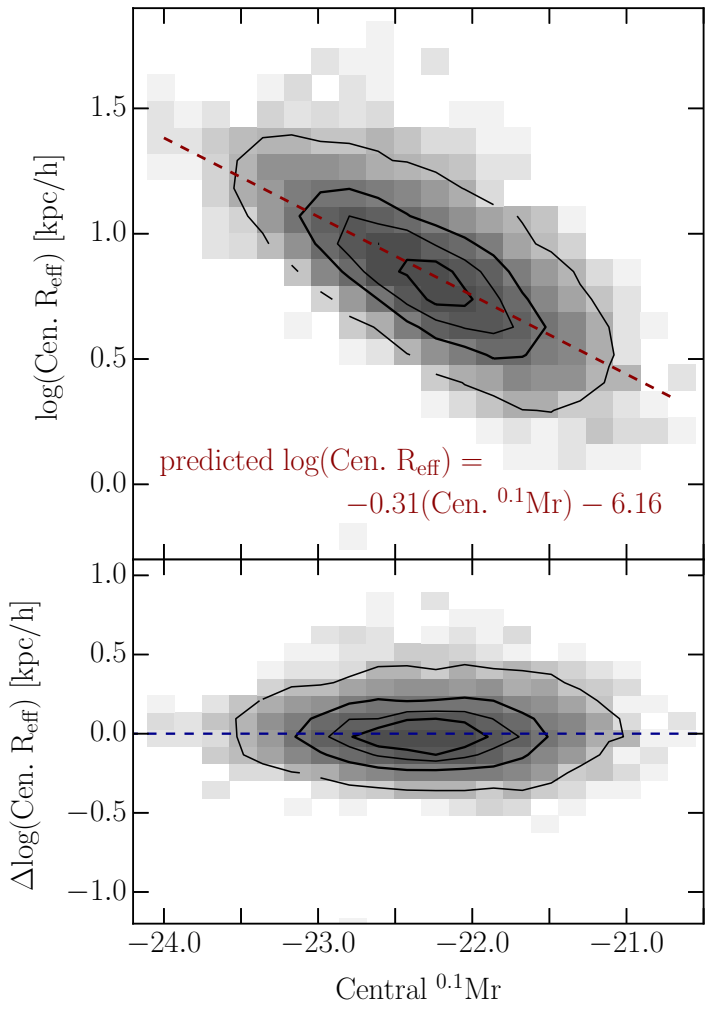

Figure 2.4: The top panel shows the contour plot of log(central R_{eff}) versus central $^{0.1}M_r$. The red dash line shows the least-squares fitting of a linear relationship between log(central R_{eff}) and central $^{0.1}M_r$, with the equation of the best fitted line shown on the plot. The bottom panel plots the residuals versus central $^{0.1}M_r$.

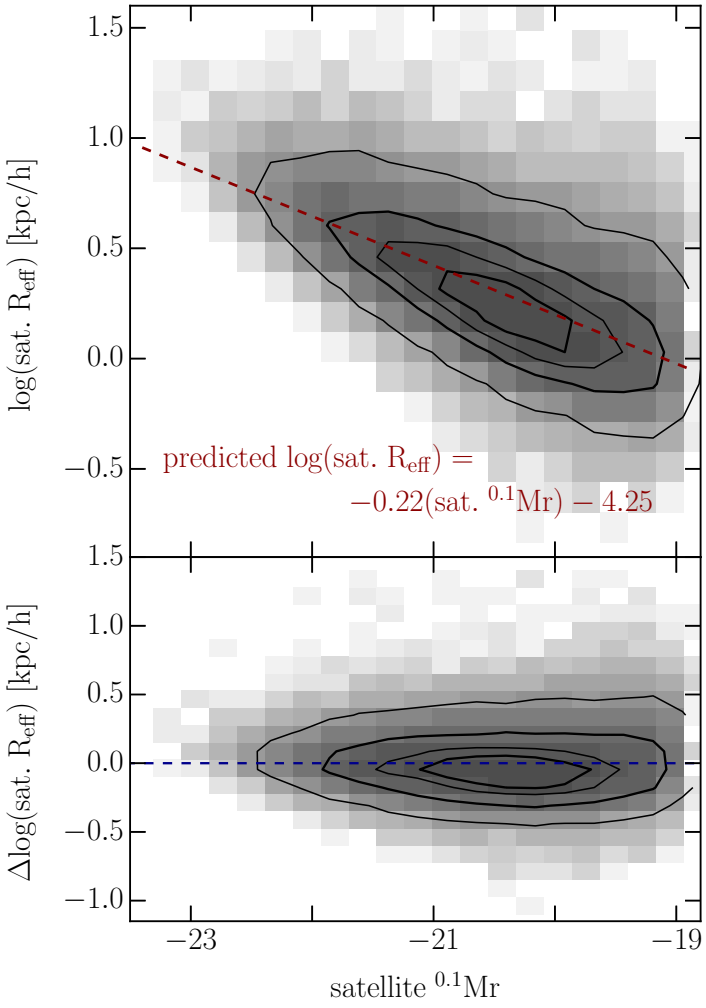

Figure 2.5: Similar to Fig. 2.4 but for cluster member galaxies instead of centrals.

− predicted $\log(R_{\rm eff})$ as our new size predictor. The bottom panel of Fig. 2.5 shows the $\Delta\log(R_{\rm eff})$ as function of ${}^{0.1}M_r$.

2.3.3 Variable selection

The goal of variable selection (e.g., Burnham & Anderson, 2003a; James et al., 2013) is to identify the subset of predictors that are important within a large pool of potential predictors. There are many statistical methods for subset selection; we adopt the "Forward-Stepwise Selection" approach (See e.g., Sec. 3.3 of Friedman et al., 2001). Beginning with a model containing no predictor, forward-stepwise selection involves fitting N models for the N predictors separately: $Y = \beta_0 + \beta_i X_i$, and selects the regressor X_p with the most significant hypothesis test on $\beta_p \neq 0$, i.e., greatest absolute t-value or smallest p-value. In the second cycle, $N - 1$ models for the remaining $N - 1$ predictors are fit via $Y = \beta_0 + \beta_p X_p + \beta_i X_i$, where $i \neq p$, and again we select the most significant regressor

Table 2.2: The 16 potential predictors used to study the central galaxy alignment effect in this work.

Central Galaxy Quantities	**Cluster Quantities**	**Satellite Quantities**
central galaxy dominance	log(richness)	$\log(r/R_{200\mathrm{m}})$
central $^{0.1}M_r$	redshift	satellite $^{0.1}M_r$
central $^{0.1}M_g - ^{0.1}M_r$ color	cluster ellipticity	satellite $^{0.1}M_g - ^{0.1}M_r$ color
central ellipticity		satellite ellipticity
$\Delta\log$(central R_{eff})	cluster member	$\Delta\log$(satellite R_{eff})
P_{cen}	concentration (Δ_{R})	ϕ_{sat}

X_q. At each stage, one predictor is selected to add to the model until the remaining regressors have p-value > 0.05, which is a common stoping choice in many statistical packages. The forward stepwise algorithm therefore considers at most $N + (N-1) + \ldots + 1 = N(N+1)/2$ models in the extreme case when all N regressors have p-value < 0.05. We then fit a model using least squares on the reduced set of variables, and determine the final t- and p-values of the selected featured predictors.

To ensure the robustness of our variable selection scheme, we compare our variable selection result with another variable selection method – "Best-Subset Selection" – which considers all 2^N possible combinations of models from the N predictors, and selects the best one based on a model-selection criterion, such as Mallow's C_p (Mallows, 1973), Akaike information criterion (AIC, Akaike 1998), Bayesian information criterion (BIC, Schwarz et al. 1978), or adjusted R^2. (By contrast, forward-stepwise selection is a so-called greedy algorithm – at each step, it selects only that one regressor that best improves the overall fit – and thus it can fail to uncover the optimal model. However, it does have the virtue of computational efficiency.) Different section criterion places different penalty on the complexity of the model. BIC penalizes heavier on models with more variables and hence tends to select smaller number of predictors, while adjusted R^2 puts less penalty thus results in selecting more predictors. In this work we use p-value < 0.05 as the criteria to pin down the total number of predictors in the forward-stepwise selection process, and this result agrees with that from best-subset selection under Mallow's C_p and AIC, validating our use of forward-stepwise selection with our dataset.

Throughout this work, we use the statistical package `StatsModels` in Python to do forward stepwise selection, and use the `leaps` package in R to perform best-subset selection.

In this work, we attempt to address two main questions: 1) What central galaxy and cluster properties are the strongest predictors of the strength of central galaxy alignments? 2) What kinds of satellites are more likely to lie along the major axis direction of their host central galaxy? To address the first question, we regress $\Delta\eta$ against the central- and cluster-related quantities, and use forward-stepwise selection to pick featured predictors. Once we have a good model in terms of central- and cluster-related quantities, we move to the second question by using θ_{cen} as a response for each central-satellite pair, and regress θ_{cen} against the individual satellite quantities. To isolate the effects of satellite properties, we must properly account for the overall effect from their host central galaxies and clusters. Thus, we start with a model containing the selected central and cluster predictors from the previous stage, and use the forward-stepwise procedure to see whether (with the presence of

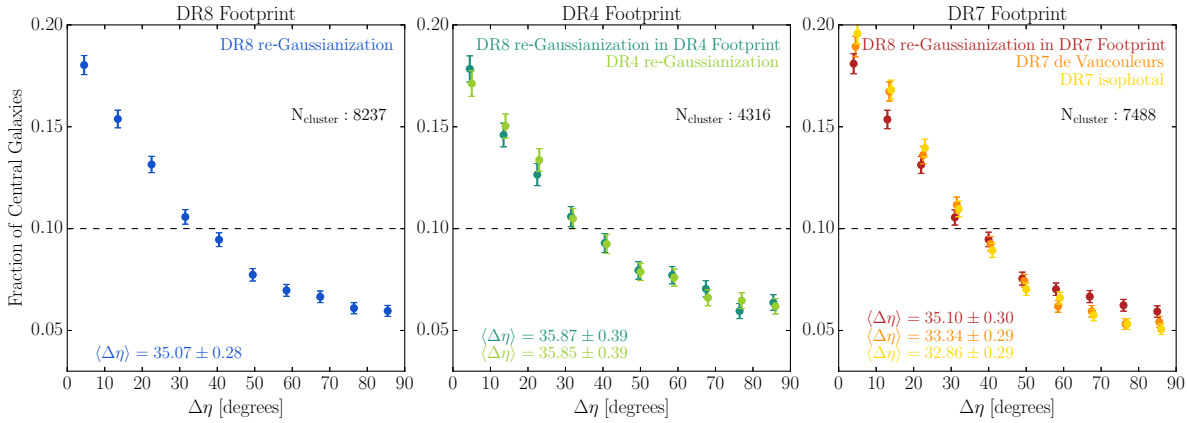

Figure 2.6: Distributions of the position angle difference between central galaxy and cluster, $\Delta\eta = |P.A._{\rm cen} - P.A._{\rm cluster}|$. The left panel shows the $\Delta\eta$ distribution of the parent 8237 centrals measured by the re-Gaussianization method in DR8. The middle panel plots the $\Delta\eta$ distributions of the 4316 centrals which are both measured by the re-Gaussianization method in the DR4 footprint, with the light (dark) green dots representing measurements based on the DR4 (DR8) photometry. The right panel shows the $\Delta\eta$ distributions of the 7488 centrals in DR7 footprint measured by re-Gaussianization (red dots), de Vaucouleurs (orange dots), and isophote (yellow dots) methods respectively. Points are slightly shifted horizontally for clarity. Error bars indicate the standard error of the mean. The horizontal black dashed line indicates the prediction for randomly-oriented central galaxies. The mean position angle difference, $\langle\Delta\eta\rangle$, is shown in the bottom left corner of each panel.

these central and cluster quantities) there are also satellite quantities that are significant enough to be selected as featured predictors.

2.4 Results

In this section, we report the results of an analysis of central galaxy alignments, including our linear regression analysis.

2.4.1 Overall signal

Distribution of $\Delta\eta$

We begin with a basic analysis of the properties of central galaxy alignments. Fig. 2.6 shows the distributions of the position angle difference between the central galaxy and cluster shapes, $\Delta\eta$, for our three cluster samples tabulated in Table 2.1, defined for the purpose of investigating systemics in various shape measurement techniques. The distributions show a highly significant degree of central galaxy alignment with cluster orientations. The bottom left corner of each panel shows the average $\Delta\eta$ value, $\langle\Delta\eta\rangle$, for each sample; they are all $\langle\Delta\eta\rangle < 45^\circ$ at high significance. Hence, if indeed the satellite galaxy distributions trace the dark matter halo shapes, then centrals also tend to align with their underlying halos.

The left panel of Fig. 2.6 is the $\Delta\eta$ distribution of the 8237 centrals measured by the re-Gaussianization method in DR8. The average $\Delta\eta$ for parent dataset is $\langle\Delta\eta\rangle = 35.07^\circ \pm 0.28^\circ$; this represents our primary result in this section, with the remaining results serving as systematics tests.

To compare the effect of sky-subtraction algorithm on the signal, we use the sample of 4316 centrals in the DR4 footprint with re-Gaussianization shape measurements using both DR8 and DR4 photometry. The middle panel of Fig. 2.6 shows the $\Delta\eta$ distributions of this sample, with the light (dark) green dots indicating measurements based on the DR4 (DR8) photometry. Within the error bars, the two $\Delta\eta$ distributions and their mean $\langle\Delta\eta\rangle$ values are consistent with each other. We therefore conclude that for the re-Gaussianization shapes, the effect of sky-subtraction does not substantially influence the overall distribution of $\Delta\eta$. However, this conclusion may not be applicable for other shape measurement methods that trace different regions on the surface brightness profile of galaxies. Re-Gaussianization shapes are weighted more toward the inner part of the light profile, which is less sensitive to sky subtraction errors, while isophotal shapes are more sensitive to the outer part and could have more systematics due to sky subtraction. However, due to the lack of isophotal shapes in DR8, we cannot test this effect by comparing different data reductions.

To investigate the effect of shape measurement methods on the detection of central galaxy alignments, we use the sample of 7488 BCGs that have re-Gaussianization, de Vaucouleurs, and isophotal shape measurements in DR7 footprint. The right panel of Fig. 2.6 shows the $\Delta\eta$ distributions of these samples, with the red, orange, and yellow dots representing shape measurements based on the re-Gaussianization method, de Vaucouleurs fit, and isophotal fit, respectively. Within the error bars, the second and third distributions agree, while the $\Delta\eta$ distribution measured using the re-Gaussianization method differs systematically. The value of $\langle\Delta\eta\rangle$ using the re-Gaussianization method ($35.10^\circ \pm 0.30^\circ$) is significantly larger than that calculated by de Vaucouleurs ($33.34^\circ \pm 0.29^\circ$) and isophotal ($32.86^\circ \pm 0.29^\circ$) shape measurements. This could be due to a systematic or caused by a true physical effect. We will discuss in detail in Sec. 2.5.

As further illustration of the alignment between the central and shape of member galaxy distribution, in Fig. 2.7 we compare the cluster and central galaxy position angles. With the overall distribution peaking around the symmetric axis of the figure, we observe the preference for centrals pointing toward the orientation directions of clusters.

Distribution of $\theta_{\rm cen}$

Fig. 2.8 shows the distributions of the central galaxy alignment angle, $\theta_{\rm cen}$, for our three sets of central-satellite pairs. The preferential alignment of satellites along the central galaxy major axis is quantified in the average central galaxy alignment angle, $\langle\theta_{\rm cen}\rangle$, in the bottom left corner of each panel. The alignment signal looks less dramatic as revealed in $\langle\theta_{\rm cen}\rangle$ value compared with $\langle\Delta\eta\rangle$ shown in Fig. 2.6. This is because $\theta_{\rm cen}$ records the individual location of each satellite with respect to its central galaxy major axis; these tend to be more randomized than simply considering the overall satellite distribution as a whole.

The left panel of Fig. 2.8 shows the $\theta_{\rm cen}$ distribution of the 94817 central-satellite pairs measured by the re-Gaussianization method in DR8. The average central galaxy alignment angle for this dataset is $\langle\theta_{\rm cen}\rangle = 41.42^\circ \pm 0.08^\circ$.

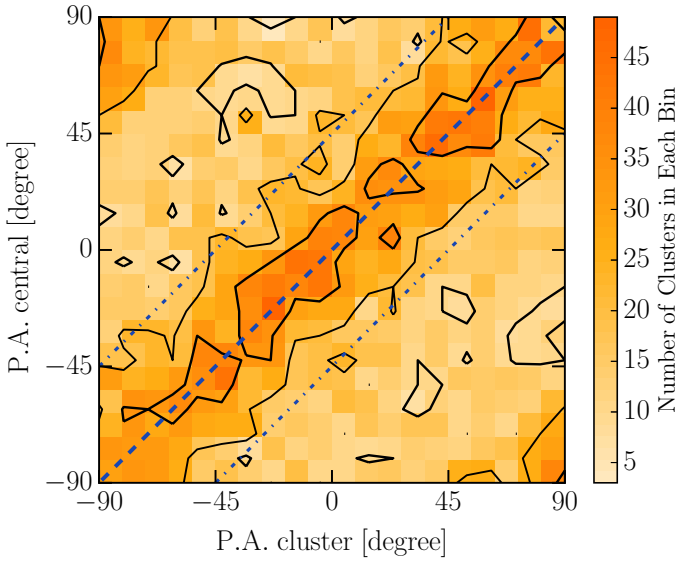

Figure 2.7: Comparison between the position angles of cluster and central galaxy. The blue dashed line indicates the case where the position angle of the central is the same as that of its cluster. The two blue dot-dashed lines delineate a region where the P.A. differences between the cluster and central galaxy are less than 45°.

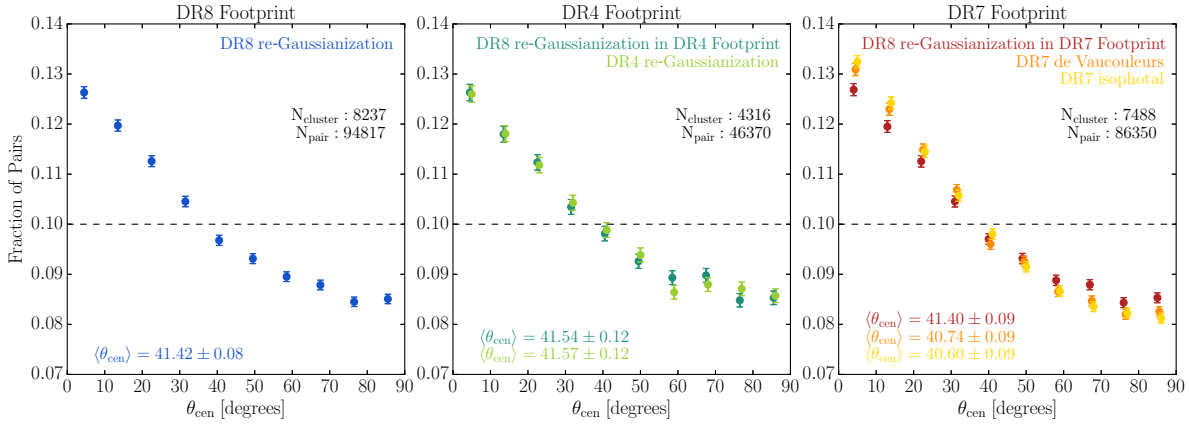

Figure 2.8: Distributions of the central galaxy alignment angle. The left panel shows the $\theta_{\rm cen}$ distribution of the 94817 central-satellite pairs measured by the re-Gaussianization method in DR8. The middle panel shows the $\theta_{\rm cen}$ distributions of the 46370 central-satellite pairs measured by re-Gaussianization in both DR8 photometry (dark green) and DR4 photometry (light green), within the DR4 footprint. The right panel shows the $\theta_{\rm cen}$ distributions of the 86350 central-satellite pairs in DR7 that are measured by re-Gaussianization (red dots), de Vaucouleurs (orange dots), and isophote (yellow dots) methods respectively. Points are slightly shifted horizontally for clarity. Error bars are represented by the standard error of the mean. The horizontal black dash line indicates the case if satellites were isotropically distributed around centrals. The mean central galaxy alignment angle, $\langle\theta_{\rm cen}\rangle$, is shown at the bottom left corner of each panel.

The middle panel shows the $\theta_{\rm cen}$ distributions for the 46370 central-satellite pairs in the DR4 footprint, using DR8 (dark green) and DR4 (light green) photometry, constructed to compare the effect of sky-subtraction technique on the measurement of $\theta_{\rm cen}$. Within the error bars, the two $\theta_{\rm cen}$ distributions and the derived $\langle\theta_{\rm cen}\rangle$ values are consistent with each other. As for $\Delta\eta$, we conclude that for the re-Gaussianization shapes, use of different SDSS photometry pipelines does not influence the results, but caution that this argument may not hold for other shape measurement methods.

To fairly compare our $\theta_{\rm cen}$ measurement with studies based on different shape measurement methods, the right panel of Fig. 2.8 shows $\theta_{\rm cen}$ measured via re-Gaussianization (red dots), de Vaucouleurs (orange dots), and isophote (yellow dots) shape measurements of the 86350 central-satellite pairs in the DR7 footprint. Within the error bars, the histograms of $\theta_{\rm cen}$ using de Vaucouleurs and isophotal shapes are consistent with each other, but that for re-Gaussianization method is systematically different, resulting in a systematically higher $\langle\theta_{\rm cen}\rangle$ ($41.40^\circ \pm 0.09^\circ$). We will discuss the measurement difference in Sec. 2.5.

2.4.2 Linear regression: central galaxy alignments with satellite distributions

To investigate the alignment of the central galaxy with its dark matter Halo, we use our observational proxy (the difference in central and cluster position angles, $\Delta\eta$) as the response variable, and apply forward-stepwise selection described in Sec. 2.3.3 to select featured predictors among the central- and cluster-related quantities. The list of predictors is defined in Sec. 2.3.2, with the observational method for determining them in Sec. 2.2.2.

Fig. 2.9 displays the scatterplot matrix between $\Delta\eta$ and all of the central- and cluster-related predictors based on the re-Gaussianization shape measurement. The diagonal panels are histograms of physical parameters, and the other panels are scatterplots between pairs of parameters, with the corresponding correlation coefficient noted on each plot.

Several important results are evident in this scatterplot matrix. First, the top row summarizes how $\Delta\eta$ is related to all ten predictors. The sign of the correlation coefficient reveals the direction of the relationship between $\Delta\eta$ and the regressor , while the magnitude of the correlation coefficient indicates the strength of this dependence. The overall impression is that $\Delta\eta$ is weakly related to most of the predictors, with a maximum correlation coefficient of ~ -0.2 with cluster ellipticity. Though the correlations are weak, we can still judge whether these dependences are statistically significant given our large sample size. Second, some of the predictors are highly correlated with each other, such as central galaxy ${}^{0.1}M_r$, central galaxy dominance and $P_{\rm cen}$. The forward-stepwise selection procedure will help determine whether we should keep them all as featured predictors; if any are jointly responsible for the same variation in $\Delta\eta$, then we will select just the most representative one among them.

After performing forward-stepwise selection, we find that cluster ellipticity is the most dominant predictor for the central galaxy alignment effect, and almost all of the central-related quantities are selected as feature predictors except for central galaxy dominance. The linear regression results, including the statistical significance of each selected predictor, are in Table 2.3, and the estimated

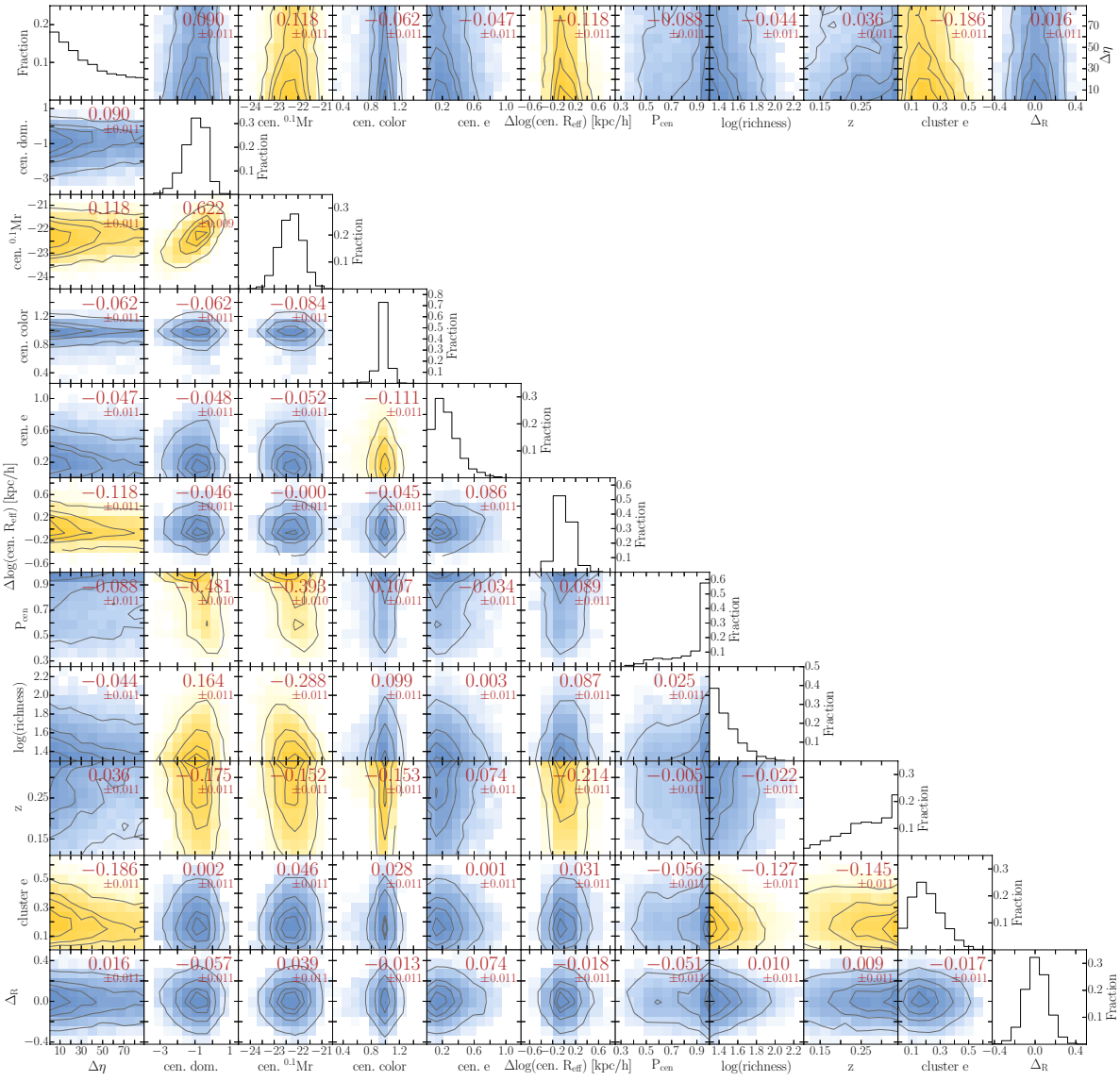

Figure 2.9: Scatterplot matrix of the position angle difference between central and cluster shapes, $\Delta\eta$, with the ten central- and cluster-related predictors. The correlation coefficient between each pair of parameters is noted on the plot. We highlight scatterplots with correlations that are significant at $> 10\sigma$ in yellow. The gray contour levels indicate 20%, 40%, 70%, and 95% number of clusters of our data.

Table 2.3: Selected featured predictors for the central galaxy-cluster alignment effect based on the 8233 DR8 clusters. The first column is the name of the selected predictor. The second column gives the regression coefficient β. Columns 3 and 4 provide the t- and p-values from the significance tests on the deviation of β from zero. Higher $|t|$ or smaller p indicates a higher significance for $\beta \neq 0$. Columns 5 and 6 are the mean and standard deviation of the corresponding predictor for the 8233 clusters, necessary in Eq. (2.12) to normalize our predictor P_i to regressor X_i.

Predictor	β	t-value	p-value	mean	σ
cluster e	-4.91	-17.8	8×10^{-70}	0.21	0.11
Δlog(cen. $R_{\rm eff}$)	-2.67	-9.7	6×10^{-22}	0.00	0.15
cen. $^{0.1}M_r$	2.42	7.8	9×10^{-15}	-22.30	0.47
cen. color	-1.29	-4.6	4×10^{-5}	0.97	0.08
$P_{\rm cen}$	-1.21	-4.0	6×10^{-5}	0.87	0.17
cen. $e^{\dagger}$	-1.03	-3.7	0.0002	0.26	0.16
log(richness)	-0.65	-2.2	0.03	1.48	0.15

†The relationship between central galaxy ellipticity and the central galaxy alignment signal is more complicated. We will provide further investigation in Sec. 2.6.5.

best-fitting equation is:

$$\begin{aligned}\Delta\eta = 35.07 &- 4.91\,\frac{\text{cluster } e - 0.21}{0.11} \\ -2.67\,\frac{\Delta\log(\text{cen. } R_{\rm eff}) - 0.00}{0.15} &+ 2.42\,\frac{\text{cen. } ^{0.1}M_r + 22.30}{0.47} \\ -1.29\,\frac{\text{cen. color} - 0.97}{0.08} &- 1.21\,\frac{P_{\rm cen} - 0.87}{0.17} \\ -1.03\,\frac{\text{cen. } e - 0.26}{0.16} &- 0.65\,\frac{\log(\text{richness}) - 1.48}{0.15}\end{aligned} \tag{2.14}$$

Here we note that since the relation between $\Delta\eta$ and these selected predictors is not truly linear and has substantial stochasticity, we cannot rely on the resulting regression equation to predict the value of $\Delta\eta$ for any given cluster. We can only use Eq. (2.14) to understand the sign and approximate strength of the variation of $\Delta\eta$ with those predictors to first order. Therefore, based on the trend of Eq. (2.14), we find that central galaxy alignment effects are strongest for clusters that are more elongated and higher richness, or clusters that have centrals with larger physical size, brighter absolute magnitude, redder color, larger ellipticity[2], and a higher centering probability.

2.4.3 Linear regression: angular segregation of satellite galaxies

In Sec. 2.4.2, we used the positions of satellite galaxies weighted by their membership probabilities to trace the cluster and underlying halo shape, without any consideration of individual satellite properties.

[2]As we will demonstrate later in Sec. 2.6.5, the dependence on central galaxy ellipticity is actually more complicated than this simple linear regression result indicates.

Table 2.4: Predictors involved in the angular segregation of satellites as analyzed in Sec. 2.4.3. The columns are the same as in Table 2.3. The bottom panel lists the already-identified central galaxy and cluster quantities. These quantities are included in the linear regression equation when doing variable selection, in order to properly account for their influence on the angular segregation of satellites. The top panel shows the four selected satellite quantities that significantly affect angular segregation.

Predictor	β	t-value	p-value	mean	σ
satellite color	-0.66	-6.7	2×10^{-11}	0.91	0.09
satellite ${}^{0.1}M_r$	0.54	5.23	1×10^{-7}	-20.46	0.76
$\log(r/\mathrm{R_{200m}})$	0.21	2.12	0.03	-0.87	0.32
satellite e	0.20	2.1	0.04	0.43	0.26
cluster e	-2.52	-25.6	2×10^{-143}	0.21	0.11
$\Delta\log(\mathrm{cen.\ R_{eff}})$	-0.64	-6.4	1×10^{-10}	0.02	0.15
cen. ${}^{0.1}M_r$	0.58	5.01	1×10^{-6}	-22.35	0.49
cen. color	-0.28	-2.8	0.005	0.98	0.07
P_{cen}	-0.46	-4.2	2×10^{-5}	0.87	0.17
cen. e	-0.42	-4.2	3×10^{-5}	0.25	0.16
log(richness)	0.09	0.8	0.4	1.58	0.21

However, satellite galaxies with different properties are known to be distributed in different ways within clusters, a phenomenon known as segregation (e.g., van den Bosch et al., 2016). Segregation is often discussed in terms of the radial direction to the cluster center. Here we investigate angular segregation with respect to the central galaxy major axis, to understand what satellite properties most strongly predict the satellite tendency to lie along the central galaxy major axis.

Fig. 2.10 shows the scatterplot matrix of θ_{cen} versus the six satellite-related quantities for the 73146 DR8 central-satellite pairs. The top row displays scatterplots between θ_{cen} and all other satellite quantities. Compared with Fig. 2.9, the absolute magnitudes of the correlation coefficients of θ_{cen} with these satellite quantities are generally smaller than the correlation between $\Delta\eta$ and central and cluster quantities. Although the correlations are weak, the large number of pairs means there is still enough statistical power to measure these correlations robustly. In general, the relationships between all pairs of predictors appear to be weak, except for ${}^{0.1}M_r$ and ellipticity, with a correlation coefficient of 0.236. The lower right corner shows the distribution of ϕ_{sat}, which is very close to flat, indicating that satellite radial alignment is a far weaker phenomenon compared to central galaxy alignments; we explore this phenomenon in more detail in future work.

Given that we already identified the important central galaxy- and cluster-related predictors that affect the central galaxy alignment signal, it is reasonable to include these predictors in our linear regression analysis in order to compensate for their influence on the angular segregation of satellites. Table 2.4 shows the results of linear regression, with the new selected satellite quantities on top and the already-known central galaxy and cluster quantities on the bottom. Almost all previously-selected quantities have an associated $p-$value below 0.05 when using θ_{cen} as the response variable, except for cluster richness λ. This may be due to the fact that higher richness clusters tend to be rounder (as

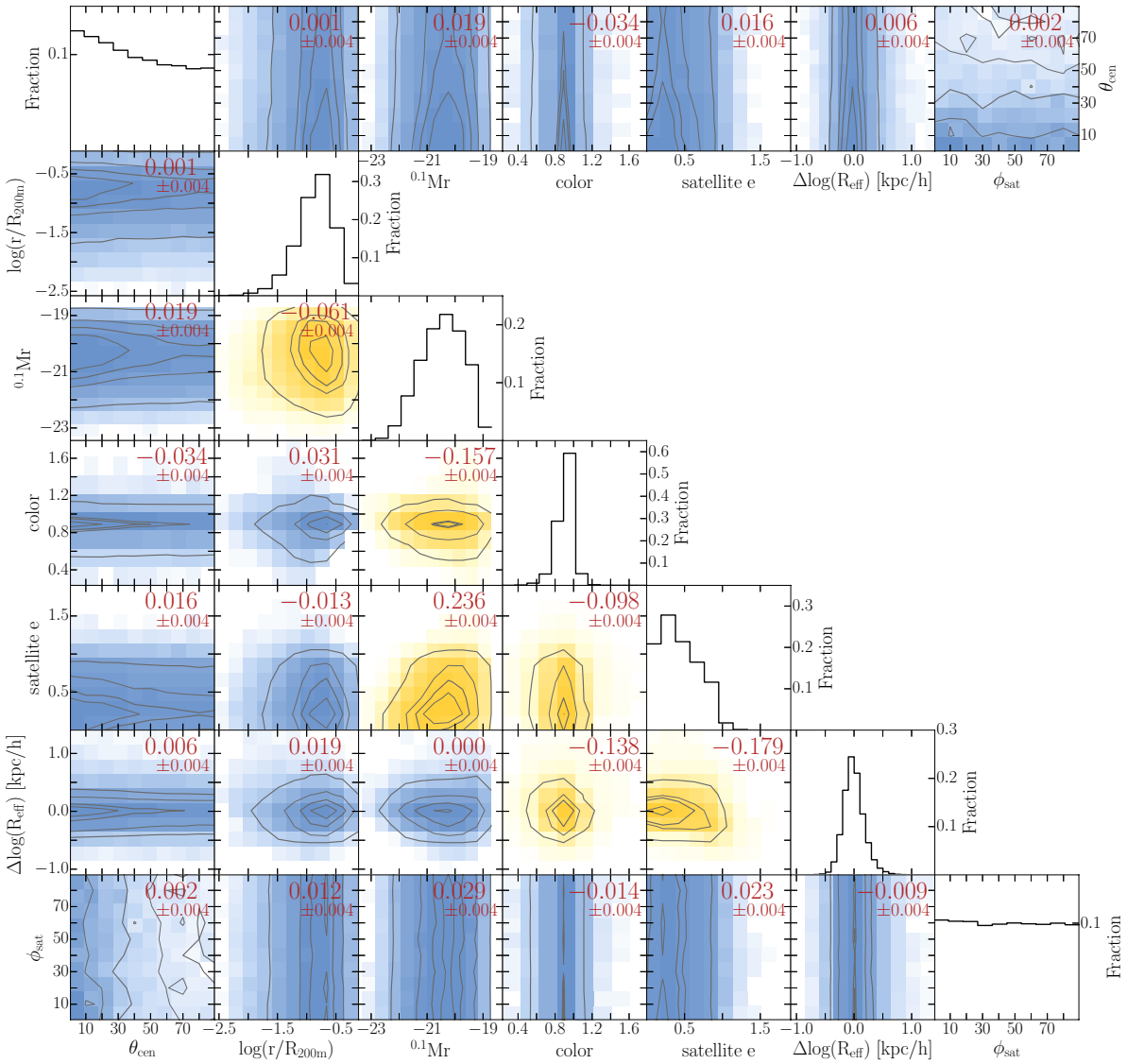

Figure 2.10: Scatterplot matrix of the central galaxy alignment angle with the six satellite related quantities. The correlation coefficient between each pair of parameters is noted on the plot. We highlight scatterplots with correlations that are significant at $> 10\sigma$ in yellow. The gray contour levels indicate 20%, 40%, 70%, and 95% number of satellites of our data.

revealed in the last row of Fig. 2.9), and thus have their member galaxies less segregated toward any specific direction. Also, although the regression slope for log(richness) is positive, we cannot infer that satellites in lower richness clusters tend to be more segregated (i.e. having smaller $\theta_{\rm cen}$). The level of angular segregation against richness is not significant enough for us to make such a conclusion. The best-fitted linear regression equation with these predictors is

$$\begin{aligned}\theta_{\rm cen} = 41.60 &- 0.66\,\frac{\text{sat. color} - 0.91}{0.09} + 0.54\,\frac{\text{sat. }^{0.1}M_r + 20.46}{0.76} \\ &+0.21\,\frac{\log(r/\mathrm{R_{200m}}) + 0.87}{0.32} + 0.20\,\frac{\text{sat. } e - 0.43}{0.26} \\ &-2.52\,\frac{\text{cluster } e - 0.21}{0.11} - 0.64\,\frac{\Delta\log(\text{cen } R_{\rm eff}) - 0.02}{0.15} \\ &+0.58\,\frac{\text{cen }^{0.1}M_r + 22.35}{0.49} - 0.28\,\frac{\text{cen color} - 0.98}{0.07} \\ &-0.46\,\frac{P_{\rm cen} - 0.87}{0.17} \\ &-0.42\,\frac{\text{cen } e - 0.25}{0.16} + 0.09\,\frac{\log(\text{richness}) - 1.58}{0.21}\end{aligned} \tag{2.15}$$

The tendency of satellites to reside along the central galaxy major axis is strongest for satellites that are redder, brighter, rounder, and located closer to the central.

2.5 The effect of shape measurement method on the central galaxy alignment signal

In the rightmost panels of Figs. 2.6 and 2.8, we compared the distributions of our response variables, $\Delta\eta$ and $\theta_{\rm BCG}$, using three different shape measurements methods. In both cases, the level of central galaxy alignment measured via de Vaucouleurs and isophotal shapes agree with each other within the error bar, while the re-Gaussianization measurement gives us a less strong central galaxy alignment effect. In this section, we discuss the interpretation of this result in terms of systematic and physical effects in these shape measurements. Our discussion also relies on results of Singh & Mandelbaum (2016), who analyzed the effect of these three shape measurement methods on the inferred galaxy alignments of luminous red galaxies (LRGs).

2.5.1 Systematic error

Different shape measurements deal with the effects of the PSF on galaxy images differently. The re-Gaussianization technique was designed for weak lensing studies requiring the most complete removal of the PSF effect on galaxy shapes. The de Vaucouleurs shape measurement only partially corrects for the PSF by using a double-Gaussian fit instead of the full PSF model, while the isophotal shape measurement does not correct for the effect of the PSF explicitly.

Another relevant aspect of systematics has to do with what part of the light profile is used for the measurement. The re-Gaussianization method has an elliptical Gaussian weight function, emphasizing the central regions of the profile. The de Vaucouleurs profile includes both the central region and

the large-scale wings of the light profile, while the isophotal shape measurement *only* uses the 25 mag/arcsec^2 isophote which is quite far out in the wings. These choices could make the latter two methods more sensitive to sky subtraction systematics than the re-Gaussianization method (for more discussion in the context of the isophotal method, see Hao et al., 2011).

One could infer that isophotal shapes would contain severe systematics due to the PSF. However, the results of Singh & Mandelbaum (2016) suggest that the impact of the PSF on the shape measured at very low surface brightness is quite small. Instead, the de Vaucouleurs shapes exhibited the most significant systematic errors of the three methods. Therefore, we may treat the detected differences in the central galaxy alignment strength between the re-Gaussianization and isophotal shapes as reflecting a true physical effect that we will discuss below. However, we should keep in mind that the systematic tests in Singh & Mandelbaum (2016) were based on a specific sample of galaxies, while our central galaxy sample (which is preferentially located in regions of high galaxy density) may still suffer from some contamination in the isophotal shapes, as suggested by Hao et al. (2011).

2.5.2 Physical effect

The higher apparent degree of central galaxy alignment using isophotal shapes compared to that using re-Gaussianization sahpes may be primarily due to a mechanism called "isophote twisting" (di Tullio, 1978, 1979; Kormendy, 1982; Romanowsky & Kochanek, 1998; Lauer et al., 2005). The physical origin of this effect is that the outer part of the galaxy light profile may respond more strongly to tidal fields than the inner part of the galaxy. Thus, by tracing the outermost isophote of the galaxy, the isophotal shape records the highest level of alignment with the tidal field.

2.6 The origin of central galaxy alignment

In Sec. 2.4.2 we applied linear regression analysis to the nine central galaxy and cluster quantities, and picked the predictors that significantly influence the alignment between central galaxy and its host cluster. We now address the origin of this alignment phenomenon and compare our results with previous studies.

2.6.1 Dependence on cluster ellipticity

Simulations have revealed that clusters are triaxial rather than spherical (Jing & Suto, 2002; Hopkins et al., 2005; Kasun & Evrard, 2005; Allgood et al., 2006; Hayashi et al., 2007), so they look elongated when projected on the sky. The last panel in the second last row of Fig. 2.9 shows the distribution of projected redMaPPer cluster ellipticities traced by the weighted member galaxy distribution (see Sec. 2.2.2 for definition of cluster ellipticity), with a mean cluster ellipticity of ~0.20 and a mean projected semi-minor to semi-major axis ratio of $\langle b/a \rangle \sim 0.67$, which agrees with the N-body simulation of Hopkins et al. (2005) ($\langle b/a \rangle \sim 0.67$, at redshift zero), but is rounder than that directly measured through gravitational lensing ($\langle b/a \rangle \sim 0.48^{+0.14}_{-0.09}$ in Evans & Bridle 2009, and $\langle b/a \rangle \sim 0.46 \pm 0.04$ in Oguri et al. 2010).

As shown in Table 2.3, we find that cluster ellipticity has the most significant influence on the central galaxy alignment signal, with centrals in more elongated clusters having a stronger alignment

with the orientation of their host clusters (see also the second-to-last panel in the first row of Fig. 2.9, which directly displays the correlation between cluster ellipticity and central galaxy alignment). Since the position angle for round clusters is not very meaningful, particularly given observational noise, we have examined the correlation trend for clusters with ellipticity > 0.2, and found the trend that more elongated clusters show stronger alignment still holds.

The influence of cluster ellipticity on central galaxy alignment can be further visualized in the left panel of Fig. 2.11, where we plot the distribution of the $p_{\rm mem}$-weighted averaged central galaxy alignment angle for all $p_{\rm mem} > 0.2$ central-satellite pairs in each cluster, $\langle\theta_{\rm cen}\rangle_{\rm cl} = \frac{\sum_i p_{{\rm mem},i}\theta_{\rm cen}}{\sum_i p_{{\rm mem},i}}$, against the cluster ellipticity. The sharp boundary on each side is due to the way we define cluster ellipticity. Since we calculate cluster ellipticity via the satellite galaxy distribution, round clusters (with satellites distributed in an almost circularly symmetric way) thus have $\langle\theta_{\rm cen}\rangle_{\rm cl} \sim 45^\circ$. More elongated clusters have more potential for going to lower or higher $\langle\theta_{\rm cen}\rangle_{\rm cl}$ values. At fixed cluster ellipticity, the distribution of $\langle\theta_{\rm cen}\rangle_{\rm cl}$ tends to cluster towards the edges of the minimum and maximum available values. As a demonstration, the right panel of Fig 2.11 shows the results of simulating two fake clusters with fake member galaxies distributed with elliptical symmetry such that the two clusters would have measured cluster ellipticity of 0.5 (green) and 0.3 (red). We then randomized the P.A. of the simulated central galaxies, and calculated the corresponding $\langle\theta_{\rm cen}\rangle_{\rm cl}$ value. From the scatter plot and histograms of P.A. central vs. $\langle\theta_{\rm cen}\rangle_{\rm cl}$, it is clear that the relationship between central galaxy P.A. and $\langle\theta_{\rm cen}\rangle_{\rm cl}$ is non-linear, and that this non-linearity is responsible for the shape of the left panel of Fig. 2.11. However, with more clusters distributed on the $\langle\theta_{\rm cen}\rangle_{\rm cl} < 45^\circ$ side across the full cluster ellipticity range shown in the left panel of Fig 2.11, centrals do prefer to align with their overall satellite distributions.

There are two mechanisms that may be responsible for the strong dependence of central galaxy alignment on cluster shape: 1) the imprint of infall of matter and galaxies into the cluster preferentially along filaments, and 2) the large-scale tidal gravitational field (either primordial, at the time of central galaxy formation, or tidal torquing over time). First, centrals and their parent clusters are both formed via accreting galaxies along filaments, which imprint preferred directions. As a result of these inflows, we expect central galaxies to be aligned with their clusters, especially for relatively young and small clusters with only one dominant filament, leaving an elongated distribution of galaxies (Knebe et al., 2004; Libeskind et al., 2005, 2015). More massive clusters may have experienced several merger events along filaments in various directions during their assembly history. This more complicated history makes the distribution of galaxies in these clusters more disturbed and randomized, resulting in a rounder shape. Indeed, as shown in the second-to-last row of Fig. 2.9, there is a weak anti-correlation between cluster ellipticity and richness in our data, with richer clusters having a smaller ellipticity. The subsequent violent merger activities may wash out the memory of the primordial filamentary structure, causing a reduction in the alignment signal (Ragone-Figueroa & Plionis, 2007).

However, over the process of virialization, the distribution of galaxies in clusters would again gradually be stretched out along the direction with the surrounding large-scale tidal field, reaching new equilibrium states with a triaxial morphology. At the same time, central galaxies would also gradually be tidally torqued along the new established direction of tidal field. A more anisotropic distribution of satellites could indicate a more intense tidal fields to torque the centrals. It is unclear how important this instantaneous torquing is; Camelio & Lombardi (2015) demonstrated that at galaxy

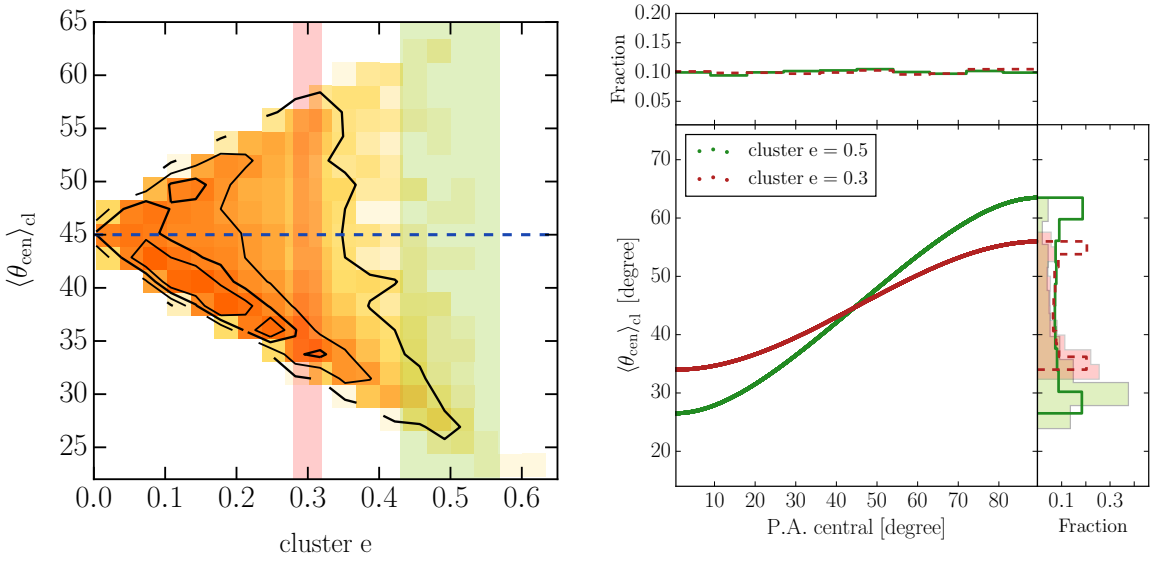

Figure 2.11: Left Panel: Contour plot between cluster ellipticity and averaged central galaxy alignment angle for all central-satellite pairs in each cluster, $\langle\theta_{\rm cen}\rangle_{\rm cl}$. The blue dashed line indicates the case $\langle\theta_{\rm cen}\rangle_{\rm cl} = 45°$, when satellites are randomly distributed within cluster. The light-green (pink) shaded area marks out clusters with ellipticity in the range of 0.43~0.57 (0.28~0.32). For each cluster ellipticity value, there are more clusters distributed in the region below the blue dash line than above, showing the tendency for central galaxy alignments. Right Panel: Non-linear relationship between central galaxy P.A. and the derived $\langle\theta_{\rm cen}\rangle_{\rm cl}$ in our simulated data. The simulated clusters with cluster ellipticity of 0.5 (0.3) are shown in green (red). With completely random distributions of simulated central galaxy P.A., the distributions of derived $\langle\theta_{\rm cen}\rangle_{\rm cl}$ tend to peak at their minimum or maximum available values. The light-green and pink shaded histograms are the distributions of $\langle\theta_{\rm cen}\rangle_{\rm cl}$ in our observational data within certain cluster ellipticity ranges as highlighted in the left panel.

scales, it is too weak to account for the observed intrinsic alignments, but it is unclear whether it is definitely subdominant for cluster mass scales.

We emphasize that the above two scenarios (anisotropic infall and tidal torquing) are not mutually exclusive and do not necessarily have some sequence in time. They could both operate at various stages of the cluster and central galaxy evolutionary process. Also, according to the linear alignment model (e.g., Catelan et al., 2001; Hirata & Seljak, 2004b), the intrinsic alignment is already set by tidal fields at the time of galaxy formation, and it is not clear how relevant these additional processes that operate later may be.

2.6.2 Dependence on central galaxy effective radius

As we have shown, the central galaxy effective radius at fixed intrinsic luminosity is also a very significant predictor of the central galaxy alignment effect, with larger-sized centrals at a given luminosity exhibiting a stronger degree of central galaxy alignment than smaller-sized centrals.

Observations and semi-analytic models have revealed that most massive galaxies grow inside-out, with their extended stellar halos dominated by accreted stars. The supply of accretion stars may originate from the stellar streams (Belokurov et al., 2006) or the diffuse intracluster light (ICL) which is composed of tidally-stripped stars that are gravitationally bound to the cluster potential (Oemler, 1976; Lin & Mohr, 2004). These massive accretion-dominated galaxies thus tend to have more extended light profiles compared to galaxies with a stellar component that primarily underwent "in situ" star formation (van Dokkum et al., 2010; Cooper et al., 2013).

There are two scenarios that can explain the dependence of central galaxy alignment on central galaxy size. First, centrals with more extended morphology may respond more strongly to tidal forces (either the primordial or instantaneous tidal field). Defined as the difference between the gravitational forces at two different positions on an object, the strength of the tidal force would be stronger for objects that have a larger spatial extent. The alternative explanation stems from the closely linked formation and evolution histories of centrals with their host clusters and the surrounding large-scale structures (Conroy et al., 2007). As reported in Zhao et al. (2015), centrals with extended cD envelopes tend to have larger $R_{\rm e}$, and are believed to be dominated by baryons from accretion. If there is an abundant supply of accretion stars in some direction aligning with the overall distribution of member galaxies, the central galaxy shape would naturally extend towards the preferred direction of accretion, and thus align with the angle of the member galaxy distribution. We are unable to distinguish between these two scenarios.

2.6.3 Dependences on central galaxy luminosity, dominance and centering probability

According to Fig. 2.9, central galaxy luminosity, dominance and centering probability are mutually highly correlated with each other, and thus are likely caused by similar physical origins. Here we discuss the dependences of central galaxy alignment on these three predictors.

As revealed in Table 2.3, we found that $\Delta\eta$ depends significantly on central galaxy ${}^{0.1}M_r$ and $P_{\rm cen}$, with centrals that are more luminous and have a higher centering probability tending to be more aligned with the cluster position angle. Central galaxy dominance, however, was not selected as a featured predictor. This does not mean that central galaxy dominance is not important, but rather that

its effect on central galaxy alignment may have been soaked up by the effects of central ${}^{0.1}M_r$ and $P_{\rm cen}$, so that knowing the central galaxy dominance provides no further help when predicting $\Delta\eta$ if the other two predictors are also known.

Our result is consistent with that of Hao et al. (2011), who also detected a strong dependence of BCG alignment on BCG luminosity based on a sample of richness ≥ 15 clusters taken from GMBCG, a cluster catalog constructed based on the red-sequence method (Hao et al., 2010). Also, due to the tight correlation between central galaxy ${}^{0.1}M_r$ and dominance, with more luminous centrals showing higher degree of central galaxy dominance, our result implies that clusters with more dominant centrals should have stronger central galaxy alignment. This agrees with the result of Niederste-Ostholt et al. (2010). They found that BCG-dominant clusters exhibit stronger BCG alignments than less BCG-dominant clusters do, with a difference significant at the 4.4σ level, based on both the maxBCG cluster catalog (Koester et al., 2007) and a matched filter cluster catalog of Dong et al. (2008).

The dependences of the central galaxy alignment signal on central ${}^{0.1}M_r$, dominance and $P_{\rm cen}$ have their common origin in the following aspects. 1) It may originate from the purity of measurement. Luminous and dominant centrals have a higher probability of sitting closer to the true center of their dark matter potential wells (Wen & Han, 2013). This kind of system suffers less contamination from wrong detections, and could therefore end up showing a higher central galaxy alignment signal. 2) Clusters with luminous and dominant centrals are typically more relaxed. More relaxed systems have experienced the uninterrupted (by mergers) influence of surrounding large-scale tidal fields for a longer period of time, and thus it may be more likely for their centrals to align.

Given that central ${}^{0.1}M_r$ and dominance are highly correlated at $\sim$0.6, it is natural to ask what causes us to select central ${}^{0.1}M_r$ rather than dominance as a featured predictor? To address this question, in Fig. 2.12, we show some example clusters with luminous but less dominant centrals. As shown, these clusters typically have several bright galaxies, and may still be undergoing significant merging and disruptive interactions. Figs. 2.12a and c show examples of clusters with their dominantly bright members still some distance away from the centrals. These systems may be not relaxed, but if the centrals' high luminosities and the distributions of their members stem from the same primary avenue of accretion, high alignment signals can still shown even if the centrals are not dominant. This explains why the importance of central ${}^{0.1}M_r$ stands out from central galaxy dominance.

Fig. 2.12b shows the case where the bright members already sank into the potential well of the cluster and are closely interacting with the central galaxy. In this case, the orientation of the central galaxy may be affected temporarily by these closely interacting galaxies, rather than reflecting the tidal field originating from the large-scale environment. The upper right corner of each panel in Fig. 2.12 shows some physical properties of the central galaxy. In the case of Fig. 2.12b, with several bright galaxies crowded in the central region of the cluster, the central $P_{\rm cen}$ tends to be low. This demonstrates that $P_{\rm cen}$ can still be selected as a featured predictor even after selecting central ${}^{0.1}M_r$, because it indicates whether there are other bright galaxies near the central that may reduce the central galaxy alignment with the large-scale tidal field through dynamical processes. While examining images of individual clusters does not give the full picture, it is a way of supplementing the statistical measure of central galaxy alignment from the linear regression analysis.

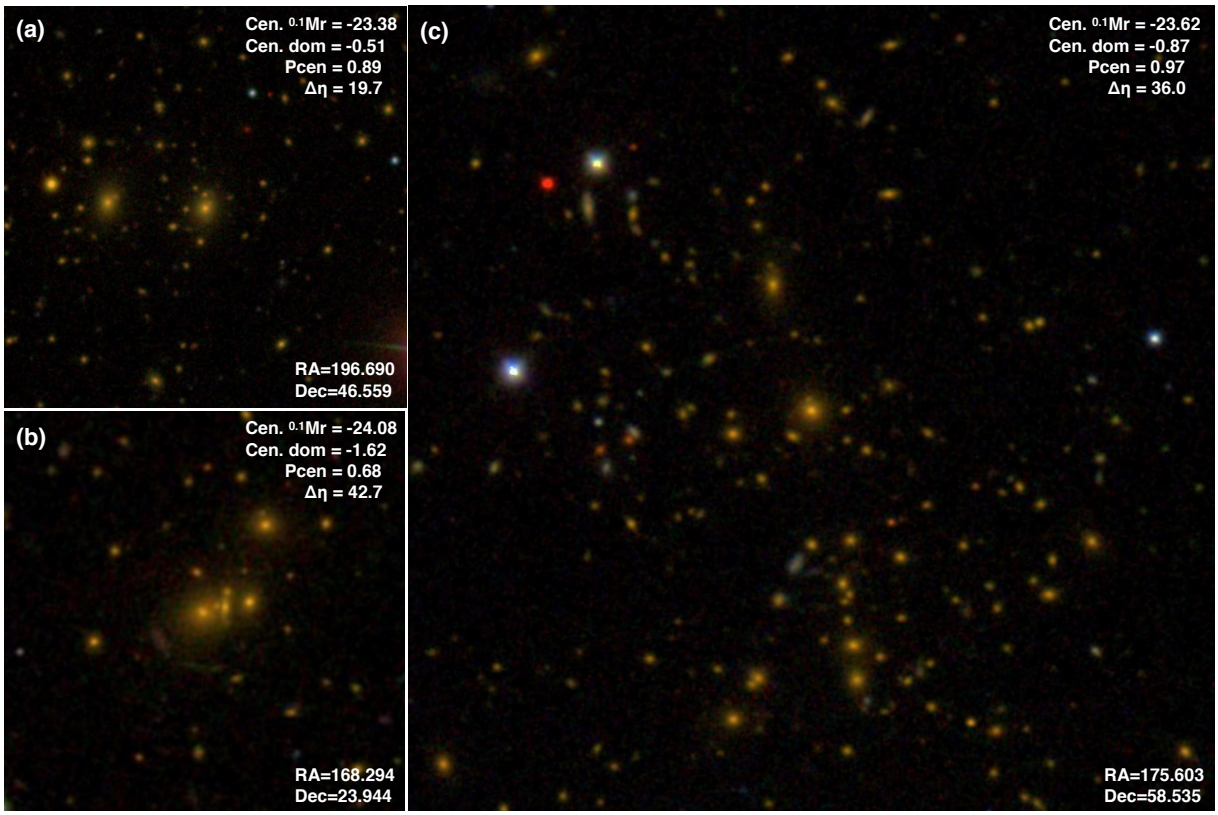

Figure 2.12: Examples of clusters with central galaxies that are luminous but not dominant. The widths of panels (a), (b), (c) are set to be $\frac{1}{4}$, $\frac{1}{5}$, and $\frac{1}{2}R_{200\mathrm{m}}$ (respectively) of their host clusters.

2.6.4 Dependence on central galaxy color

We observed that redMaPPer centrals with redder color show stronger central galaxy alignments. The enhancement of the central galaxy alignment signal among red hosts has also been observed in systems across a wide range in halo masses. Based on a sample of isolated host galaxies with typically 1–2 csatellites, Azzaro et al. (2007) and Agustsson & Brainerd (2010) found an excess of satellites along the major axis of their centrals only in red-colored hosts, while satellite distributions are consistent with isotropic around blue hosts. Based on group catalogs spanning from isolated host to cluster scale halos, Yang et al. (2006), Wang et al. (2008), and Siverd et al. (2009) all found that the alignment signal is only detected in groups with red centrals, and is strongest when considering red centrals and red satellites.

Unlike those previous works, our sample is selected based on the red-sequence method, so the centrals all belong to the red galaxy population. Within the red population, we nonetheless found that the central galaxy alignment depends on the $^{0.1}Mg\ -^{0.1}\ Mr$ color of central galaxy in cluster scale. Galaxy color indicates the age of the stellar populations. Recent star formation activities induced by the supply of gas from surrounding materials or merger events would cause the central galaxy color to become less red. Our result thus suggests that central galaxy alignment signal preferentially exists in centrals with relatively old stellar population. For clusters with bluer central galaxies, the alignment of centrals may be disturbed by the recent merger events that also triggered star formation and contributed to the bluer color.

2.6.5 Dependence on central galaxy ellipticity

Our linear regression shows that central galaxy ellipticity (as defined in Eq. 2.2) is negatively correlated with $\Delta\eta$, which means that centrals with larger ellipticity exhibit stronger central galaxy alignment. However, the complication in detecting this trend is that it is more difficult to accurately determine the position angles for round centrals. Statistical scatter in measuring the position angles of more round centrals could in principle drive the effect we have observed, rather than it being a true physical effect. Many studies have required the central galaxy ellipticity to exceed some value in order to avoid this effect, at the expense of introducing some systematic selection effect.

To address this issue, in Fig. 2.13 we show what happens to the correlation between central galaxy ellipticity and central galaxy alignment angle when we divide the original full sample (left panel) into two ellipticity bins at a value of 0.2, with 3554 centrals in the < 0.2 bin, and 4679 centrals in the other. This division reveals that the detected negative correlation of -0.047 in the full cluster sample is dominated by centrals with ellipticity below 0.2 (middle panel), in which a correlation coefficient of -0.12 is measured. These centrals are particularly sensitive to measurement error in the position angle, so the observed negative correlation may arise at least in part from measurement error. It may be also possible that this negative correlation originates from real physical mechanisms. The morphology of centrals reflect their formation history. More elliptical centrals may have experienced more anisotropic accretion that contributes to a stronger alignment effect. Distinguishing between measurement error and this real physical effect is difficult.

If focusing on systems with ellipticities above 0.2 (right panel), the central galaxy alignment angle becomes positively correlated at 0.044 ± 0.015, meaning that more elongated centrals have smaller

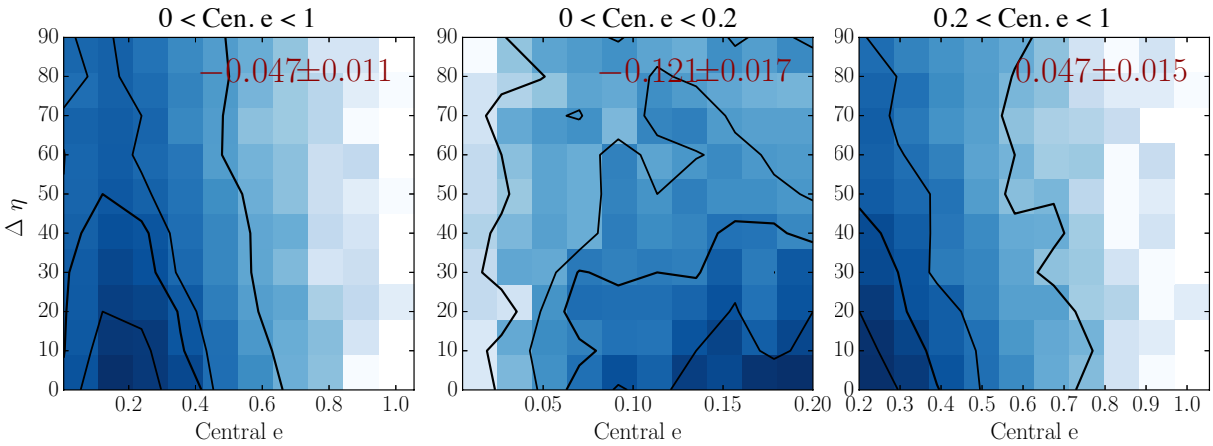

Figure 2.13: Contours of scatterplots of central galaxy ellipticity v.s. the position angle difference between central galaxy and cluster ($\Delta\eta$) in different central galaxy ellipticity bins. The left panel shows all of our cluster sample, the middle panel shows only clusters with central galaxy ellipticity below 0.2, while the right panel plots clusters with their central galaxy ellipticity above 0.2. The correlation coefficient between $\Delta\eta$ and central galaxy ellipticity is shown at the upper right corner in each panel.

alignment signals. We also find that the observed positive correlation is largely driven by the 8% highest ellipticity centrals, with ellipticity ≥ 0.5. Our result agrees with that of Yang et al. (2006) (see their Fig. 2), who found the same tendency using groups with central galaxy ellipticity[3] ≥ 0.2.

What causes high-ellipticity centrals to be less aligned? To partially address this question, we visually inspected the images of centrals with very high ellipticities (≥ 0.6) and presented some examples in Fig. 2.14. Surprisingly, besides the expected cases of high-ellipticity centrals that are more blue and exhibit disky structures (Fig. 2.14a) or those with anisotropic ICL (Fig. 2.14b), we found that in many instances, high-ellipticity centrals are systems with ≥ 2 bright cores in a single extended envelope (Fig. 2.14c, 2.14d). These multiple-core centrals are currently undergoing mergers. During the violent coalescence processes, the position angles of centrals change rapidly and no longer reflect the large-scale matter distribution, resulting in a wide spread in $\Delta\eta$.

We conclude that we should ignore central galaxy ellipticity as an predictor, although it is significantly identified through our variable selection process. The observed negative correlation is mostly driven by rounder centrals whose P.A. determination is more likely affected by systematics. For more elongated centrals, positive correlation with $\Delta\eta$ is found, and this correlation is possibly driven by centrals at higher ellipticity end. So far we cannot draw a clear conclusion about the impact of central ellipticity on central galaxy alignments. Larger sample size and improved shape measurement method in the future would help us to analyze the non-linear relation between $\Delta\eta$ and central galaxy ellipticity.

[3]The definition of galaxy ellipticity adopted in Yang et al. (2006) is 1-b/a, based on SDSS isophotal measurement.

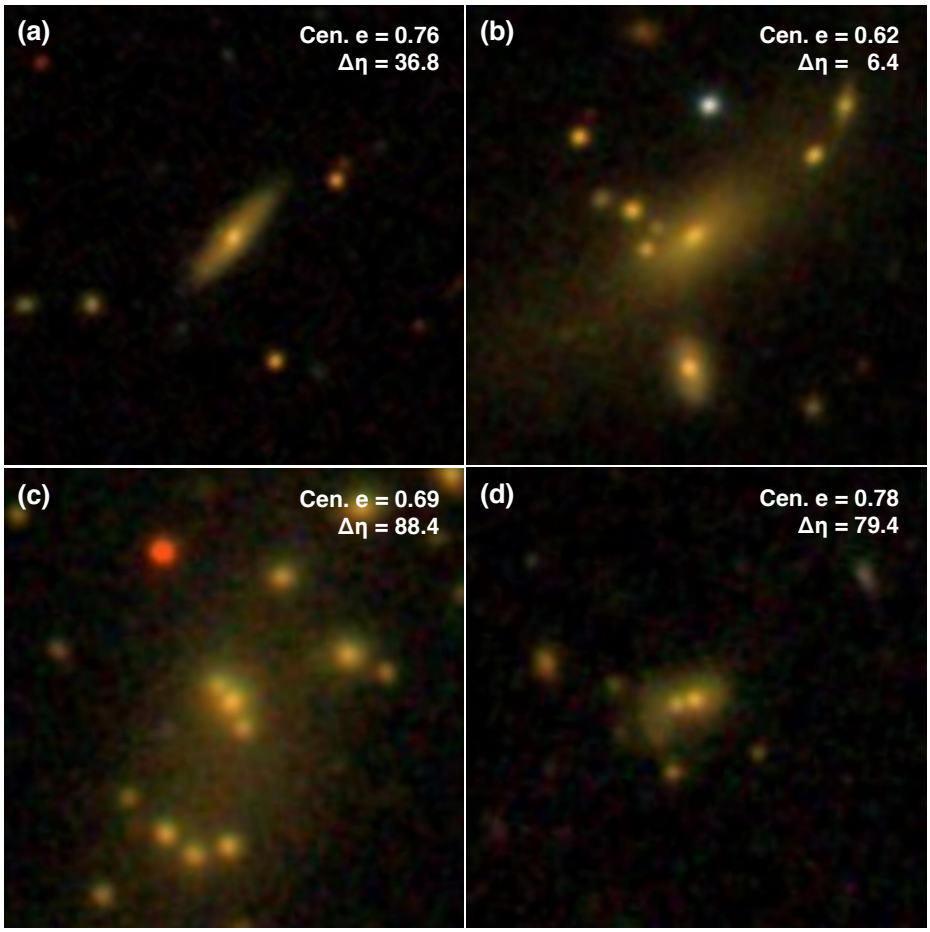

Figure 2.14: Examples of centrals with measured ellipticity ≥ 0.5. The central galaxy ellipticity and position angle difference between the central galaxy and cluster member galaxy distribution ($\Delta\eta$) is shown in the upper right corner of each panel. All panels are 150 kpc on each side. (a) Disky structure central with blueish color. (b) Central galaxy with elongated ICL. (c)&(d) Centrals with double or more bright cores within common extended envelopes.

2.6.6 Dependence on richness

Richness was selected as a statistically significant predictor when using $\Delta\eta$ as the response variable, but not for the response variable $\theta_{\rm cen}$. This result suggests that the impact of richness on the central galaxy alignment signal is marginal. We refer the reader back to the ending of Sec. 2.4.3 for related discussion. At similar cluster mass scales, Niederste-Ostholt et al. (2010) also found a slight indication that richer clusters show stronger alignment signals, at 2.3σ significance, while Hao et al. (2011) detected no dependence of BCG alignment on richness.

Observationally, richness is a good estimator for the underlying cluster dark matter halo mass (Rykoff et al., 2012). The weak dependence on richness may be due to the limited range of halo masses covered by the redMaPPer cluster sample. In what follows, we compare papers in which the mean central galaxy alignment angles, $\langle\theta_{\rm cen}\rangle$, are provided, and summarize the comparison results in Table 2.5. Since almost all of the previous works used the isophotal shape measurements, we also turn to our isophotal measurements to fairly compare the $\langle\theta_{\rm cen}\rangle$ values. At the mass scale corresponding to galaxy groups, many studies have observed that there is a stronger alignment tendency in richer groups (Yang et al., 2006; Wang et al., 2008; Siverd et al., 2009). As shown in Table 2.5, the $\langle\theta_{\rm cen}\rangle$ value in the highest mass bin of Yang et al. (2006) is consistent with our isophotal $\langle\theta_{\rm cen}\rangle$. Going down to even smaller systems, Brainerd (2005) and Agustsson & Brainerd (2010) have measured the $\langle\theta_{\rm cen}\rangle$ using a sample of isolated host centrals. The values of $\langle\theta_{\rm cen}\rangle$ are generally larger than that measured in cluster scales. Therefore, we suggest that there truly is some effect of host halo mass on alignments, despite our marginal findings using richness as a mass tracer on cluster mass scales.

Another possible reason that richness may be a less significant predictor is due to the cluster assembly process. Perhaps originally more massive and richer clusters had a stronger primordial alignment with the tidal field, but the subsequent mergers and other major events washed them out, making central galaxy alignments depend only weakly on richness.

Table 2.5: Summary of central galaxy alignment measurements. Here we provide a detailed comparison of the observed average central galaxy alignment angle, $\langle\theta_{\rm cen}\rangle$, from previous work using a variety of datasets in order to test for the potential evolution of $\langle\theta_{\rm cen}\rangle$ with halo mass. Relevant properties of the sample used in these studies are also listed.

paper	$\langle\theta_{\rm cen}\rangle$	redshift	shape measurement method	SDSS pipeline	Npair	cluster catalog properties
This work DR8 re-Gaussianization	41.4±0.1		re-Gaussianization	DR8	94817	• redMaPPer
DR7 de Vaucouleurs	40.7±0.1	0.1-0.35	de Vaucouleurs	DR7	86350	• halo mass $\gtrsim 10^{14}\ h^{-1}{\rm M}_\odot$
DR7 isophotal	40.6±0.1		isophotal	DR7	86350	• richness $\gtrsim 20$
Yang et al. (2006)						• Weinmann et al. (2006) group catalog, based on the group finder of Yang et al. (2005)
$\log[M_{\rm halo}/(h^{-1}{\rm M}_\odot)]$:12-13	43.1±0.4					
$\log[M_{\rm halo}/(h^{-1}{\rm M}_\odot)]$:13-14	42.6±0.3	0.01-0.2	isophotal	DR2	24728	• 9220 binary, 3073 triplet, 3270 member > 3 groups
$\log[M_{\rm halo}/(h^{-1}{\rm M}_\odot)]$:14-15	40.7±0.5					• restricted to groups with BCG ellipticity > 0.2
Wang et al. (2008)						
$\log[M_{\rm halo}/(h^{-1}{\rm M}_\odot)]$:12-13	43.4±0.1					• Yang et al. (2007) group catalog
$\log[M_{\rm halo}/(h^{-1}{\rm M}_\odot)]$:13-14	42.4±0.1	0.01-0.2	isophotal	DR4	62212	
$\log[M_{\rm halo}/(h^{-1}{\rm M}_\odot)]$:14-15	41.3±0.4					
Brainerd (2005) Sample1	42.1±0.5	$z_{\rm median}$: 0.05	isophotal	DR3	3292	• isolated host galaxy • dominated by systems containing 1~2 satellites
Agustsson & Brainerd (2010)	42.9±0.5	0.01-0.15	isophotal	DR7	7399	• isolated host galaxy • same selection criteria as Brainerd (2005) Sample1

2.6.7 Dependence on redshift

We did not find any significant redshift dependence of central galaxy alignment within the limited redshift range of 0.1–0.35. In agreement with our observation, Kang et al. (2007) studied the alignment strength from redshift 2 to 0 and found no redshift evolution based on N-body simulations with a semi-analytical model for galaxy formation. Based on hydrodynamic simulations, Tenneti et al. (2015a) showed a weak redshift dependence on the intrinsic alignment amplitude at galaxy mass scales, with the alignment signal decreasing at lower redshift. However, based on samples at cluster scale, both Niederste-Ostholt et al. (2010) and Hao et al. (2011) have found that the BCG alignment signal is stronger as redshift decreases within the redshift ranges of $0.08 < z < 0.44$ and $z < 0.4$, respectively. The discrepancies between their results and ours may arise from the following: 1) The two previous studies have considered slightly wider redshift ranges than us such that the redshift-dependent trends become detectable. 2) The observed redshift evolution may be just a reflection of possible combined evolutions with other physical predictors, since those two studies did not consider as many parameters as we do. 3) For studies that based on isophotal shape, there may be more contamination from systematic errors at lower redshift, since for an apparently brighter BCG (at fixed luminosity), its 25 mag/arcsec^2 isophote traces a larger radius where the light of BCG is more easily confused with that from other neighboring satellites. For our redMaPPer sample, when using isophotal shape measurements, we find that the correlation coefficient between $\Delta\eta$ and z is $\sim$1.5 times higher than that based on re-Gaussianization shape. As discussed in Sec. 2.5, this could be partly due to a systematic and partly driven by a real physical effect.

Studying the redshift evolution of the overall central galaxy alignment signal is important for understanding the physical mechanism that is responsible for it. If the central galaxy alignment largely stems from the primordial tidal field at the time of cluster formation (Catelan et al., 2001; Hirata & Seljak, 2004b), later merging or virialization processes may weaken the primordial signal (Hopkins et al., 2005). However, if the central galaxy alignment is dominated by signals established from underlying tidal fields acting during the entire lifetime of clusters, or as suggested by Niederste-Ostholt et al. (2010), the primordial alignment signals could be enhanced by the secondary infall episodes, we may expect stronger alignment toward lower redshifts. Currently we lack data to make a convincing conclusion about redshift evolution of central galaxy alignment; further simulations or deeper observational data pushing to higher redshift are needed to further investigate this problem.

2.6.8 Dependence on cluster concentration Δ_R

Miyatake et al. (2016) observed that separating redMaPPer clusters with similar richness and redshift distributions into large-$\overline{R}_{\rm mem}$ and small-$\overline{R}_{\rm mem}$ populations (see Eq. 2.9 for definition of $\overline{R}_{\rm mem}$) yields two cluster subsamples with similar halo masses, but different large-scale biases. Based on the N-body simulation in the work of More et al. (2016), $\overline{R}_{\rm mem}$ is found to be a good indicator for cluster mass accretion rate. Miyatake et al. (2016) thus interpreted the detected difference in large-scale bias as evidence for halo assembly bias, wherein the clustering of halos depends not only on their mass, but also on other properties related to their assembly histories, such as halo formation time, mass accretion rate, concentration, and spin (see, e.g., Gao et al. 2005; Wechsler et al. 2006; Gao & White 2007; Dalal et al. 2008; Lin et al. 2016). Regardless of whether this result indicates assembly bias

or some other physical effect can explain the differences in large-scale bias, $\overline{R}_{\rm mem}$ does correlate with the concentration of the cluster member galaxy distribution, and it is nonetheless interesting to test whether $\overline{R}_{\rm mem}$ influences central galaxy alignments. Here we use the parameter $\Delta_{\rm R}$, which removes the richness and redshift dependence of the observed concentration of the member galaxy distribution (Eq. (2.10)).

We found that $\Delta_{\rm R}$ has no effect on the central galaxy alignment. In fact, the correlation coefficient between $\Delta\eta$ and $\Delta_{\rm R}$ is the smallest (0.016) among our predictors, as shown in the upper right corner of Fig. 2.9. Moreover, the last row of Fig. 2.9 shows that $\Delta_{\rm R}$ does not have any $> 10\sigma$ correlations with other parameters, and is therefore relatively independent from the rest of the parameter space considered in this work.

2.7 The origin of angular segregation of satellites

We find that the angular segregation of satellites with respect to their central galaxy major axis direction depends strongly on satellite color and ${}^{0.1}M_r$, and weakly but still significantly on $\log(r/R_{\rm 200m})$ and satellite ellipticity, as shown in Table 2.4 in Sec. 2.4.3. In the following we discuss the possible origins of these dependencies, and compare our results with previous work. We remind the reader that instead of considering all satellite galaxies, our analysis is only based on red-sequence satellites with membership probability above 0.8 according to the redMaPPer algorithm.

2.7.1 Dependence on satellite color

The color of the red-sequence satellites is the strongest predictor of their angular segregation, with redder satellites tending to preferentially lie along the major axis direction of centrals. This result agrees with previous work that considered satellites in a wider color range and revealed that the distribution of redder satellites shows more anisotropy than that of bluer ones (Yang et al., 2006; Azzaro et al., 2007; Faltenbacher et al., 2007; Wang et al., 2008; Agustsson & Brainerd, 2010).

Part of the dependence on satellite color may originate from galaxy properties in filaments connected to clusters. Clusters assembled mainly by accreting satellites from surrounding filaments (e.g., Onuora & Thomas, 2000; Lee & Evrard, 2007). As a result, galaxy properties in filaments may leave some imprint on substructures within clusters. Using a filament catalog (Chen et al., 2016) constructed from SDSS, Chen et al. (2017) found that red galaxies are on average closer to filaments than blue galaxies. Hence, the observed angular segregation of redder satellites may be due to their being preferentially accreted along filaments, which likely have more tendency to align with the major axes of centrals (see also Kang et al. 2007).

Another possible explanation for the angular segregation by color is related to environmental quenching. Galaxies in denser environments are redder than galaxies of similar mass in less dense environments (Peng et al., 2010, 2012). Thus, satellites falling along denser filamentary channels would tend to be redder than those falling into the cluster from the field (Martínez et al., 2016). Those falling into the cluster along filaments already pre-quenched. Also, satellites orbiting closer to the major axis direction of centrals should experience higher environmental quenching efficiency due to the higher matter density there.

2.7.2 Dependence on satellite luminosity

More luminous satellites are more likely to lie along the major axis directions of centrals. For isolated host-satellite systems, Agustsson & Brainerd (2010) have also found a consistent trend.

The satellite luminosity dependence may also have its origin from galaxy properties in filaments. By analyzing galaxies in filaments, Chen et al. (2017) found that more massive galaxies tend to be closer to filaments than lower mass galaxies. Li et al. (2013) observed that there is a significant alignment between the orientations of brightest satellite galaxies with the major axes of their groups, suggesting that brightest satellite galaxies entered their host groups more recently than other satellites. Using N-body simulations, van den Bosch et al. (2016) have also shown that subhalos with a larger mass at the time of accretion (a quantity used to link with galaxy stellar mass through abundance matching) tend to be accreted at a later time (see their Fig. 5) with smaller orbital energy (i.e., on more bound orbits, see their Fig. 9). Combining these previous findings, the physical picture is that more luminous satellites are more likely in-falling from filaments connected to clusters. Since they are accreted by the cluster at a later time, they have not yet orbited enough to lose the imprint of their original large-scale structure. Furthermore, with smaller orbital energy at infall, their dynamics would be more easily influenced by the overall mass distribution in the cluster, and thus as they settle into orbit in the cluster potential well they are more likely to remain along the major axis direction of the central galaxy.

2.7.3 Dependence on satellite-central distance

We found that the satellite-central distance is a statistically significant predictor of the angular segregation of satellites, with those closer to centrals being more likely to be located along the major axis directions of central galaxies. This may seem puzzling given that the second panel in the first row of Fig. 2.10 shows that the correlation coefficient between $\log(r/\mathrm{R_{200m}})$ and $\theta_{\rm cen}$ is consistent with zero within the error bar. Apparently, $\log(r/\mathrm{R_{200m}})$ is selected as a feature predictor due to some interplay with another predictor. To identify which other predictor is responsible, we removed one predictor at a time in Eq. (2.15) to find which one, when removed, caused $\log(r/\mathrm{R_{200m}})$ to no longer be selected as a feature predictor.

The result of this process was that satellite-central distance was selected due to the presence of cluster ellipticity in the model. The reason why adding cluster ellipticity results in the selection of $\log(r/\mathrm{R_{200m}})$ is illustrated in Fig. 2.15. For satellites with projected distances $r < b$ (the semi-minor axis of the cluster), the possible values of $\theta_{\rm cen}$ can vary between 0° and 90°, while for those with $r > b$, their $\theta_{\rm cen}$ values are confined within 0° and $\theta_{\rm r}{}^\circ < 90^\circ$ due to the boundary of the region contained by the circularized halo radius. Thus, if satellites were randomly distributed within the elliptical footprint of a cluster, we would expect that more elliptical clusters exhibit a stronger anti-correlation between $\log(r/\mathrm{R_{200m}})$ and $\theta_{\rm cen}$, with larger $\log(r/\mathrm{R_{200m}})$ showing smaller $\theta_{\rm cen}$. The fact that that anti-correlation is not observed suggests that galaxies are not randomly distributed within the elliptical footprint of a cluster, but rather are preferentially located on the major axis to a degree that is more significant at smaller values of $\log(r/\mathrm{R_{200m}})$. Or viewing in the other way, central galaxies tend to point toward nearby satellites, whose distribution reflects local, smaller-scale tidal field.

Several previous studies have also investigated the dependence of projected distance on $\theta_{\rm cen}$.

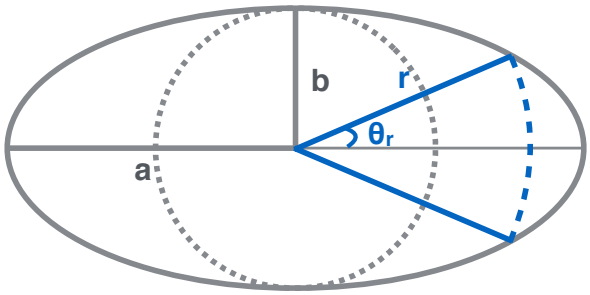

Figure 2.15: Illustration of how cluster ellipticity can lead to a false detection of dependence of $\theta_{\rm cen}$ on $\log(r/{\rm R}_{\rm 200m})$.

For isolated host scale, Brainerd (2005) found that strength of anisotropy increases with decreasing projected distance, while Azzaro et al. (2007) claimed that the degree of anisotropy is independent of the projected distance and Agustsson & Brainerd (2010) also reported no distance dependence for red host galaxies. For galaxy group scale, both Yang et al. (2006) and Siverd et al. (2009) detected stronger central galaxy alignment effects at smaller projected distance. Also, in Fig. 2 of Faltenbacher et al. (2007), $\theta_{\rm cen}$ is smaller in the inner part of halos than in the outer part for red satellites.

The general physical picture regarding angular segregation of satellites is that it is due to large-scale tidal fields, which leads to preferential infall of satellites along the connected filaments. This picture is also reflected in the identification of cluster ellipticity as an predictor described in Sec. 2.6.1. If a cluster's small-scale tidal field always followed it's large-scale tidal field, then with the presence of predictor cluster ellipticity (reflecting the direction large-scale tidal field), $\log(r/{\rm R}_{\rm 200m})$ (reflecting small-scale tidal field) would not be selected out, as all of its effect would be absorbed in cluster ellipticity. During the chaotic assembly process, a cluster's inner tidal field may differ from it's large-scale tidal field. The positive correlation between $\theta_{\rm cen}$ and $\log(r/{\rm R}_{\rm 200m})$ found here implies that smaller-scale local tidal field, either newly established or following along the large-scale tidal field, does play some role in torquing the central galaxies to align with satellites located relatively nearby as well.

2.7.4 Dependence on satellite ellipticity

We observed a (marginally) statistically significant dependence of the angular segregation of satellites along the central galaxy major axis on satellite ellipticity, with rounder satellites exhibiting a stronger tendency to lie along the central galaxy major axis direction.

An intuitive way of interpreting the effect of satellite ellipticity is to link it with related galaxy properties. Rounder galaxies have less disk component and an older stellar population, and thus look redder in color. Also, luminous galaxies tend to be rounder in morphology. Given the relation between satellite ellipticity, color, and luminosity, they may share similar origins, as we have discussed in Secs. 2.7.1 and 2.7.2. However, notice in Fig. 2.10 that the correlation coefficients for satellite ellipticity with ${}^{0.1}M_r$ and color are ~ 0.2 and -0.1 respectively, meaning that there exists other physical origins different from the effects of ${}^{0.1}M_r$ or color. We must seek other physical mechanisms that are more tightly linked to the satellite ellipticity itself.

One possible mechanism for the preference of rounder satellites to lie along the major axis directions of centrals may be their frequent interaction with nearby galaxies. According to Kuehn & Ryden (2005), harassment processes due to close encounters with neighboring galaxies make galaxies rounder. Also, Rodríguez et al. (2016) found that elliptical galaxies in groups, where more disturbing events are likely to happen, are more spherical than field elliptical galaxies with similar intrinsic properties. Therefore, satellites residing near the major axis directions of centrals are more likely to be harassed due to the higher number density there. Besides the effect of shaping galaxies, higher frequency interactions with other members let satellites experience through more phase mixing and relation processes, thus speeding up their sinking onto the plane of central galaxy, as the gravitational potential is deeper there.

2.8 Summary and conclusion

In this work, we investigate the central galaxy alignment effect using the redMaPPer cluster catalog. We use three kinds of measurements of the central galaxy position angle from the SDSS derived from previous work: re-Gaussianization, de Vaucouleurs, and isophotal shapes, compare the derived central galaxy alignment strength among them, and discuss possible systematic effects. To identify the dominant predictors of the central galaxy alignment signal, we include as many potential physical parameters as possible, and apply forward-stepwise linear regression to quantify the statistical significance of these parameters as predictors, as well as to properly account for correlations between them.

Our analysis has two steps. In step one, we regress the position angle difference between the central galaxy and cluster shape (as traced by the member galaxy distribution, a proxy for the dark matter halo shape), $\Delta\eta$, against central galaxy and cluster related quantities. The goal of this step is to identify the central galaxy and cluster properties that most significantly affect their alignment. In step two, we regress the angular location $\theta_{\rm cen}$ of each member galaxy with reference to its central galaxy major axis direction against several satellite-related quantities, in order to identify important predictors for the angular location of the satellite with respect to the central galaxy major axis. Our key results are as follows.

1. The detected central galaxy alignment signal is strongest based on isophotal shape, followed by de Vaucouleurs and re-Gaussianization shape (see the right panels in Figs. 2.6 and 2.8). This may be caused by the fact that the isophotal shape traces a galaxy's outermost regions, which are more susceptible to the external tidal fields.
2. The central galaxy-cluster alignment is strongest for clusters that are more elongated and higher richness, or that have centrals with larger physical size, higher luminosity, redder color, and higher centering probability[4].
3. The tendency of satellites to reside along the central galaxy major axis direction is strongest for satellites with redder color, higher luminosity, located closer to its central galaxy and with

[4]Although central galaxy ellipticity is found to be a significant predictor as listed in Table 2.3, we discussed in Sec. 2.6.5 that the correlation between central galaxy ellipticity and $\Delta\eta$ is more complicated than a simple linear relation, which requires further investigation in future work.

smaller ellipticity.

As shown, we have selected many predictors that have a statistically significant influence on the central galaxy alignment effect. This implies that central galaxy alignment is a complicated phenomenon potentially involved multiple relevant physical processes during galaxy and cluster formation and evolution, such that it cannot be straightforwardly explained by just few dominant factors. We have discussed in great detail the potential physical origins of these selected predictors in Secs. 2.6 and 2.7. The most relevant factors seem to be that central galaxy alignment may originate from the filamentary accretion processes, but also possibly affected by the tidal field (either the large-scale primordial tidal field, or the newly-established small-scale tidal field after the redistribution of satellites). Also, merger events tend to destroy alignment. From this work, we cannot fully disentangle the relative contributions from the above three effects, or rule out contributions from other possible mechanisms that can increase or reduce central galaxy alignment. We expect future investigations either based on observations or simulations to put tighter constraints on possible central galaxy alignment scenarios.

Acknowledgements

We thank Shadab Alam, Tereasa Brainerd, Yun-Hsin Huang, Wentao Luo, Melanie Simet, Sukhdeep Singh, and Ying Zu for useful comments and discussions. This work was supported by the National Science Foundation under Grant No. AST-1313169. YC is supported by William S. Dietrich II Presidential Ph.D. Fellowship Award. EB is partially supported by the US Department of Energy Grant No. DE-SC0007901.

3 Intrinsic Alignment in redMaPPer clusters – II. Radial alignment of satellites toward cluster centers

Hung-Jin Huang[1], Rachel Mandelbaum[1], Peter E. Freeman[1,2], Yen-Chi Chen[1,2,3], Eduardo Rozo[4], Eli Rykoff[5]

[1]McWilliams Center for Cosmology, Department of Physics, Carnegie Mellon University, Pittsburgh, PA 15213, USA
[2]Department of Statistics, Carnegie Mellon University, Pittsburgh, PA 15213, USA
[3]Department of Statistics, University of Washington, Seattle, WA 98195, USA
[4]Department of Physics, University of Arizona, 1118 E. Fourth St., Tucson, AZ 85721, USA
[5]SLAC National Accelerator Laboratory, Menlo Park, CA 94025, USA

Abstract

We study the orientations of satellite galaxies in redMaPPer clusters constructed from the Sloan Digital Sky Survey at $0.1 < z < 0.35$ to determine whether there is any preferential tendency for satellites to point radially toward cluster centers. We analyze the satellite alignment (SA) signal based on three shape measurement methods (re-Gaussianization, de Vaucouleurs, and isophotal shapes), which trace galaxy light profiles at different radii. The measured SA signal depends on these shape measurement methods. We detect the strongest SA signal in isophotal shapes, followed by de Vaucouleurs shapes. While no net SA signal is detected using re-Gaussianization shapes across the entire sample, the observed SA signal reaches a statistically significant level when limiting to a subsample of higher luminosity satellites. We further investigate the impact of noise, systematics, and real physical isophotal twisting effects in the comparison between the SA signal detected via different shape measurement methods. Unlike previous studies, which only consider the dependence of SA on a few parameters, here we explore a total of 17 galaxy and cluster properties, using a statistical model averaging technique to naturally account for parameter correlations and identify significant SA predictors. We find that the measured SA signal is strongest for satellites with the following characteristics: higher luminosity, smaller distance to the cluster center, rounder in shape, higher bulge fraction, and distributed preferentially along the major axis directions of their centrals. Finally, we provide physical explanations for the identified dependences, and discuss the connection to theories of SA.

3.1 Introduction

The projected orientations of galaxies observed on sky are not random, but rather exhibit some coherent patterns related to the matter distribution in the Universe. Galaxy shapes tend to point

towards overdense regions, leaving a net preference of correlated orientations. This phenomenon, known as "intrinsic" alignments (IA), contains important information about structure formation and galaxy evolution (for recent reviews, see Joachimi et al. 2015; Kirk et al. 2015; Kiessling et al. 2015). Besides the physically-induced alignment signal, the images of galaxies located behind overdense structures tend to be distorted tangentially with respect to those structures, producing the apparent tangential alignment signal that is the key characteristic of gravitational lensing. This lensing effect is used as a tool to map the distribution of dark matter in the Universe, to study the growth of structure, and to constrain cosmological parameters (see e.g. Massey et al. 2010; Weinberg et al. 2013; Mandelbaum et al. 2013). The presence of IA challenges the process of interpreting the observed shape correlations (intrinsic+apparent) in terms of the basic physics that generates lensing signals. Ongoing surveys such as the Dark Energy Survey (DES, Dark Energy Survey Collaboration et al. 2016), the Kilo-Degree Survey (KiDS, de Jong et al. 2015), Hyper Suprime-Cam Survey (HSC, Miyazaki et al. 2012), and future surveys like the Large Synoptic Survey Telescope (LSST, LSST Science Collaboration et al. 2009), Euclid (Laureijs et al., 2011), and the Wide Field Infrared Survey Telescope (WFIRST, Spergel et al. 2015) aim to constrain the cosmological constants to sub-percent precision, which requires precise removal of all possible systematics including intrinsic alignments (e.g., Blazek et al., 2012; Krause et al., 2016). Quantifying the strength of IA signal and developing models that will enable its removal thus becomes one of the key steps to reach this goal.

IA have been detected over a wide range of scales. On scales above several Mpcs, red dispersion-dominated galaxies preferentially point towards overdense regions (see e.g., Mandelbaum et al. 2006; Hirata et al. 2007; Okumura et al. 2009; Joachimi et al. 2011; Singh et al. 2015 from the observational side, and Tenneti et al. 2015a; Chisari et al. 2015 from numerical simulation). Part of this observed correlation originates from the tendency of galaxies to align towards overdensities and with filamentary structures (see e.g., observation: Zhang et al. 2013; Tempel et al. 2015, and simulation: Chen et al. 2015). For red galaxies located in sheets, Zhang et al. (2013) observed that they tend to have their major axes aligned parallel to the plane of the sheets. For blue angular momentum-dominated galaxies, there is no significant detection of alignment so far (Mandelbaum et al., 2011). Besides the alignment of galaxies, people also found alignment between the shape of clusters with respect to the underlying density field (observation: Smargon et al. 2012; van Uitert & Joachimi 2017; simulation: Hopkins et al. 2005).

The other alignment at intra-halo scale is satellite alignment, i.e. the preference of satellites to align radially toward the cluster center. The SA signal is relatively subtle compared with the strength of central galaxy alignment; along with the difficulty of achieving accurate shape measurements on faint satellites whose light profiles are more subject to contamination from neighboring galaxies, many conflicting observational results have been published. Earlier works based on SDSS isophotal shape measurement, which trace the very outer part of the galaxy light profiles, have reported detections of SA signal (Pereira & Kuhn, 2005; Agustsson & Brainerd, 2006; Faltenbacher et al., 2007). However, later studies claimed that when using de Vaucouleurs shape, which puts relatively more weight on the galaxy inner light profiles, satellite orientations are consistent with random (Siverd et al., 2009; Hao et al., 2010). Studies that used shape measurements that are optimized for lensing, which requires corrections for many observational systematics, reported non-detection of satellite alignments (Schneider et al., 2013; Sifón et al., 2015). There is therefore some tension between past

measurements, and reconciliation of that tension may require investigation into the different galaxy populations used for these measurements and/or false SA signals generated by systematics in isophotal shape measurements (e.g., Hao et al., 2010).

Our current theoretical understanding of IA for red dispersion-dominated galaxies is that their orientations are affected by the tidal field of the surrounding environment. On large scales, the linear alignment model (Catelan et al., 2001; Hirata & Seljak, 2004b) suggests that the shapes of proto-galaxies are largely set by the primordial tidal field at their formation time, so that their shape correlation with the matter field is frozen in since then and simply grows with the matter power spectrum. The primordial tidal field also leaves its imprint on the assembly history of clusters by channeling the majority of satellites into clusters through accretion along filamentary structures, which results in the observed cluster alignment phenomenon (Hopkins et al., 2005). At small scales, the orientation of cluster central galaxies would also be generated by the same primordial tidal field, leaving the observed central galaxy alignment (see discussions in Paper I). While later non-linear evolutionary processes such as mergers or baryonic feedback from galaxies may erase the alignment signals set by primordial tidal fields (Tenneti et al., 2017), the late-time re-arranged structures can set up new tidal environments that gradually torque galaxies to align (Ciotti & Dutta, 1994; Kuhlen et al., 2007; Pereira et al., 2008; Faltenbacher et al., 2008). The timescales for tidal locking of satellites under the cluster potential depend on the eccentricity of infalling orbits as well as properties of satellites (e.g. angular momentum, morphology). As shown in the simulations of Pereira & Bryan (2010), within the time of one orbital period (~ 5 Gyr), a triaxial DM subhalo orbiting in circular orbit around a cluster potential becomes tidally locked, and it takes a lag of $\lesssim$2 Gyr, depending on the initial conditions, for the stellar components to respond.

In this work, we carry out SA measurements using re-Gaussianization, de Vaucouleurs and isophotal shapes that differ in sensitivity to the outskirt of a galaxy's light profile. The size of the redMaPPer cluster catalogue provides the necessary statistical power to contrain SA signals at halo masses $\gtrsim 10^{14} M_\odot\,\mathrm{h}^{-1}$. The two main questions we aim to address in this paper are 1) What causes the detected discrepancies in SA signals using different shape measurement methods? 2) Which satellite properties associated with which central galaxy and cluster properties are correlated with stronger SA signals? We estimate the level of possible noises and systematics that could cause the inconsistent galaxy position angle (PA) measurements. As in paper I, we explore a large parameter pool which contains characteristic satellite, central galaxy, and cluster properties to identify important predictors of SA effect using linear regression analysis.

The paper is organized as follows. In Sec. 3.2, we describe our data and definitions of the physical parameters involved in the analysis. Sec. 3.3 presents the overall signal of SA alignment measured in redMaPPer clusters. Details of the linear regression and variable selection results are described in Sec. 3.4. Sec. 3.5 explores possible factors that cause the discrepancy in the measured SA angle using three different shape measurement methods, and provides estimates of the degree of contribution from each factor. The physical origins of our identified featured predictors on the SA effect are discussed in Sec. 3.6. We conclude and summarize our key findings in Sec. 3.7.

Throughout this paper, we adopt the standard flat ΛCDM cosmology with $\Omega_m = 0.3$ and $\Omega_\Lambda = 0.7$. All length and magnitude units use $H_0 = 100\,\mathrm{km\,s^{-1}\,Mpc^{-1}}$. We use log as shorthand for the 10-based logarithm.

3.2 Data and Measurements

All data used in this paper come from the SDSS (York et al., 2000) surveys. Here we describe the catalogs involved in our analysis, sample construction, and definitions of the cluster- and galaxy-related parameters. Most of the data and parameters remain the same as in Paper I, although some small differences exist, as we will highlight in the relevant subsections below. In order to properly interpret the measured satellite alignments, Paper II puts more focus on exploring systematics in the different shape measurement approaches. New samples for systematic tests are constructed and described below.

3.2.1 Galaxy cluster catalog

Our cluster member galaxy sample is taken from the SDSS DR8 (Aihara et al., 2011) redMaPPer v5.10 cluster catalog[1], constructed based on a red-sequence cluster finding approach. Details of the algorithm and the cluster properties can be found in Rykoff et al. (2014); Rozo & Rykoff (2014); Rozo et al. (2015a,b). Some features of the redMaPPer cluster catalog are briefly summarized here.

For each cluster, it identifies five most probable central galaxies, with their corresponding central probability, $P_{\rm cen}$. Each cluster member galaxy is assigned with a membership probability, $p_{\rm mem}$, according to its color, magnitude, and position information. The photometric redshift z for each cluster is estimated from high-probability members. The cluster sample is approximately volume-limited in the redshift range of $0.1 \leq z \leq 0.35$. The cluster richness, λ, is defined by summing the membership probabilities over all possible cluster members. Most of the clusters have $\lambda \gtrsim 20$, corresponding to an approximate halo mass threshold of $M_{\rm 200m} \gtrsim 10^{14}\ {\rm h^{-1}M_\odot}$ (Rykoff et al., 2012; Simet et al., 2017).

3.2.2 Galaxy shapes

Shape-related parameters

We adopt the following definition of ellipticity/distortion components in a global Cartesian frame to measure each galaxy's ellipticity:

$$(e_1,\ e_2) = \frac{1-(b/a)^2}{1+(b/a)^2}(\cos 2\alpha,\ \sin 2\alpha), \tag{3.1}$$

where b/a is the minor-to-major axis ratio and α the position angle (PA) of the major axis of the galaxy. Here e_1 measures the projected distortion in the RA/dec directions, and e_2 in diagonal directions. The total galaxy ellipticity e can then be calculated as

$$e = \sqrt{e_1^2 + e_2^2} = \frac{1-(b/a)^2}{1+(b/a)^2}. \tag{3.2}$$

Once the PA α of a galaxy is obtained by one of the methods described in Sec. 3.2.2, we can then derive its central galaxy alignment angle $\theta_{\rm cen}$ and satellite alignment angle $\phi_{\rm sat}$ as illustrated in Fig. 3.1.

[1]http://risa.stanford.edu/redmapper/

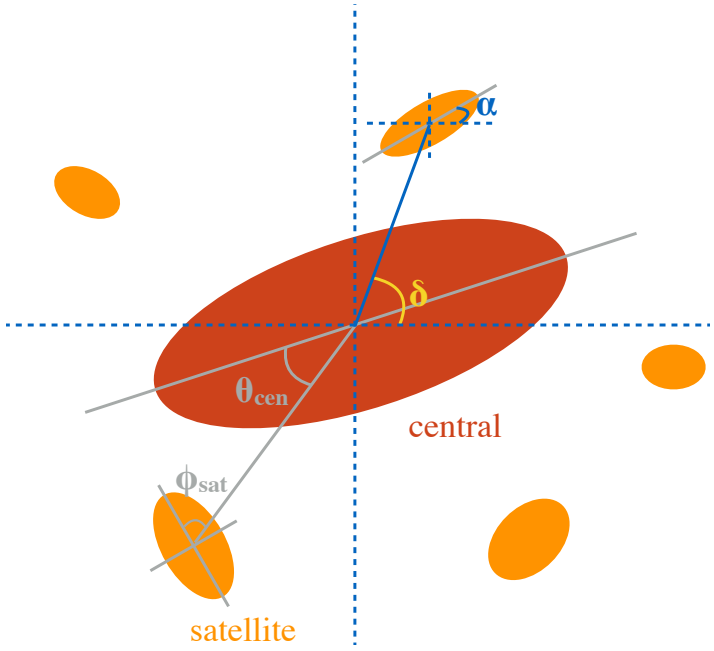

Figure 3.1: Illustration of the galaxy alignment angles. The satellite alignment angle, $\phi_{\rm sat}$, defined as the angle between a satellite's major axis and its orientation towards the central galaxy, is the main focus of this paper. The central galaxy alignment angle, $\theta_{\rm cen}$, defined as the angular location of a satellite relative to its central galaxy's major axis direction, is the area of focus in our previous Paper I.

The central galaxy alignment angle ($\theta_{\rm cen}$) is defined as the angle between the major axis of the central galaxy and the line connecting the central to the satellite galaxy. We only need a viable shape measurement for the central galaxy (but not the satellites) to derive $\theta_{\rm cen}$. The analysis of central galaxy alignments in redMaPPer clusters has already been reported in Paper I. The satellite alignment angle ($\phi_{\rm sat}$) is defined as the angle between the major axis of the satellite galaxy and the line connecting its center to the central galaxy. Deriving $\phi_{\rm sat}$ requires a shape measurement for the satellite galaxy. In this paper, we focus on the satellite alignments, and will use the central galaxy alignment angle $\theta_{\rm cen}$ as one of the candidate predictors in our parameter pool. We use the highest-probability centrals provided in redMaPPer for calculation of both $\theta_{\rm cen}$ and $\phi_{\rm sat}$.

We restrict both $\theta_{\rm cen}$ and $\phi_{\rm sat}$ to the range $[0°, 90°]$ due to symmetry. By definition, $\theta_{\rm cen} = 0°/90°$ indicates a satellite located along the major/minor axis of the central. A satellite is radially/tangentially aligned with the central if $\phi_{\rm sat} = 0°/90°$.

Besides using $\phi_{\rm sat}$ to quantify the degree of SA signal, another commonly-used parameter is e_+, the distortion in the radial-tangential direction in a new frame with the original axes rotated to the radial-tangential directions of each central-satellite pair. From simple algebra, we have:

$$(e_+,\ e_\times) = \frac{1-(b/a)^2}{1+(b/a)^2}(\cos 2(\delta-\alpha),\ \sin 2(\delta-\alpha)), \tag{3.3}$$

where α is the PA of the satellite, and δ the azimuthal angle of the satellite projected position with respect to the cluster central galaxy, as indicated in Fig. 3.1. A positive e_+ indicates a radial alignment of the satellite toward cluster center, while a negative e_+ indicates a tangential alignment. Therefore, if satellite galaxies do preferentially align in the radial direction, we expect $\langle e_+\rangle > 0$ when taking the average over all central-satellite pairs. The $e_\times$ component is the distortion at ±45° from the radial/tangential direction. It is is commonly used as an indicator for certain systematics. Due to symmetry, $\langle e_\times\rangle$ should be consistent with zero.

Shape data

We will measure satellite alignments using three shape measurement methods: re-Gaussianization, isophotal, and de Vaucouleurs shapes, to compare differences in the signals and investigate systemics. Details of these methods have been described in Paper I (Sec. 2.3), and we only briefly summarize here.

The re-Gaussianization shape measurement method (Hirata & Seljak, 2003) is specifically designed for weak lensing studies, which require great care in removing the point spread function (PSF) effect on the observed galaxy images. This method has a Gaussian weight function that emphasizes the inner, brighter regions of galaxy profiles in order to reach higher precision distortion measurement especially for faint galaxies. In this work, we take the distortion measurement (e_1 and e_2) from a re-Gaussianization shape catalog of Reyes et al. (2012) with shapes measured in the r and i bands based on the SDSS DR8 photometry.

Isophotal shape measurement does not include an explicit correction for the effect of the PSF. It determines a galaxy's shape by fitting the surface brightness at 25 mag/arcsec^2, which traces the outer part of a galaxy's profile. Since isophotal shapes were not released in DR8, we take the isophotal position angle in r band from DR7 to compute satellite alignment angles.

The de Vaucouleurs shape measurements were determined by fitting each galaxy's image with a de Vaucouleurs model (Stoughton et al., 2002), which is a good description for typical elliptical galaxies (which includes the majority of the galaxies in this work, since they were selected based on a red-sequence method). It partially corrects for the PSF effect using an approximate PSF model, and overall is sensitive to light profiles on scales between those measured by re-Gaussianization and isophotal methods. We use the de Vaucouleurs fit position angle in r band provided from the SDSS DR7 in this work [2].

3.2.3 The central-satellite pair sample

To fairly compare the measured alignment signal across redshift, we restrict our analysis to a volume-limited cluster sample within $0.1 \leq z \leq 0.35$ from the redMaPPer catalog. Besides this, an appropriate membership probability cut of $p_{\rm mem} \geq 0.55$ is applied on satellite galaxies, which results in a total of 305997 central-satellite pairs in 10749 distinct clusters (before requiring galaxies to have shape measurements). The choice of the $p_{\rm mem} = 0.55$ cut comes from optimizing the S/N for detection of SA signals, as explained in Appendix 3.A.

While applying a lower $p_{\rm mem}$ cut returns us more central-satellite pairs into analysis, the resulting satellite alignment signal will be diluted due to the inclusion of more pairs with "satellite" galaxies that are not actually in clusters. Throughout this work, we will reduce this contamination by applying $p_{\rm mem}$ as the weighting factor on each central-satellite pair.

We define two sets of central-satellite pair samples for analysis in this work.

1. **DR8 footprint sample**: The first set is within the SDSS DR8 footprint, constructed by acquiring that the 305997 $p_{\rm mem} \geq 0.55$ satellites have well-defined re-Gaussianization shape measurements. There are 174180 central-satellite pairs within 8121 distinct clusters in this data set. The effective total number of pairs in DR8 footprint sample after weighting by $p_{\rm mem}$ is $\sum_i p_{{\rm mem},i} \approx 132072$ pairs.
2. **DR7 footprint sample**: The second data set is constructed for comparing the level of satellite alignment signals via three different shape measurement methods. We require satellites in this subsample to have all three kinds of shape measurements, and thus this data set covers the smaller DR7 footprint. In total, there are 158537 central-satellite pairs within 7385 distinct clusters, or effectively 120200 after weighting by $p_{\rm mem}$.

The resulting redshift and luminosity distributions of satellites in the constructed DR8 and DR7 sample sets are almost indistinguishable, indicating that the selection functions for different shape measurements are quite similar.

In Paper I, to investigate the effect of the sky-subtraction technique on the measured central galaxy alignment signal, we have reported the results based on a set of DR4 footprint satellites, which have re-Gaussianianization shape measurement based on both DR4 and DR8 SDSS photometric pipelines. We found that within error bars, the measured central galaxy alignment signals are very similar when

[2]We have tried fixing the shape measurement method to re-Gaussianzation but varying SDSS photometry pipeline between DR4 and DR8. We found that the derived shape parameters based on different pipelines are statistically consistent. Similarly, we expect that using DR7 photometry for de Vaucouleurs shapes should give consistent results as using those based on DR8.

different photometric pipelines are used, and therefore concluded that the effect of sky-subtraction does not substantially influence the central galaxy alignment measurement. In this work for satellite alignment, we have also examined whether sky-subtraction is an issue for the detecting signal using the DR4 footprint data set, but did again failed to find any disagreement. For this reason, to simplify the analysis we will only report the measured satellite alignment results for the DR8 and DR7 footprint sample.

3.2.4 Systematic test sample

We construct three systematic test samples to study potential systematic effects in the crowded cluster environment. All of the samples are constructed from the red-sequence Matched filter Galaxy v6.3 Catalog (redMaGiC) (Rozo et al., 2016), a photometrically-selected luminous red galaxy (LRG) catalog with very high quality photo-z estimation based on the SDSS DR8 photometric data. Overall, the bias, defined as the median value of $z_{\rm photo} - z_{\rm spect}$, of the DR8 redMaGiC photo-z is less than 0.005. The 1σ scatter of $(z_{\rm photo} - z_{\rm spect})/(1 + z_{\rm spect})$ is $\lesssim 0.02$.

1. **Foreground & background of redMaPPer**: The foreground and background sample is composed of galaxies that are in the same sky area as redMaPPer clusters, but are not physically associated with the cluster. This sample is constructed as follows. For each central galaxy in the redMaPPer cluster, we use $1.5R_c(\lambda)$ as a searching radius to select out LRGs within the projected area in the redMaGiC catalog. The $R_c(\lambda)$ is the radius within which $p_{\rm mem}$ is assigned in the original redMaPPer catalog, and it is estimated that $R_{200c} \approx 1.5R_c(\lambda)$ (Rykoff et al., 2012, 2014). Next we select LRGs whose photo-z < (>) $z_{\rm cluster}$ as foreground (background) candidates. To improve the purity of the sample, we further exclude $p_{\rm mem} > 0.2$ galaxies in the "ubermem" version of the redMaPPer catalog. This "ubermem" catalog extends the $p_{\rm mem}$ estimation out to $1.5R_c(\lambda)$ and down to fainter galaxies ($mag\ i < 21$), thus enabling us to remove potential cluster members at $1 \sim 1.5R_c(\lambda)$ and those that are relatively faint, unlike in the original redMaPPer catalog. After this cut, 95% of foregrounds and 99% of backgrounds have their $\Delta z = |z_{\rm photo} - z_{\rm cluster}| \gtrsim 0.02$, suggesting that the above procedures return a set of clean foreground and background galaxies. After requiring these galaxies to have re-Gaussianization shape measurements, we have 45030 fake central-satellite pairs in the DR8 footprint, of which 4459 and 40571 are foreground and background galaxies, respectively. Further requiring these galaxies to have de Vaucouleurs and isophotal shapes in DR7, leaves us with 4134 and 36941 foreground and background galaxies, respectively.
2. **Non-cluster field sample**: To highlight the effect of the crowded cluster environment on the shape measurement of galaxies within the cluster area on the sky (either physically-associated member galaxies or just foreground/background galaxies), we construct a sample of galaxies that are not in the footprint of redMaPPer cluster fields, and call it the "non-cluster field sample". We do so by simply taking the full redMaGiC catalog, and excluding all galaxies ($p_{\rm mem} \geq 0$) that belong to the redMaPPer cluster member sample as well as galaxies in the foreground and background sample constructed above. After requiring that these galaxies have all three shape measurements, we have 697308 galaxies within the DR7 footprint.
3. **Foreground & background of m_r<19 non-cluster field bright galaxies**: In order to understand

Table 3.1: Sample sets used in this work. The upper part of the table shows the two cluster subsamples used for the overall measurement of the satellite alignment effect, as described in Sec. 3.2.3. The columns indicate the total number of satellites (N_{sat}), total number of distinct clusters ($N_{cluster}$), and the effective number of central-satellite pairs for each sample after weighting by p_{mem} (N_{eff}). The lower part of the table summarizes the subsamples used for systematic tests, as described in Sec. 3.2.4. The columns indicate the total number of galaxies (N_{tot}), number of foreground (N_{fore}) and background objects (N_{back}), respectively.

Cluster system sample	N_{sat}	$N_{cluster}$	N_{eff}
DR8 footprint sample	174180	8121	132072
DR7 footprint sample	158537	7385	120200

Systematic test sample	N_{tot}	N_{fore}	N_{back}
Foreground & background of redMaPPer (DR8 footprint)	45030	4459	40571
Foreground & background of redMaPPer (DR7 footprint)	41075	4134	36941
Non-cluster field sample	697308		
Foreground & background of m_r<19 non-cluster field bright galaxies	278204	6990	271214

the level of contamination caused by the extended light profile of bright central galaxies on nearby satellites, we select bright galaxies with m_r<19 from our non-cluster field sample described above, and construct a sample composed of the corresponding foreground and background galaxies around these bright galaxies. We again find the foreground/background galaxies from redMaGiC, and require their z_{photo} to be at least 0.04 smaller/greater than that of their nearby bright galaxies. Here 0.04 is chosen to be about 2σ given the average photo-z error of redMaGiC. Requiring that all foreground and background galaxies having well-defined shape measurements yields 281114 galaxies in total.

Table 3.1 summarizes the data sets we have defined in Secs. 3.2.3 and 3.2.4, with detailed sample size information provided.

3.2.5 Summary of physical parameters

Similar to our analysis in Paper I, we aim to identify predictors that significantly influence the satellite alignment effect from a large parameter pool. Almost all of the physical parameters explored in this work are the same as in Paper I, except for one newly added variable: *fracDeV*.

The *cmodel* magnitude systems in SDSS pipeline tries to fit galaxy light profile by taking the linear combination of both de Vaucouleurs and exponential profiles, and stores the coefficient of the de Vaucouleurs term in the quantity *fracDeV*, which describes the fraction of light from a fit to a de Vaucouleurs profile. For a galaxy that can be best fitted by pure exponential profile, *fracDeV* = 0, while *fracDeV* = 1 for pure de Vaucouleurs profile. In general, the brightness distribution of disks follows the exponential profile, whereas bulges are better described with a de Vaucouleurs profile. The *fracDeV* parameter thus can be viewed as a tracer for a galaxy's angular momentum content or its

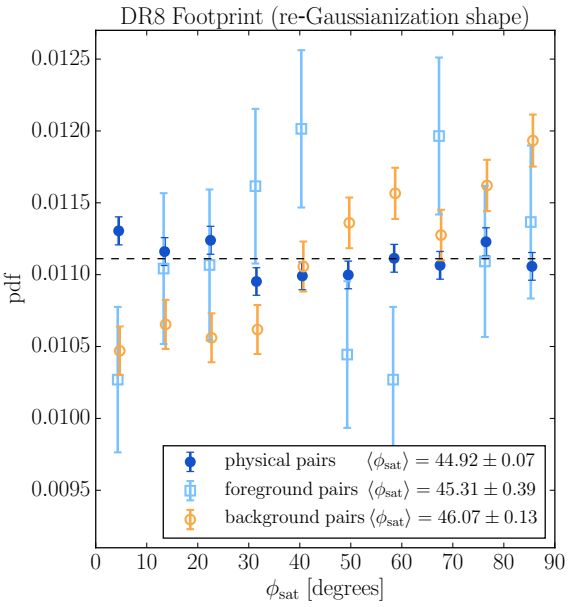

Figure 3.2: $p_{\rm mem}$-weighted probability density distribution of SA angle, $\phi_{\rm sat}$, for the 174180 $p_{\rm mem} > 0.55$ pairs measured using the re-Gaussianization method. The dark blue filled circles indicate the pdf of $\phi_{\rm sat}$ for central-satellite pairs of redMaPPer clusters selected using $p_{\rm mem} > 0.55$. *The weighted averaged SA angle, $\langle\phi_{\rm sat}\rangle$, is consistent with 45° within error bar, indicating that the overall SA signal measured based on re-Gaussianization shape is not very significant.* The open markers show the probability density function (pdf) of $\phi_{\rm sat}$ for foreground (light blue square) and background (orange circle) pairs in the footprint of redMaPPer clusters. As expected, the $\langle\phi_{\rm sat}\rangle$ value for foreground is consistent with random, and there is tangential alignment signal $\langle\phi_{\rm sat}\rangle > 45°$ for backgrounds. The horizontal black dashed line shows the expected result for randomly oriented satellite galaxies.

overall morphology, which has similar but not identical information to galaxy color. It is interesting to check the dependence of angular momentum on SA signal.

In total, we have one response variable ($\phi_{\rm sat}$) and 17 other variables constituting the pool of possible predictors for $\phi_{\rm sat}$. We classify the 17 parameters into three categories: satellite-related quantities, central galaxy-related quantities and cluster-related quantities. A brief summary of important information about these parameters is in Table 3.2; we refer readers to Sec. 2.2 of Paper I for details.

3.3 Overall Signal of Satellite Alignment

3.3.1 Distribution of $\phi_{\rm sat}$

The dark blue filled circles in the left panel of Fig. 3.2 indicate the $p_{\rm mem}$-weighted distribution of the SA angle, $\phi_{\rm sat}$, for our 174180 satellites in the DR8 footprint, based on the re-Gaussianization shape measurements. The weighted average SA angle is $\langle\phi_{\rm sat}\rangle = 44.92° \pm 0.07°$, consistent with no net tendency for SA.

Table 3.2: A summary of the 17 parameters used to study the satellite alignment effect.

Response Variable	**Properties**
$\phi_{\rm sat}$	• Satellite alignment angle, as demonstrated in Fig. 3.1. • We use this parameter as a response variable to quantify the level of satellite alignment. Smaller $\phi_{\rm sat}$ indicates a stronger satellite alignment effect.

Satellite Galaxy Quantities	**Properties**
$\log(r/R_{\rm 200m})$	• Member distance from the cluster central galaxy, normalized by $R_{\rm 200m}$
satellite ${}^{0.1}M_r$	• r-band absolute magnitude of the satellite, k-corrected to $z = 0.1$
satellite ${}^{0.1}M_g - {}^{0.1}M_r$	• Color of the satellite galaxy, k-corrected to $z = 0.1$
satellite ellipticity	• Satellite ellipticity as defined in Eq. 3.2
$\Delta\log$(satellite $R_{\rm eff}$)	• The excess of galaxy size with respect to the predicted size at the same luminosity $\Delta\log$(satellite $R_{\rm eff}$) $\equiv$ measured log(satellite $R_{\rm eff}$) $-$ predicted log(satellite $R_{\rm eff}$) • The predicted log(satellite $R_{\rm eff}$)= -0.20(satellite ${}^{0.1}M_r$)-3.84, derived by linearly fit to all $p_{\rm mem} > 0.55$ satellites in the DR8 footprint sample. A relevant figure is presented in Fig. 5 of Paper I, except that the derived predicted log(satellite $R_{\rm eff}$) is slightly different from Paper I due to the inclusion of lower $p_{\rm mem}$ satellites in Paper II.
fracDeV	• The fractional flux contribution of the de Vaucouleurs profile, see Sec. 3.2.5 for detail. • *fracDeV*=0 for a pure exponential profile; *fracDeV*=1 for a pure de Vaucouleurs profile.
$\theta_{\rm cen}$	• Central galaxy alignment angle, as demonstrated in Fig. 3.1 • Smaller $\theta_{\rm cen}$ indicates that the satellite is residing closer to the major axis direction of its central galaxy.

Central Galaxy Quantities	**Properties**
central galaxy dominance	• Magnitude gap between the central galaxy and the mean of the 2nd and 3rd brightest satellites Central dominance $\equiv$ Central ${}^{0.1}M_{\rm r} - \frac{{}^{0.1}M_{\rm r,\,1st} + {}^{0.1}M_{\rm r,\,2nd}}{2}$ • A smaller value indicates a more dominant central galaxy.
central ${}^{0.1}M_r$	• r-band absolute magnitude of the central, k-corrected to $z = 0.1$
central ${}^{0.1}M_g - {}^{0.1}M_r$	• Color of the central galaxy, k-corrected to $z = 0.1$
central ellipticity	• Ellipticity of central galaxy as defined in Eq. 3.2.
$\Delta\log$(central $R_{\rm eff}$)	• The excess of central galaxy size with respect to the predicted size of centrals at the same luminosity. $\Delta\log$(central $R_{\rm eff}$) $\equiv$ measured log(cental $R_{\rm eff}$) $-$ predicted log(central $R_{\rm eff}$) • The predicted log(central $R_{\rm eff}$)= -0.31(central ${}^{0.1}M_r$)-6.16, derived by linearly fit to all centrals in the DR8 footprint sample. See also Fig. 4 in Paper I for more more detail.
$P_{\rm cen}$	• Central galaxy probability provided in redMaPPer. • $P_{\rm cen}$ is an indicator of whether a cluster system contains only a single dominant central galaxy or has multiple central galaxy candidates.

Cluster Quantities	**Properties**
log(richness)	• Cluster richness taken from the redMaPPer catalog.
redshift	• Cluster redshift estimated by redMaPPer.
cluster ellipticity	• Calculated based on the distribution of member galaxies. See Sec. 2.2.3 of Paper I for detail. • A cluster with larger cluster ellipticity has more elongated satellite distribution.
cluster member concentration, $\Delta_{\rm R}$	• Derived based on the average projected distance of member galaxies from the cluster center, with some normalization towards cluster richness and redshift. See Sec. 2.2.9 of Paper I for detail definition. • By construction, negative $\Delta_{\rm R}$ value means the cluster has a more compact member galaxy distribution than the average cluster at similar richness and redshift.

However, it does not rule out the possibility of a statistically significant SA detection for subsamples of the satellite population. We will show later in Sec. 3.4.2 that when focusing on brighter satellites, we can still detect a statistically significant SA signal using re-Gaussianization shapes.

3.3.2 SA measurement in e_+

Besides using the parameter $\phi_{\rm sat}$ to quantify the degree of SA signal, it is also useful to calculate the mean radial ellipticity $\langle e_+ \rangle$, especially when quantifying the level of IA systematics to weak lensing signals (e.g., Schneider et al., 2013; Sifón et al., 2015). Here we also compute mean radial ellipticities in order to compare with previous work. For the definition of e_+, we refer readers back to Sec. 3.2.2 for more detail. Under our definition, a satellite with $e_+ > 0$ tends to point radially toward its host central galaxy.

The dark blue filled circles in Fig. 3.3 show the averaged $\langle e_+ \rangle$ component based on re-Gaussianization shapes for all DR8 footprint satellites, divided into bins in projected separation from their own central galaxy. The corresponding error bars are simply the standard error of the mean. We observe that the SA signal is consistent with zero within 3σ across all radial bins, meaning that we do not detect any significant SA effect in the overall redMaPPer satellite population. The grey triangles indicate the measured averaged ellipticity component $\langle e_\times \rangle$, which provides a 45° systematic test (also known as B-mode test). By symmetry, the expected $\langle e_\times \rangle$ value should be zero, unaffected by either lensing or SA effects, which only contribute to the e_+ component. We find that our measured $\langle e_\times \rangle$ is consistent with zero in all radial bins, suggesting that systematic errors that would generate a B-mode signal are negligible.

While there is no coherent radial orientation of satellites across the entire DR8 sample, as we will show later in Sec. 3.4.2, more luminous satellites tend to have stronger SA signal. Here we demonstrate that a subsample of satellites with ${}^{0.1}Mr < -21$ has $\langle e_+ \rangle \approx 0.014 \pm 0.0042$ ($\sim 3.3\sigma$) and $\langle e_+ \rangle \approx 0.0062 \pm 0.0028$ ($\sim 2.3\sigma$) in the two smallest radial bins at $\sim r < 0.2R_{\rm 200m}$, as shown in the red pentagons of Fig. 3.3. In comparison, Sifón et al. (2015) found no significant SA across all radial bins for satellites with ${}^{0.1}Mr < -21$ (see their Fig. 10) when using satellites of 91 massive galaxy clusters with shape measurements optimized for lensing. Similarly, Schneider et al. (2013) also found no apparent SA signal across all radial bins for early-type satellites based on members of galaxy groups (see their Fig. 7).

3.3.3 SA signal based on different shape measurements

To investigate the effect of shape measurement methods on the detection of SA signals, we use satellites within the DR7 footprint, as defined in Sec. 3.2.3 (see also Table 3.1), which have re-Gaussianization, deVaucouleurs, and isophotal shape measurements. The left panel of Fig. 3.4 shows the $p_{\rm mem}$-weighted distribution of $\phi_{\rm sat}$ for this sample set, with the teal green circles, yellow green diamonds and olive triangles representing shape measurements based on the re-Gaussianization method, de Vaucouleurs fits, and isophotal fits, respectively. The isophotal shape measurement produces the strongest SA signal ($\langle \phi_{\rm sat} \rangle = 44.35° \pm 0.08°$), followed by de Vaucouleurs fits ($\langle \phi_{\rm sat} \rangle = 44.71° \pm 0.08°$) and finally re-Gaussianization shapes ($\langle \phi_{\rm sat} \rangle = 44.91° \pm 0.08°$). However, as described in Hao et al. (2011), we still must test whether the detected SA signal is real (due to physical alignments) or fake (due to

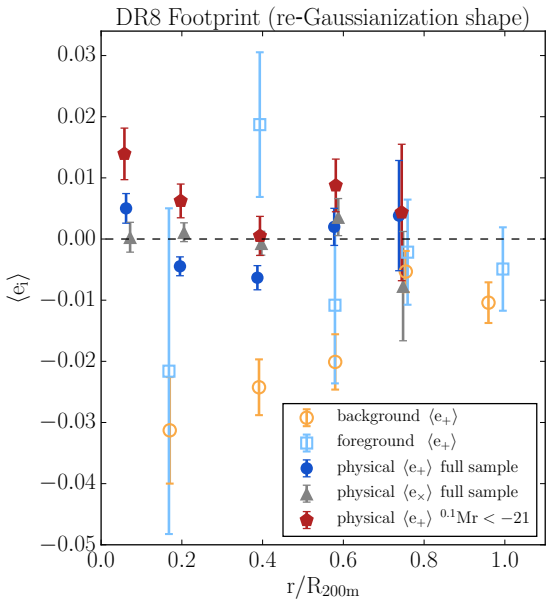

Figure 3.3: Satellite alignment signal measured in $\langle e_+ \rangle$ (dark blue filled circle) in bins of normalized projected distance based on re-Gaussianization shapes for the 174180 DR8 redMaPPer $p_{\rm mem} > 0.55$ satellites. Under our definition, $\langle e_+ \rangle > 0$ indicates radial alignment. *The measured SA signal is consistent with zero within 3σ across all radial bins.* The $\langle e_+ \rangle$ signals for foregrounds (light blue square) and backgrounds (orange open circle) in redMaPPer cluster fields are also shown. The $\langle e_\times \rangle$ component for physical pairs, indicated in grey triangles, is consistent with zero in all radial bins. *This suggests that systematics that would cause a B-mode signal in the re-Gaussianization shapes are negligible.* When focusing on a subsample of brighter satellites with ${}^{0.1}Mr < 21$ (red pentagon), we find $\langle e_+ \rangle \approx 0.014 \pm 0.0042$ ($\sim 3.3\sigma$) and $\langle e_+ \rangle \approx 0.0062 \pm 0.0028$ ($\sim 2.3\sigma$) in the two smallest radial bins at $\sim r < 0.2 R_{\rm 200m}$. *This indicates that we reach a significant SA detection using re-Gaussianization shapes with satellites that are more luminous and located closer to central galaxies.*

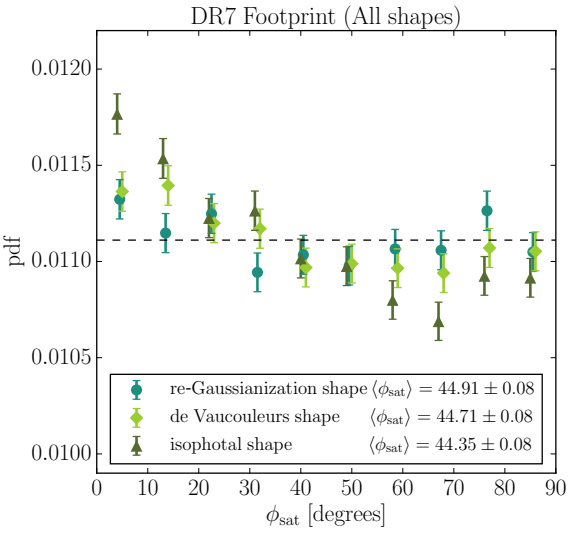

Figure 3.4: $p_{\rm mem}$-weighted probability density distribution of $\phi_{\rm sat}$ for the 158537 $p_{\rm mem} > 0.55$ redMaPPer satellites in the DR7 footprint based on re-Gaussianization (teal green circle), de Vaucouleurs (yellow green diamond), and isophotal (olive triangle) shape measurements. *The weighted average SA angles, $\langle\phi_{\rm sat}\rangle$, for both de Vaucouleurs and isophotal shapes are less than 45°, indicating we have observed SA effect significantly based on these two shape measurements. However for re-Gaussianization shape, $\langle\phi_{\rm sat}\rangle$ is consistent with 45° within error bars.*

systematics). We will investigate possible systematic effects in Sec. 3.5.

3.3.4 Foreground and background systematic tests

We examine our SA measurement using sample sets of foreground and background galaxies in the footprint of redMaPPer cluster field. For construction of foreground and background samples, we refer readers back to Sec. 3.2.4. For foregrounds, we expect galaxies to be randomly oriented in the measured $\phi_{\rm sat}$ with respect to the central galaxies of redMaPPer clusters in the same field. For backgrounds, we expect galaxies to exhibit tangential alignment because of the gravitational lensing effect. The light blue sqares/orange open circles in Fig. 3.2 show the distribution of $\phi_{\rm sat}$ measured using re-Gaussianization shapes for our foreground/background samples. The observed $\phi_{\rm sat}$ distributions are consistent with our expectation. This indicates that there are no severe systematics due to the complexity of measuring shapes in cluster fields based on re-Gaussianization method. However, the test we applied is not very sensitive for low-level systematics due to the lack of foreground pairs.

Besides the test for re-Gaussianization shape, Fig. 3.5 shows the foreground (light blue square) and background (orange open circle) tests for de Vaucouleurs shape (left panel) and isophotal shape (right panel). For foregrounds, the p-values of KS tests, as indicated in the legend below the figures, show that the distribution is consistent with uniform distribution. For backgrounds, we also observe the expected lensing effect in de Vaucouleurs and isophotal shaps.

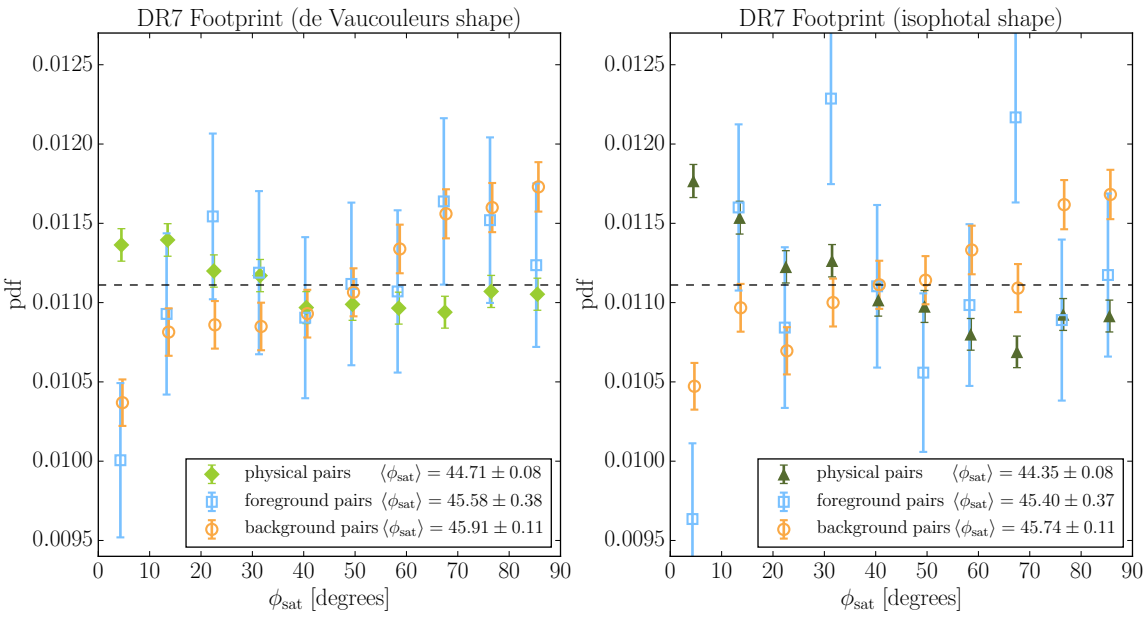

Figure 3.5: Foreground (light blue open square) and background (orange open circle) tests for de Vaucouleurs (left panel) and isophotal shape (right panel) measurements.

3.4 Linear Regression Analysis

We apply linear regression analysis and variable selection techniques to properly account for correlations among various parameters and to identify featured predictors that significantly affect the SA phenomenon. The variable selection methods are quite similar (but not identical) to those described in Sec. 3 of Paper I. Below, we briefly summarize the approaches, including the new methodology in this paper, and report the results.

3.4.1 Methodology

Overview of Linear Regression

Linear regression is a method to study the relationship between a response variable Y and a variety of regressors vectorized as $\mathbf{X} = (X_1, X_2, X_3, ..., X_N)$. One tries to estimate optimal values of the free parameters by minimizing the squared residuals of the following model:

$$Y = f(\mathbf{X}) = \beta_0 + \beta_1 X_1 + ... + \beta_i X_i + ... + \beta_N X_N + \epsilon, \tag{3.4}$$

where the intercept β_0 and the slopes β_i are the unknown regression coefficients, and ϵ represents random observational error, usually assumed to be distributed normally with mean zero and some dispersion.

In our analysis, we use $\phi_{\rm sat}$ as the response variable Y, regressed against the 17 parameters in our parameter pool, as listed in Table 3.2. In short, we have 7 satellite-related, 6 central galaxy-related and 4 cluster-related quantities. When fitting the regression Eq. (3.4), we standardize the parameters

P_i:

$$X_i = \frac{P_i - \langle P \rangle_i}{\sigma_{P_i}}, \tag{3.5}$$

where $\langle P \rangle_i$ and σ_{P_i} are the sample mean and standard deviation respectively of the parameter P_i, with the latter representing the width of the intrinsic scatter combined with measurement error. Table 3.3 lists the $\langle P \rangle$ and σ_P for our 17 parameters for DR8 redMaPPer satellites. The standardization means that even though our predictors P_i have different magnitudes and spreads, the fitted values β_i all have essentially the same meaning: larger $|\beta_i|$ indicates a stronger effect of the regressor X_i on $\phi_{\rm sat}$. We also quantify the level of significance for any identified correlations using the t-value. The t-value, defined as the ratio of β_i to its standard error, can be positive or negative depending on the sign of β_i. A larger $|t|$ indicates a higher likelihood that $\beta_i \neq 0$, which means a stronger relationship between $\phi_{\rm sat}$ and X_i. Statistically, under the assumption that β_i is asymptotically normal,[3] there is a direct link between the t-value and p-value on the hypothesis test of whether $\beta_i = 0$ or not. A p-value of 0.05 corresponds to a 95% confidence interval for β_i that does not overlap with zero. We will count predictors with p-value < 0.05 as having significant effect on SA signal when doing model selection later.

Model Averaging

The next issue we need to face is how to choose a model with predictors that truly affect $\phi_{\rm sat}$. A linear model with all possible predictors has many free parameters to tune to fit the data well, but may cause high variance. By contrast, a model with only few predictors is more stable, but may underfit the data yielding a high bias. A good model results from achieving a balance between goodness of fit and complexity. With 17 predictor candidates in our parameter pool, there are a total of 2^{17} (= 131 072) possible models.

In Paper I, we applied standard "Forward Stepwise" and "Best Subset" model selection methods to identify a single best model, and interpreted our results based on that model alone. However, SA is a relatively weak signal, so identifying predictors that reflect the true underlying physics rather than noise requires a careful treatment of model uncertainty, which can lead to the selection of a model that by random chance includes uninformative predictors. Thus in this work, we apply the "model averaging" technique (see e.g. Burnham & Anderson 2003b and Grueber et al. 2011, and references therein), which combines a portion of 'good models' from the parent model pool by taking a weighted-average based on the performance scores of each model measured by some information criterion (such as AIC; **?**). Through the model averaging process, fluctuations due to noise can be averaged out and the combined model is thus more stable.

The detailed model averaging analysis proceeds as follows:

1. As was the case in Paper I, we use best-subset selection to fit each of the 2^{17} possible models using R's `leaps` package, and for each we estimate the AIC:

$$AIC_i = \frac{1}{n\hat{\sigma}_i^2}(RSS_i + 2d_i\hat{\sigma}_i^2), \tag{3.6}$$

[3]Suppose we do many measurements on β_i, with different but statistically similar sets of data, and plot the distribution of the resulting β_i. We say β_i is asymptotically normal if the distribution is a gaussian at the mean of the true β_i value with certain variance.

where RSS_i is the residual sum of squares, d_i is the number of predictors used in the $i^{\rm th}$ model, $\hat{\sigma}_i^2$ is an estimate of the variance of observational error ϵ shown in Eq. (3.4), and n is the total number of satellite-central pairs. A lower AIC value indicates a better-fitting model.

2. We convert each AIC value to a relative quantity:

$$\Delta AIC_i = AIC_i - \min(AIC), \tag{3.7}$$

where $\min(AIC)$ represents the smallest AIC value of all possible models in the previous step.

3. Given the set of relative AIC values, we compute the model-averaging weight for each model:

$$w_i = \frac{\exp\left(-\Delta AIC_i/2\right)}{\sum_{k=1}^{2^{17}} \exp\left(-\Delta AIC_k/2\right)}\,. \tag{3.8}$$

4. For computational efficiency, we apply a cut of $\Delta AIC = 12$, meaning that we only average that subset of 485 models with $\Delta AIC_i < 12$. For this cut, the sum of weights is 0.996.

5. The final averaged regression estimate $\tilde{\beta}_j$ and variance estimate $\tilde{\sigma}_j^2$ for each of the 17 predictors are given by

$$\tilde{\beta}_j = \sum_i w_i \beta_{j,i} \mathbf{I}(\beta_j \in \mathcal{M}_i) \tag{3.9}$$

$$\tilde{\sigma}_j^2 = \sum_i w_i [\sigma_{j,i}^2 + (\beta_{j,i} - \tilde{\beta}_j)^2] \mathbf{I}(\beta_j \in \mathcal{M}_i)\,. \tag{3.10}$$

The first summation can be read as "taking weighted average of the of the $j^{\rm th}$ regression coefficient over all models with $\Delta AIC_i < 12$ where the $j^{\rm th}$ regressor appears" (as indicated by the indicator function $\mathbf{I}$). The second summation is the variance of the $j^{\rm th}$ regressor. If the estimated $\tilde{\beta}_j$ is more than 1.96 $\tilde{\sigma}_j$ away from zero, assuming $\tilde{\beta}_j$ is distributed normally with mean zero, this corresponds to a p value < 0.05 that $\tilde{\beta}_j \neq 0$. One can interpret that the predictor j is important for the SA signal.

We note that the way in which $\tilde{\beta}_j$ is computed has the effect of shrinkage: the smaller number of models in which $\tilde{\beta}_j$ appears, the closer $\tilde{\beta}_j$ gets to zero. This method for computing $\tilde{\beta}_j$ is dubbed the zero method (Burnham & Anderson 2003b), which is contrasted against the natural average method, where we normalize the predictor estimate by dividing by $\sum_i w_i \mathbf{I}(\beta_j \in \mathcal{M}_i)$. The zero method is preferable in situations such as ours where the aim is to determine which predictors have the strongest effects on the response variable.

3.4.2 Featured Predictor Selection – re-Gaussianization shape

In this subsection, we report the predictor selection result for our DR8 footprint sample with $\phi_{\rm sat}$ measured using the re-Gaussianization method. All analyses below are properly weighted by $p_{\rm mem}$ for each satellite-central pair.

Table 3.4 lists those models that have $\Delta AIC < 3$, with the first row containing the model with the smallest AIC value, i.e., the model that would be selected in a traditional implementation of best-subset selection using AIC as the fit metric (or equivalently using Mallow's C_p, which is proportional

to AIC). The first column indicates the total number of regressors included in a model, and the subsequent 2nd to the 18th columns records the regression coefficients β_j formulated in Eq. (3.4). Some predictors, such as $\log(r/R_{200\mathrm{m}})$ and satellite luminosity ${}^{0.1}Mr$, appear in all of the top models, while less important predictors appear only occasionally. In Table 3.5 we lists the values of $\tilde{\beta}$ and $\tilde{\sigma}$, as well as the absolute t value, for each predictor after averaging over all models with $\Delta AIC < 12$ (485 models in total; see eqs. (3.9) and (3.10)). Predictors with $|t| > 1.96$ are identified as significant in affecting SA. Under the re-Gaussianization shape measurement, we identify $\log(\mathrm{r/R_{200m}})$, ${}^{0.1}\mathrm{Mr}$, satellite ellipticity $\mathrm{e_{sat}}$, and $fracDeV$ as significant predictors. To reiterate a point made above, in this work we are not interested in using the $\tilde{\beta}$ values to predict ϕ_{sat}; our interest lies in quantifying the significances of the predictors (as indicated by t values) and in exhibiting their effect on ϕ_{sat} (as indicated in the sign of $\tilde{\beta}$).

Fig. 3.6 illustrates these trends by plotting the averaged value of ϕ_{sat} in bins of each selected featured predictor, with the correlation coefficient between ϕ_{sat} and each predictor also provided. Clearly the satellite luminosity (${}^{0.1}Mr$) and separation from the central galaxy in units of $R_{200\mathrm{m}}$ ($\log(r/\mathrm{R_{200m}})$) are prominent predictors for satellite alignments. There are sub-populations with measured $\langle\phi_{\mathrm{sat}}\rangle > 45°$, although with less than 3σ significance, for example at faint luminosity or low $fracDeV$. This may in part be due to lensing contamination from background galaxies that are wrongly included in the satellite sample. The orange triangular points shown in Fig. 3.6 are the estimates of lensing contamination based on the assumption that the p_{mem} values accurately reflect reality; we refer readers to Appendix 3.B for details. The estimated contribution from lensing contamination to $\langle\phi_{\mathrm{sat}}\rangle \approx 45.1°$ across all subsamples.

In Sec. 3.3.1 and 3.3.2, no SA signal was detected based on re-Gaussianization shape measurement, when averaging over all satellite-central pairs. The results in this section demonstrate that there do exist statistically significant SA effects for certain subsamples of satellites, such as those that are intrinsically brighter or located closer to their host central galaxies. We further discuss these selected predictors in Sec. 3.6.

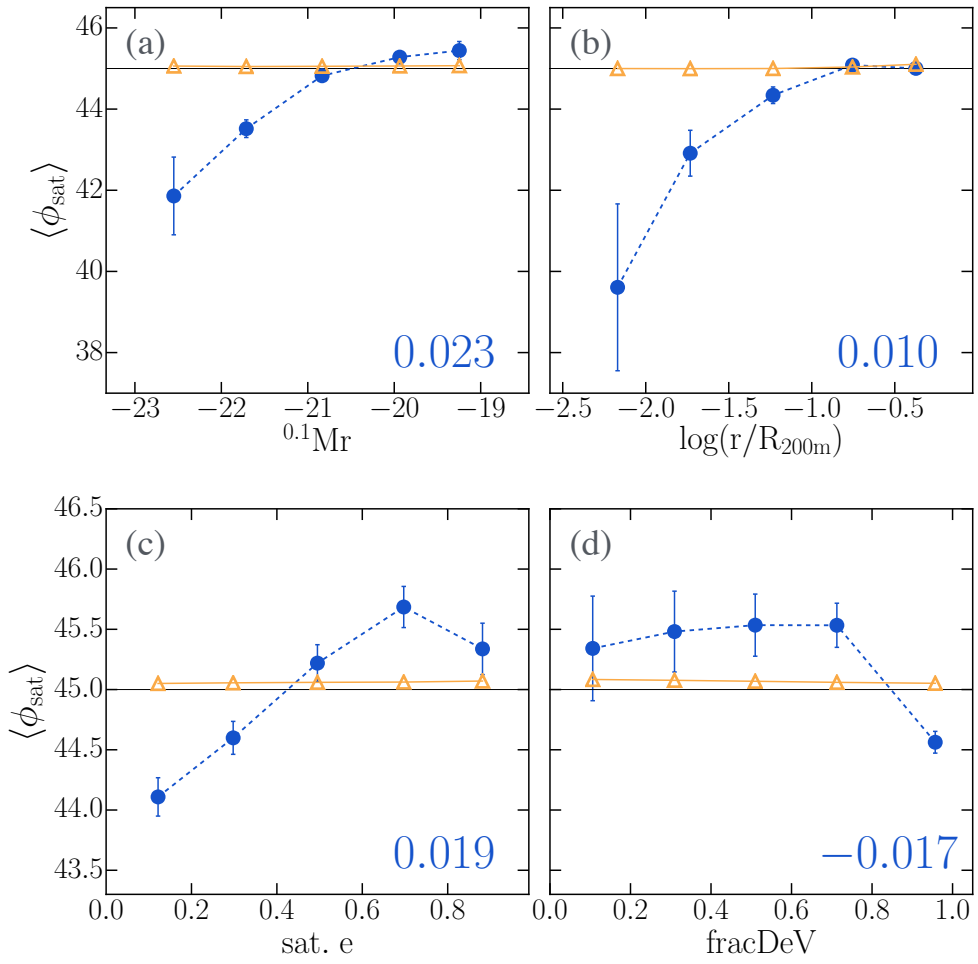

Figure 3.6: Averaged satellite alignment angle $\langle\phi_{\rm sat}\rangle$ of redMaPPer member galaxies in the SDSS DR8 footprint sample as a function of the 4 significant predictors whose $|t| > 1.96$ shown in Table 3.5. The correlation coefficient between $\phi_{\rm sat}$ and each predictor is labeled on the lower-right corner of each panel. *One can see that $\langle\phi_{\rm sat}\rangle < 45°$ for satellites that have higher luminosity, are located closer to cluster center, are rounder in shape, and have a higher $fracDeV$. Especially for the subsamples of luminous satellites, we detect a very significant SA signal.* The triangular orange markers show the estimated level of lensing contamination from background galaxies that are wrongly included in the SA analysis (see Appendix 3.B for details), resulting in $\langle\phi_{\rm sat}\rangle \sim 45.1°$ across all bins.

Table 3.3: Mean and standard deviation values (weighted by $p_{\rm mem}$) of the 17 parameters for our DR8 $p_{\rm mem} > 0.55$ redMaPPer satellites.

	$\log(r/R_{200m})$	$^{0.1}$Mr	color	e_{sat}	$R_{eff,sat}$	θ_{cen}	fDeV	dom	$^{0.1}Mr_{cen}$	$color_{cen}$	e_{cen}	$R_{eff,cen}$	P_{cen}	λ	z	$e_{cluster}$	Δ_R
mean	-0.68	-20.40	0.89	0.45	1.32	42.09	0.77	-0.89	-22.35	0.98	0.25	0.02	0.87	41.99	0.24	0.20	0.01
std.	0.34	0.76	0.12	0.26	0.20	26.09	0.30	0.60	0.49	0.07	0.16	0.15	0.17	25.01	0.07	0.11	0.11

Table 3.4: A subset of top regression models ranked by the goodness of performance for DR8 re-Gaussianization shape measurements. The 1st column is the total number of predictors involved in a model, columns 2 ∼ 18 show the regression coefficients for our 17 predictors listed in the same order as that of Table 3.2. The 2nd last column lists the ΔAIC values, and the last column shows the weighting factor for each model that we applied when doing model averaging.

Np	$\log(r/R_{200m})$	$^{0.1}$Mr	color	e_{sat}	$R_{eff,sat}$	θ_{cen}	fDeV	dom	$^{0.1}Mr_{cen}$	$color_{cen}$	e_{cen}	$R_{eff,cen}$	P_{cen}	λ	z	$e_{cluster}$	Δ_R	ΔAIC	weight
6	0.32	0.49		0.28	-0.14		-0.28		-0.16									0	0.0296
7	0.32	0.49		0.28	-0.14	0.08	-0.28		-0.16									0.82	0.0196
7	0.32	0.48		0.29	-0.14		-0.28		-0.16			0.06						1.49	0.014
7	0.31	0.47		0.29	-0.14		-0.3		-0.17						-0.06			1.52	0.0138
7	0.32	0.49		0.28	-0.14		-0.28		-0.16		0.05							1.64	0.013
7	0.32	0.49		0.28	-0.14		-0.28	-0.05	-0.13									1.81	0.012
7	0.32	0.49		0.28	-0.14		-0.28		-0.17	-0.04								1.83	0.0118
5	0.31	0.5		0.32			-0.23		-0.17									1.9	0.0115
6	0.32	0.48		0.28	-0.14		-0.28	-0.14										2.01	0.0108
7	0.32	0.49		0.28	-0.14		-0.28		-0.16							-0.02		2.15	0.0101
7	0.32	0.49	-0.02	0.28	-0.14		-0.27		-0.16									2.22	0.0098
7	0.32	0.49		0.28	-0.14		-0.28		-0.16								0.01	2.24	0.0097
8	0.32	0.48		0.28	-0.14	0.08	-0.28		-0.16			0.06						2.25	0.0096
7	0.32	0.49		0.28	-0.14		-0.28		-0.16				0.01					2.26	0.0096
7	0.32	0.49		0.28	-0.14		-0.28		-0.16					0				2.27	0.0095
8	0.31	0.47		0.29	-0.14	0.08	-0.29		-0.17						-0.06			2.31	0.0093
8	0.32	0.49		0.28	-0.14	0.08	-0.28		-0.16		0.05							2.44	0.0087
8	0.32	0.49		0.28	-0.14	0.08	-0.28	-0.06	-0.13									2.61	0.008
8	0.32	0.49		0.28	-0.14	0.07	-0.27		-0.17	-0.04								2.67	0.0078
7	0.32	0.48		0.28	-0.14		-0.28	-0.15						0.08				2.68	0.0078
6	0.31	0.5		0.31		0.07	-0.23		-0.17									2.76	0.0075
7	0.32	0.48		0.28	-0.14	0.08	-0.28	-0.14										2.83	0.0072

Table 3.5: Model averaged result for our DR8 footprint sample (see Table 3.1) based on re-Gaussianization shape measurements. The 1st row shows the estimated regression coefficient based on Eq.(3.9). The 2nd row lists the standard error of $\tilde{\beta}$. The 3rd row is the absolute value of the t value = $|\tilde{\beta}/\tilde{\sigma}|$. Parameters with $|t| > 1.96$ is identified as important predictors in affecting SA effect. Here we find that log(r/R_{200m}), $^{0.1}$Mr, satellite ellipticity, and $fracDeV$ are selected as significant predictors.

	log(r/R_{200m})	$^{0.1}$Mr	color	e_{sat}	$R_{eff,sat}$	θ_{cen}	fDeV	dom	$^{0.1}Mr_{cen}$	$color_{cen}$	e_{cen}	$R_{eff,cen}$	P_{cen}	λ	z	$e_{cluster}$	Δ_R
$\tilde{\beta}$	0.314	0.48	-0.003	0.289	-0.115	0.032	-0.273	-0.028	-0.133	-0.008	0.011	0.012	0.001	0.005	-0.016	-0.003	0.001
$\tilde{\sigma}$	0.063	0.07	0.026	0.068	0.065	0.049	0.074	0.059	0.069	0.032	0.035	0.035	0.023	0.03	0.043	0.024	0.02
$\|t\|$	4.982	6.892	0.111	4.257	1.781	0.639	3.71	0.469	1.932	0.258	0.317	0.325	0.037	0.152	0.377	0.123	0.052

Table 3.6: Model averaged result for our DR7 footprint sample (see Table 3.1) based on de Vaucouleurs shape measurements. The selected significant predictors ($|t| > 1.96$) are: log(r/R_{200m}), $^{0.1}$Mr, satellite ellipticity, θ_{cen}, and $fracDeV$.

	log(r/R_{200m})	$^{0.1}$Mr	color	e_{sat}	$R_{eff,sat}$	θ_{cen}	fDeV	dom	$^{0.1}Mr_{cen}$	$color_{cen}$	e_{cen}	$R_{eff,cen}$	P_{cen}	λ	z	$e_{cluster}$	Δ_R
$\tilde{\beta}$	0.628	0.617	-0.021	0.41	-0.02	0.229	-0.218	-0.01	-0.094	-0.035	0.016	0.024	0.046	0.065	0.001	0	-0.003
$\tilde{\sigma}$	0.066	0.072	0.046	0.07	0.046	0.065	0.073	0.044	0.074	0.054	0.041	0.048	0.062	0.067	0.021	0.016	0.022
$\|t\|$	9.536	8.62	0.448	5.886	0.433	3.506	2.977	0.227	1.268	0.657	0.397	0.497	0.742	0.979	0.069	0.002	0.133

Table 3.7: Similar to Table 3.6 but for results based on isophotal shape measurements. The selected significant predictors ($|t| > 1.96$) are: log(r/R_{200m}), $^{0.1}$Mr, satellite ellipticity, θ_{cen}, $fracDeV$, and redshift.

	log(r/R_{200m})	$^{0.1}$Mr	color	e_{sat}	$R_{eff,sat}$	θ_{cen}	fDeV	dom	$^{0.1}Mr_{cen}$	$color_{cen}$	e_{cen}	$R_{eff,cen}$	P_{cen}	λ	z	$e_{cluster}$	Δ_R
$\tilde{\beta}$	0.953	0.713	-0.154	0.451	0.003	0.371	-0.325	0.014	-0.022	0.002	0.003	0.001	0.107	0.055	0.177	-0.052	-0.008
$\tilde{\sigma}$	0.067	0.079	0.071	0.069	0.03	0.066	0.076	0.051	0.056	0.028	0.028	0.028	0.068	0.062	0.076	0.06	0.033
$\|t\|$	14.282	9.074	2.163	6.498	0.093	5.629	4.301	0.279	0.397	0.063	0.105	0.03	1.57	0.895	2.32	0.868	0.239

3.4.3 Featured Predictor Selection – de Vaucouleurs and isophotal shapes

Here we repeat the predictor selection process as in the previous section, now using the DR7 sample satellites that have $\phi_{\rm sat}$ well-measured using all three shape measurement methods. Using both de Vaucouleurs and isophotal shapes result in a nonzero net SA signal detection in the overall sample as shown in Sec. 3.3.3. It is therefore interesting to check if the predictor selection result is consistent with that based on re-Gaussianization shape, where the detected SA signal is small. If we select a different set of predictors, we must consider whether they are caused by a fake systematic alignment signal captured in de Vaucouleurs and isophotal shapes, or they could be physically reasonable predictors that are authentically associated with the SA phenomenon, but are not selected out in the re-Gaussianization shape due to its sensitivity to different regions of the galaxy light profiles.

We summarize our predictor selection results for de Vaucouleurs and isophotal shapes in Tables 3.6 and 3.7. Under the criterion of $|t| > 1.96$, for de Vaucouleurs shape, in addition to the predictors that have been identified based on re-Gaussianization shape (Table 3.5), one extra predictor, $\theta_{\rm cen}$, is added with a fairly high t-value. For isophotal shape, we identify two new predictors compared to those from re-Gaussianization shapes: $\theta_{\rm cen}$ and redshift. As revealed in the sign of the $\tilde{\beta}$, satellites with smaller $\theta_{\rm cen}$ (stronger central galaxy alignment with the shape of the satellite galaxy distribution) and smaller redshift have stronger isophotal SA signal.

Fig. 3.7 shows the averaged SA angle $\langle\phi_{\rm sat}\rangle$ of our DR7 footprint sample in bins of the identified predictors. The correlation coefficients measured between $\phi_{\rm sat}$ using the three shape measurements and each predictor are shown in the legend. The correlations become tighter as we move from re-Gaussianization to isophotal shapes for most predictors – $\log(r/{\rm R}_{\rm 200m})$, satellite $^{0.1}Mr$, satellite ellipticity, $\theta_{\rm cen}$, and $fracDeV$. However, the correlation coefficient for the redshift has a different sign when measured in isophotal shape vs. the other two shapes. We will discuss the redshift dependence in more detail in Sec. 3.6.

In general, for all differences between methods, we must consider whether they originate from systematic effects, or from real differences between the methods due to their sensitivity to different parts of the galaxy light profiles and isophotal twisting.

3.5 Origin of discrepancy in detected Satellite Alignment signal with different shape measurement methods

As reported in Fig. 3.4, the detected SA signal strength depends on shape measurement methods. The isophotal shape detects the strongest SA signal, followed by de Vaucouleurs shape then re-Gaussianization shape. This trend is consistent with the large-scale IA measurement done by Singh & Mandelbaum (2016) using these three shape measurement algorithms.

In this section, we discuss possible reasons for this discrepancy. We note that in cluster systems, the difference in SA angle ($|\phi_{\rm sat,iso} - \phi_{\rm sat,reG}|$) is identical to the PA difference, $|{\rm PA}_{\rm iso} - {\rm PA}_{\rm reG}|$ measured in the RA-dec frame. We can therefore use $|{\rm PA}_{\rm iso} - {\rm PA}_{\rm reG}|$ for our tests, which allows us to introduce galaxies that do not belong to any cluster for tests of statistical and systematic errors.

In what follows, we classify the origin of the discrepancy in the measured galaxy PA into three dominant factors, as summarized in Fig. 3.8. Our high-level goal is to consider all possible factors that

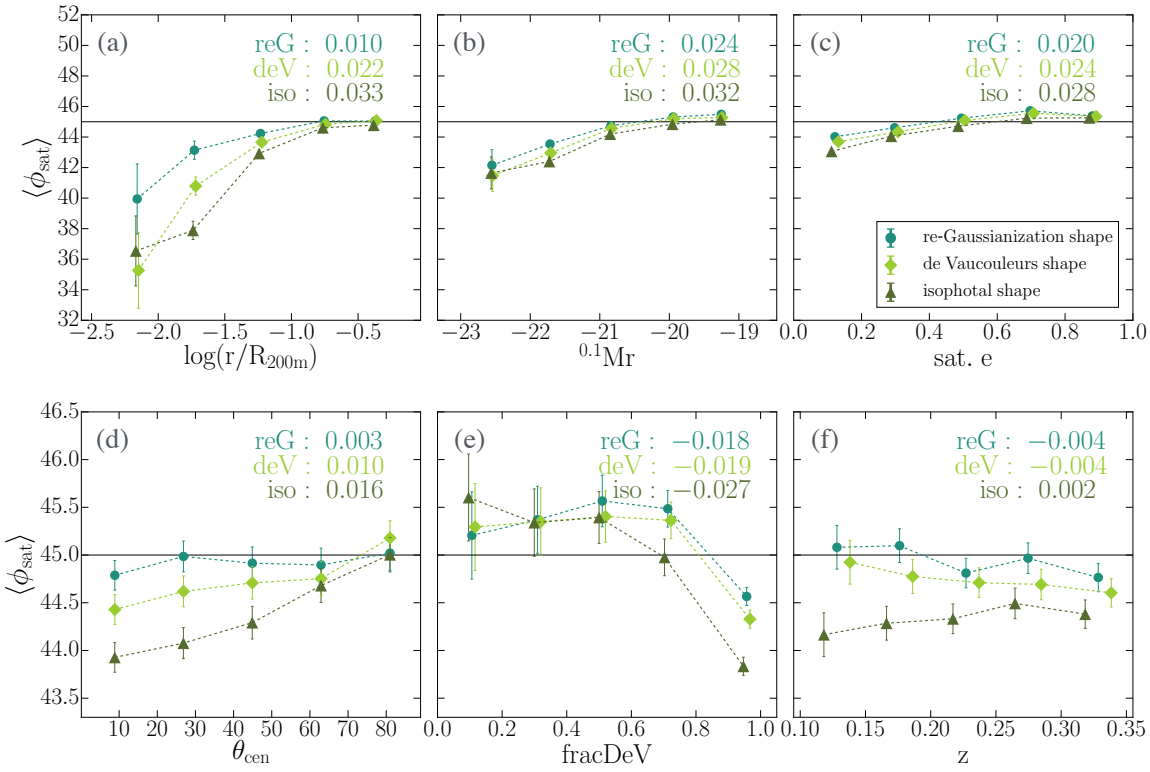

Figure 3.7: Averaged satellite alignment angle $\langle\phi_{\rm sat}\rangle$ of redMaPPer members in the SDSS DR7 footprint as a function of the 6 significant predictors whose $|t| > 1.96$ as shown in Tables 3.6 and 3.7. Correlation coefficients between $\phi_{\rm sat}$ and x-axes parameters are shown in the upper right corner of each panel.

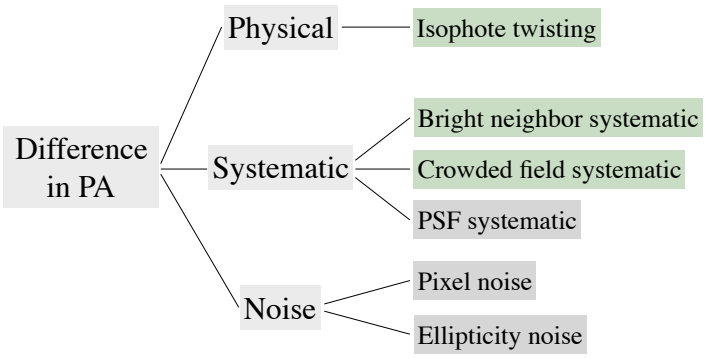

Figure 3.8: The origin of discrepancies in PA differences measured with different shape measurement methods. Three origins for these discrepancies are explored: discrepancies due real physical isophote twisting effect (Sec. 3.5.3), discrepancies caused by systematic errors, and discrepancies due to noise. The systematic origins can be further classified into three factors: the bright neighbor and crowded field systematics (Sec. 3.5.2) and the PSF systematic (Sec. 3.5.2). The origins of noise are separated into two sources: pixel (Sec. 3.5.1) and ellipticity noises (Sec. 3.5.1). The items colored in green background are factors that especially important for galaxies residing in cluster fields, while the ones colored in grey background are relevant in all possible environments.

may contribute to the measured difference in average SA angle for our redMaPPer cluster sample, and determine whether the result is dominated by noises and systematics, or we do detect any interesting physical effects.

3.5.1 PA discrepancies due to noise

The first factor that affects the difference in PA is simply noise. We further separate the origin of noise into ellipticity noise and pixel noise.

Ellipticity noise

The ellipticity noise is perhaps the most dominant factor in determining how precisely the PAs are measured. For a given S/N ratio of a detection, the uncertainty in the PA is larger for rounder galaxy (see Table 1 of Refregier et al. 2012). We demonstrate this effect in Fig. 3.9a using our non-cluster field sample, as defined in Sec. 3.2.4. We plot the PA differences between isophotal and re-Gaussianization shapes as a function of the ellipticity based on re-Gaussianization measurement. The filled circle shows the mean of the $|\mathrm{PA_{iso}} - \mathrm{PA_{reG}}|$ value in ellipticity bins, revealing that the averaged differences in PA become larger when galaxies are rounder.

Pixel noise

Pixel noise arises from the Poisson noise in the sky and object flux in CCD measurements. Its impact is strongest on the images of faint galaxies, which have relatively low signal but still experience all the Poisson noise due to the background level. Pixel noise makes it difficult to measure the shape of

low S/N galaxies, especially when those galaxies are also poorly resolved compared to the PSF (e.g., Refregier et al., 2012). As a consequence, there may also be an apparent redshift trend.

Figs. 3.9b, 3.9c, and 3.9d show the scatter plots for $|\mathrm{PA_{iso}} - \mathrm{PA_{reG}}|$ as a function of apparent r-band magnitude, r-band resolution factor[4], and photo-z respectively from the non-cluster field sample. We can see that the averaged differences in PA (filled circle) go up for galaxies with fainter m_r, lower resolution, and higher z as expected.

3.5.2 PA discrepancies due to systematic errors

Systematic errors due to data analysis methods or contamination from nearby objects (see Fig. 3.8) may also cause PA discrepancies between different methods.

PSF systematics

Different shape measurements correct for the effects of the PSF on galaxy images at different levels. If not removed properly, the residuals of PSF would bias the resulting shape parameters: In the case that PSFs are round and galaxies have elliptical isophotes, on average, the PA will be unaffected by the PSF convolution, with only the magnitude of the galaxy shape being affected. If PSFs are elongated toward specific directions, then both the measured ellipticity and PA of galaxies are contaminated.

Isophotal shapes do not explicitly correct for the PSF convolution; de Vaucouleurs shapes partially correct for the PSF using an approximate (double-Gaussian) PSF model. The re-Gaussianization shapes consider a full PSF model to remove PSF systematics in order to recover small weak lensing signals. Therefore, part of the discrepancy in PA measured based on different shape measurements may be due to different levels of PSF anisotropy removal.

Singh & Mandelbaum (2016) explored the additive bias in galaxy shape measurements due to residual PSF anisotropy, resulting in a coherent additive bias in the measured shapes of SDSS LOWZ galaxies using these three shape measurements. They found that for both re-Gaussianization and isophotal shapes, their additive biases are quite small. However, for de Vaucouleurs shapes, the additive bias is about a factor of 10 larger than with the other two shape measurements (see their Fig. 5). They claimed that this may be due to the fact that the de Vaucouleurs modeling uses an approximate PSF model. If those results are relevant for galaxies in cluster fields, then part of the PA discrepancy between de Vaucouleurs shape and the other two is contributed by the residual PSF anisotropy in the galaxy shapes. In fact, they should be even more important here, because the galaxies used in our analysis are smaller and fainter, resulting in a greater susceptibility to PSF anisotropy modeling errors.

Bright neighbor and crowded field systematics

Different shape measurement methods determine galaxy PA based on different parts of the galaxy's light profile. The re-Gaussianization method puts more emphasis on the central region of a galaxy's profile. The de Vaucouleurs shape includes both central and outer extended wings of the light profile

[4]The resolution factor reflects how resolved a galaxy is compared to its PSF, with 0 (1) indicating a completely unresolved (perfectly well-resolved) galaxy. See Appendix A of Reyes et al. (2012) for its definition.

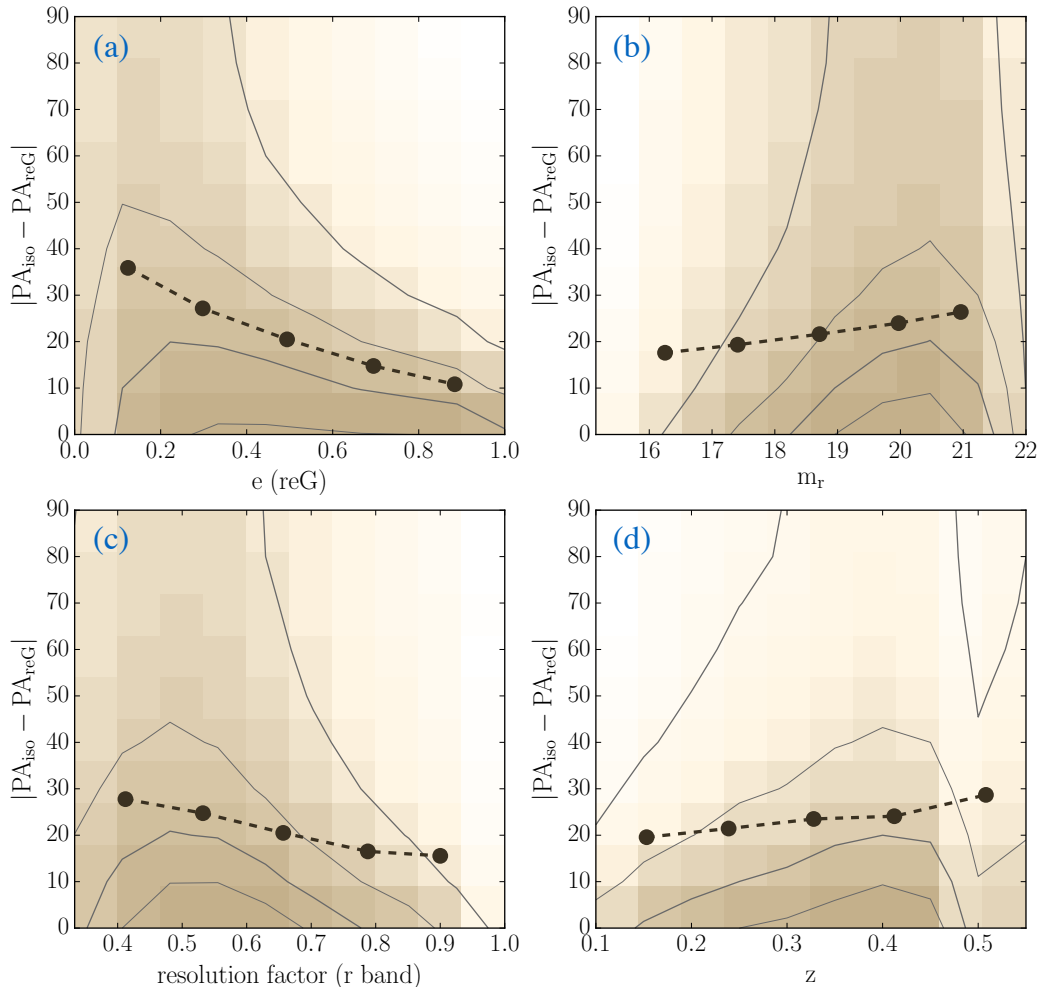

Figure 3.9: Absolute PA differences between isophotal and re-Gaussianization shapes as a function of galaxy ellipticity, mag r, r-band resolution factor, and redshift. The grey contour levels indicate the level below which 20%, 45%, 70%, and 95% of the central-satellite pairs are located. The filled solid dots indicate the averaged $|PA_{iso} - PA_{reG}|$ values in bins of the horizontal axes values. *As shown, the averaged differences in PA increase for galaxies that are rounder in shape, with fainter m_r, lower resolution, and located at higher z.*

to fit PA, while the isophotal shape traces the outermost region of a galaxy along the 25 mag/arcsec^2 isophote. These choices may make the latter two methods more sensitive to artifacts in the de-blending and sky subtraction processes, leading to spurious SA signals. The two dominant systematics that affect the de-blending and sky subtraction processes and further contribute to the PA discrepancy are bright neighbor and crowded field systematics. The bright neighbor systematic arises due to the contamination of light from nearby bright neighbors in the galaxy for which we are attempting to measure a shape. In cluster-like high density regions, the measured galaxy PA could be biased coherently pointing toward the high-density direction due to the intracluster light or due to the fact that the large number of bright galaxies causes a misestimated sky gradient. We refer this second effect as the crowded field systematic.

Below we start by estimating the level of bright neighbor systematic. In the left panel of Fig. 3.10, we show the measured mean absolute PA discrepancy (hereafter, MAPAD) between isophotal and re-Gaussianization shapes as a function of projected sky separation for galaxies that have a bright $m_r < 19$ non-physically associated neighbor, as defined in (iii) of Sec. 3.2.4 (plotted in purple open points). We see that the MAPAD increases to $\sim 27^\circ$ for the innermost sky separation bin, indicating potentially more contamination from bright neighbors at closer sky separation.

Besides systematics, there is also a noise contribution (see Sec. 3.5.1) to the measured MAPAD, which must be estimated in order to properly constrain the level of bright neighbor and crowded field systematics. Note that for the MAPAD data points shown in purple open circles in Fig. 3.10, there is no contribution from a physical effect like isophotal twisting, due to our use of foreground/background galaxies at different redshifts from the bright central galaxies.

To distinguish between bright neighbor systematic and noise, we re-weight the galaxies in our non-cluster field sample (as defined in Sec. 3.2.4, (ii)) to match the distributions of m_r, z, and ellipticity in the sample around bright galaxies used here. This reweighting is done separately within each bin in projected sky separation. We can then record the weighting factors in the m_r-z-ellipticity space, and use these weighting factors to calculate the weighted-MAPAD from galaxies in the non-cluster field sample. The resulting weighted-MAPAD value is then a proper estimation of the noise level for galaxies in each sky separation bin, assuming that those three quantities are the main ones determining the statistical uncertainty in the MAPAD. The triangular data points in both panels of Fig. 3.10 show the resulting estimation of the noise level. The convergence of the triangular points towards the circular points at larger separations appears to validate the assumption behind this method.

After subtracting the noise contribution in the left panel of Fig. 3.10, the remaining signal shown in Fig. 3.11 (purple open circles) should be dominated by MAPAD due to bright neighborhood systematics. This figure shows that for large sky separations ($\gtrsim 0.4'$), the detected MAPAD is consistent with our prediction for the noise. For the innermost bin in sky separation, the excess of MAPAD, $\Delta \langle |\mathrm{PA_{iso}} - \mathrm{PA_{reG}}| \rangle$, increases to $\sim 7^\circ$ for galaxies that have a bright ($m_r < 19$) neighbor. The best-fitting models of the form

$$\Delta \left\langle |\mathrm{PA_{iso/deV}} - \mathrm{PA_{reG}}| \right\rangle = A\ (\text{sky separation})^B \tag{3.11}$$

are provided in the legend of Fig. 3.11, and will later be used to estimate the level of MAPAD due to bright neighbor systematics. The right panel of Fig. 3.11 shows the same results as in the left panel, but for de Vaucouleurs (rather than isophotal) vs. re-Gaussianization shapes. The trends in both panels

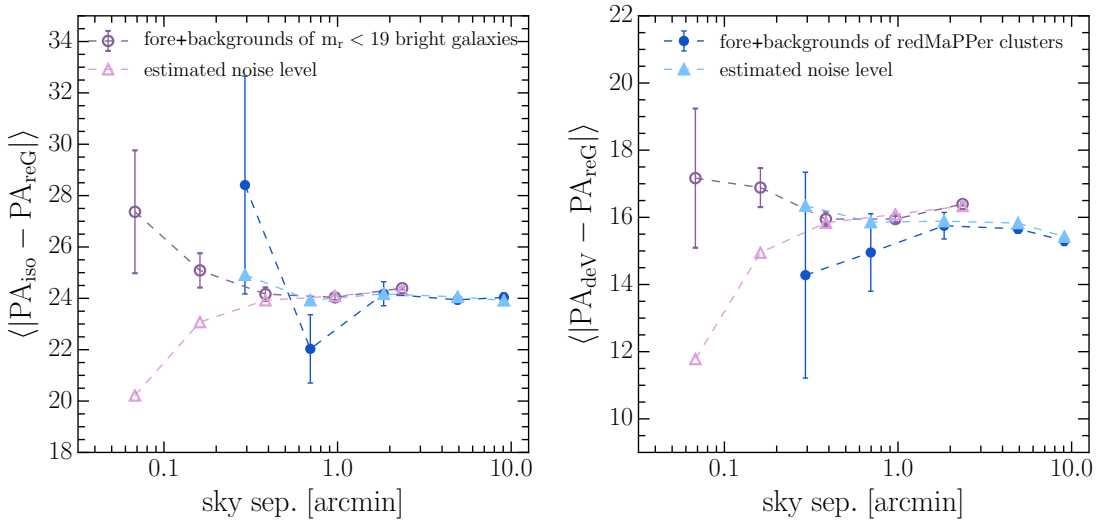

Figure 3.10: Left panel: mean absolute PA differences (MAPAD) between isophotal and re-Gaussianization shapes as a function of projected angular separation on the sky for galaxies that are in the foreground and background of m_r <19 non-cluster field bright galaxies (purple open circle), and for galaxies in the foreground and background of redMaPPer clusters (dark blue filled circle). The lighter color points shown with triangular symbols indicate the estimated $\langle|\mathrm{PA_{iso}} - \mathrm{PA_{reG}}|\rangle$ contribution from noise (see the text for details). Right panel: similar to the left panel but for the MAPAD between de Vaucouleurs and re-Gaussianization shapes, $\langle|\mathrm{PA_{deV}} - \mathrm{PA_{reG}}|\rangle$. *As shown, the MAPAD increases toward small sky separation.*

are similar.

Aside from the simple diagnostics shown here, Mandelbaum et al. (2005) and Aihara et al. (2011) have also pointed out other ways that the imperfect deblending and sky-subtraction can affect the measured properties of the faint galaxy populations around bright galaxies in SDSS DR4 and DR8 photometry pipelines. We conclude that bright neighbor systematic does play some role in the measured MAPAD between different shape measurement methods in the data, and its effect increases for galaxies around brighter neighbors.

We attempt to measure the strength of the crowded field systematic by measuring the MAPADs for foreground and background galaxies of redMaPPer clusters as defined in sample (i) of Sec. 3.2.4. The right panel of Fig. 3.10 shows the resulting estimate, with the estimated noise contribution shown as well. The difference between the two sets of data points, as shown in the blue filled circles in Fig. 3.11, indicates the joint contribution of MAPAD due to both bright neighborhood and crowded field systematics in the redMaPPer cluster field. Unfortunately here we lack pairs at small projected sky separation, resulting in a very noisy estimate of these combined effects.

3.5.3 PA discrepancies due to physical effects

Finally, in the case that a pair of galaxies are physically associated, aside from noise and systematics, some portion of the measured MAPAD could be explained by a real physical effect known as "isophote

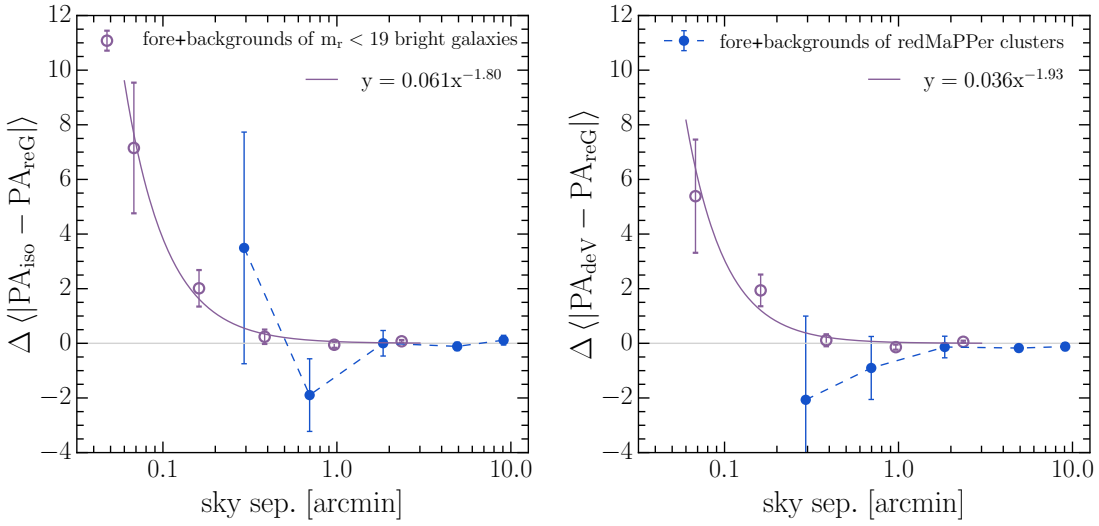

Figure 3.11: Left panel: Excess of mean absolute PA differences (MAPAD) between isophotal and re-Gaussianization shapes caused by bright neighbor or crowded field systematics as a function of projected angular separation on the sky, for galaxies in the foreground and background of m_r <19 (purple open circle) and for galaxies in the foreground and background of redMaPPer (blue filled circle). Right panel: similar to the left panel, but for the excess of MAPAD between de Vaucouleurs and re-Gaussianization shapes. *As shown, the level of bright neighbor and crowded field systematics increases toward small sky separation bins.* The fitted models (see Eq. 3.11) between $\Delta \left\langle |PA_{iso/deV} - PA_{reG}| \right\rangle$ and sky separation are provided in the legend with x = sky separation measured in arcmin and $y = \Delta \left\langle |PA_{iso/deV} - PA_{reG}| \right\rangle$.

twisting" (di Tullio, 1978; Kormendy, 1982). The origin of this phenomenon is that the galaxy outer light profile may be more sensitive to external tidal fields, and hence could show a stronger SA signal compared with its inner light profile.

From N-body simulations, at one halo length scale, Pereira & Bryan (2010) detected a significant amount of isophotal twisting for triaxial galaxies orbiting in a cluster potential (see their Figs. 6 and 8). Also, Tenneti et al. (2015a) found in cosmological hydrodynamic simulations that the measured IA signal at all spatial separations becomes larger when defining galaxy shapes and orientations in a way that emphasizes the outer parts of the galaxy light profile.

Observationally, since the isophotal shape traces the outermost part of the light profile, the measurement based on isophotal shapes should detect the strongest SA signals, followed by de Vaucouleurs and re-Gaussianization shapes, if isophotal twisting is occurring at a significant level. Singh & Mandelbaum (2016) detect a stronger IA amplitude with isophotal shapes than with re-Gaussianization shapes at large separations ($\gtrsim$ 5Mpc). After considering possible systematic errors, they conclude that this difference most likely originates from isophotal twisting.

In this work, since we focus particularly on galaxies in cluster environments, we need to reassess whether systematics may be contributing in a significant way to the measured MAPADs between the two shape measurement methods compared to what was found in Singh & Mandelbaum (2016). Only after doing so can we draw conclusions about possible detections of isophotal twisting.

The effect of isophote twisting should be more intense for galaxies in a stronger gravitational field. Thus we expect to detect a larger MAPAD for satellites located physically closer, not just looked closer in projection, to the centers of clusters. Therefore, in Fig. 3.12, we make similar plots for redMaPPer members (teal green circles) as that shown in Fig. 3.11, but change the x-axis from sky separation to physical projected separation. We process similar noise estimation as what we have done in Fig. 3.10, i.e. by reweighting non-cluster field galaxies to have similar z, m_r, and ellipticity distributions as that of redMaPPer members, but now operate it in bins of physical projected separation. After the removal of noise, the values of y-axis shown in Fig. 3.12 should be caused largely by bright neighbor and crowded field systematics, as well as physical isophote twisting effects. The left panel of Fig. 3.12 is the excess of MAPAD between isophotal and re-Gaussianization shapes, while the right panel plots that between de Vaucouleurs and re-Gaussianization shapes. In the following, we will first try to estimate how much of the excess MAPAD is contributed by the bright neighbor systematic, and then based on that we can judge whether there is leftover isophotal twisting signal.

To estimate what fraction of the excess MAPAD in Fig. 3.12 is due to the bright neighbor systematic, we apply the following procedure: for each central-satellite pair of redMaPPer member, we use its projected sky separation as input in the derived best-fitting $\Delta\left\langle|\mathrm{PA}_{\mathrm{iso/deV}} - \mathrm{PA}_{\mathrm{reG}}|\right\rangle$–(sky separation) relation (in the form of Eq. 3.11) shown in Fig. 3.11 to estimate the level of systematics in cluster field. Next, we take averages for all central-satellite pairs in each physical r bin. The solid purple line in Fig. 3.12 indicates the resulting estimated contribution due to bright neighbor systematics. We observe that at the smallest r bin, the bright neighbor systematic could potentially contribute more than 50% of the measured $\Delta\left\langle|\mathrm{PA}_{\mathrm{iso/deV}} - \mathrm{PA}_{\mathrm{reG}}|\right\rangle$. However, the actual level of bright neighbor systematic in cluster environments could be larger, since the central galaxies have (on average) brighter apparent magnitudes than the sample of non-centrals used to estimate the bright neighbor systematic.

Roughly, the remaining differences in the y-axes between the green dashed and purple solid lines

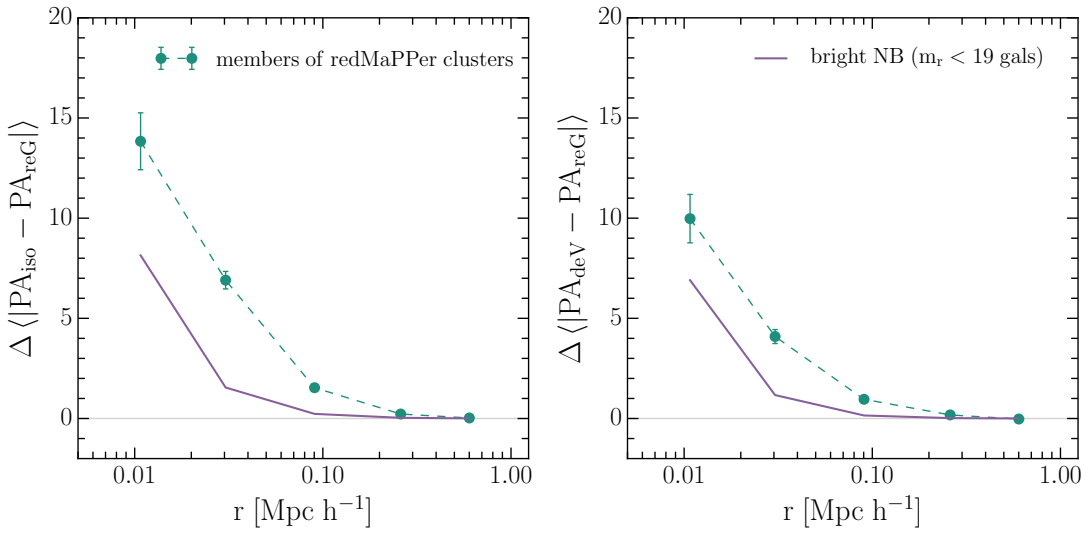

Figure 3.12: Left panel: Excess of mean absolute PA differences (MAPAD) between isophotal and re-Gaussianization shapes, $\Delta\langle|PA_{iso} - PA_{reG}|\rangle$, as a function of projected physical separation for members in redMaPPer clusters (teal green circles). Right panel: similar to the left panel but with $\Delta\langle|PA_{deV} - PA_{reG}|\rangle$ in the y-axis. The purple line is the estimated level of bright neighbor systematic derived using the best-fitting models shown in Fig. 3.11. *We observe that at the smallest r bin, the bright neighbor systematic could potentially contribute more than 50% of the measured* $\Delta\langle|PA_{iso/deV} - PA_{reG}|\rangle$. *Roughly, the remaining differences in the y-axes between the green dashed and purple solid lines are contributed by real physical isophote twisting signal and the crowded field systematic (for which we lack a good estimate), and probably some residual bright neighbor systematic due to the fact that the average apparent magnitude of cluster central galaxies is brighter than that of the galaxy sample used to estimate the bright neighbor systematic.*

are contributed by real physical isophote twisting signal and the crowded field systematic (for which we lack a good estimate). Residual bright neighbor systematic error may also play a role since the average apparent magnitude of cluster central galaxies is brighter than that of the galaxy sample used to estimate the bright neighbor systematic. Unfortunately, we have no good way to empirically estimate the crowded field systematic more accurately, due to the small size of the foreground and background samples in cluster fields. Simulation pipelines associated with future large surveys may be a better tool to estimate and remove various sources of systematic contamination and provide constraints on isophote twisting effects in cluster environments.

3.6 The dependence of satellite alignment on the selected predictors

In Sec. 3.4, we apply linear regression analysis and apply the model averaging technique to identify predictors that have a significant influence on the variation of the SA signal (as summarized in Tables 3.5, 3.6 and 3.7 for different shape measurements). We now address possible reasons for the observed relationship between $\phi_{\rm sat}$ and these selected predictors.

3.6.1 Dependence on satellite luminosity

As shown in Figs. 3.6a and 3.7b, we found that satellite $^{0.1}Mr$ has a very significant influence on the SA signal, with more luminous satellites being more likely to have their long axes oriented toward their host central galaxies.

Our result is consistent with the observation of Hung & Ebeling (2012). Based on high quality HST/ACS data for shape measurement they also detected a statistically significant trend for the dependence of $\langle\phi_{\rm sat}\rangle$ on satellite luminosity (see their Fig. 6) for members in 12 X-ray clusters at $z \sim 0.5$–0.6.

Based on N-body simulations, Pereira et al. (2008) reported that there is no apparent dependence of subhalo alignment signals on the subhalo mass (see their Fig. 3). In a cosmological hydrodynamic simulation, Tenneti et al. (2014) found that the misalignment between a galaxy's own DM subhalo and its luminous component becomes larger for less massive galaxies. Therefore, the observed relationship between $\langle\phi_{\rm sat}\rangle$ and satellite luminosity may be due to this misalignment dependence on luminosity. For faint galaxies, which are typically less massive, they appear to be more randomly oriented because their luminous components are not good tracers of the orientation of their own DM halos.

3.6.2 Dependence on satellite-central distance

Satellite-central distance is another significant factor determining the strength of the SA effect, with satellites located closer to their centrals having a stronger SA signal. Many previous observational studies that have reported detections of SA also found dependence of $\langle\phi_{\rm sat}\rangle$ on satellite-central distance (Pereira & Kuhn, 2005; Agustsson & Brainerd, 2006; Faltenbacher et al., 2007; Siverd et al., 2009; Hung & Ebeling, 2012).

The satellite-central distance dependence naturally reflects the fact that SA is triggered by tidal forces from the DM potential of the host halo. Hence, the strength of the tidal force would be stronger for satellites located closer to the central region of the host halo. However, as discussed in Sec. 3.5.2,

part of this trend could coming from bright neighbor and crowded field systematics, especially for galaxies located near the cluster central region.

From the simulation side, where this radius-dependence can be measured to small scales without observational systematics, Pereira et al. (2008) showed that the relationship between the subhalo SA signal and satellite-central distance is actually non-linear. As shown in their Fig. 4, the SA signal first rises gradually when satellites are closer to cluster center, peaks at around 0.5 times the virial radius, then decreases again toward the center. This is because when falling into the cluster along an eccentric orbit, a subhalo's orbiting speed becomes too fast for the tidal torquing to be effective at the orbital pericenter, so the alignment cannot keep up with the satellite subhalo's own motion (see Fig. 8 of Pereira et al. 2008), leading to the decrease in SA signal at very small radius (see also discussion in Sec. 6 of Kuhlen et al. 2007).

3.6.3 Dependence on satellite ellipticity

We identified a statistically significant SA signal dependence on satellite ellipticity, with rounder satellites exhibiting a stronger tendency to radially point toward their cluster central galaxy. Since it is difficult to accurately determine the PA of a satellite with a round shape, we divide our samples into two ellipticity bins at the boundary of 0.2, and see if the resulting correlation is still strong enough that satellite ellipticity can be selected as an important indicator of the SA effect through the variable selection process. Our result is that this quantity is still selected as a feature predictor. Fig. 3.13 plots the $\langle\phi_{\rm sat}\rangle$ value in bins of satellite ellipticity. We see that the net SA signal is fairly strong for satellites with ellipticity < 0.2 (Fig. 3.13b), and that the detected positive correlation is still quite significant for satellites with ellipticity ≥ 0.2 (Fig. 3.13c).

According to Pereira & Bryan (2010), for galaxies orbiting in cluster potentials, their stellar components tend to become more spherical with time (see their Fig. 18). Also it takes time for satellites to become tidally locked and pointing radially toward central. We propose that the observed correlation between $\langle\phi_{\rm sat}\rangle$ and the ellipticity of satellites reflects this physical picture.

3.6.4 Dependence on the $fracDeV$ parameter

In the work of Siverd et al. (2009), based on a catalog of group-mass systems, they have studied the effect of $fracDeV$, an indicator of a galaxy's bulge fraction, on the SA signal. They reported that the level of SA strength is most strongly dependent on the $fracDeV$ parameter. To compare with their result, we have added $fracDeV$ into our parameter pool for use during the variable selection process.

Our analysis also showed that $fracDeV$ is a statistically-significant predictor for the satellite alignment effect, with de Vaucouleurs profile-dominated (higher bulge fraction) galaxies having stronger SA signal compared to galaxies with exponential dominated-profile (higher disk fraction). As shown in the $\phi_{\rm sat}$-$fracDeV$ plots of Figs. 3.6d and 3.7e, the observed SA signal is mostly coming from satellites with high $fracDeV$ values.

Typically a galaxy with higher luminosity, rounder shape, and redder color tends to have a higher bulge fraction, and thus higher $fracDeV$. Therefore, it is important to ensure that the dependence between $\phi_{\rm sat}$ and $fracDeV$ is not caused by correlations of $fracDeV$ with other parameters. (Although linear regression is a useful tool to break out degeneracies among parameters, since SA is a weak sig-

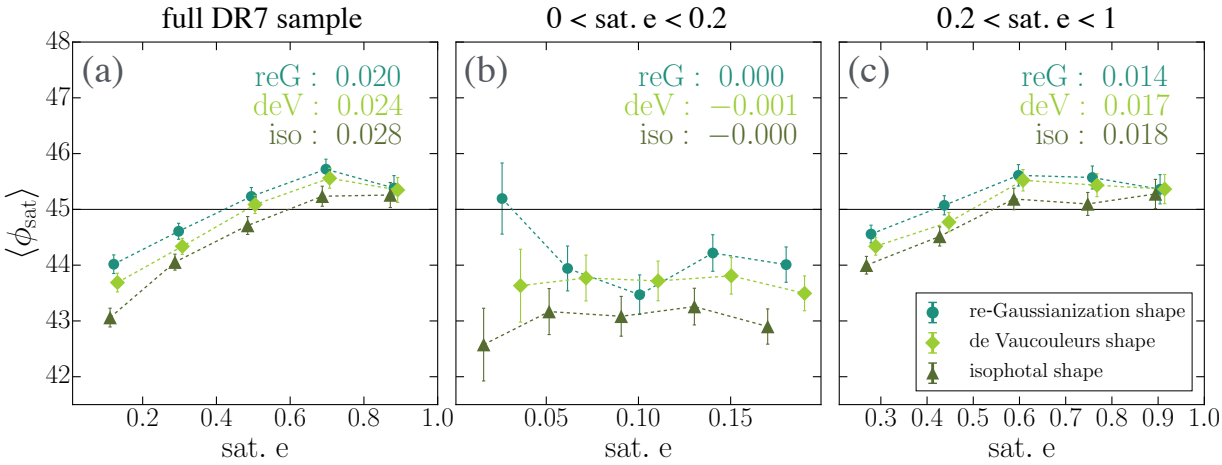

Figure 3.13: The averaged SA angle, $\langle\phi_{\rm sat}\rangle$, in bins of satellite ellipticity. The left panel shows all satellites in our DR7 footprint sample; the middle panel shows only satellites with ellipticity < 0.2, while the right panel shows satellites with ellipticity ≥ 0.2. The correlation coefficients between $\phi_{\rm sat}$ and satellite ellipticity measured in various shapes are provided in the upper right corner for each of subsamples. *We see the observed significant trend of positive correlation in the full satellite sample is still there for satellites with ellipticity* ≥ 0.2*, whose PA (and thus* $\phi_{\rm sat}$*) measurements are more robust.*

nal, we still need to pay extra attention on the possible degeneracy issue.) To check whether $fracDeV$ is a representative parameter with its own distinct effect on $\langle\phi_{\rm sat}\rangle$, we construct five subsamples by excluding satellites of the top 20% most luminous, smallest satellite-central distance, roundest, and reddest color from the parent DR8 sample pool each time. After that, we can check if the remaining 80% of the satellites still exhibit a significant correlation between $fracDeV$ and $\phi_{\rm sat}$. In Fig. 3.14, we plot the averaged $\phi_{\rm sat}$ in bins of $fracDeV$ for these five subsample sets. One can see that although excluding these satellite subsets decreases the overall SA signal strength, the trend between $fracDeV$ and $\langle\phi_{\rm sat}\rangle$ remains similar as in the original full sample. This finding confirms that $fracDeV$ really is a special parameter with its own distinct effect on the SA signal.

We propose that $fracDeV$ is chosen as an important predictor because it encapsulates information about the importance of angular momentum in the dynamics of each galaxy. It has been observed that SA signal only appears in samples of red bulge-dominated galaxies, while blue disky galaxies generally have random orientation within clusters (see e.g. Pereira & Kuhn 2005; Faltenbacher et al. 2007; Siverd et al. 2009 based SDSS isophotal shapes and Hung & Ebeling 2012 based on high quality HST images). Since material in disks has higher angular momentum compared with that in bulges, it becomes less effective to torque disks to align with the surrounding tidal field. According to the N-body simulation results of Pereira & Bryan (2010), galaxies with initial figure rotation generally take longer to become radially aligned than non-rotating galaxies (see their Sec 5.5). Tenneti et al. (2016) also found using cosmological hydrodynamic simulations that the misalignment angle between disky galaxies with the shape of their host DM subhalos is larger compared with ellipticals. In that case, they used an angular-momentum based discriminator for disk vs. elliptical galaxies, so again $fracDeV$ should be relevant.

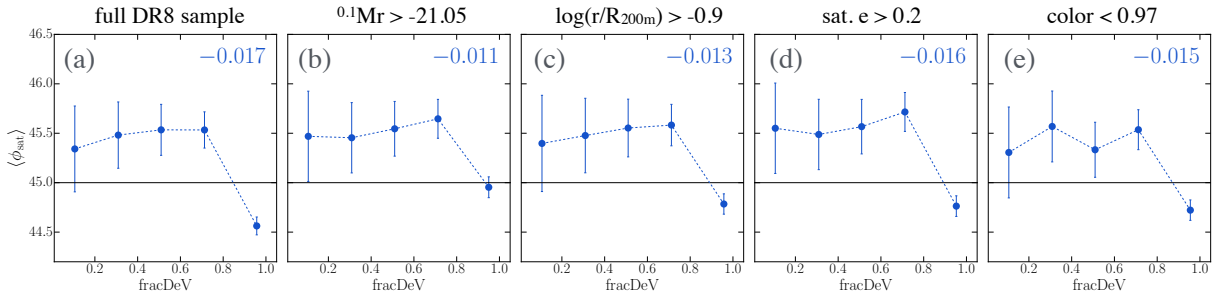

Figure 3.14: The averaged SA angle, $\langle\phi_{\rm sat}\rangle$, in bins of $fracDeV$ for different subsamples of the redMaPPer satellites as indicated in the title of each plot. The correlation coefficient between $\phi_{\rm sat}$ and $fracDeV$ for each subsample is shown in the upper right corner. *After excluding part of satellites with properties that correlate with $fracDeV$, the correlation trend between $fracDeV$ and $\phi_{\rm sat}$ still remains similar as the original full sample. This confirms that $fracDeV$ as its own distinct effect on the SA signal.*

We remind the readers that our work only includes fairly red galaxies, since the redMaPPer members are selected based on the red-sequence method. This may lead to the result that $fracDeV$ (tracing angular momentum) appears to be a more important predictor than color (which directly reflects the gas contain of a galaxy). However, based on hydrodynamical simulations, Debattista et al. (2015) pointed out that "gas" is a key factor affecting the degree of misalignment between a disky galaxy and its own subhalo. A red, gas poor disk can have a stable orientation governed by halo torques, but when there is gas cooling onto a disk, the blue disk could have arbitrary orientations set by the balance between halo torques and angular momentum of the ongoing gas accretion.

3.6.5 Dependence on central galaxy alignment angle $\theta_{\rm cen}$

For de Vaucouleurs and isophotal shapes, we detected a positive correlation between $\phi_{\rm sat}$ and $\theta_{\rm cen}$, with satellites located closer to the central galaxy major axis direction showing a stronger SA signal.

In Paper I, we have explored the angular segregation of satellites in redMaPPer clusters and concluded that the angular segregation may be due to 1) preferential infall of satellites along the filamentary structure aligned with the large-scale primordial tidal field (see Paper I Sec. 6.1) or 2) the newly-established local tidal field produced by the current configuration of satellites which torques centrals to align (see Paper I Sec. 7.3). The observed dependence of $\phi_{\rm sat}$ on $\theta_{\rm cen}$ can also be explained based on the above two scenarios. Assuming that a central galaxy is aligned with its most dominant primordial tidal field, since many satellites are fed into clusters along this direction, some satellites located near the edge of the cluster may still remember their original orientations along this primordial tidal field because of their relatively late entrance into the clusters. Thus, for satellites with small $\theta_{\rm cen}$, it is natural that they will point radially toward central galaxy (Faltenbacher et al., 2008). For the second scenario, if later dynamical evolution has changed the central galaxy's orientation to align with its newly established local tidal field, satellites near cluster central region would also show tendency to align along this tidal field, especially those located at small $\theta_{\rm cen}$, forming a local filamentary structure. Note it is likely that the later local tidal field still follows the direction with its primordial large-scale

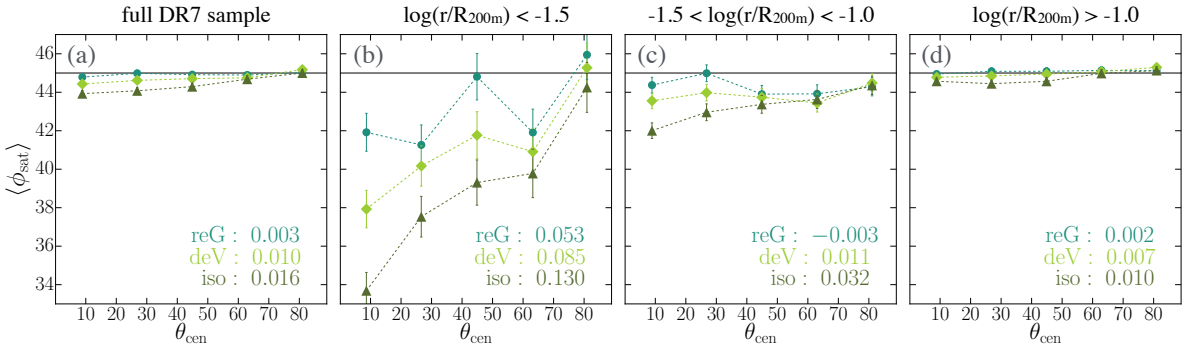

Figure 3.15: The relationship between $\langle\phi_{\rm sat}\rangle$ and $\theta_{\rm cen}$ for the DR7 footprint sample in different satellite-central separation bins as indicated in the title of each plot. The correlation coefficients between $\phi_{\rm sat}$ and $\theta_{\rm cen}$ measured in various shapes are provided in the upper right corner for each of subsamples. *We see that the originally observed significant correlation in the full sample is dominated by satellites located closer to cluster central region.*

tidal field.

One way to check the above scenarios is to look at the correlation between $\theta_{\rm cen}$ and $\phi_{\rm sat}$ for satellites at small and large satellite-central separations, as plotted in Fig. 3.15. We observe that there is almost no signal at the largest $\log(r/{\rm R_{200m}})$ bin (Fig.3.15d). The correlation is mostly driven by satellites at small $\log(r/{\rm R_{200m}})$ bin (Fig.3.15b). Thus if the detected correlation is real, then the local tidal field is the most likely cause for the correlation between $\theta_{\rm cen}$ and $\phi_{\rm sat}$.

Besides the physical origin, the correlation between $\theta_{\rm cen}$ and $\phi_{\rm sat}$ could be induce by systematics. At small satellite-central distances, $\phi_{\rm sat}$ measurements based on de Vaucouleurs and isophotal shapes may suffer from bright neighbor systematic (see Sec. 3.5.2) due to the central galaxies' extended light profiles. Satellites located on the major axes directions of the centrals would be more strongly affected by this systematic. This may be the reason why $\theta_{\rm cen}$ is identified as an important predictor only in de Vaucouleurs and isophotal shape measurements. It therefore remains interesting to check whether we can detect robust dependence between $\theta_{\rm cen}$ and $\phi_{\rm sat}$, especially at small scale, using simulation data in the future.

3.6.6 Dependence on redshift

For the isophotal shape measurements, we observed that there is stronger SA for satellites at lower redshift. As shown in Fig. 3.7f, the correlation coefficient between z and $\langle\phi_{\rm sat}\rangle$ is very small (0.002), but the correlation is still identified using our variable selection procedure.

However, we suspect that the correlation detected in isophotal shapes here may be dominated by systematics. For a galaxy at lower redshift, its 25 mag/arcsec^2 isophote traces a larger area on the sky, and thus would have more fake alignment signal from bright neighbor and crowded field systematics (see Sec. 3.5.2). Besides, the correlation coefficients observed between $\phi_{\rm sat}$ and z measured in re-Gaussianization and de Vaucouleurs shapes are both negative, meaning that satellites at higher redshift show stronger SA signal (although not a strong enough dependence to be identified through our variable selection procedure).

Comparing with other observational work, Hao et al. (2010) also observed an increase of the SA signal toward lower z based on isophotal shape, but detected no SA signal across all redshift bins using de Vaucouleurs shapes. Schneider et al. (2013) reported stronger SA at higher redshift for early-type galaxies in groups based on 2D Sersic model shape measurements.

From the simulation side, Pereira et al. (2008) found that the SA strength increases steadily with time for all of their simulated clusters (see their Fig. 5), suggesting that IA strength within the one-halo regime requires time to develop. This trend is inconsistent with the current best theoretical model for IA of galaxies at large scales. The linear alignment model (Catelan et al., 2001; Hirata & Seljak, 2004b) suggests that IA stems from the primordial tidal field at the time when galaxies form. This implies that later merging or baryonic processes of galaxy evolution may weaken this primordial signal, as shown in the N-body simulation work of Hopkins et al. (2005), who found that the strength of cluster alignments (not galaxy alignments within clusters) decreases at later times.

Currently, our technique is not good enough yet to completely demonstrate proper removal of systematics contamination and measure the evolution of SA signals with redshift robustly. Future exploration on the dependence of SA particularly with redshift is important in a sense that it may have different theoretical origin compared with current large-scale linear alignment model, which needs to be investigated to properly extend the linear alignment model down to smaller scale (see e.g. Schneider & Bridle 2010 for smaller scale IA modeling).

3.7 Summary

In this work, we investigate the radial alignment of satellites in redMaPPer clusters based on three different shape measurement methods: re-Gaussianization, de Vaucouleurs and isophotal shapes. We compare the observed SA signals among these measurements, and explore possible systematic effects. To identify the predictors that are relevant to the variation of the SA signal, we perform linear regressions on all possible models and apply the model averaging technique on a total of 17 physical parameters related to satellite, central galaxy, and cluster properties (see Table 3.2), and quantify the significance of their relationship with the satellite alignment angle, $\phi_{\rm sat}$.

Our main results are summarized as follows:

1. Based on re-Gaussianization shape measurements, which puts more weight on a galaxy's inner light profile, we do not detect any convincing SA signal in the overall $p_{\rm mem} > 0.55$ satellite population of redMaPPer clusters (Fig. 3.2). However, a statistically significant SA signal is observed for the entire sample when using de Vaucouleurs shapes, and the overall SA strength reaches to its strongest level in isophotal shape, which traces the outermost light profile of a galaxy (Fig. 3.4).

2. Despite the lack of detection of satellite alignments for the entire sample, there are nonetheless distinct subpopulations that carry highly significant satellite alignments signals when measuring using re-Gaussianization. The SA strength is strongest for satellites with higher luminosity, located closer to their central galaxies, with smaller ellipticity, and have higher bulge fraction in the light profiles. (Fig. 3.6). We also find that satellites located closer to the major axis directions of their central galaxies show higher SA signal, when using de Vaucouleurs and

isophotal shape measurements for satellite shapes (Fig. 3.7).

3. The selected predictors that show significant influence on the SA effect highlight the roles of tidal torquing mechanism, the primordial pre-infall alignment, the process of violent relaxation in clusters, and the angular momentum of galaxies in causing the observed SA dependences.
4. We discuss possible factors that could cause the observed different strength of SA among these three shape measurement methods (Fig. 3.8), provide an estimate of the noise level and discuss contributions from systematics and physical isophote twisting effect.

Over the past decade, there has been some disagreement in the literature regarding the existence and strength of the SA effect. Here we report detections of SA phenomenon based on a well-understood shape measurement method using nearly 10^4 clusters, which provides great statistical power in constraining SA. We identify the regions of parameter space where SA signals become significant, which in some cases can explain previous reported non-detections (e.g., in measurements dominated by satellites in the regions of parameter space where we also find no significant detection of SA). Our results will be useful in improving IA modeling at small scale, for example by building a more realistic halo model of intrinsic alignments (building on work by Schneider & Bridle, 2010), and further helps constrain systematics from IA in weak lensing analysis. We also discuss possible physical origins of the SA signal based on the galaxy and cluster properties that most strongly predict it, and point out directions for future work with even larger cluster samples that are becoming available with next-generation imaging surveys.

Acknowledgments

We thank Eric Baxter for providing galaxy concentration parameter used in the work, and Sukhdeep Singh for helpful comments and discussions. We also thank Sivaraman Balakrishnan for sharing his view on various model selection criteria. This work was supported by the National Science Foundation under Grant No. AST-1313169 and by NASA ROSES 12-EUCLID12-0004.

3.A The choice of membership probability cut of our sample

There are several considerations driving the choice of $p_{\rm mem}$ cut when defining the sample to use for measuring SA. In general, a higher $p_{\rm mem}$ cut would result in a stronger SA signal because brighter and redder satellites tend to have a higher $p_{\rm mem}$ in redMaPPer, and these galaxies are more likely to point radially toward cluster centers. However, raising the threshold in $p_{\rm mem}$ results in a smaller sample size, and thus larger statistical uncertainty. Setting a lower $p_{\rm mem}$ cut would increase the sample size (reduce statistical errors), but also results in a lower signal due to both the inclusion of lower luminosity satellites which carry less signal, and due to the higher contamination rate from non-cluster members. In this appendix, we attempt to estimate the SA signal and noise as a function of the $p_{\rm mem}$ cut. Based on the observed dependences, we can then determine a $p_{\rm mem}$ cut that maximizes the S/N of SA.

Here we define the signal S to be the weighted averaged SA angle over all potentail central-satellite

pairs indexed i,

$$S = \langle 45^\circ - \phi_{\rm sat} \rangle = \frac{\sum_i w_i (45^\circ - \phi_{{\rm sat},i})}{\sum_i w_i}, \tag{3.12}$$

where w_i is the weighting factor for each central-satellite pair. In practice, we use $w_i = p_{{\rm mem},i}$. We shift $\phi_{\rm sat}$ by 45° such that for pairs with no alignment, their signal $S = 0$. Some of the central-satellite pairs used in our calculation may be contaminated by foreground/background galaxies that are not physically associated with the cluster system. These fake pairs are assumed to contribute nothing to the numerator of Eq. (3.12); in other words, we are ignoring the lensing of background galaxies, which would lead to $\langle \phi_{\rm sat} \rangle > 45^\circ$. We can rewrite Eq. (3.12) as

$$S = \frac{\sum_{\text{real pair},j} w_j (45^\circ - \phi_{{\rm sat},j})}{\sum_i w_i}, \tag{3.13}$$

with the summation in the numerator (indexed j) now including only contributions from real central-satellite pairs. The contaminating pairs do contribute to the denominator, thereby diluting the signal. Under the assumption that the $p_{\rm mem}$ values in the redMaPPer catalogue represent a correct statistical description of cluster membership (but see Zu et al., 2017), the summation $\sum_{\text{real pair},j}$ should be statistically equivalent to $\sum_i p_{{\rm mem},i}$. Also, we find that a linear model is a good description for the relationship between the strength of the SA signal ($45^\circ - \phi_{\rm sat}$) and $p_{\rm mem}$ [5].

With these two simplifications and also putting $w_i = p_{{\rm mem},i}$ in Eq. (3.13), we conclude that the signal S is described as

$$S \propto \frac{\sum_i p_{{\rm mem},i}^3}{\sum_i p_{{\rm mem},i}}. \tag{3.14}$$

The first $p_{{\rm mem},i}$ in the numerator comes from replacing the summation over real central-satellite pairs with the summation over all potential pairs; the second comes from the weight; and the third from the approximation that individual SA signal to lowest order are proportional to $p_{{\rm mem},i}$

For the noise N, we simply apply standard error of the mean as the level of noise here, i.e. $N = \sigma_{\phi_{\rm sat}}/\sqrt{N_{\rm eff}}$. Here the standard deviation of $\phi_{\rm sat}$ ($\sigma_{\phi_{\rm sat}}$) is around 26° per $p_{\rm mem}$ bin, while the the effective number of central-satellite pairs ($N_{\rm eff}$) is ranging from 10^4 to 5×10^4 across various $p_{\rm mem}$ bins. Therefore, the variation in the noise on the measurement of the average $\phi_{\rm sat}$ value with the $p_{\rm mem}$ cut value is mostly driven by the change in $N_{\rm eff}$. We assume that the noise N is proportional to the Poisson noise on the mean value, defined as

$$N \propto \frac{1}{\sqrt{N_{\rm eff}}} = \frac{1}{\sqrt{\sum_i p_{{\rm mem},i}}} \tag{3.15}$$

[5] We have tried fitting the relation between ($45^\circ - \phi_{\rm sat}$) and $p_{\rm mem}$ with linear, quadratic, and other higher order of power law models. Unfortunately, our data does not have the power to constrain more complicated models very well, so we simply apply the linear model here.

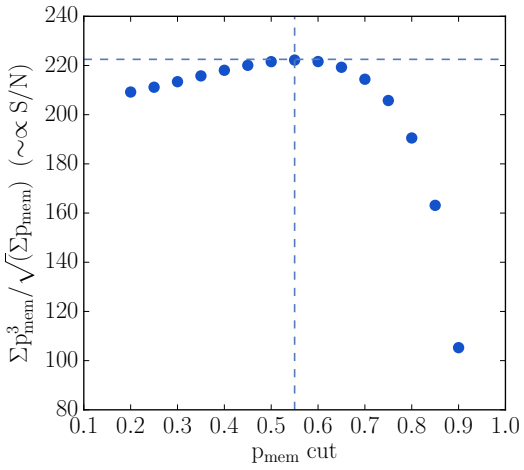

Figure 3.16: Satellite alignment S/N optimization with different $p_{\rm mem}$ thresholds. The S/N is maximized at $p_{\rm mem}$ cut = 0.55. Note that the absolute normalization of the curve is arbitrary; only the relative changes as a function of the $p_{\rm mem}$ cut are meaningful.

The signal to noise ratio S/N would then be proportional to:

$$S/N \propto \frac{\sum_i p_{{\rm mem},i}^3}{\sqrt{\sum_i p_{{\rm mem},i}}}. \tag{3.16}$$

This is a quantity that we can easily calculate for all central-satellite pairs in our catalog, as a function of the lower limit on $p_{\rm mem}$. The results are shown in Fig. 3.16. A $p_{\rm mem}$ cut at 0.55 gives the highest S/N, so we adopt this value throughout our analysis.

3.B Estimating $\langle\phi_{\rm sat}\rangle$ with contamination from background lensing signal

In Fig. 3.6, we saw that there are some subsamples with measured $\langle\phi_{\rm sat}\rangle > 45°$, meaning that satellites in these data bins show a net preferred tangential alignment signal. Part of the excess may come from lensing of galaxies that are actually in the background, because we allow a $p_{\rm mem}$ cut at 0.55 when doing our analysis. Here we provide a rough estimate of the degree of this contamination based on the re-Gaussianization shape results [6].

We begin by defining two quantities: fraction of expected contamination from fake members (f_x) and fraction of expected contribution from true members (f_v). Assuming that the $p_{\rm mem}$ values provide a correct statistical reflection of reality, we can estimate these via summations over all central-satellite

[6]In principle, lensing contamination comes into all shape measurements, but for de Vaucouleurs and isophotal shapes, it is hard to extract the hidden lensing signal due to higher levels of systematics in these shape measurements.

pairs with $p_{\rm mem} > 0.55$, indexed i:

$$f_x = \frac{\sum_i w_i(1 - p_{\rm mem})}{\sum_i w_i} \tag{3.17}$$

$$f_v = \frac{\sum_i w_i(p_{\rm mem})}{\sum_i w_i} \tag{3.18}$$

Here the weighting factor is just $p_{\rm mem}$, and by definition, $f_x + f_v = 1$.

After f_x and f_v are calculated, we can estimate the predicted value of $\langle\phi_{\rm sat}\rangle$ due to background contamination by:

$$\langle\phi_{\rm sat}\rangle_{\rm pred} = f_v \times 44.92 + f_{\rm back} f_x \times 46.07 + (1 - f_{\rm back}) f_x \times 45.0 \tag{3.19}$$

Here $f_{\rm back}$ is a free parameter that controls the fraction of contaminating pairs for which the contaminating galaxy is in the background (while $1 - f_{\rm back}$ is the fraction of contaminating pairs consisting of foregrounds). The predicted $\langle\phi_{\rm sat}\rangle$ value from each component is taken from that shown in the legend of Fig. 3.2. For real cluster members, $\langle\phi_{\rm sat}\rangle = 44.92$; for background pairs $\langle\phi_{\rm sat}\rangle = 46.07$, while for foregrounds, we expect $\phi_{\rm sat}$ to have $\langle\phi_{\rm sat}\rangle = 45.0$. The triangular orange data points shown in Fig. 3.6 are estimated based on setting $f_{\rm back} = 0.6$. Although here we do not have a good estimation for $f_{\rm back}$, we find that the derived $\langle\phi_{\rm sat}\rangle_{\rm pred}$ are all roughly around 45.1°, insensitive to the setting of $f_{\rm back}$ values ranging from 0.5~1.

4 Modeling baryonic physics in future weak lensing surveys

Hung-Jin Huang[1], Tim Eifler[2,3], Rachel Mandelbaum[1] and Scott Dodelson[1]

[1]McWilliams Center for Cosmology, Department of Physics, Carnegie Mellon University, Pittsburgh, PA 15213, USA
[2]Steward Observatory/Department of Astronomy, University of Arizona, 933 North Cherry Avenue, Tucson, AZ 85721, USA
[3]Jet Propulsion Laboratory, California Institute of Technology, Pasadena, CA 91109, USA

Abstract

Modifications of the matter power spectrum due to baryonic physics are one of the major theoretical uncertainties in cosmological weak lensing measurements. Developing robust mitigation schemes for this source of systematic uncertainty increases the robustness of cosmological constraints, and may increase their precision if they enable the use of information from smaller scales. Here we explore the performance of two mitigation schemes for baryonic effects in weak lensing cosmic shear: the PCA method and the halo-model approach in HMcode. We construct mock tomographic shear power spectra from four hydrodynamical simulations, and run simulated likelihood analyses with CosmoLike assuming LSST-like survey statistics. With an angular scale cut of $\ell_{\rm max} < 2000$, both methods successfully remove the biases in cosmological parameters due to the various baryonic physics scenarios, with the PCA method causing less degradation in the parameter constraints than HMcode. For a more aggressive $\ell_{\rm max}$ =5000, the PCA method performs well for all but one baryonic physics scenario, requiring additional training simulations to account for the extreme baryonic physics scenario of Illustris; HMcode exhibits tensions in the 2D posterior distributions of cosmological parameters due to lack of freedom in describing the power spectrum for $k > 10\ h^{-1}$Mpc. We investigate variants of the PCA method and improve the bias mitigation through PCA by accounting for the noise properties in the data via Cholesky decomposition of the covariance matrix. Our improved PCA method allows us to retain more statistical constraining power while effectively mitigating baryonic uncertainties even for a broad range of baryonic physics scenarios.

4.1 Introduction

The origin of the accelerated expansion of the Universe has been one of the most profound mysteries in modern cosmology since its discovery (Riess et al., 1998; Perlmutter et al., 1999). The ΛCDM framework is currently consistent with observations of the expansion history of our Universe from early (Planck Collaboration et al., 2016) to late times (Abbott et al., 2018). Ongoing photometry surveys

such as KiDS (Kilo-Degree Survey[1]), HSC (Hyper Suprime-Cam[2]) and DES (Dark Energy Survey[3]) or future experiments such as LSST (Large Synoptic Survey Telescope[4]), Euclid[5], and WFIRST (Wide-Field Infrared Survey Telescope[6]) experiments aim to constrain cosmological parameters to higher precision and search for deviations from ΛCDM in order to understand the nature of dark energy and General Relativity.

Weak gravitational lensing (WL), the deflection of light by the gravitational potential of cosmic structure, is one of the most promising cosmological probes to discriminate between dark energy models (Weinberg et al., 2013; Mandelbaum, 2018). Tomographic WL measurements, in which galaxy shapes are cross-correlated within and across bins in redshift space (e.g. Hu & Jain 2004), are directly sensitive to structure growth, with secondary dependence on the relative distance ratios. In order to use tomographic WL measurements to constrain cosmological parameters, an accurate model for matter density power spectrum, $P_\delta(k, z)$, is required. It has been estimated that $P_\delta(k, z)$ must be predicted to approximately 1% accuracy for $k \leq k_{\rm max} \sim 10\ h^{-1}$Mpc in order to avoid biasing cosmological parameter constraints in the era of LSST (Huterer & Takada, 2005; Eifler, 2011; Hearin et al., 2012).

In the linear and quasi-linear regime, perturbation theory can be used to calculate the matter power spectra for a set of given cosmological parameters (Bernardeau et al., 2002). On smaller scales, N-body simulations are needed in order to capture the complicated non-linear evolution of structure growth. For example, the Halofit method employs a functional form of $P_\delta(k, z)$ derived from halo models, and calibrates the model parameters from N-body simulations at various cosmological parameters (Smith et al., 2003; Takahashi et al., 2012). Alternatively, the Cosmic emu package emulates $P_\delta(k, z)$ by directly interpolating the N-body simulation results at a range of cosmological models (Heitmann et al., 2010, 2014; Lawrence et al., 2017). However, only gravitational physics is included in these dark-matter-only (DMO) simulations, which neglects any modification of the matter distribution due to baryonic physics processes such as star formation, radiative cooling and feedback (e.g. Cui et al. 2014; Velliscig et al. 2014; Mummery et al. 2017). These processes can modify $P_\delta(k, z)$ by tens of per cent compared to the DMO power spectra from $k \approx 1$ to 10 h^{-1}Mpc at $z = 0$ (van Daalen et al., 2011). The changes in the matter power spectrum due to baryonic physics can affect our inferences on dark energy (e.g. Copeland et al. 2018) and neutrino mass parameters (e.g. Harnois-Déraps et al. 2015) as they have similar effects on part of the power spectrum, but the different scale and redshift dependencies can help in breaking some of the degeneracies.

There are several approaches to mitigating the impact of uncertainty in how the baryonic physics modifies the matter power spectrum. The simplest approach is to eliminate data points that may be severely affected by this uncertainty, so that limitations in small-scale modeling do not bias the inferred cosmology (e.g., see Krause et al. 2017 for the determination of the redshift-dependent angular scale cuts for the DES-Y1 analysis or see Taylor et al. 2018 for another method relating angular scale cuts to physical (k) space). This approach results in a loss of cosmological constraining power, especially

[1]http://www.astro-wise.org/projects/KIDS/
[2]http://hsc.mtk.nao.ac.jp/ssp/
[3]www.darkenergysurvey.org/
[4]http://www.lsst.org/lsst
[5]sci.esa.int/euclid/
[6]http://wfirst.gsfc.nasa.gov/

when the statistical precision of the data increases in the future, resulting in the need for even more conservative scale cuts. A more economical way of discarding data is through peak clipping (Simpson et al., 2011, 2013). By cutting the most extreme peaks in the density fields of both observed and mock data sets, the derived summary statistics become less sensitive to the poorly-modeled non-linear regime, while still allowing the use of a wider range of scales to extract cosmological information (Giblin et al., 2018). Eifler et al. (2015) propose the principal component analysis (PCA) framework (see also Kitching et al., 2016), which utilizes suites of hydrodynamical simulations to build a set of principal components (PCs) describing the modification of the observables by baryonic physics. The first few PC modes point toward directions in observable space where deviation from DMO power spectra due to baryons are most dominant. One can then efficiently remove the vast majority of baryonic uncertainties by discarding the first $3 \sim 4$ PC modes. Mohammed & Gnedin (2018) point out that the training hydro simulations used to construct PCs have to be sufficiently broad in order to offer flexible degrees of freedom to span the possible baryonic scenarios for our Universe.

Other methods focus on modeling the ratio of power spectra that includes baryons to those that do not, with the goal of finding functional forms to describe the range of possible behavior of $P_{\delta,\mathrm{bary}}(k,z)/P_{\delta,\mathrm{DMO}}(k,z)$. Harnois-Déraps et al. (2015) use a parametric form with 15 parameters that is able to describe the power spectrum ratio of several OWLS simulations (van Daalen et al., 2011) to within 10% precision up to $k \approx 20\ h^{-1}$Mpc and $z < 1.5$. Chisari et al. (2018) show that the above parametric form is sufficiently flexible to fit the power spectra ratio in the Horizon-AGN (Dubois et al., 2014) simulation to within 3% across $z \lesssim 4$ up to $k \approx 30\ h^{-1}$Mpc, but with the downside of involving too many free parameters. The authors propose a more compact model with 4 parameters that is capable of providing a fit to Horizon-AGN to within < 5%.

Based on the fact that baryonic physics mainly affects the matter power spectrum by altering the structure of dark matter halos, another proposed approach is to model the deviations in the matter power spectrum through the framework of the halo model (Peacock & Smith, 2000; Seljak, 2000; Cooray & Sheth, 2002). Zentner et al. (2008, 2013) demonstrate that incorporating the halo concentration-mass relation and its redshift evolution into the halo model framework and marginalizing over the associated free parameters can successfully mitigate baryonic bias for Stage III surveys such as DES, but is insufficient for Stage IV experiments. In addition to the degree of freedom that governs halo concentration, Mead et al. (2015, 2016) consider a parameter that characterizes the mass dependence of feedback, with publicly available software available for this model in HMcode[7]. Copeland et al. (2018) further extend HMcode, introducing a core radius parameter to characterize the inner halo structure that is believed to be an outcome of baryonic effects (Martizzi et al., 2012). There are also approaches that go beyond NFW (Navarro-Frenk-White, Navarro et al. 1996) halo profiles, focusing on modeling the radial density distributions of stellar, gas, and DM components of halos to capture the main features of baryonic feedback (Semboloni et al., 2011, 2013; Mohammed et al., 2014; Schneider & Teyssier, 2015; Schneider et al., 2019). The improvement of the halo model approach is an active research area, in particular on constraining the prior range. These halo model approaches potentially enable us to jointly constrain halo structural information and cosmological parameters from data.

Baryonic effects can be mitigated also via a joint analysis through optimized combination of different cosmological probes, as demonstrated in Osato et al. (2015). Finally, a gradient-based

[7]https://github.com/alexander-mead/HMcode

Table 4.1: Basic information for the hydrodynamical simulations used in this work.

Simulation	Box Length	Total Particle #	DM particle mass	initial gas particle mass	force softening length	cosmology
OWLS	100 h^{-1}Mpc	2×512^3	4.06×10^8 $h^{-1}\mathrm{M}_\odot$	8.66×10^7 $h^{-1}\mathrm{M}_\odot$	0.78 h^{-1}kpc	WMAP3
MassiveBlack-II	100 h^{-1}Mpc	2×1972^3	1.1×10^7 $h^{-1}\mathrm{M}_\odot$	2.2×10^6 $h^{-1}\mathrm{M}_\odot$	1.85 h^{-1}kpc	WMAP7
Illustris	75 h^{-1}Mpc	2×1820^3	4.41×10^6 $h^{-1}\mathrm{M}_\odot$	8.87×10^5 $h^{-1}\mathrm{M}_\odot$	1.4 h^{-1}kpc	WMAP7
Eagle	67.77 h^{-1}Mpc	2×1504^3	6.57×10^6 $h^{-1}\mathrm{M}_\odot$	1.23×10^6 $h^{-1}\mathrm{M}_\odot$	1.8 h^{-1}kpc	Planck2013
Horizon-AGN	100 h^{-1}Mpc	2×1024^3	1.1×10^7 $h^{-1}\mathrm{M}_\odot$	2.2×10^6 $h^{-1}\mathrm{M}_\odot$	1.85 h^{-1}kpc	WMAP7

method is proposed recently by Dai et al. (2018). Dark matter particles in N-body simulations are moved along the gradient of estimated thermal pressure to mimic the effect of baryonic feedback. This method can be implemented as a post-processing step on N-body simulations to produce fast hydrodynamical-like simulations.

In this paper, we focus on studying two of the above baryonic mitigation methods – the PCA method and HMcode. We test the effectiveness of these baryonic physics mitigation techniques on a broad range of possible baryonic scenarios by applying them to LSST-like mock observables constructed from hydrodynamical simulations of MassiveBlack-II (Khandai et al., 2015), Illustris (Vogelsberger et al., 2014), Eagle (Schaye et al., 2015), and Horizon-AGN (Dubois et al., 2014), and comparing their cosmological parameter constraints. In addition, for the PCA method, we investigate different ways of constructing the PCs, and provide a modification to the original formalism to improve their efficiency.

This paper is organized as follows. In §4.2, we give an overview on the hydrodynamical simulations used in this work for the construction of our training and test sets. §4.3 describes the setup of our simulated LSST-like likelihood simulations . In §4.4, we provide the detailed theoretical formalism for the baryonic mitigation techniques from literatures and our improved PCA scheme applied in this work. §4.5 presents the main results of the likelihood simulations under various baryonic scenarios and compares the performances of different mitigation methods. We summarize our findings in §4.6, and discuss the prospects of PCA-based methods for future investigation.

4.2 Baryonic Effects in Simulations

In this section, we introduce the hydrodynamical simulations involved in our analysis (summarized in Table 4.1), and compare the impact of the baryonic physics considered on the matter distributions.

4.2.1 OWLS Simulation Suite

The OWLS simulations are a large suite of cosmological hydrodynamical simulations with varying implementations of subgrid physics to enable investigations of the effects of altering or adding a single physical process on the total matter distribution (Schaye et al., 2010). Here we adopt 9 different baryonic simulations from OWLS. We refer readers to van Daalen et al. (2011) for a more detailed description.

- REF: The baseline simulation that contains many of the physical processes known to be important for galaxy formation except for the AGN feedback mechanism. REF includes prescriptions

of radiative cooling and heating for 11 different elements, star formation assuming the Chabrier (2003) stellar initial mass function (IMF), stellar evolution, mass loss, chemical enrichment, and SN feedback in kinetic form (wind mass loading factor $\eta = 2$ and initial wind velocity $v_w = 600$ km s^{-1} ; all together ηv_w^2 determines the energy injected into the winds per unit stellar mass). The other 8 hydro simulations are based on REF, with modifications indicated below.

- NOSN: Exclude SN feedback.
- NOZCOOL: Exclude metal-line cooling. Only assume primordial abundances when computing cooling rates.
- NOSN_NOZCOOL: Exclude both SN feedback and metal-line cooling.
- WML1V848: Adopt the same SN feedback energy per unit stellar mass as for REF, but reduce the mass loading factor by a factor of 2 ($\eta = 1$) and increase the wind velocity by a factor of $\sqrt{2}$ ($v_w = 848$ km s^{-1}).
- WDENS: Adopt the same SN feedback energy per unit stellar mass as that of REF, but let η and v_w depend on gas density ($v_w \propto n_H^{1/6}$; $\eta \propto n_H^{-1/3}$).
- WML4: Double SN feedback per unit stellar mass by increasing the mass loading factor by a factor of 2 ($\eta = 4$).
- DBLIMFV1618: Once the gas reaches a certain pressure threshold, 10% of the star formation activity follows a top-heavy IMF. In this case, more high-mass stars are produced, which leads to higher SN energy feedback.
- AGN: In addition to physics included in the REF model, add a subgrid model for BH evolution and AGN feedback following the prescription of Booth & Schaye (2009). BHs inject 1.5% of the rest mass energy of the accreted gas into the surrounding matter in the form of heat.

The simulation cube for OWLS is $L = 100\,h^{-1}$Mpc in comoving scale on a side. The OWLS-DMO simulation contains 512^3 collisionless DM particles; the 9 hydro simulations contain an additional 512^3 particles in the form of collisional gas or collisionless stars to capture the baryonic processes. The DM and (initial) gas particle masses are $\approx 4.06\times10^8\,h^{-1}\mathrm{M}_\odot$ and $8.66\times10^7\,h^{-1}\mathrm{M}_\odot$, respectively. The gravitational softening length is $\epsilon \approx 0.78\,h^{-1}$kpc in comoving scale, and is limited to a maximum physical scale of $2\,h^{-1}$kpc. The cosmological parameters used in the simulation are based on WMAP3 results (Spergel et al., 2007): $\{\Omega_m,\ \Omega_b,\ \Omega_\Lambda,\ \sigma_8,\ n_s,\ h\} = \{0.238, 0.0418, 0.762, 0.74, 0.951, 0.73\}$.

The OWLS simulation sets are not specifically fine-tuned to match with key observables. As indicated in McCarthy et al. (2017), the original OWLS models underpredict the abundance of $M_* < 10^{11}\mathrm{M}_\odot$ galaxies at the present day due to overly efficient stellar feedback (see their Fig. 1). The successor BAHAMAS simulation lowers the wind velocity v_w from 600 to 300 km s^{-1} in order to provide a better fit to the observed abundance of low-to-intermediate mass galaxies.[8]

[8]Due to the low resolution of BAHAMAS, we are not able to include it as one of the hydrodynamical scenarios in this work (see Appendix 4.B.2 for details of our resolution requirement).

4.2.2 Eagle Simulation

The Eagle simulation (Schaye et al., 2015) is conducted in a cubic periodic box of side length $L = 67.77\ h^{-1}$Mpc (comoving). There are 1504^3 DM particles in both hydrodynamical and DMO simulations, and an approximately equal number of baryonic particles in the hydrodynamical run. The mass of each DM particle is $6.57 \times 10^6\ h^{-1}\mathrm{M}_\odot$ and the initial baryonic mass resolution is $1.23 \times 10^6\ h^{-1}\mathrm{M}_\odot$. The gravitational softening length is $\epsilon = 1.8\ h^{-1}$kpc in comoving units (The EAGLE team, 2017). The cosmological parameters used in Eagle are consistent with Planck 2013 results (Planck Collaboration et al., 2014): $\{\Omega_\mathrm{m},\ \Omega_\mathrm{b},\ \Omega_\Lambda,\ \sigma_8,\ n_\mathrm{s},\ h\} = \{0.307, 0.04825, 0.693, 0.8288, 0.9611, 0.6777\}$.

The subgrid physics used in Eagle is based on OWLS. The physical models include radiative cooling and photoionization heating; star formation associated with stellar mass loss and energy feedback; BH mergers, gas accretion, and AGN feedback. The most important changes compared to OWLS are: star forming feedback energy changing in terms of thermal form rather than kinetic; accounting for angular momentum during the accretion of gas onto BHs; inclusion of a metallicity-dependence in the star formation law. In contrast to many hydrodynamical simulations, Eagle employs stellar and AGN feedback only in thermal form, which captures the collective effects of mechanisms such as stellar winds, radiation pressure, SN feedback, radio- and quasar-mode AGN feedback. One major improvement in the treatment of thermal feedback is that it can be performed without turning off radiative cooling and hydrodynamical forces.

The galaxy stellar mass function of Eagle matches extremely well with observations at $z = 0.1$, because its stellar and AGN feedback related parameters are specifically calibrated at each resolution to reproduce this observable (see Crain et al. 2015; Schaye et al. 2015 for details of calibration philosophy).

4.2.3 MassiveBlack-II Simulation

The MassiveBlack-II (hereafter MB2) simulation is a high-resolution ΛCDM cosmological simulation (Khandai et al., 2015). Both DMO (Tenneti et al., 2015b) and hydrodynamical MB2 simulations are conducted in a cubic simulation box with sides of length $L = 100\ h^{-1}$Mpc in comoving scale. There are 1972^3 DM particles in both the MB2-hydro and MB2-DMO simulations, with an additional 1972^3 initial number of gas particles in the hydro run. The mass of each DM particle is $1.1 \times 10^7\ h^{-1}\mathrm{M}_\odot$ and the initial baryonic mass resolution is $2.2 \times 10^6\ h^{-1}\mathrm{M}_\odot$. The gravitational softening length is $\epsilon = 1.85\ h^{-1}$kpc in comoving units. The cosmological parameters in MB2 are consistent with WMAP7 results (Komatsu et al., 2011): $\{\Omega_\mathrm{m},\ \Omega_\mathrm{b},\ \Omega_\Lambda,\ \sigma_8,\ n_\mathrm{s},\ h\} = \{0.275, 0.046, 0.725, 0.816, 0.968, 0.701\}$.

The subgrid models of baryonic physics in MB2 includes a multiphase interstellar medium model with star formation and associated feedback by SN and stellar winds (Springel & Hernquist, 2003); BH accretion, merger, and associated AGN feedback in quasar-mode (Di Matteo et al., 2005; Springel et al., 2005).

The AGN feedback efficiency of MB2 is relatively weak compared with other hydrodynamical simulations that have AGN subgrid physics involved in this work. One outcome of this is that MB2 overpredicts the abundance of massive galaxies at low redshift (Khandai et al., 2015).

4.2.4 Illustris Simulation

The Illustris simulation (Vogelsberger et al., 2014) is carried out in a cubic periodic box with sides of length $L = 75\ h^{-1}$Mpc (comoving). We download the highest resolution snapshot data from the public release website (Nelson et al., 2015) to calculate power spectra for both hydrodynamical and DMO runs. There are 1820^3 DM particles in both hydrodynamical and DMO simulations, and an approximately equal number of baryonic particles in the hydrodynamical run. The mass of each DM particle is $4.41 \times 10^6\ h^{-1}\mathrm{M}_\odot$ and the initial baryonic mass resolution is $8.87 \times 10^5\ h^{-1}\mathrm{M}_\odot$. The gravitational softening length is $\epsilon = 1.4\ h^{-1}$kpc in comoving units. The cosmological parameters adopted in Illustris are consistent with WMAP7 results (Komatsu et al., 2011): $\{\Omega_\mathrm{m},\ \Omega_\mathrm{b},\ \Omega_\Lambda,\ \sigma_8,\ n_\mathrm{s},\ h\} = \{0.2726, 0.0456, 0.7274, 0.809, 0.963, 0.704\}$.

Illustris incorporates a broad range of galaxy formation physics (Vogelsberger et al., 2013): gas cooling in primordial and metal-lines; stellar evolution associated with chemical enrichment and stellar mass-loss; kinetic stellar feedback driven by SN; BH accretion, merging, and related AGN feedback in terms of quasar- and radio-modes as well as associated radiative electromagnetic feedback.

Illustris is run using the moving-mesh-based code AREPO (Springel, 2010), which is more efficient in cooling compared with classical particle-based SPH codes (e.g. Springel 2005). The energy input from feedback is designed to be strong to avoid efficient stellar mass buildup. Even with this setting, Illustris still overshoots the observed low redshift stellar mass function on both high and low mass ends. The radio-mode AGN feedback is also too violent for the gas component, under predicting the baryon content in lower-redshift high mass halos where the radio-mode feedback is the dominant heating channel (Genel et al., 2014; Haider et al., 2016). The successor IllustrisTNG simulation replaces the intense thermal energy dump of radio-mode feedback with kinematic kicks to heat up affected gas particles (Weinberger et al., 2018).

4.2.5 Horizon-AGN Simulation

The Horizon-AGN (Dubois et al., 2014) is carried out in a cubic periodic box of side length $L = 100\ h^{-1}$Mpc (comoving). There are 1024^3 DM particles in both the DMO and hydrodynamical runs, with the DM particle mass of $9.9 \times 10^7\ h^{-1}\mathrm{M}_\odot$ for the DMO run, and $8.3 \times 10^7\ h^{-1}\mathrm{M}_\odot$ for the hydrodynamical run. The initial gas particle mass is about $1 \times 10^7\ h^{-1}\mathrm{M}_\odot$. The cosmological parameters used in the simulation are compatible with WMAP7 cosmology (Komatsu et al., 2011): $\{\Omega_\mathrm{m},\ \Omega_\mathrm{b},\ \Omega_\Lambda,\ \sigma_8,\ n_\mathrm{s},\ h\} = \{0.272, 0.045, 0.728, 0.81, 0.967, 0.704\}$.

Subgrid physics models for a variety of baryonic physics effects are implemented in Horizon-AGN. Gas is allowed to cool down to 10^4 K via transition lines of hydrogen and helium as well as metals using the Sutherland & Dopita 1993 model. When the hydrogen number density exceeds a threshold of 0.1 H cm^{-3}, star formation is triggered following a random Poisson process (Rasera & Teyssier, 2006; Shandarin & Zeldovich, 1989). SN feedback is taken into account assuming an IMF with a low-mass cut-off at 0.1 $\mathrm{M}_\odot$ and a high-mass cut-off at 100 $\mathrm{M}_\odot$. Chemical enrichment happens along with SN explosions and stellar winds. The AGN feedback is modeled in a combination of two different modes: the kinematic radio mode when $\dot{M}_\mathrm{BH}/\dot{M}_\mathrm{Edd} < 0.01$ and the thermal quasar mode otherwise (Dubois et al., 2012).

Although Horizon-AGN is not specifically tuned to reproduce the galaxy stellar mass function

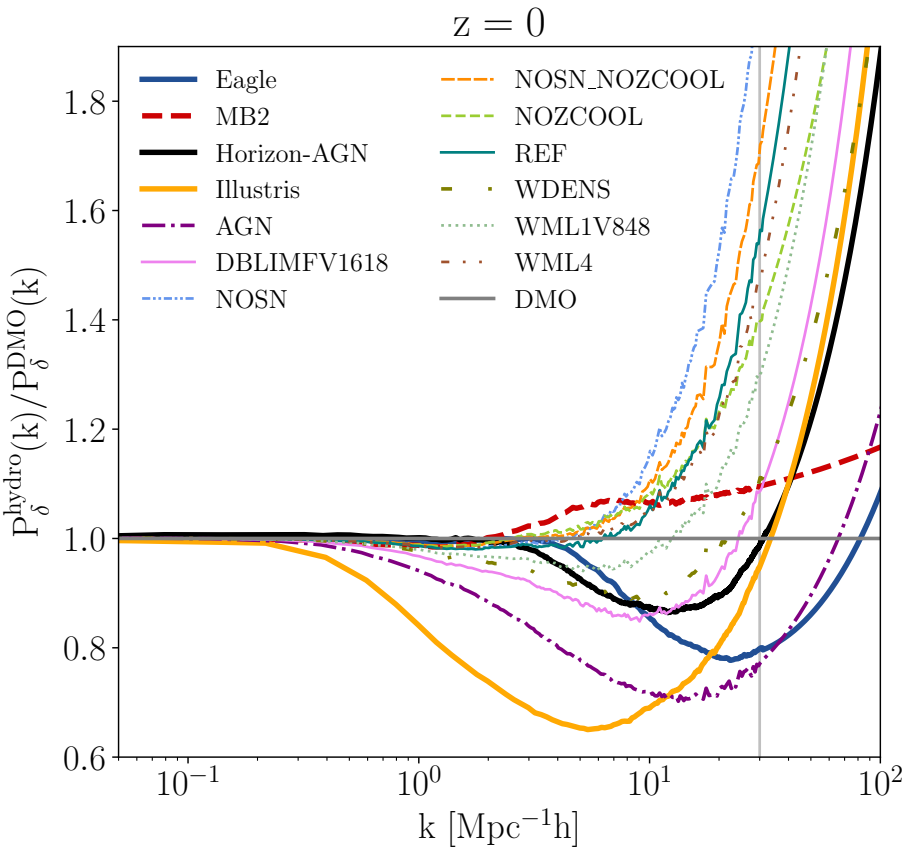

Figure 4.1: The ratios of the matter power spectra in different hydrodynamical simulations with respect to their counterpart DMO simulations at $z = 0$. The thick lines show results for the Eagle, MB2 and Illustris simulations, while the thin lines indicate the 9 different baryonic scenarios in OWLS simulation suite. The gray vertical line separates between regions where the data points come from direct measurement ($k \lesssim 30\ h^{-1}$Mpc) and from extrapolation with a quadratic spline fit ($k \gtrsim 30\ h^{-1}$Mpc; see Appendix 4.B for further details).

at local Universe, it shows reasonable consistency with observations, with slight overproduction of galaxies at the low mass end (Kaviraj et al., 2017).

4.2.6 Comparison of Power Spectra in Hydrodynamical versus DMO Simulations

From the snapshot data release of Eagle, MB2 and Illustris, we calculate the matter power spectra as detailed in Appendix 4.A. For OWLS and Horizon-AGN simulations, we use the computed results from van Daalen et al. (2011) and Chisari et al. (2018), respectively. Power spectra from DMO simulations, with the same initial condition as their paired hydrodynamical simulations, are also computed in order to perform a fair comparison across simulations with different cosmological parameters and with reduced cosmic variance. For each paired simulation set, only a single realization was available to construct the power spectrum ratio.

Figure 4.1 shows the $z = 0$ ratio of power spectra from different hydrodynamical simulations with

respect to their counterpart DMO simulations. The thin lines indicate the nine different baryonic scenarios in the OWLS simulation suite. For the eight baryonic scenarios without AGN feedback, the common feature is a rapid increase in power on small scales. The power enhancement is due to efficient cooling of gas which eventually leads to formation of galaxies within halos, and further concentrates the DM distribution (Blumenthal et al., 1986). Simulations without SN feedback (NOSN, NOSN_NOZCOOL) tend to have an even stronger increase in power compared to the reference simulation REF due to the enhanced cooling effect. When adding AGN feedback to REF, the power is suppressed dramatically, with 1% reduction for $k \approx 0.3\ h^{-1}$Mpc and exceeding 10% for $k \gtrsim 2\ h^{-1}$Mpc (van Daalen et al., 2011). The suppression of power is due to baryons being pushed outward by the energetic AGN feedback processes.

The thick lines represent power spectra ratio for Eagle, MB2, Illustris and Horizon-AGN simulations. Although they all involve a broad range of astrophysical processes that are believed to be relevant to galaxy formation, the resulting power spectra show significant differences. The feedback mechanism in Illustris drastically suppresses the power by 35% at $k \approx 5\ h^{-1}$Mpc. Eagle reaches its maximum suppression of power of 20% at $k \approx 20\ h^{-1}$Mpc. A similar trend is also observed in Horizon-AGN, but it reaches its minimum amplitude reduction of 10% at $k \approx 10\ h^{-1}$Mpc. Going towards higher k, we start to see that the ratio curves bend upward and keep increasing beyond k of 30 h^{-1}Mpc. The MB2 power spectrum behaves relatively similar to DMO, but still the baryonic prescription prevents the power spectrum ratio from growing too quickly compared to the OWLS scenarios without AGN feedback, which suffer from severe overcooling effect (e.g. Tornatore et al. 2003; McCarthy et al. 2011).

The input cosmologies ($\boldsymbol{p}_{\rm co,sim}$) for the five simulation suites are different. In order to predict matter power spectra with baryonic effects for arbitrary cosmological parameters, we take the power spectrum ratios shown Fig. 4.1 and apply the following equation:

$$P_\delta^{\rm hydro}(k, z \mid \boldsymbol{p}_{\rm co}) = \frac{P_\delta^{\rm hydro,sim}(k, z \mid \boldsymbol{p}_{\rm co,sim})}{P_\delta^{\rm DMO,sim}(k, z \mid \boldsymbol{p}_{\rm co,sim})} P_\delta^{\rm theory}(k, z \mid \boldsymbol{p}_{\rm co})\,, \tag{4.1}$$

where $P_\delta^{\rm hydro,sim}(k, z \mid \boldsymbol{p}_{\rm co,sim})$ denotes the hydrodynamical run from a given simulation; $P_\delta^{\rm DMO,sim}(k, z \mid \boldsymbol{p}_{\rm co,sim})$ is the corresponding DMO run; $P_\delta^{\rm theory}(k, z \mid \boldsymbol{p}_{\rm co})$ is the theoretical power spectrum calculated from Halofit (Takahashi et al., 2012) or HMcode (Mead et al., 2015), which are calibrated by DMO simulations.

Eq. (4.1) illustrates the most important assumption in this work: we assume that baryonic effects on the power spectrum can be represented as a fractional change in the power spectrum, and that this fractional change is independent of cosmology. The cosmology enters our analysis only through the theoretical power spectrum $P_\delta^{\rm theory}(k, z \mid \boldsymbol{p}_{\rm co})$. This is a reasonable assumption. According to van Daalen et al. (2019), the power spectrum ratio remains more or less the same when varying cosmologies (see their Fig. 6).

4.3 Likelihood Analysis Methodology

Here we present our methodology in estimating the cosmological constraining power for an LSST-like survey. We start by describing the theoretical models used in the work, our mock observations,

the covariance matrix constructed for an LSST-like survey, and finally the likelihood formalism used in estimating the posterior distribution of cosmological parameters. The cosmological model considered in our likelihood simulation is flat wCDM, with varying cosmological parameters $\boldsymbol{p}_{\rm co} = \{\Omega_{\rm m},\ \sigma_8,\ \Omega_{\rm b},\ n_{\rm s},\ w_0,\ w_{\rm a},\ h\}$.

4.3.1 Theoretical Models

We rely on two main theoretical models to fit our mock observables in this work. The first one is the Takahashi et al. (2012) version of Halofit. It adopts empirically-motivated functional forms to characterize the variation of power spectra with cosmology. Having been calibrated with high-resolution N-body simulations, it provides an accurate prediction of the nonlinear matter spectrum with 5% precision at $k \leq 1\ h^{-1}$Mpc and 10% at $1 \leq k \leq 30\ h^{-1}$Mpc within the redshift range of $0 \leq z \leq 10$.

The second fitting routine is HMcode, constructed by M15. It utilizes the halo-model formalism to describe the cosmological change of power spectra via physically motivated parameters. HMcode has prescriptions for capturing the impact of baryons on the matter power spectrum via two free parameters: the amplitude of the concentration-mass relation (A; see Eq. (14) in M15), and a halo bloating parameter (η_0; see Eqs. (26), (29) in M15) controlling the change of dark matter halo profiles in a halo mass-dependent way to account for different feedback energy levels. When allowing A and η_0 to vary, it can successfully fit the power spectra from various baryonic scenarios of OWLS (M15). When fixing $A = 3.13$ and $\eta_0 = 0.6044$, HMcode functions as a regular DMO-based emulator, which is calibrated with high-resolution N-body simulations to an accuracy of $\approx 5\%$ at $k \leq 10\ h^{-1}$Mpc for $z \leq 2$. We note that the $\approx 5\%$ discrepancy between the DMO mode of HMcode and Halofit is non-negligible within LSST statistics. We therefore construct two sets of mock observables based on each theoretical model.

4.3.2 Mock Observational Data

We rely on four hydrodynamical simulations: Eagle, MB2, Illustris and Horizon-AGN to construct mock observables, and investigate the performances of the PCA method (Eifler et al., 2015, hereafter E15) and the halo model approach (Mead et al., 2015, hereafter M15) on mitigating baryonic effects. These methods will be described in more detail in §4.4. For simplicity, besides baryonic effects, our mock data vectors do not include any other source of noise or systematics.

We consider tomographic weak lensing shear power spectra as the summary statistics. These are defined as:

$$C^{ij}(\ell) = \frac{9H_0^4\Omega_m^2}{4c^4}\int_0^{\chi_{\rm h}} {\rm d}\chi \frac{g^i(\chi)g^j(\chi)}{a^2(\chi)} P_\delta\left(\frac{\ell}{f_K(\chi)}, \chi\right)\ . \tag{4.2}$$

Here $C^{ij}(l)$ is the convergence power spectrum for tomographic bin combination $\{i, j\}$ at angular wavenumber l, χ is the comoving distance, $\chi_{\rm h}$ is the comoving horizon distance, $f_K(\chi)$ is the comoving angular diameter distance (set to χ since we assume a flat Universe), $a(\chi)$ is the scale factor, and P_δ is the 3D matter power spectra. The lens efficiency in the i-th tomographic interval is defined as

$$g^i(\chi) = \int_\chi^{\chi_{\rm h}} {\rm d}\chi' n^i(\chi')\frac{f_K(\chi'-\chi)}{f_K(\chi')} \tag{4.3}$$

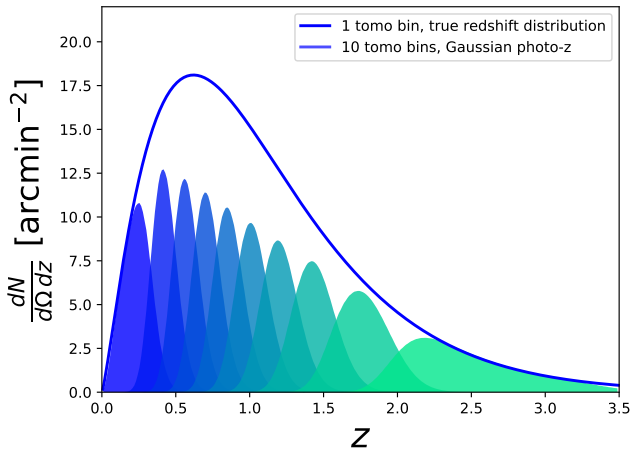

Figure 4.2: The normalized galaxy number density split into ten Gaussian tomographic photo-z bins as shaded regions from blue (low z) to green (high z). For comparison, we show the true underlying redshift distribution as a solid blue line.

with $n^i(\chi'(z))$ being the redshift distribution of source galaxies in tomographic bin i. The overall source redshift distribution is parametrized in the form of

$$n(z) \propto z^\alpha \exp\left[-\left(\frac{z}{z_0}\right)^\beta\right], \tag{4.4}$$

where $\alpha = 1.27$, $\beta = 1.02$, and $z_0 = 0.5$ following Table 2 in Chang et al. (2013), which mimics an LSST cosmic shear source galaxy sample after deblending. The number density of source galaxies is 26/arcmin^2.

We perform a tomographic analysis by dividing the sources into 10 tomographic bins with equal total number of galaxies in each bin. We also smooth the redshift distribution with a Gaussian kernel to characterize potential photo-z uncertainties. Fig. 4.2 shows the exact redshift distribution in each bin. This results in 55 unique combinations of auto- and cross- correlation shear tomographic power spectra. For each of the tomographic power spectra, we consider 18 equally spaced logarithmic bins in angular wavenumber ℓ ranging from $23 \sim 2060$. This results in a total of $55 \times 18 = 990$ data points in our data vector. For the main analysis of this paper, we adopt an upper limit of $\ell_{\rm max} \approx 2000$. This limit is driven by the resolution of the hydrodynamical simulations used in this work. We refer readers to Appendix 4.B for further details on how we extrapolate power spectra to perform the integration to derive $C^{ij}(\ell)$, and how the decision on the $\ell_{\rm max} \approx 2000$ cut is made.

The fiducial cosmology $\boldsymbol{p}_{\rm co,fid}$ of the data vectors is set to be consistent with the Planck 2015 (TT+TE+EE+lowP and assuming ΛCDM) results (Planck Collaboration et al., 2016) as summarized in Table 4.2.

Our mock data vectors for various baryonic physics scenarios are computed with the P_δ term in Eq. (4.2) generated from Eq. (4.1). Since Halofit and HMcode (in DMO mode) agree at the level of $\lesssim 5\%$ to $k = 10\ h^{-1}$Mpc, and $\lesssim 10\%$ out to $k \leq 100\ h^{-1}$Mpc (see Fig. 4 of M15), we create two sets of Eagle/MB2/Illustris/Horizon-AGN data vectors, with $P_\delta^{\rm theory}(k, z \mid \boldsymbol{p}_{\rm co,fid})$ generated from Halofit

Table 4.2: Fiducial cosmology, minimum and maximum of the flat prior on the cosmological parameters, and halo-structural parameters in HMCODE.

Parameter	Fiducial	Prior
Ω_m	0.3156	flat (0.05, 0.6)
σ_8	0.831	flat (0.5, 1.1)
n_s	0.9645	flat (0.84, 1.06)
w_0	-1.0	flat (-2.1, 0.0)
w_a	0.0	flat (-2.6, 2.6)
Ω_b	0.0049	flat (0.04, 0.055)
h_0	0.6727	flat (0.4, 0.9)
A	-	flat (0.5, 10)
η_0	-	flat (0.1, 1.2)

or HMCODE, and incorporate the baryonic features through the power spectrum ratio. Throughout our experiment, when relying on HALOFIT or HMCODE as the theoretical model to perform fitting, we use the same fitting function to generate the mock observational data vectors for the fiducial cosmology. This way, when comparing the performance of different baryonic mitigation schemes, if one of the methods fails to recover the fiducial cosmological parameters, we can be assured that this failure is purely because of that method's inability to mitigate the modification of the matter power spectrum due to baryonic physics, not because of an inherent discrepancy between the mock data and the DMO matter power spectrum model.

In Fig. 4.3 we show the ratio of baryonic to DMO $C^{00}(\ell, \boldsymbol{p}_{\rm co,fid})$ shear power spectrum for various simulations. The thin lines indicate the nine baryonic scenarios from the OWLS simulation suite. The thick lines represent the Eagle/MB2/Illustris/Horizon-AGN universes, which are the data vectors that we will use for the LSST-like experiment. One can see that in this lowest tomographic bin, even for large scales at $\ell \approx 100$, the baryonic scenario of Illustris already causes a deviation from DMO at the 5% level, with even more severe suppressions at smaller angular scales. For higher redshift tomographic bins, the deviations between hydrodynamical and DMO simulations are less severe. Semboloni et al. (2011) showed that a scale cut of $\ell_{\rm max} \approx 500$ would be needed to avoid w_0 bias for a Euclid-like survey if the baryonic scenario of our Universe is like OWLS-AGN. When applying the traditional way of mitigating baryonic uncertainty by omitting small scale information, we would need to discard a considerable amount of data before we can rely on DMO-based theoretical model to achieve an unbiased cosmological inference.

One subtle feature shown in Fig. 4.3 is that there is a small but noticeable large-scale excess of power ($< 0.4\%$) in the Horizon-AGN simulation. This is because the power spectrum ratio between hydrodynamical and DMO runs of Horizon-AGN has $< 0.1\%$ excess at large scales (see Fig. 4.1), even though they share the same initial conditions. The true cause of this subtle excess is not clear. After exploring, Chisari et al. (2018) concluded that this may originate from the box being too small to reach the linear regime at large scales. However, the other simulations studied here are similar in

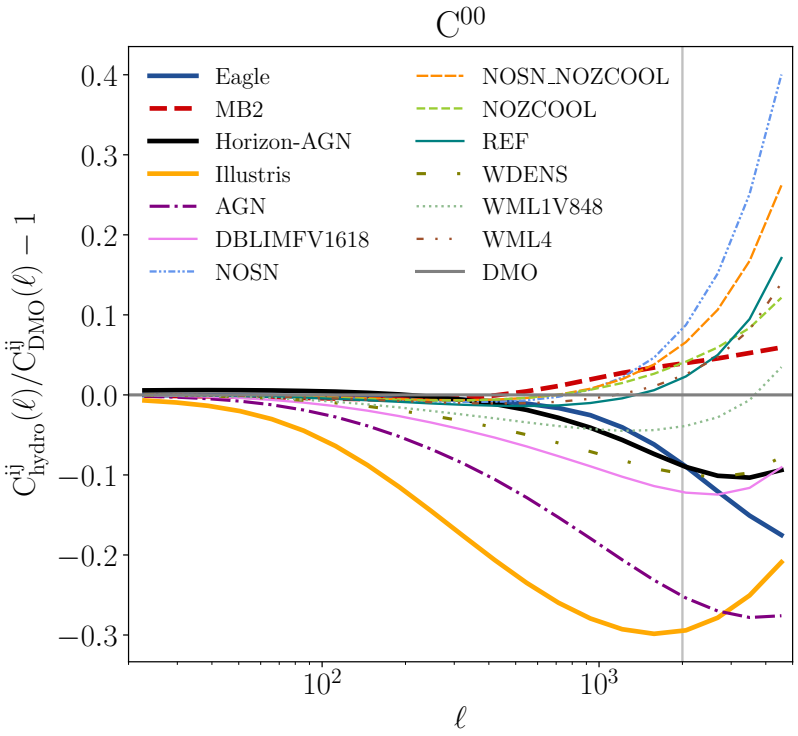

Figure 4.3: The ratio of tomographic shear power spectra of different hydrodynamical simulations with respect to their counterpart DMO simulations for the lowest auto-correlation tomographic bin with the cosmology set at the Planck 2015 result (Table 4.2). The thick lines represent the cases for Eagle/MB2/Illustris/Horizon-AGN simulations, while the thin lines indicate the 9 different baryonic scenarios in OWLS simulation suit.

size and do not exhibit this feature.

4.3.3 Covariance Matrix

We generate the analytical covariance matrix of tomographic shear power spectra using CosmoLike (Eifler et al., 2014; Krause & Eifler, 2017). Briefly, our covariance matrix contains both Gaussian and non-Gaussian parts. The Gaussian covariance matrix contains contributions from cosmic variance and shape noise, derived under the assumption that the 4pt-function of the shear field can be expressed in terms of 2pt-functions (Hu & Jain, 2004; Takada & Bridle, 2007). The non-Gaussian part is given by the convergence trispectrum derived using the halo model (Cooray & Sheth, 2002), which contains one-, two-, three-, and four-halo terms and a halo sample variance term characterizing the scatter of halo number density due to large-scale density fluctuations (Cooray & Hu, 2001; Takada & Jain, 2009; Sato et al., 2009). The exact equations of our implementation can be found in the appendix of Krause & Eifler (2017).

We assume 18,000 deg^2 as the survey area in our covariance matrix and adopt the same redshift distribution and source galaxy number density (26/arcmin^2) as depicted in Fig. 4.2. The shape noise is set to be $\sigma_\epsilon = 0.26$ in each ellipticity component.

4.3.4 Likelihood Formalism

Given a data vector $\boldsymbol{D}$ (at some fiducial cosmology and with baryonic effects from Eagle/MB2/Illustris/Horizon-AGN), one can infer the corresponding posterior probability distribution of cosmological parameters $\boldsymbol{p}_{\rm co}$ and potential nuisance parameters $\boldsymbol{p}_{\rm nu}$ via Bayes' theorem:

$$P(\boldsymbol{p}_{\rm co}, \boldsymbol{p}_{\rm nu}|\boldsymbol{D}) \propto L(\boldsymbol{D}|\boldsymbol{p}_{\rm co}, \boldsymbol{p}_{\rm nu}) P_r(\boldsymbol{p}_{\rm co}, \boldsymbol{p}_{\rm nu}) \,, \tag{4.5}$$

where $P_r(\boldsymbol{p}_{\rm co}, \boldsymbol{p}_{\rm nu})$ denotes the prior probability distribution and $L(\boldsymbol{D}|\boldsymbol{p}_{\rm co}, \boldsymbol{p}_{\rm nu})$ is the likelihood. In this work, we assume a Gaussian likelihood function for the observables,

$$L(\boldsymbol{D}|\boldsymbol{p}_{\rm co}, \boldsymbol{p}_{\rm nu}) \propto \exp\left(-\frac{1}{2} \underbrace{\left[(\boldsymbol{D}-\boldsymbol{M})^t \, \mathbf{C}^{-1} \, (\boldsymbol{D}-\boldsymbol{M})\right]}_{\chi^2(\boldsymbol{p}_{\rm co}, \boldsymbol{p}_{\rm nu})}\right) . \tag{4.6}$$

We further assume that the covariance $\mathbf{C}$ is constant in parameter space for simplicity (but see Eifler et al. 2009; Morrison & Schneider 2013 for likelihood analysis with cosmology-dependent covariance matrix). As described in §4.3.1, the model vector $\boldsymbol{M}$ may be derived based on Halofit which is a pure function of cosmology $\boldsymbol{M} = \boldsymbol{M}(\boldsymbol{p}_{\rm co})$, or it can be a function of some nuisance parameters $\boldsymbol{M} = \boldsymbol{M}(\boldsymbol{p}_{\rm co}, \boldsymbol{p}_{\rm nu})$ as well, with factors that are known to affect $\boldsymbol{D}$ absorbed in $\boldsymbol{p}_{\rm nu}$. For example, in HMcode, we have A and η_0 acting as nuisance parameters to account for the baryonic effects (see §4.3.1 for details). The final posterior distribution on cosmological parameters then can be derived by marginalizing over all other nuisance parameters in the model

$$P(\boldsymbol{p}_{\rm co}|\boldsymbol{D}) \propto \int \mathrm{d}\boldsymbol{p}_{\rm nu} \; P(\boldsymbol{p}_{\rm co}, \boldsymbol{p}_{\rm nu}|\boldsymbol{D}) \,. \tag{4.7}$$

We use the python `emcee` package (Foreman-Mackey et al., 2013), which relies on the algorithm of Goodman et al. (2010) to sample the parameter space spanned by $\boldsymbol{p}_{\rm co}$ ($\{\Omega_{\rm m},\ \sigma_8,\ \Omega_{\rm b},\ n_{\rm s},\ w_0,\ w_{\rm a},\ h_0\}$)

Table 4.3: Summary of baryonic physics mitigation techniques. The first column is the label of each method, which we refer to in the text and plots throughout the work. The second column has simple descriptions that highlight the essential elements of each method. The third column presents the exact χ^2 equations that go into the likelihood analysis. Finally, the last column provides a section number where more information can be found for each method.

Method	Brief description	χ^2 equation	Section reference
A	PCA in difference matrix, with exclusion	$[(\boldsymbol{D}-\boldsymbol{M})_{\rm pc,cut}]^{\rm t}\,\mathbf{C}^{-1}_{\rm pc,cut}\,[(\boldsymbol{D}-\boldsymbol{M})_{\rm pc,cut}]$	§4.4.1
B	PCA in difference matrix, with marginalization	$[\boldsymbol{D}-\boldsymbol{M}_{\boldsymbol{B}}(\boldsymbol{p}_{\rm co},\boldsymbol{Q})]^{\rm t}\,\mathbf{C}^{-1}\,[\boldsymbol{D}-\boldsymbol{M}_{\boldsymbol{B}}(\boldsymbol{p}_{\rm co},\boldsymbol{Q})]$	§4.4.1
C	PCA in $\mathbf{L}^{-1}$ weighted difference matrix, with exclusion	$[\mathbf{U}_{\rm ch}\mathbf{P}\mathbf{U}^{\rm t}_{\rm ch}\mathbf{L}^{-1}(\boldsymbol{D}-\boldsymbol{M})]^{\rm t}\,\mathbf{I}\,[\mathbf{U}_{\rm ch}\mathbf{P}\mathbf{U}^{\rm t}_{\rm ch}\mathbf{L}^{-1}(\boldsymbol{D}-\boldsymbol{M})]$	§4.4.2
D	PCA in fractional difference matrix, with marginalization	$[\boldsymbol{D}-\boldsymbol{M}_{\boldsymbol{R}}(\boldsymbol{p}_{\rm co},\boldsymbol{Q})]^{\rm t}\,\mathbf{C}^{-1}\,[\boldsymbol{D}-\boldsymbol{M}_{\boldsymbol{R}}(\boldsymbol{p}_{\rm co},\boldsymbol{Q})]$	§4.4.3
M	Halo model parameter marginalization	$[\boldsymbol{D}-\boldsymbol{M}_{\rm HMcode}(\boldsymbol{p}_{\rm co},A,\eta_0)]^{\rm t}\,\mathbf{C}^{-1}\,[\boldsymbol{D}-\boldsymbol{M}_{\rm HMcode}(\boldsymbol{p}_{\rm co},A,\eta_0)]$	§4.4.4

as well as $\boldsymbol{p}_{\rm nu}$ (if needed depending on the model). Altogether, we have conducted ~250 likelihood simulations to present the results for this paper. The MCMC (Markov Chain Monte Carlo) chains contain ~ 200000 to 400000 MCMC steps (after discarding 100000 steps as burn-in phase), depending on the dimension of the parameter space which ranges from 7~16. For simplicity, we assume flat priors for all of our parameters, with their minimum and maximum values summarized in Table 4.2. For likelihood simulations with informative priors based on Planck, we refer readers to E15. Informative priors help to better constrain n_s, Ω_b, and h, to which cosmic shear is not very sensitive.

We will present in §4.4 on how we implement various baryonic mitigation schemes in the likelihood analysis. But before that, in Fig. 4.4 we show the posterior distribution of cosmological parameters derived from our LSST likelihood simulation, when naively applying the HALOFIT model on fitting the data vectors contaminated with baryonic effects from Eagle/MB2/Horizon-AGN/Illustris simulations. For ease of visualization, we only show posteriors in the subspace of four cosmological parameters out of seven in total. Depending on the intensity of baryonic feedback as reflected in the ratio of hydrodynamical to DMO power spectra shown in Fig. 4.1, the resulting cosmology constraints can be severely biased in the case of Illustris ($2\sigma \sim 13\sigma$ depending on cosmological parameters) or at $1\sigma \sim 2\sigma$ level in the other three cases. We note that the degree of bias depends on the $\ell_{\rm max}$ used in the analysis. Fig. 4.4 presents the result when applying a cut at $\ell_{\rm max} \approx 2000$ on $\boldsymbol{D}$, which is the default setting in the paper. In §4.5.4, we will show how this result changes when extending data vectors to $\ell_{\rm max} \approx 5000$.

4.4 Methods of mitigating baryonic effects

In this section, we describe the methods used to mitigate the impact of baryonic physics on the cosmological parameter estimates from weak lensing. The methods can be classified into two categories: PCA-based methods and the halo-model based approach. We discuss several PCA-based methods that are minor variants of each other in §4.4.1 to §4.4.3. The halo-model based approach is described in §4.4.4. Throughout the work, we use the nine OWLS simulations as our 'training sample' to construct PCs for the PCA-based methods, and use the four mock data vectors constructed from Eagle/MB2/Illustris/Horizon-AGN simulations as 'test sample' to test methods listed in Table 4.3.

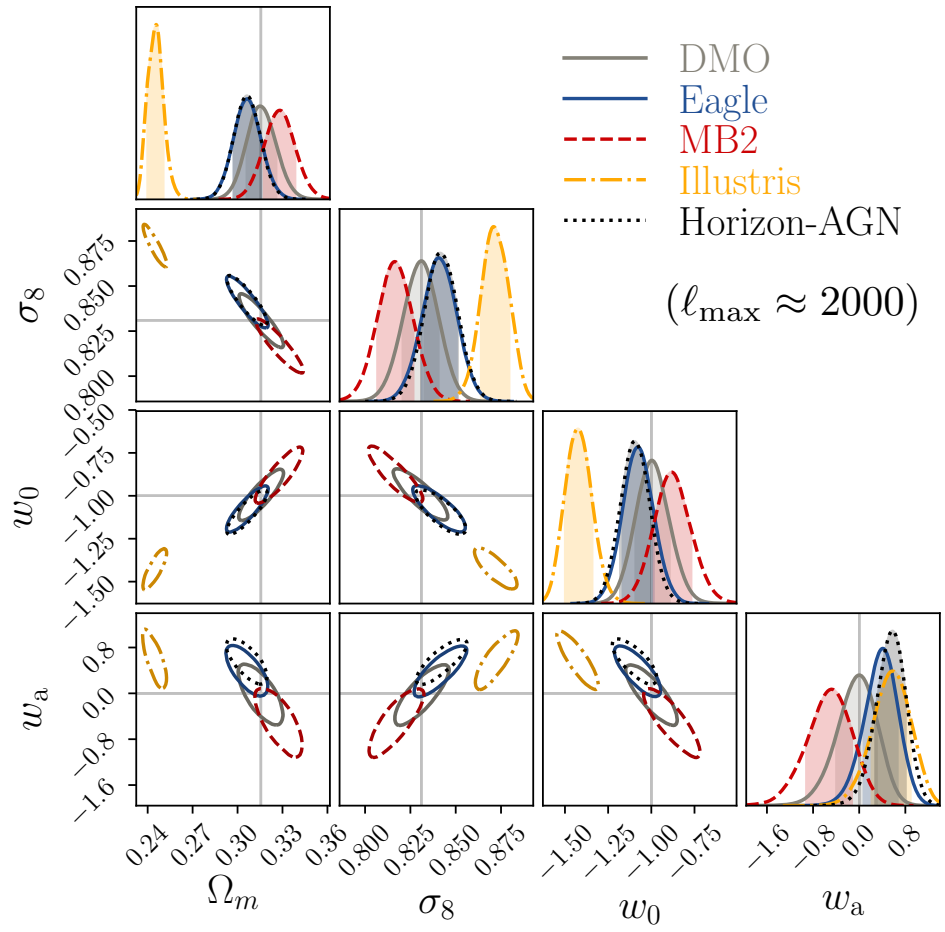

Figure 4.4: Cosmological parameter constraints for an LSST-like weak lensing survey with data vectors generated using various baryonic physics scenarios: pure DM (gray/solid) and the Eagle (blue/solid), MB2 (red/dashed), Illustris (yellow/dot-dashed) and Horizon-AGN (black/dotted) hydrodynamical simulations. In all cases, baryonic physics was ignored during the likelihood analysis, hence providing a worst-case scenario for biases due to baryonic physics. The analyses are carried out assuming non-informative priors on the parameters. Here, and in all such 2D posterior plots below, the contours depict the 68% confidence levels. *Depending on the intensity of the baryonic feedback, the resulting posterior distributions can be significantly away from the fiducial cosmology (marked in gray lines).*

4.4.1 PCA in Difference Matrix

Summary of the PCA framework (Method A)

The original framework for using PCA to mitigate the impact of baryonic physics for weak lensing is described in Eifler et al. (2015). The essential idea is that even though hydrodynamical simulations with different baryonic prescriptions predict a range of variations on the matter power spectra (Fig. 4.1), we can still extract the common features of those diversity using PCA, and build an empirical model to mitigate baryonic uncertainty based on these hydrodynamical simulations. Below we provide a step-by-step description of the PCA framework.

Firstly, we collect the tomographic shear power spectra constructed from the nine OWLS simulations as our training sample, and label these nine data vectors as $\boldsymbol{B}_1, ..., \boldsymbol{B}_9$. Next we build a difference matrix $\boldsymbol{\Delta}(\boldsymbol{p}_{\rm co})$ with dimension of $N_{\rm data} \times N_{\rm sim} = 990 \times 9$. Each column records the deviation between the baryonic data vector and the DMO model vector $\boldsymbol{M}$ at any arbitrary cosmology (recomputed for each MCMC step) in terms of their difference

$$\boldsymbol{\Delta}(\boldsymbol{p}_{\rm co}) = \begin{bmatrix} | & | & & | \\ \boldsymbol{B}_1 - \boldsymbol{M} & \boldsymbol{B}_2 - \boldsymbol{M} & \dots & \boldsymbol{B}_9 - \boldsymbol{M} \\ | & | & & | \end{bmatrix}_{N_{\rm data} \times N_{\rm sim}} . \tag{4.8}$$

The left panel of Fig. 4.6 provides a visualization of the entries of the difference vectors used to construct $\boldsymbol{\Delta}$. Here notice that both $\boldsymbol{B}_x(\boldsymbol{p}_{\rm co})$ and $\boldsymbol{M}(\boldsymbol{p}_{\rm co})$ are functions of cosmology, and therefore so is $\boldsymbol{\Delta}$. We refer readers to Appendix 4.C for details of how we compute the baryon-contaminated data vectors at different $\boldsymbol{p}_{\rm co}$.

The second step is to perform the PCA on the difference matrix, with the goal of identifying the few dominant principle components (PCs) that signify the directions of largest discrepancy between the baryonic and DMO data vectors from the nine OWLS simulations. To find the PCs, we apply the (full) singular value decomposition (SVD) on $\boldsymbol{\Delta}$,

$$\boldsymbol{\Delta} = \mathbf{U}\, \boldsymbol{\Sigma}\, \mathbf{V}^{\rm t} . \tag{4.9}$$

As shown in Fig. 4.5, SVD decomposes $\boldsymbol{\Delta}$ into the product of three matrices. Both $\mathbf{U}$ and $\mathbf{V}$ are square unitary matrices with dimensions of $N_{\rm data} \times N_{\rm data}$ (990×990) and $N_{\rm sim} \times N_{\rm sim}$ (9×9) respectively. The upper $N_{\rm sim} \times N_{\rm sim}$ (9×9) block of $\boldsymbol{\Sigma}$ is a diagonal matrix consisting of $N_{\rm sim}$ (9) positive real singular values $\sigma_1 ... \sigma_9$ arranged in descending order, and the remaining $N_{\rm data} - N_{\rm sim}$ (981) rows have only zeros (indicated by the dashed square). The $N_{\rm data}$ (990) columns of $\mathbf{U}$ are eigenvectors of $\boldsymbol{\Delta}\boldsymbol{\Delta}^{\rm t}$, with eigenvalues in the diagonal entries of $\boldsymbol{\Sigma}\boldsymbol{\Sigma}^{\rm t}$.

The first 9 eigenvectors constitute a set of orthogonal PCs in order of decreasing importance according to the amount of variation they capture in the different training vectors. The right panel of Fig. 4.6 shows these 9 PC modes in projection on the C^{00} tomographic bin. The PC modes span a 9-dimensional subspace within the 990 dimensional space which covers entirely the degrees of freedom to explain baryonic uncertainties in the nine OWLS hydro simulations. In other words, any given $\boldsymbol{B}_x(\boldsymbol{p}_{\rm co}) - \boldsymbol{M}(\boldsymbol{p}_{\rm co})$, can be described with 9 free parameters via

$$\boldsymbol{B}_x(\boldsymbol{p}_{\rm co}) - \boldsymbol{M}(\boldsymbol{p}_{\rm co}) = \sum_{n=1}^{9} Q_n\, \mathbf{PC}_n(\boldsymbol{p}_{\rm co}) , \tag{4.10}$$

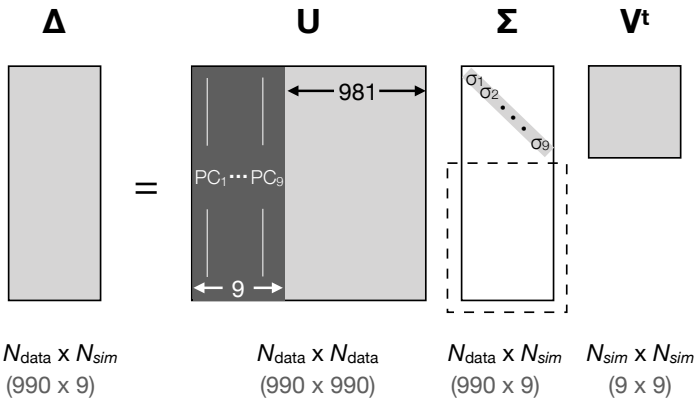

Figure 4.5: We perform singular value decomposition (SVD) on the difference matrix $\mathbf{\Delta}$ built based on the 9 baryonic scenarios of OWLS (see Eq. (4.8)). $\mathbf{U}$ is a unitary matrix with columns that form an orthonormal basis set to span the 990-dimensional space of our data vector. Among them, the first 9 PCs of $\mathbf{U}$ form a complete description of the modifications of the data vector due to baryonic physics in the nine OWLS hydro simulations. We will test whether these 9 PCs can also describe the impact of baryonic physics in the Eagle/MB2/Illustris/Horizon-AGN simulations.

with Q_n being the amplitude of $\mathbf{PC}_n$. The remaining 981 columns of $\mathbf{U}$ are silent orthogonal vectors which extends $\mathbf{U}$ into a unitary matrix. With 9 baryonic scenarios as our training sample, we have at most 9 independent PCs to describe modifications to the observables due to baryonic physics. One of the goals of this work is to understand how effectively the PCA basis can describe baryonic physics scenarios in other more recent hydrodynamical simulations.

The third step is to transform everything to PC basis, and mitigate baryonic uncertainty by excluding PC modes. In PC basis, our data and model vectors are defined as

$$\boldsymbol{D}_{\rm pc} = \mathbf{U}^{\rm t}\boldsymbol{D} \tag{4.11a}$$

$$\boldsymbol{M}_{\rm pc} = \mathbf{U}^{\rm t}\boldsymbol{M}\,, \tag{4.11b}$$

and the covariance matrix is

$$\mathbf{C}_{\rm pc} = \mathbf{U}^{\rm t}\,\mathbf{C}\,\mathbf{U}\,. \tag{4.12}$$

Viewing from PC coordinate, the majority of the baryonic uncertainties between $\boldsymbol{D}_{\rm pc}$ and $\boldsymbol{M}_{\rm pc}$ would be absorbed in the first N elements. We can then directly cut the data vector $\boldsymbol{D}_{\rm pc}$ to obtain a shorter vector $\boldsymbol{D}_{\rm pc,cut}$, and do the same to the model vector $\boldsymbol{M}_{\rm pc} \rightarrow \boldsymbol{M}_{\rm pc,cut}$ to avoid modeling challenges on these data points.

When doing MCMC analysis, we modify the original Eq. (8) from E15 to properly account for the change of covariance matrix due to loss of information after PC mode removal. We cut the corresponding rows and columns on $\mathbf{C}_{\rm pc}$, and use the corresponding sub-matrix, $\mathbf{C}_{\rm pc,cut}$ to calculate the inverse covariance $\mathbf{C}^{-1}_{\rm pc,cut}$ for $\boldsymbol{D}_{\rm pc,cut}$. The χ^2 equation can then be written as:

$$\chi'^2(\boldsymbol{p}_{\rm co}) = (\boldsymbol{D}-\boldsymbol{M})^{\rm t}_{\rm pc,cut}\,\mathbf{C}^{-1}_{\rm pc,cut}\,(\boldsymbol{D}-\boldsymbol{M})_{\rm pc,cut}\,, \tag{4.13}$$

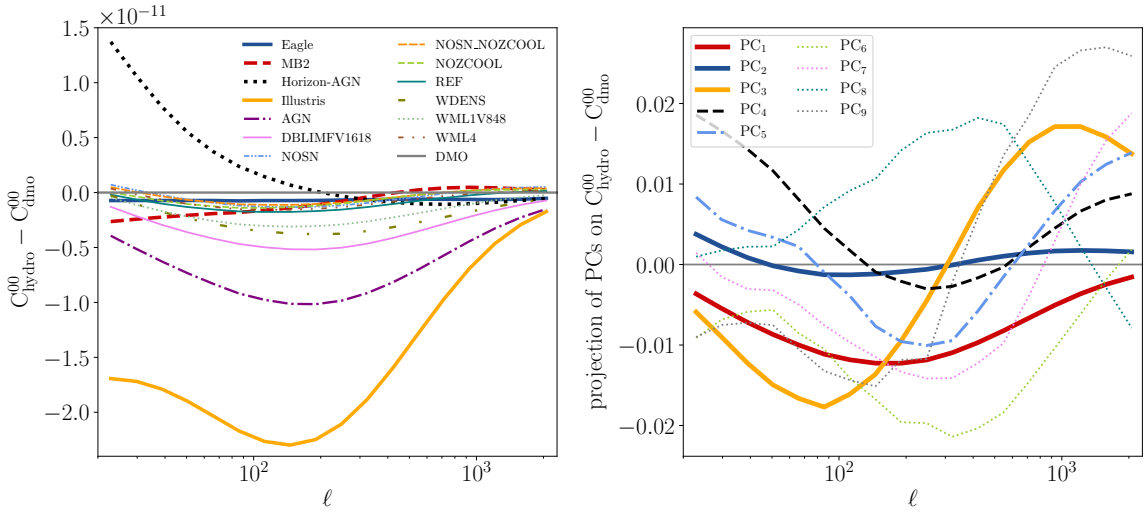

Figure 4.6: Left: The difference vectors, $\boldsymbol{B}-\boldsymbol{M}$, from the OWLS simulation set used to construct PCs as input in columns of Eq. (4.8). The thicker lines indicate the difference vectors for Eagle/MB2/Horizon-AGN/Illustris simulations as our test set. Right: The PC modes constructed from the OWLS simulation set in projection on the difference vector space for the tomographic bin C^{00}. *The goal of this work is to check whether these PC modes can flexibly describe the baryonic physics scenarios in the test set hydrodynamical simulations.*

and the likelihood equation:

$$L(\boldsymbol{D}|\boldsymbol{p}_{\rm co}) \propto \exp\left(-\frac{1}{2}\underbrace{\left[(\boldsymbol{D}-\boldsymbol{M})^{\rm t}_{\rm pc,cut}\,\mathbf{C}^{-1}_{\rm pc,cut}\,(\boldsymbol{D}-\boldsymbol{M})_{\rm pc,cut}\right]}_{\chi'^2(\boldsymbol{p}_{\rm co})}\right). \tag{4.14}$$

The marginalization version of the PCA framework (Method B)

We refer to 'PC marginalization' as a method that includes (up to nine) amplitudes of PCs as free parameters to parametrize the impact of baryonic physics on the tomographic shear power spectra. As shown in Eq. (4.10), the current 9 PCs fully span the baryonic degrees of freedom in the 9 OWLS simulations. We can further check whether they are also effective in describing the impact of baryonic physics on the observables in our test set of hydrodynamic simulations by building a new model with the following parametric form:

$$\boldsymbol{M}_B(\boldsymbol{p}_{\rm co}, \boldsymbol{Q}) = \boldsymbol{M}(\boldsymbol{p}_{\rm co}) + \sum_{n=1}^{m} Q_n\, \mathbf{PC}_n(\boldsymbol{p}_{\rm co})\,. \tag{4.15}$$

where $m \leqq 9$, and $\boldsymbol{Q} = \{Q_1, Q_2, ..., Q_m\}$ are free parameters in addition to the cosmological parameters. The likelihood function for the cosmological parameters can be derived by marginalizing over

the amplitude parameters:

$$L(\boldsymbol{D}|\boldsymbol{p}_{\rm co}) \propto \int d\boldsymbol{Q} \times \exp\left(-\frac{1}{2}\left[(\boldsymbol{D}-\boldsymbol{M}_B(\boldsymbol{p}_{\rm co},\boldsymbol{Q}))^{\rm t}\,\mathbf{C}^{-1}\,(\boldsymbol{D}-\boldsymbol{M}_B(\boldsymbol{p}_{\rm co},\boldsymbol{Q}))\right]\right). \tag{4.16}$$

Theoretically, one can prove that the likelihood functions of Eq. (4.14) (method A) and Eq. (4.16) return identical results if the priors on the PC amplitudes are uninformative. We will provide comparisons of the posterior distributions of $\boldsymbol{p}_{\rm co}$ in §4.5.1 and further comment on both methods there.

4.4.2 Noise-weighted PCA – Cholesky Decomposition (Method C)

As noted at the end of §2.2 of E15, performing PCA on the difference matrix $\boldsymbol{\Delta}$ (Eq. (4.8)) is not necessarily the most optimal choice. They suggested an option of conducting the PCA on the 'noise'-weighted $\boldsymbol{\Delta}$. As a result of re-weighting, the derived PCs would be more sensitive in accounting for deviations in data vectors due to baryonic physics at well-measured data points, where larger weighting factors are applied. Therefore, when doing PC mode removal, we tend to more effectively remove baryonic physics degrees of freedom that impact better-measured (lower noise) scales, which may more effectively reduce cosmological parameter biases.

To find the weights, we first decompose our covariance matrix by applying a Cholesky Decomposition

$$\mathbf{C} = \mathbf{L}\mathbf{L}^{\rm t}\,, \tag{4.17}$$

where $\mathbf{L}$ is a lower triangular matrix with real and positive diagonal entries. We can then weight our $\boldsymbol{D}$ and $\boldsymbol{M}$ vectors as

$$\begin{aligned}\boldsymbol{D}_{\rm ch} &= \mathbf{L}^{-1}\boldsymbol{D}\,,\\ \boldsymbol{M}_{\rm ch} &= \mathbf{L}^{-1}\boldsymbol{M}\,.\end{aligned} \tag{4.18}$$

After this transformation, our new data vector $\boldsymbol{D}_{\rm ch}$ has an identity covariance matrix $\mathbb{1}$, which can be easily proved as follows

$$\begin{aligned}\mathbf{C}_{\rm ch} &= \left\langle(\boldsymbol{D}_{\rm ch}-\overline{\boldsymbol{D}}_{\rm ch})(\boldsymbol{D}_{\rm ch}-\overline{\boldsymbol{D}}_{\rm ch})^{\rm t}\right\rangle = \left\langle\mathbf{L}^{-1}(\boldsymbol{D}-\overline{\boldsymbol{D}})(\mathbf{L}^{-1}(\boldsymbol{D}-\overline{\boldsymbol{D}}))^{\rm t}\right\rangle\\ &= \mathbf{L}^{-1}\left\langle(\boldsymbol{D}-\overline{\boldsymbol{D}})(\boldsymbol{D}-\overline{\boldsymbol{D}})^{\rm t}\right\rangle(\mathbf{L}^{-1})^{\rm t} = \mathbf{L}^{-1}\mathbf{C}^{-1}(\mathbf{L}^{-1})^{\rm t} = \mathbb{1}\,.\end{aligned} \tag{4.19}$$

In other words, after applying Eq. (4.18), we not only re-weight but also decorrelate the data vector.

Similar to Eq. (4.8), we build the new difference matrix as

$$\begin{aligned}\boldsymbol{\Delta}_{\rm ch}(\boldsymbol{p}_{\rm co}) &= \begin{bmatrix} | & & | \\ \boldsymbol{B}_{1,\rm ch}-\boldsymbol{M}_{\rm ch} & \dots & \boldsymbol{B}_{9,\rm ch}-\boldsymbol{M}_{\rm ch} \\ | & & | \end{bmatrix}_{N_{\rm data}\times N_{\rm sim}}\\ &= \mathbf{L}^{-1}\boldsymbol{\Delta}(\boldsymbol{p}_{\rm co}) = \mathbf{U}_{\rm ch}\,\boldsymbol{\Sigma}_{\rm ch}\,\mathbf{V}_{\rm ch}^{\rm t}\,.\end{aligned} \tag{4.20}$$

Here each of the OWLS training data vectors is weighted by $\mathbf{L}^{-1}$ as $\boldsymbol{B}_{\rm x,ch} = \mathbf{L}^{-1}\boldsymbol{B}_{\rm x}$. The $\boldsymbol{\Delta}_{\rm ch}$ matrix is equivalent to performing a $\mathbf{L}^{-1}$ matrix transformation on $\boldsymbol{\Delta}$ shown in Eq. (4.8). We can then apply

SVD to derive the PC basis set as stored in the $\mathbf{U}_{\rm ch}(\boldsymbol{p}_{\rm co})$ matrix. The first 9 PCs form natural bases to span the weighted difference vector for various baryonic effects

$$\boldsymbol{B}_{\rm ch} - \boldsymbol{M}_{\rm ch} = \mathbf{L}^{-1}(\boldsymbol{B} - \boldsymbol{M}) = \sum_{n=1}^{9} Q_n \, \mathbf{PC}_n \, . \tag{4.21}$$

In Fig. 4.7, we show the $\boldsymbol{B}_{\rm ch} - \boldsymbol{M}_{\rm ch} = \mathbf{L}^{-1}(\boldsymbol{B} - \boldsymbol{M})$ vectors in our lowest tomographic bin, at $\boldsymbol{p}_{\rm co,fid}$. The thicker lines represent our four test simulations; the thinner lines are for the nine baryonic scenarios in OWLS, which compose the columns of $\mathbf{\Delta}_{\rm ch}$ in Eq. (4.20). Comparing with the left panel of Fig. 4.6, one can see that after re-weighting by $\mathbf{L}^{-1}$, we more strongly emphasize baryonic fluctuations at smaller scales, so the PCs should also be more effective in accounting for small-scale baryonic features.[9]

Similar to §4.4.1, to perform the PC mode removal, we transform everything to the PC basis:

$$\boldsymbol{D}_{\rm ch,pc} = \mathbf{U}^{\rm t}_{\rm ch} \boldsymbol{D}_{\rm ch} \tag{4.22a}$$

$$\boldsymbol{M}_{\rm ch,pc} = \mathbf{U}^{\rm t}_{\rm ch} \boldsymbol{M}_{\rm ch} \tag{4.22b}$$

$$\mathbf{C}_{\rm ch,pc} = \mathbf{U}^{\rm t}_{\rm ch} \, \mathbf{C}_{\rm ch} \, \mathbf{U}_{\rm ch} = \mathbb{1} \, , \tag{4.22c}$$

and then cut all the elements from the data and model vectors and the covariance matrix for the PC modes that are to be removed. Here since $\mathbf{C}_{\rm ch}$ is an identity matrix, it and its inverse $\mathbf{C}^{-1}_{\rm ch,pc}$ in the PC basis remain the same after coordinate transformation. The final PC mode removal χ^2 equation becomes:

$$\begin{aligned} \chi^2_{\rm ch}(\boldsymbol{p}_{\rm co}) &= (\boldsymbol{D}_{\rm ch} - \boldsymbol{M}_{\rm ch})^{\rm t}_{\rm pc,cut} \, \mathbf{C}^{-1}_{\rm ch,pc\ cut} \, (\boldsymbol{D}_{\rm ch} - \boldsymbol{M}_{\rm ch})_{\rm pc,cut} \\ &= (\boldsymbol{D}_{\rm ch} - \boldsymbol{M}_{\rm ch})^{\rm t}_{\rm pc,cut} \, (\boldsymbol{D}_{\rm ch} - \boldsymbol{M}_{\rm ch})_{\rm pc,cut} \end{aligned} \tag{4.23}$$

The marginalization version of method C can be viewed as the following. By reorganizing Eq. (4.21), we can build a baryonic model generator as

$$\boldsymbol{M}_C(\boldsymbol{p}_{\rm co}, \boldsymbol{Q}) = \boldsymbol{M}(\boldsymbol{p}_{\rm co}) + \mathbf{L} \sum_{n=1}^{m} Q_n \, \mathbf{PC}_n(\boldsymbol{p}_{\rm co}) \, , \tag{4.24}$$

where $m \leqq 9$. The cosmological parameter-dependence comes in through the DMO model vector, while the amplitudes of PCs are used as higher order correction for baryonic effects.

4.4.3 PCA in Fractional Difference Matrix (Method D)

Instead of using the difference matrix $\mathbf{\Delta}$ to perform PCA, Mohammed & Gnedin (2018) identified PCs based on the fractional difference matrix $\boldsymbol{R}$ defined as:

$$\begin{aligned} \boldsymbol{R} &= \left[\begin{array}{cccc} | & | & & | \\ \frac{\boldsymbol{B}_1 - \boldsymbol{M}}{\boldsymbol{M}} & \frac{\boldsymbol{B}_2 - \boldsymbol{M}}{\boldsymbol{M}} & \cdots & \frac{\boldsymbol{B}_9 - \boldsymbol{M}}{\boldsymbol{M}} \\ | & | & & | \end{array} \right]_{990\times 9} \\ &= \mathbf{U}_{\rm R} \, \mathbf{\Sigma}_{\rm R} \, \mathbf{V}^{\rm t}_{\rm R} \, . \end{aligned} \tag{4.25}$$

[9] Although we plot $\boldsymbol{D}_{\rm ch} - \boldsymbol{M}_{\rm ch}$ vs. ℓ in Fig. 4.7, we note that actually the new data points are not strictly functions of the original ℓ because of the non-zero off-diagonal terms in $\mathbf{L}^{-1}$. However, our take-away point from Fig. 4.7 still holds due to the fact that our covariance matrix is dominated by Gaussian noise, and thus the off-diagonal terms in $\mathbf{L}^{-1}$ are small.

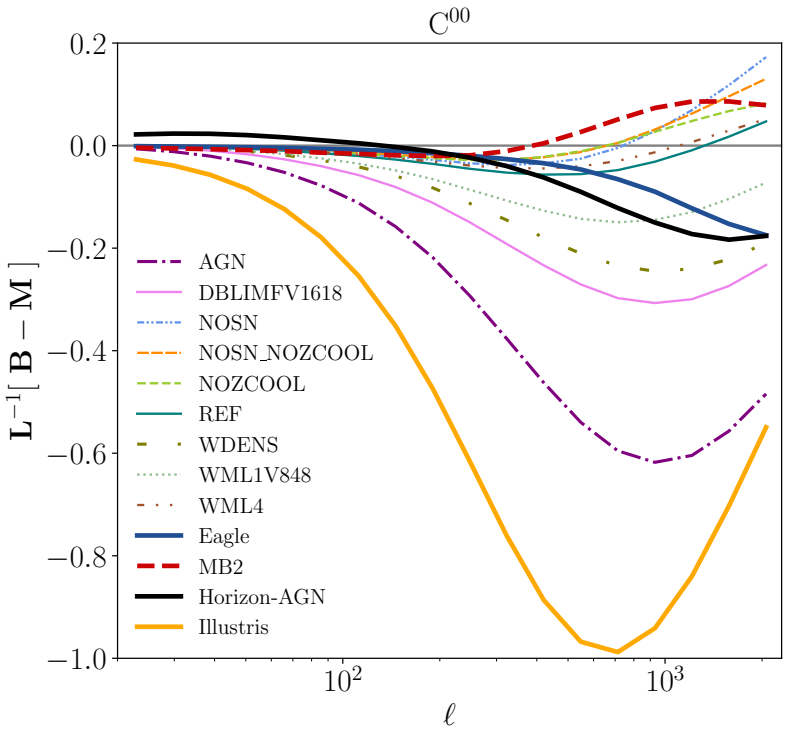

Figure 4.7: The discrepancy between baryon-contaminated data vectors and model in terms of $\boldsymbol{B}_{\rm ch} - \boldsymbol{M}_{\rm ch}$ for various hydrodynamical simulations in the lowest tomographic bin. This is similar to the left panel of Fig. 4.6, but here shows results for the case when applying Cholesky decomposition on our $\boldsymbol{B}$ and $\boldsymbol{M}$ vectors. The nine OWLS baryonic scenarios (thinner lines) compose columns of $\boldsymbol{\Delta}_{\rm ch}$, which are used to build PCs. These PCs are used to span the variation of Eagle/MB2/Illustris/Horizon-AGN simulations in $\boldsymbol{D}_{\rm ch} - \boldsymbol{M}_{\rm ch}$ space. *After Cholesky decomposition, the largest data-model inconsistency shifts to smaller scales compared with the upper panel of Fig. 4.6, indicating the PCs trained from* $\boldsymbol{\Delta}_{\rm ch}$ *are more efficient at describing small-scale variations in the matter power spectrum due to baryonic physics compared with performing PCA on* $\boldsymbol{\Delta}$.

One fundamental difference between the fractional difference matrix $\boldsymbol{R}$ and the difference matrices $\boldsymbol{\Delta}$ or $\boldsymbol{\Delta}_{\rm chy}$ is that $\boldsymbol{R}$ does not depend on cosmology, given our assumption of Eq. (4.45). After the $\mathbf{U}_{\rm R}$ is derived by SVD analysis, a model for the observables with baryonic physics degrees of freedom spanned by OWLS can be built as:

$$\boldsymbol{M}_R(\boldsymbol{p}_{\rm co}, \boldsymbol{Q}) = \boldsymbol{M}(\boldsymbol{p}_{\rm co}) \left[1 + \sum_{n=1}^{m} Q_n \, \mathbf{PC}_n\right], \tag{4.26}$$

where $m \leqq 9$, and $\boldsymbol{Q} = \{Q_1, Q_2, ..., Q_m\}$ are free parameters controlling the amplitudes of PCs, and $\mathrm{PC}_1 \sim \mathrm{PC}_9$ are in the first nine columns of $\mathbf{U}_{\rm R}$. Similar to the methodology in §4.4.1, the likelihood function for the cosmological parameters can be derived by marginalizing over the amplitude parameters:

$$\begin{aligned} L(\boldsymbol{D}|\boldsymbol{p}_{\rm co}) \propto & \int d\boldsymbol{Q} \times \\ & \exp\left(-\frac{1}{2}\left[(\boldsymbol{D} - \boldsymbol{M}_R(\boldsymbol{p}_{\rm co}, \boldsymbol{Q}))^{\rm t}\, \mathbf{C}^{-1}\, (\boldsymbol{D} - \boldsymbol{M}_R(\boldsymbol{p}_{\rm co}, \boldsymbol{Q}))\right]\right). \end{aligned} \tag{4.27}$$

Similar to the concept mentioned in §4.4.2, performing PCs on the matrix $\boldsymbol{R}$ can be viewed as putting the weight of $1/\boldsymbol{M}$ into the PCA analysis. Since $\boldsymbol{M}$ decreases with increasing ℓ, and the overall amplitude of $\boldsymbol{M}$ increases toward higher redshift, after taking its inverse, we upweight data points at smaller scales and lower redshift. The fractional difference vectors of OWLS that go into columns of $\boldsymbol{R}$ are plotted in Fig. 4.3. The PCs derived from $\boldsymbol{R}$ are expected to be more efficient in accounting for smaller scale and lower redshift variation of the observables due to baryonic physics.

4.4.4 HMcode (Method M)

Finally, we compare the above PCA-based methods with the halo model-based approach proposed from Mead et al. (2015), HMcode. HMcode utilizes two halo profile-related parameters to capture the impact of baryonic physics on the matter power spectrum: the amplitude of the concentration-mass relation (A) and a halo bloating parameter (η_0) controlling the (mass-dependent) change of halo profiles. We refer readers back to §4.3.1 for a brief summary of this approach.

There exists some level of degeneracy between A and η_0, as shown in Fig. 6 of M15. Thus, when implementing the likelihood analysis, one can either vary both of the parameters, or change only the single parameter A while fixing

$$\eta_0 = 0.98 - 0.12A. \tag{4.28}$$

For example, Joudaki et al. (2017) applied only varying A to marginalize over baryonic physics in CFHTLenS cosmic shear, while MacCrann et al. (2017) and Troxel et al. (2018) varied both parameters to marginalize over baryonic physics in the Dark Energy Survey (DES).

Equation (4.28) is derived based on the OWLS simulation suite. We will test whether it remains valid for the baryonic physics scenarios in Eagle/MB2/Illustris/Horizon-AGN for our forecasted scenario with LSST-like statistical power. Also, we will compare the performances of HMcode (marginalization over halo model parameters) with the above PCA-based methods.

4.5 Performances of Baryonic Mitigation Techniques

In this section, we present our simulated likelihood analysis for the different baryonic mitigation schemes listed in Table 4.3. We refer readers back to § 4.3 for a description of the simulated likelihood analysis setup.

Ideally, we need a baryonic physics mitigation strategy that can reduce the biases in cosmological parameters due to inaccuracies in theoretical modeling (as demonstrated in Fig. 4.4) to a level that is much smaller than the statistical uncertainties. In addition, we hope that the increase in statistical errors on cosmological parameters due to the additional nuisance parameters will be as small as possible.Throughout this section, we will use a criterion of bias $< 0.5\sigma$ (where σ represents the marginalized statistical error) for individual cosmological parameters to evaluate whether a method is effective in mitigating the uncertainties due to baryonic physics under various baryonic scenarios. We also compare their performance based on the degradation of cosmological constraining power through the size of the 1D marginalized uncertainties on cosmological parameters.

4.5.1 PC Mode Exclusion versus Marginalizing Over PC Amplitude

We start by presenting the results for methods A and B (see Table 4.3) with their PCs described using the same difference matrix $\mathbf{\Delta}$. In Method A, we modify the data vector by excluding the first few PC modes and modify the covariance self-consistently as well. In method B, the data vector and covariance matrix are unmodified, but we introduce free parameters describing the PC amplitudes to marginalize over in the likelihood analysis.

Mathematically, methods A and B are equivalent if no priors are set on the baryonic physics parameters. From an information perspective, when removing data points (and the corresponding covariance elements), we lose all of the information that can constrain the amplitudes of the excluded PC modes. Thus, this should be equivalent to marginalizing over PC amplitudes with uninformative priors.

In Fig. 4.8, we use simulated likelihood analyses based on Horizon-AGN (yellow dot-dashed & black dotted) and Illustris (blue solid & red dashed) to demonstrate the excellent consistency between PC mode exclusion and PC amplitude marginalization. For the case of Illustris, large residual biases still exist after performing the baryonic physics mitigation. We will discuss this issue in §4.5.3. Although not shown, we have also confirmed the consistency between methods A & B for Eagle and MB2.

In conclusion, we have demonstrated with examples that the PC exclusion formula shown in Eq. (4.13) gives consistent results as when marginalizing over PC amplitudes with an uninformative prior. Method B can provide baryonic information through the constrained PC amplitudes, which can be used as a standard to quantify baryonic effects. So far, we allow the PC amplitudes to vary from $(-\infty, \infty)$. Reducing the prior ranges on PC amplitudes could potentially increase the constraining power on cosmology if we can develop a consistent way of setting the priors on PC amplitudes, given our knowledge of baryonic physics. The downside of method B is that it requires running longer MCMC chains to ensure convergence due to an increase in the dimensionality of parameter space. Therefore if one does not care to learn about baryonic physics, and would simply like to marginalize over it, we recommend method A.

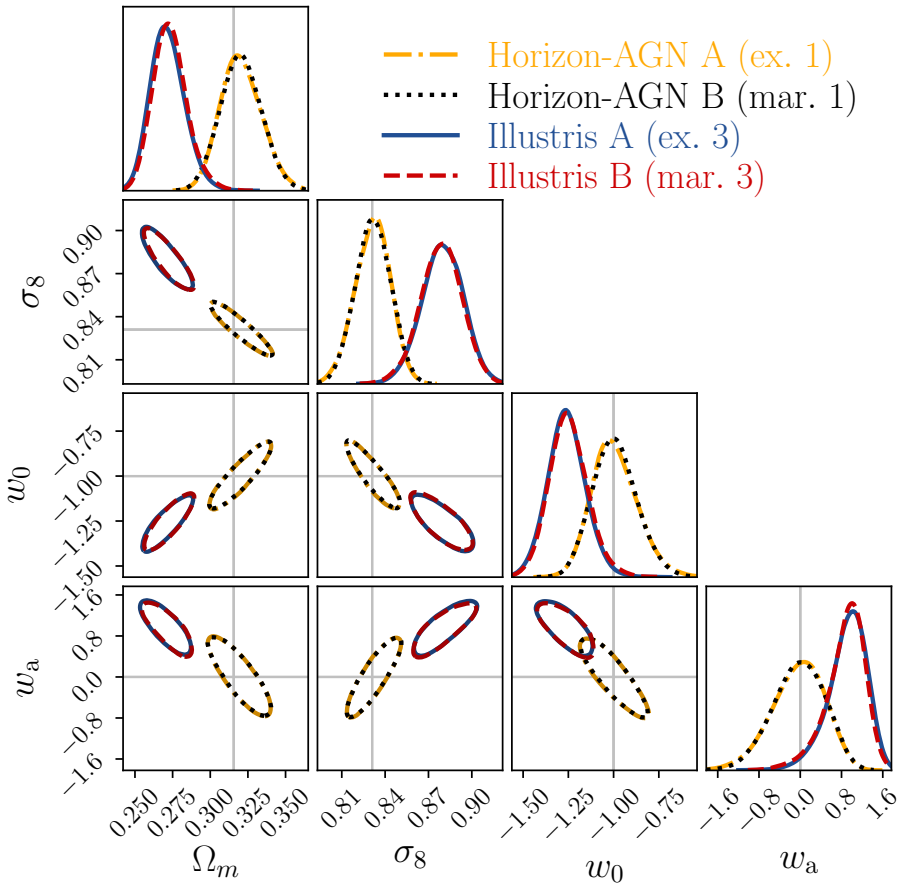

Figure 4.8: Comparison of the posterior distributions of cosmological parameters between baryonic physics mitigation techniques A & B listed in Table 4.3. The yellow dot-dashed and black dotted contours indicate the 1σ contours of the posterior probability distributions obtained from methods A and B, respectively, for the Horizon-AGN simulation after excluding or marginalizing over the first PC modes. Similarly, the blue solid and red dashed contours indicate the case for Illustris after excluding or marginalizing over 3 PC modes. *The excellent match between the posterior probability distributions for cosmological parameters between methods A and B confirms that the PC exclusion formula shown in Eq.* (4.13) *is conceptually equivalent to marginalizing over PC amplitudes.*

4.5.2 Comparison between various PC construction methods

Here we compare the performances of the PCA-based methods listed Table 4.3. We have already shown in §4.5.1 that PC mode exclusion (method A) is equivalent to marginalizing over PC amplitudes (method B), so here we only compare methods A, C, and D.

The fundamental difference between these PCA methods is the way the PCs are constructed from the training simulations, which affects their efficiency in describing how baryonic physics modifies the data vectors on larger or smaller scales. We refer readers back to §4.4 for more details about this formalism. Briefly, when PCs are derived from $\mathbf{\Delta}$ (method A; Eq. (4.8)), they are most efficient in describing the difference vector $\boldsymbol{D} - \boldsymbol{M}$. For PCs trained from $\mathbf{\Delta}_{\rm chy}$ (method C; Eq. (4.20)), they are most efficient in describing the noise-weighted difference, $\boldsymbol{D}_{\rm chy} - \boldsymbol{M}_{\rm chy} = \mathbf{L}^{-1}(\boldsymbol{D} - \boldsymbol{M})$, due to baryonic physics. Finally, PCs trained from $\boldsymbol{R}$ (method D; Eq. (4.25)) are most efficient in describing variations in the fractional difference $\frac{\boldsymbol{D}-\boldsymbol{M}}{\boldsymbol{M}}$ from baryonic effects.

Figure 4.9 shows the median of the marginalized 1D posteriors of cosmological parameters under different baryonic physics mitigation techniques for data vectors derived from our four test simulations. The lower and upper error bars represent for the 16 and 84th quantiles of the 1D marginalized posterior distribution. The $x-$axes indicate numbers of PC modes excluded or numbers of marginalization parameters used in the analysis. We select some cases from Fig. 4.9 and present their 1D and 2D posteriors in Fig. 4.10. The brown crosses in Fig. 4.9 indicate the case when no baryonic physics mitigation scheme is applied. One can see that the deviations from the fiducial cosmological parameters exceeds 1σ for all of our test baryonic scenarios. This is also shown in Fig. 4.4 on the 2D posterior contours. The blue-circle, red-triangle, and yellow-square markers indicate the results of performing baryonic physics mitigation by PCA-based methods A, C, and D, respectively. When the modifications of the data vectors due to baryonic physics are relatively weak as in MB2/Eagle/Horizon-AGN, we find that removing up to 2 PC modes is sufficient to marginalize baryonic bias to within 1σ[10] for the cosmological parameters presented here. For the Illustris simulation, due to its strong baryonic feedback, we need to remove up to 6 PCs for the 1σ posteriors to include the fiducial cosmological parameters.

Method C is superior to methods A and D

In Fig. 4.11 we plot the w_0 bias (in color-filled markers; defined as $|w_{0,\text{best fit}} - w_{0,\text{fid}}|$, with $w_{0,\text{best fit}}$ being the median value of the marginalized posterior distribution of w_0) and the 0.5σ error of w_0 (in open markers; with σ defined as the half difference between the 16th and 84th percentile of the 1D marginalized posterior of w_0) for various baryonic physics mitigation schemes. For a method to be effective in mitigating baryonic-induced parameter biases, we require that the bias be below the 0.5σ errors. For all baryonic physics scenarios, we observe that at fixed number of excluded PC modes, the biases of method C (red-solid triangles) are nearly always smaller than methods A (blue-solid circles) and D (yellow-solid squares). If focusing on the lower left panel of Fig. 4.10, using Illustris when removing 3 PC modes as an examples, one can see that the 2D 1σ posteriors of method C (red

[10]The 1σ criterion is a looser condition than the 0.5σ constraint we will later use for defining acceptability; we use this looser condition here as we are just trying to compare the basic behavior of the different PCA methods here. Once we are comparing the best-performing PCA methods with HMCode, we will consistently impose a 0.5σ constraint on both.

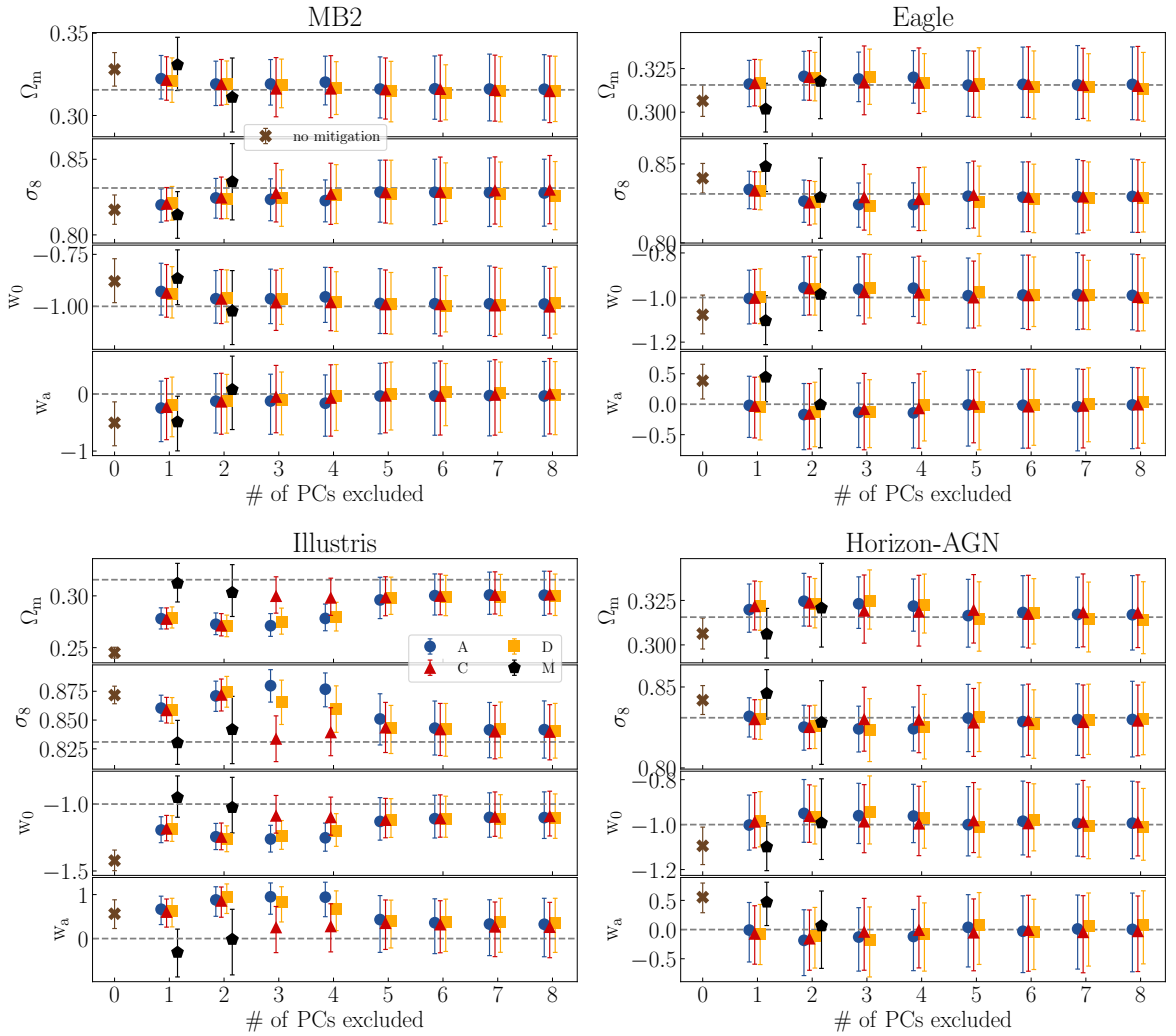

Figure 4.9: Marginalized 1D constraints on cosmological parameters when using different baryonic physics mitigation techniques from Table 4.3. Each panel is for a different input data vector based on a different hydrodynamical simulation as explained in the plot title. The gray dashed horizontal lines indicate the fiducial cosmological values. The marker position, the lower and upper error bars indicate the median, the 16th and the 84th percentiles of marginalized 1D posteriors. The brown crosses indicate the results when fitting the data vectors with the DMO-based emulator (HALOFIT) without applying any baryonic physics mitigation technique. The blue circles, red triangles and yellow squares show the results when applying PCA-based methods A, C, and D respectively, with their positions in the $x-$direction indicating how many PC modes are excluded or numbers of marginalization parameters used when doing the analysis. The black pentagons located at $x = 1$ indicate the result when only marginalizing over A in HMCODE (with η_0 fixed via Eq. (4.28)). The black pentagons located at $x = 2$ are the results when marginalizing over both A and η_0 in HMCODE. *For PCA-based methods, we find the 1σ posteriors start to enclose the fiducial cosmology after removing 2 PC modes for MB2/Eagle/Horizon-AGN, while excluding 6 PC modes is required for more extreme baryonic scenarios of Illustris. When using HMCODE to perform marginalization, except for the Illustris simulation for which marginalizing over A alone is enough, generally it is required to vary both A and η_0 to mitigate baryonic effects to within 1σ.*

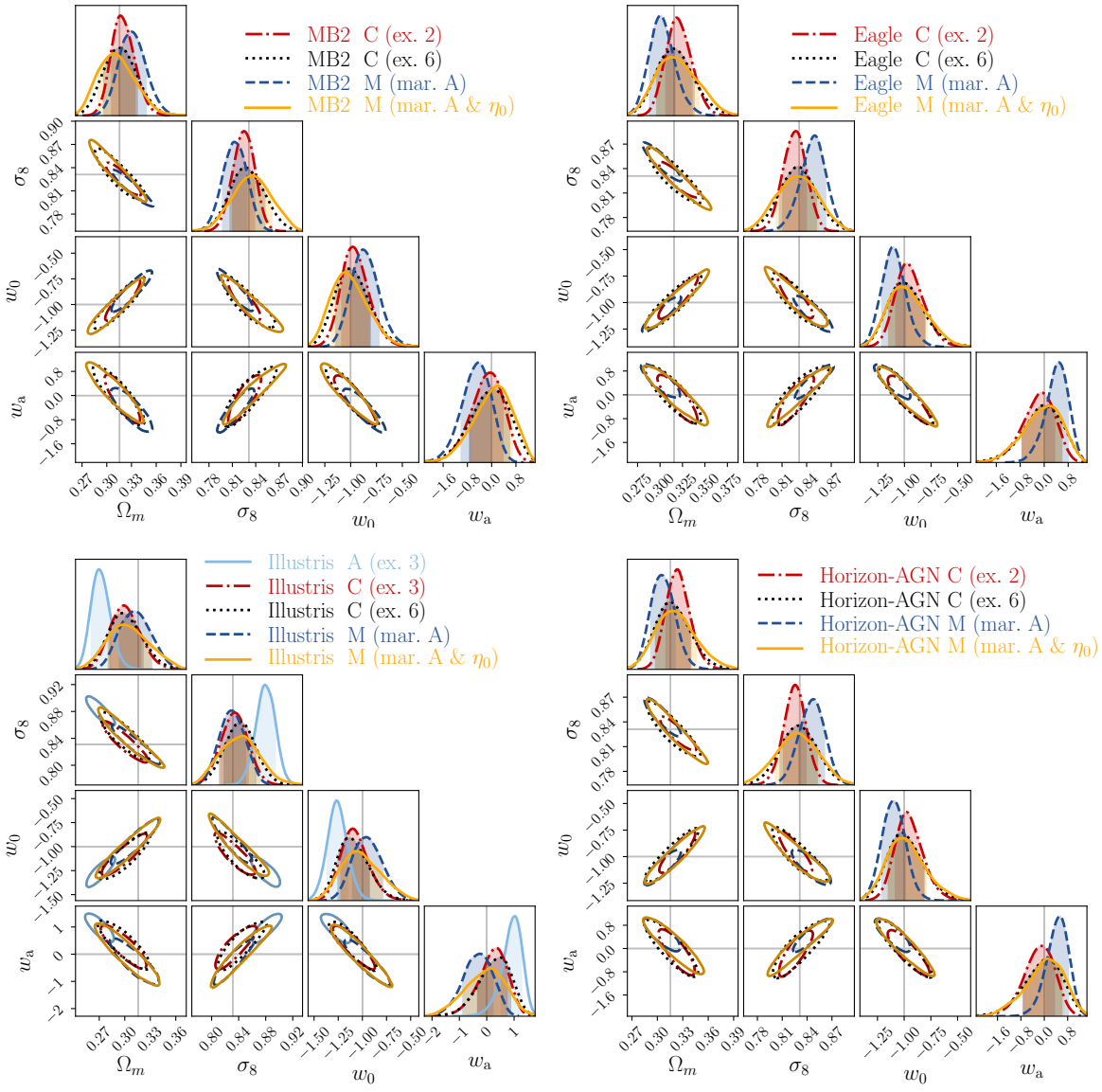

Figure 4.10: The 2D posterior distributions on cosmological parameters for some selected cases shown in Fig. 4.9. Each panel is for a different input data vector based on a different baryonic physics scenario as labeled in the legend. The legend also describes which baryonic mitigation techniques are applied, and how many PC modes are excluded or the HMCODE parameters marginalized over.

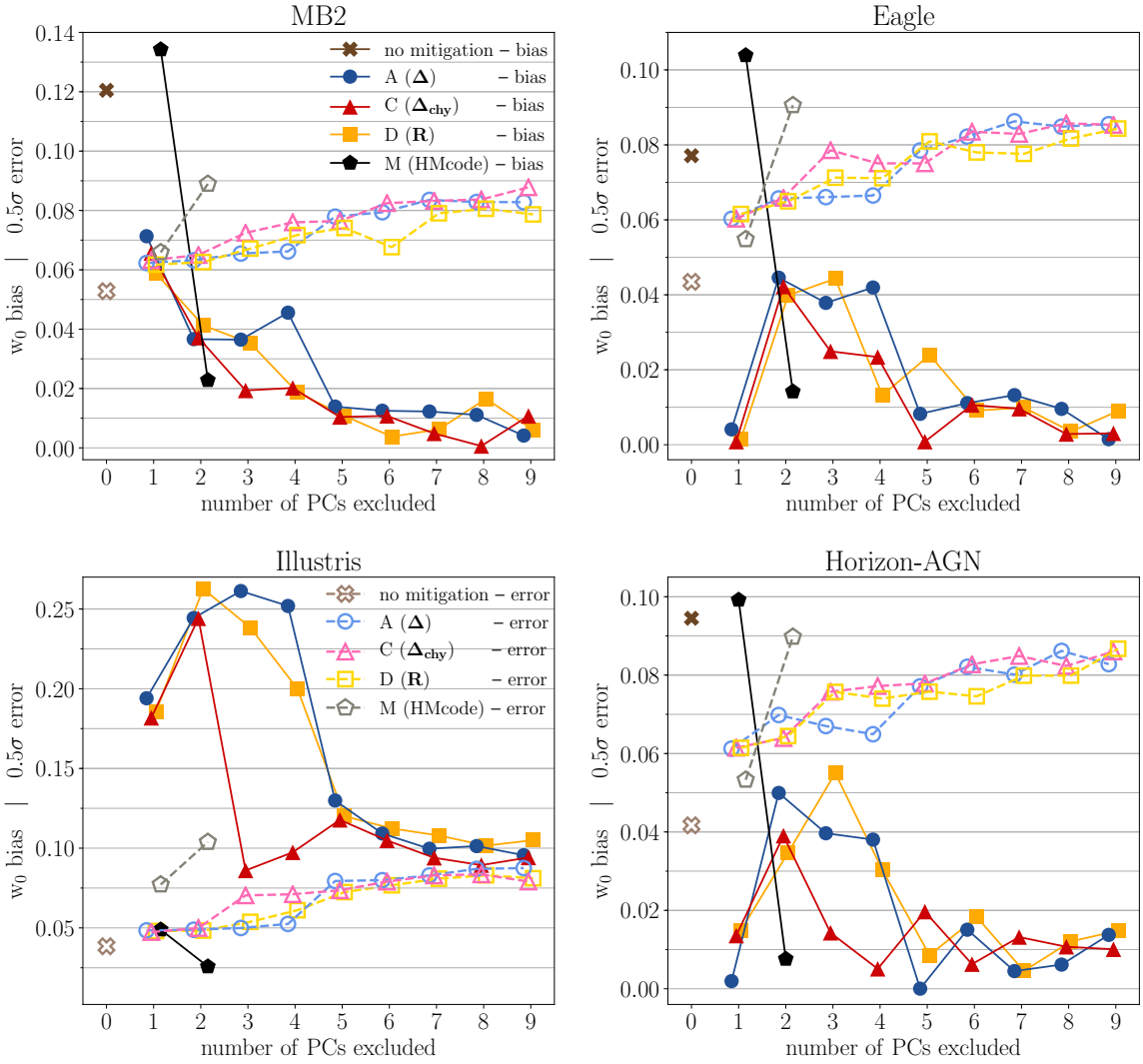

Figure 4.11: The w_0 bias and statistical uncertainty under various baryonic physics mitigation techniques listed in Table 4.3. The darker colored-filled markers indicate the level of w_0 bias, defined as $|w_{0,\text{best fit}} - w_{0,\text{fid}}|$. The fainter unfilled markers indicate the 0.5σ statistical uncertainty, with 1σ defined as the half difference between the 16th and 84th quantiles of the marginalized 1D w_0 posterior distribution. We adopt a criterion of residual bias $< 0.5\sigma$ error in this work when determining how many PC modes are required to mitigate biases due to baryonic physics. *The four main lessons from this plot are that: i) Of various PCA methods, at fixed number of excluded PC modes, the biases of method C are nearly always smaller than methods A and D, indicating method C is the most efficient PCA method. ii) For MB2/Eagle/Horizon-AGN simulations, removing ≥ 2 PC modes is enough to mitigate baryonic physics-induced bias to 0.5σ. For the Illustris simulation, all PCA methods fail to pass the bias $< 0.5\sigma$ criteria even after 9 PC modes are removed. iii) No matter which PCA method (A, C or D) is applied, after removing ≥ 6 PC modes, the statistical errors on w_0 converge to similar values. iv) HMcode works particularity well for the Illustris simulation. For MB2/Eagle/Horizon-AGN, marginalizing over both A and η_0 is required to safely mitigate baryons to 0.5σ.*

dot-dashed curves) enclose the fiducial cosmology, while the posteriors of method A (light blue solid curves) are several σ away. Based on these, we conclude that PCs build from $\mathbf{\Delta}_{\rm chy}$ are potentially more effective than others to mitigate baryonic effects.

To understand why method C performs better, we can go back to the χ^2 equation when both $\boldsymbol{D}$ and $\boldsymbol{M}$ are set at $\boldsymbol{p}_{\rm co,fid}$:

$$\begin{aligned}\left\langle \chi^2_{\rm bary} \right\rangle + \langle \text{Noise} \rangle &= \left\langle [\boldsymbol{D} - \boldsymbol{M}(\boldsymbol{p}_{\rm co,fid})]^{\rm t}\, \mathbf{C}^{-1}\, [\boldsymbol{D} - \boldsymbol{M}(\boldsymbol{p}_{\rm co,fid})] \right\rangle \\ &= \left\langle [\boldsymbol{D} - \boldsymbol{M}]^{\rm t}\, \mathbf{L}^{-1^{\rm t}} \mathbf{L}^{-1}\, [\boldsymbol{D} - \boldsymbol{M}] \right\rangle \\ &= \left\langle [\boldsymbol{D}_{\rm ch} - \boldsymbol{M}_{\rm ch}]^{\rm t}\, \mathbb{1}\, [\boldsymbol{D}_{\rm ch} - \boldsymbol{M}_{\rm ch}] \right\rangle \ .\end{aligned} \tag{4.29}$$

$\left\langle \chi^2_{\rm bary} \right\rangle$ quantifies the amount of χ^2 caused by baryonic uncertainties. The noise term in our likelihood simulation is zero by construction. Our goal is to reduce $\left\langle \chi^2_{\rm bary} \right\rangle$ to avoid bias in cosmological parameters due to baryonic physics. From Eq. (4.29), one can see that when doing PC mode exclusion in $\boldsymbol{D}_{\rm ch} - \boldsymbol{M}_{\rm ch}$ (with PCs constructed in $\mathbf{\Delta}_{\rm chy}$), there is a direct connection in reducing $\left\langle \chi^2_{\rm bary} \right\rangle$, while when doing PC mode exclusion in $\boldsymbol{D} - \boldsymbol{M}$ (with PCs constructed in $\mathbf{\Delta}$), the covariance matrix in between makes the reduction of baryonic uncertainties less direct.

Error bars converge for all PCA methods

Going back to Fig. 4.11, and focusing on the trend in the 0.5σ error bars of w_0 shown in open fainter-colored markers. Generally, error bars grow as more PC modes are excluded (see also Fig. 4.10 for the growth of error ellipse on 2D posteriors). The size of the error bars varies among the different PCA methods when fewer PC modes are excluded, but eventually converge/saturate to similar error bar sizes when excluding $\gtrsim 6$ PC modes, independent of how PCs are constructed. This means that the PCs fully absorb the range of matter power spectrum modifications due to baryonic physics across the nine OWLS simulation, characterizing them using 6 dominant degrees of freedom; the last 3 PC modes are subjected to very small singular values (σ as depicted in Fig. 4.5) such that only a tiny amount of baryonic fluctuation would be projected on them. In principle, including more training samples with different features would enrich the PC pool, increasing the number of effective degrees of freedom to characterize other possible baryonic scenarios.

4.5.3 PCA framework versus HMcode

We now move to a more detailed comparison of the two main ways to marginalize over baryonic uncertainties, namely the PCA-based methods and the halo-model based approach. Since we already compared in §4.5.2 that of all PCA methods listed in Table 4.3, method C is more efficient than the other two in mitigating biases in cosmological parameters due to baryonic physics. In the following, we will use method C as a representative for PCA-based methods, and compare it with HMcode (method M).

Comparison on the effectiveness (criterion: bias $< 0.5\sigma$)

We begin by discussing the performance of HMcode when using only one (A) vs. two (both A and η_0) parameters to marginalize over baryonic physics. When only the parameter A is used, HMcode sets the η_0 value via Eq. (4.28). Going back to Fig. 4.11, with w_0 as an example, the pentagons at an x-axis value of 1 indicate the bias (black-solid) and 0.5σ error (gray-open) of only varying A in HMcode. Similarly, the pentagons at an x-axis value of 2 indicate the option for HMcode varying both A and η_0. For the Illustris simulation, both options can successfully mitigate the baryonic bias on w_0 to within our 0.5σ criterion. However, apart from Illustris, for the baryonic scenarios of MB2, Eagle, and Horizon-AGN, we find that varying only A while setting η_0 following Eq. (4.28) is not sufficient to mitigate baryonic bias. This implies that the current empirical relation described in Eq. (4.28) may not be precise enough for MB2/Eagle/Horizon-AGN-like data vectors with LSST-like statistical power. We therefore recommend that the extra freedom carried by η_0 is needed for upcoming weak lensing surveys to effectively mitigate the impact of baryonic physics on cosmological weak lensing measurements. This is even more true in light of recent findings that indicate that our Universe is not like Illustris, for which the AGN feedback is known to be too strong such that the baryon fractions in massive halos are too low compared with observations (Haider et al., 2016). In Fig. 4.19 of Appendix 4.D, we also provide similar bias and error plots for other cosmological parameters: Ω_m, σ_8, and w_a. The same conclusion holds for HMcode on these cosmological parameters (as shown in the filled and open pentagons), except for the w_a constraint for Illustris (Fig. 4.19l), where varying only A is not enough to mitigate w_a bias to within 0.5σ.

For the PCA-based method C, as indicated in red triangles of Fig. 4.11 for w_0 and Fig. 4.19 for Ω_m, σ_8, and w_a), we find that removing ≥ 3 PC modes is sufficient to mitigate baryonic uncertainties to within 0.5σ for all cosmological parameters considered here, if our Universe has a baryonic physics scenarios like MB2/Eagle/Horizon-AGN.

For the case of the Illustris simulation, we find that the PCA method fails to mitigate baryonic biases to within 0.5σ for w_0 and Ω_m (Fig. 4.19d), even after 9 PC modes are removed, but just passes the threshold for σ_8 (Fig. 4.19h) and w_a (Fig. 4.19l) after removing 7 PC modes. We note that this is likely not a major concern as the baryonic effects of Illustris are unrealistically large, and the next generation IllustrisTNG hydrodynamical simulation (Pillepich et al., 2018a; Springel et al., 2018) will address the defects of the old version.

We provide a summary of the results from the above discussion in Table 4.4. In Appendix 4.E, we further provide the χ^2 values computed at the best-fitted cosmological parameters from various baryon mitigation models.

Comparison on the level of degradation on cosmology

We now compare the error bars on cosmological parameter constraints between PCA method C and HMcode, on baryonic scenarios of MB2/Eagle/Horizon-AGN, where both methods successfully mitigate the baryonic biases to within 0.5σ. The pink open triangles in Fig. 4.11 indicate the 0.5σ error of w_0 under method C, and the gray open pentagons indicate the same for HMcode. Besides w_0, other cosmological parameters are also shown in Fig. 4.19. As discussed in §4.5.2, one nice feature of the PCA method is that the error bars converge to a certain level when excluding ≥ 6

Table 4.4: Summary of the effectiveness of baryonic physics mitigation methods in reducing biases to within 0.5σ for various cosmological parameters under different baryonic scenarios. A cosmological parameter is struck out if a mitigation method fails to pass our criterion of bias $< 0.5\sigma$, where σ represents the marginalized statistical error (see §4.5.3 for detail).

	MB2/Eagle/Horizon-AGN	Illustris
HMCODE (A)	all fail	Ω_m σ_8 w_0 ~~w_a~~
HMCODE (A, η_0)	all pass	all pass
PCA (trained by 9 sims)	all pass	~~Ω_m~~ σ_8 ~~w_0~~ w_a

PC modes. We find that the converged error bars for method C generally are smaller than those for HMCODE, even though HMCODE only utilizes 2 parameters to marginalize over baryonic physics uncertainties while the PCA method needs 3 parameters to mitigate baryonic effects to 0.5σ in the case of MB2/Eagle/Horizon-AGN. A similar result can be seen from the 1σ 2D posteriors shown in Fig. 4.10.

Baryonic feature constraint from HMCODE

In Fig. 4.12, we plot the 2D posterior distributions on A and η_0 for various baryonic scenarios in colored contours, along with Eq. (4.28) shown in the black line. We can see that although relying on this A-η_0 relationship is not effective enough to mitigate baryonic bias in most of baryonic recipes under LSST-like survey, the suggested relationship is still good enough to pass the 68% contours in all cases. Therefore, instead of following a fixed relationship like Eq. (4.28) or allowing both A and η_0 to vary unboundedly, setting an A-dependent prior on η_0 may help recover some cosmological constraining power while still reducing biases in cosmological parameters when using HMCODE.

In Fig. 4.13, we compare the power spectra generated from HMCODE at the best-fitted values of A, η_0 (cross symbols in Fig. 4.12) to the original power spectra derived directly from the hydrodynamical simulations at redshift $z = 0, 1, 2, 3$. We note that this is not a fair comparison because the underlying $P_\delta(k, z)$ is not constrainable from the projected tomographic power spectra, unless the tomographic bins are fine enough to recover the full 3D information.[11] Here we simply use these plots to understand the effects of HMCODE parameters on $P_\delta(k, z)$. Firstly, HMCODE does not have degrees of freedom for the cooling feature of hydro simulations, which leads to a turn-over in the power spectrum ratio at $k \gtrsim 10\ h^{-1}$Mpc. This is expected as according to M15, the halo-model power is accurate to $\approx 5\%$ only for $k \leq 10\ h^{-1}$Mpc and $z \leq 2$. Because of this limitation, HMCODE tends to produce a shallower suppression of power for a given k (when $k \leq 10\ h^{-1}$Mpc) compared with MB2/Eagle/Horizon-AGN, in order to compensate for the lack of cooling prescription at $k > 10\ h^{-1}$Mpc. Secondly, the redshift evolution of HMCODE power spectra is too monotonic, lacking freedom to capture the complicated evolutionary pattern that generally exists in hydrodynamical simulations. The redshift

[11] If using HMCODE to directly fit the 3D matter power spectrum including baryonic effects at some specific redshift, according to M15, by adjusting $A(z)$, and $\eta_0(z)$, HMCODE has enough degrees of freedom to match the baryonic power spectra from the OWLS simulations to $k \gtrsim 10\ h^{-1}$Mpc.

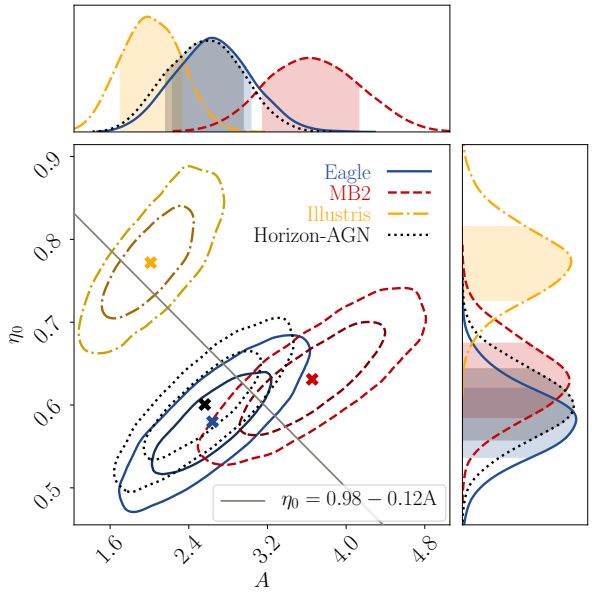

Figure 4.12: The 2D constraints on the HMcode halo structure parameters A and η_0 from our simulated likelihood analysis for baryonic scenarios of Eagle (blue/solid), MB2 (red/dotted), Illustris (green/dot-dashed), and Horizon-AGN (yellow/dashed). The black line plots the relationship between A and η_0 that is used to provide single-parameter fit in HMcode. Both 68% and 95% confidence levels are shown.

evolution patterns can be very different for various baryonic scenarios. HMcode's inability to model redshift evolution may be due to the fact that only two nuisance parameters are involved in describing the complex scale and redshift dependences of baryonic effects seen in the simulations. One straightforward suggestions is to add redshift dependence to A and η_0. Further development of halo model approaches to account for the modification of the matter power spectrum for $k > 10\ h^{-1}$Mpc is also needed. Although the current model does not describe all the complexity of possible modifications of $P(k)$ due to baryonic physics, we can still use HMcode to gain insight into the strength of feedback from the constrained values of A and η_0. As shown in Fig. 4.12, the Illustris-like universe tends to have small A and large η_0.

4.5.4 Pushing to even smaller angular scales: $\ell_{\rm max}$ of 5000

Until now, all elements of our analysis have been based on mock tomographic shear data vectors with $\ell_{\rm max} \approx 2000$, which is a conservative choice under the limitation that we lack accurate power spectra at $k > 30\ h^{-1}$Mpc. The $\ell_{\rm max} \approx 2000$ cut assures that various extrapolation curves on $P_\delta(k)$ ratio out to $k > 30\ h^{-1}$Mpc would not cause significant change on the resulting $C^{ij}(\ell)$ data vector (see Appendix 4.B for details on how the scale cut limit is determined).

To further test the limits of the proposed baryonic mitigation techniques, we generate mock $C^{ij}(\ell)$ data vectors with $\ell_{\rm max} \approx 5000$ (based on the quadratic extrapolation trends derived by fitting the $P_\delta(k)$ ratio in $k \in [10, 30]\ h^{-1}$Mpc, see the red curve in Fig. 4.16 as a demonstration), and then perform the

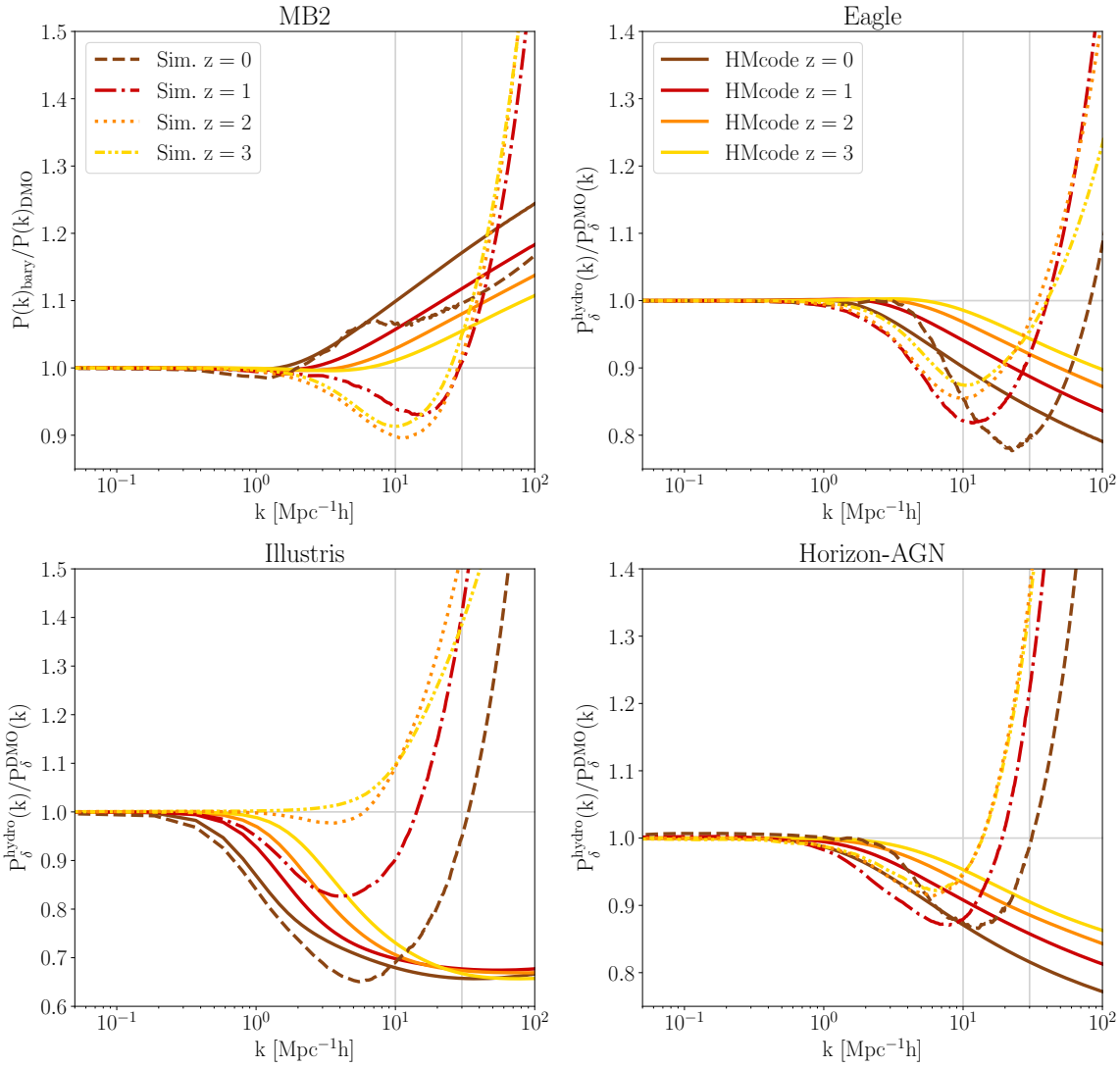

Figure 4.13: Comparisons of power spectra generated from HMCODE at the best-fitted A and η_0 values (solid lines) and power spectra directly derived from hydrodynamical simulations (dotted or dashed lines) at z = 0, 1 , 2, 3. *The discrepancy indicates that HMCODE lacks degrees of freedom to account for the cooling effect at high k, and that it is too simplified to capture the complex redshift evolution patterns present in hydrodynamical simulations.*

Table 4.5: Similar to Table 4.4, but now for the likelihood simulations with mock observables pushing to $\ell_{\rm max} \approx 5000$.

	MB2/Eagle	Horizon-AGN	Illustris
HMCODE (A)	all fail	all fail	all fail
HMCODE (A, η_0)	all pass	$\Omega_{\rm m}$ σ_8 w_0 ~~w_a~~	~~$\Omega_{\rm m}$~~ ~~σ_8~~ w_0 w_a
PCA (trained by 9 sims)	all pass	all pass	all fail
PCA (trained by 12 sims)			all fail

same simulated likelihood analyses with mitigation techniques described in §4.3 and §4.4. The only difference is that we append 3 extra data points that with equal logarithmic spacing in $\ell \in [2060, 5000]$ to the original data vector $\boldsymbol{D}$ in each tomographic bin. The new length of $\boldsymbol{D}$ is thus extended to $55 \times (18 + 3) = 1155$ data points (see §4.3.2 for the original format of $\boldsymbol{D}$). The covariance matrix is also updated accordingly.

The dark gray contours in Fig. 4.14 indicate the 2D posterior distributions of the cosmological parameters, when no baryonic physics mitigation technique is applied. Compared with the similar plot shown in Fig. 4.4, but for $\ell_{\rm max} \approx 2000$, the biases on cosmological parameters increases to $2\sigma \sim 19\sigma$ for the various cosmological parameters in an Illustris-like universe, and around $1.5\sigma \sim 6\sigma$ for the other cases. This amount of bias is consistent with Fig. 5 of E15, who showed the posterior distributions for $\ell_{\rm max} \sim 5000$ for the OWLS baryonic physics scenarios for an LSST-like likelihood simulations.

Since we showed in §4.5.2 that method C is the most efficient of the PCA-based methods, we only run simulated likelihood analyses with PCA-based method C, compared with method M using HMCODE for $\ell_{\rm max} \approx 5000$. In Fig. 4.15, we plot the marginalized w_0 bias (color-filled symbols) and 0.5σ w_0 uncertainty (open symbols) as a function of the number of excluded PC modes in method C (blue diamonds) and HMCODE (yellow hexagons). (The red triangles and black pentagons are simply copies of the data points shown in Fig. 4.11, to enable easier comparison of results with $\ell_{\rm max}$ of 2000 versus 5000.) The bias and error plots for $\Omega_{\rm m}$, σ_8 and w_a are also provided in Fig. 4.19.

Similar to §4.5.3, we rely on the bias $< 0.5\sigma$ criterion to validate the effectiveness of baryonic physics mitigation methods, with the results summarized in Table 4.5. First of all, for HMCODE, varying only A is not sufficient to mitigate the bias to within 0.5σ for the Illustris simulation, which HMCODE is particularly good at describing. Both A and η_0 must be varied to meet our criterion for MB2 and Eagle. For Horizon-AGN and Illustris, HMCODE works well for some cosmological parameters, while it fails for the others. For the PCA method, it still works for baryonic scenarios of MB2/Eagle/Horizon-AGN when pushing to $\ell_{\rm max} \approx 5000$, but continues to fail to meet our criterion for the Illustris scenario.

In terms of degradation on cosmological parameter constraints after marginalization, for the cases of MB2 and Eagle, the scenarios in which both PCA and HMCODE succeed in mitigating the bias to within 0.5σ, we see that PCA method yields smaller converged error bars (light blue open diamonds) compared with HMCODE using 2 parameters (yellow open hexagons) to do marginalization.

Does extending the data vectors to $\ell_{\rm max} \approx 5000$ help to better constrain cosmological parameters

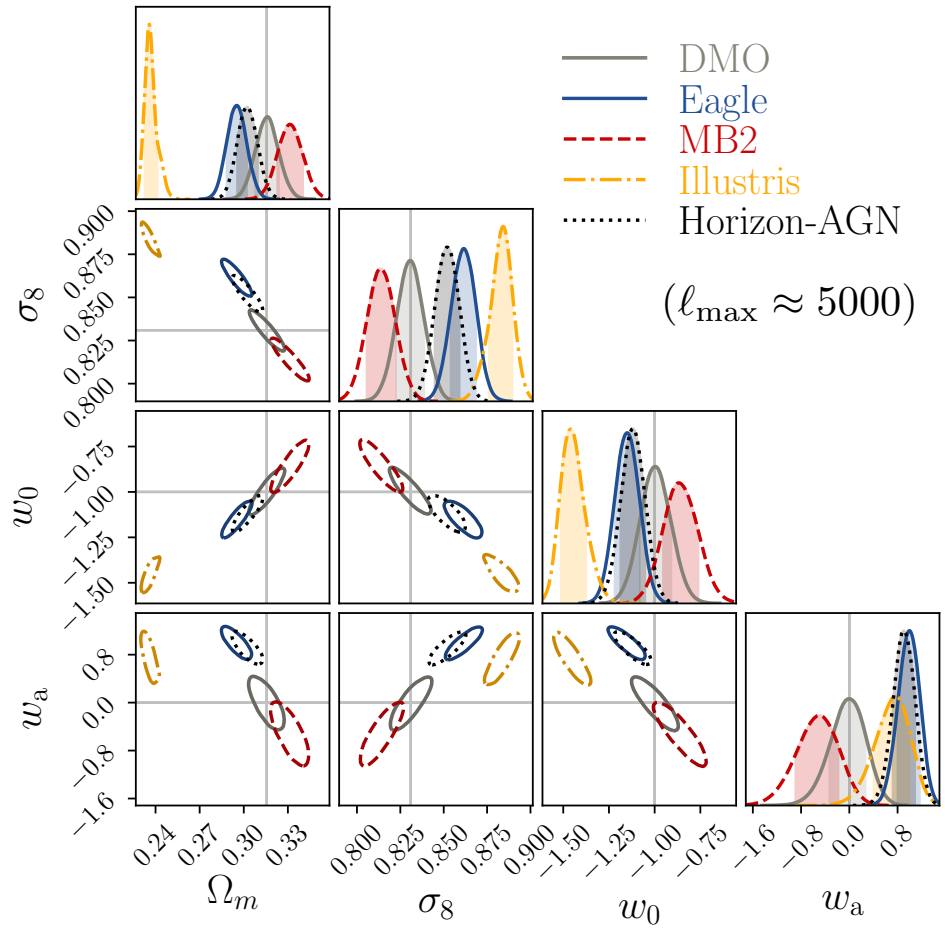

Figure 4.14: Similar to Fig. 4.4, but for the cases when pushing our mock observables toward $\ell_{\rm max} \approx 5000$.

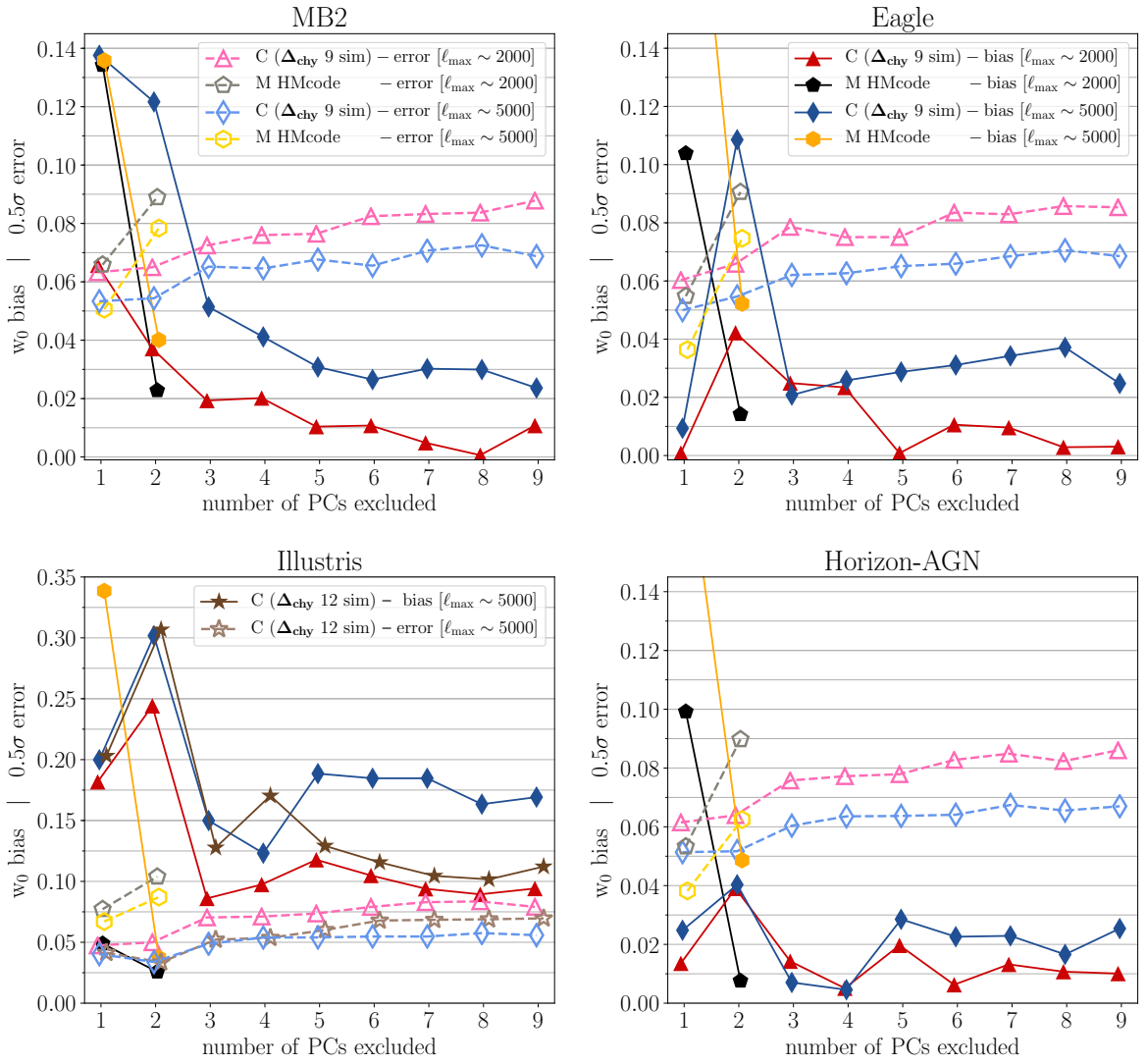

Figure 4.15: The w_0 bias and uncertainty for the baryonic physics mitigation methods C (as our representative for PCA-based method) and M (halo model-based method/HMCODE) (see Table 4.3 for details). The darker colored-filled markers indicate the level of w_0 bias, defined as $|w_{0,\text{best fit}} - w_{0,\text{fid}}|$. The fainter colored-open markers indicate the 0.5σ w_0 uncertainty, with 1σ defined as the half difference between the 16th and 84th percentile of the marginalized 1D w_0 posterior distribution. *The four key results on this plot are: i) the PCA method (blue diamonds) mitigates bias to within 0.5σ for the milder baryonic physics scenarios – MB2, Eagle, and Horizon-AGN – after excluding more than 3 PC modes, but fails for the Illustris scenario. ii) When marginalizing over both A and η_0, HMCODE (yellow hexagons) mitigates w_0 to within 0.5σ for all baryonic scenarios. iii) For baryonic scenarios of MB2 and Eagle, the cases for which both methods work, the error bars for the PCA method (light blue open diamonds) converge to smaller values compared with HMCODE (yellow open hexagons). iv) Including more small-scale data in the analysis reduces the statistical error to* $\sim$ 20% *for PCA method (light blue open diamonds v.s. pink open triangles) and to about* 12% $\sim$ 30% *for HMCODE (yellow open hexagons v.s. gray open pentagons). v) Including more training simulations in PCA improves reducing the w_0 bias induced by neglecting baryonic effects to* $\sim$ 15% *for the case of Illustris (brown solid stars v.s. blue solid diamonds), although the improvement on residual bias is not reaching our criterion of* $< 0.5\sigma$.

compared with $\ell_{\rm max} \approx 2000$? As shown in Fig. 4.11, for the PCA method, we observe that the converged w_0 errors for the $\ell_{\rm max} \approx 5000$ cases (light blue open diamonds) are smaller by $\sim 20\%$ compared with the errors for $\ell_{\rm max} \approx 2000$ (pink open triangles). For the cases of HMcode when varying both A and η_0, the w_0 errors reduce by $\sim 12\%$ for MB2, $\sim 18\%$ for Eagle, and $\sim 30\%$ for Horizon-AGN, after extending data points to $\ell_{\rm max} \approx 5000$ (yellow open hexagons) from $\ell_{\rm max} \approx 2000$ (gray open pentagons). This means that we do benefit from additional constraining power when including more small-scale data in the analysis, if the baryonic physics effect in our Universe is near the physics implemented in Eagle/MB2/Horizon-AGN.

4.5.5 Including more AGN prescriptions in the training set

The reason why the PCA method fails to mitigate the impact of baryonic physics on the matter power spectrum in Illustris is that the PCs built from the current training set do not capture the strong variation with k to explain its intense feedback feature. As also discussed in Mohammed & Gnedin (2018), it is better to have a training set that comprises adequately exotic but reasonable models. Of the nine training OWLS simulations, only the OWLS-AGN contains an AGN feedback prescription, and we rely on this single AGN model to explain Illustris. However, this shortcoming can be fixed by incorporating more training simulations into the PCA, so that the resulting PCs will include more degrees of freedom to explain the broader range of outcomes due to baryonic physics.

We try to address the above Illustris problem by including the baryonic scenarios of MB2/Eagle/Horizon-AGN in our training set, and then build a $\mathbf{\Delta}_{\rm ch}$ matrix with 12 columns to extend the capability of the derived PCs. In the bottom left panel of Fig. 4.15, we plot the marginalized w_0 bias (brown filled stars) and error (light brown open stars) for Illustris simulation with PCs trained from the 12 baryonic scenarios, and a scale cut at $\ell_{\rm max} \approx 5000$. (The results for other cosmological parameters can be found in the last column of Fig. 4.19 as well.) With this expanded training set, the PCA method now reduces the w_0 bias from 1.5σ (blue filled diamonds) to 0.8σ (brown filled stars), which is an improvement but still does not enable us to meet our criterion of bias $< 0.5\sigma$.

The error bars when using 12 simulations in the training set converge after removing ≥ 6 PC modes. Notice that the converged errors become bigger when the PCs are trained from 12 simulations rather than just the 9 OWLS simulations. By including more simulations to construct the PCs, we also enlarge the range of baryonic uncertainties, which is a trade-off to ensure a more effective removal of biases due to baryonic physics for a broad range of baryonic physics scenarios. However, we can also imagine trying to rely on external information from independent observations to rule out baryonic scenarios that fail to describe our Universe. By carefully controlling the uncertainty range of the training set, we could potentially improve the cosmological constraining power after mitigation.

4.6 Summary and Discussion

We have explored the two major approaches to mitigate uncertainties in cosmic shear tomographic power spectra due to baryonic physics, with the goal of understanding their performance on cosmological constraints for the upcoming LSST survey. The first approach is the PCA-based analysis proposed by E15. Based on a set of training hydrodynamical simulations with various baryonic prescriptions

(spanned by OWLS in this work), a difference matrix (Eq. (4.8)) is computed. Its columns are filled with difference vectors between these hydro and DMO simulations. PCA is then performed on the difference matrix to find dominant PC modes that can be used to model baryonic effects in other hydro simulations. The second approach is the halo model-based method coded in the package of HMCODE by M15, which utilizes two halo structural parameters (A and η_0) related to the halo concentration-mass relation to marginalize over baryonic uncertainties.

We examine the basics of the PCA formalism and provide a modification to properly account for the change of covariance matrix after removal of PC modes. Under the new formalism, we demonstrate that PC mode removal is equivalent to marginalization over PC amplitudes (see §4.5.1). Instead of difference matrices, we also investigate PCA on other kinds of matrix forms with their columns filled with the fractional difference (Eq. (4.25)) or noise-weighted difference vectors (Eq. (4.20)) to quantify deviations in the matter power spectrum due to baryonic physics. The derived PC bases from different matrices vary in their efficiency in explaining baryon fluctuations at different angular scales. Difference matrix PCs can more effectively account for large scale baryonic fluctuations, fractional difference matrix PCs are more effective at describing the small scale fluctuations, and noise-weighted difference matrix PCs most effectively describe the scales at which the S/N is maximal. We find that performing PCA on the noise-weighted difference matrix, with the weighting factor derived via performing Cholesky decomposition on the covariance matrix (§4.4.2), is the most efficient way to mitigate the impact of baryonic physics on inferred cosmological parameters (§4.5.2). Therefore, for future application on real data, we recommend applying the noise-weighted PCA technique.It should be noted that except for method D, the current PCs are wiggling slightly in their directions at each MCMC step, when cosmology changes. If we would like to quantify baryon physics via PC amplitudes, we hope the constrained PC amplitudes are subjected to a fixed set of PCs. A more complete design of PCA algorithm therefore would be an iteration process. We will first use the current setting to find the best-fitted cosmology, and once the $\boldsymbol{p}_{\rm co,best\ fit}$ is determined, we will fix PC basis at $\boldsymbol{p}_{\rm co,best\ fit}$, and constrain the posteriors of PC amplitudes subjected to this PC set.

We apply both the PCA and HMCODE techniques on mock shear tomographic data vectors ($C^{ij}(\ell)$) with baryonic physics scenarios of MB2/Eagle/Illustris/Horizon-AGN. We test whether these mitigation techniques can reduce the bias in cosmological parameters induced by neglecting baryonic effects to within 0.5σ. With a scale cut at $\ell_{\rm max} \approx 2000$, and for milder baryonic physics scenarios like MB2/Eagle/Horizon-AGN, both methods succeed in mitigating the impact of baryonic effects on the inferred cosmological parameters. For the PCA method, we find that excluding 3 PC modes is sufficient to mitigate the bias to within 0.5σ for $\Omega_{\rm m}, \sigma_8, w_0$ and $w_{\rm a}$. For HMCODE, we find that it is safer to vary both A and η_0 when performing marginalization, rather than varying only one of them and having the other follow the suggested relation in M15, at least at the level of LSST statistical power. For the Illustris scenario, only HMCODE is sufficient to mitigate the bias to within 0.5σ. The PCA method fails to pass our criterion even after removing 9 PC modes. With a more aggressive $\ell_{\rm max}$ of 5000, the PCA methods still work for MB2/Eagle/Horizon-AGN, but fail for Illustris. HMCODE remains sufficient for MB2/Eagle after marginalizing over 2 parameters but only works partially on some of the cosmological parameters for Horizon-AGN and Illustris, as summarized in Table 4.5.

We found that HMCODE is most effective at mitigating the impact of baryonic physics for a strong feedback scenario like Illustris, because HMCODE is designed to describe the impact of baryonic

physics on the matter power spectrum for $k \leq 10\ h\mathrm{Mpc}^{-1}$, where the main feature is the suppression of power due to feedback (Fig. 4.1). HMcode and halo model-based approaches in general have the advantage over PCA that they have cosmology dependence built in. Although the current version of HMcode lacks the complexity to fully describe various baryonic scenarios (Fig. 4.13), it provides a good summary of the level of feedback strength through two nuisance parameters (Fig. 4.12). Future improvements of the halo model to smaller scales of $k \geq 10\ h\mathrm{Mpc}^{-1}$, as well as adding parameters to allow additional freedom in the redshift evolution of baryonic physics effects, may constrain halo structural parameters and baryonic power spectra ratio curve together with cosmology. Exploring the prior ranges on halo model parameters also help to improve cosmological parameter constraint. For example, we can use the posterior constraints from realistic hydrodynamical simulations as shown in Fig. 4.12 to narrow down the allowed ranges of A and η_0. Joint constraints from galaxy-galaxy lensing together with cosmic shear may also provide additional information from the data itself on the halo structure parameters (Zentner et al., 2008).

There are several advantages of the PCA method. Firstly, it successfully mitigates quite general baryonic fluctuations and complex redshift evolution patterns, when collecting several representative training hydrodynamical simulations to conduct PCA. The complex baryonic behaviors as well as the redshift evolution would then be naturally absorbed in only a few dominant PC modes, and we can use the amplitudes of these PC modes to perform marginalization (or, equivalently, PC mode exclusion). Secondly, the PCA method efficiently accounts for baryonic uncertainties without losing too much cosmological constraining power. As discussed in §4.5.3, whenever both methods are successful in removing baryonic bias, the error bars are generally smaller for PCA methods compared with the errors of HMcode. It is quite important to note that even if we do not know in advance how many PC modes must be excluded to safely remove baryonic bias in our Universe, excluding all effective PC modes does not unacceptably increase the errors, which saturate at a certain limit. The maximum number of effective PC modes one can remove is equal to the total number of training simulations used in the PCA (see §4.4.1 for detail). Finally, the PCA method has significant flexibility to make adjustments as our knowledge of baryonic physics improves. For example, in §4.5.4 we tried to improve the bias mitigation of the Illustris simulation by including more realistic baryonic scenarios with AGN prescriptions in our training set, which enriches the space of possible baryonic uncertainties that the PCs can describe. After the inclusion of MB2/Eagle/Horizon-AGN as well as the original 9 OWLS scenarios in our training set, we can further decrease the residual cosmological parameter bias compared with the results when only using the 9 OWLS simulations as training set. The cost is that we lose some constraining power. The flexibility of the PCA framework makes it easy to adjust the model based on changes in our knowledge of baryonic physics, and allows us to regulate errors by controlling the input training simulations in the PCA.

There are several aspects regarding the PCA framework that we do not explore within this work. Firstly, our training hydro simulations are all run under the flat ΛCDM model, and we assume that the baryonic fluctuations, as quantified in terms of power spectrum ratios between hydrodynamical and DMO simulations, remain fixed when cosmology changes. In reality, baryonic and cosmological effects vary jointly. Currently, there is no easy way to investigate this assumption, but future fast hydrodynamical simulations under development would be an ideal tool to systematically study this issue. Secondly, we adopted a power law extrapolation scheme for $P_\delta(k)$ ratio at $k \geq 30\ h\mathrm{Mpc}^{-1}$ (see

Appendix 4.B). The most relevant physics that governs the high k behavior is the cooling and inner stellar density profile of galaxies. Current large-volume cosmological hydrodynamical simulations lack the resolution to resolve the physics of galaxy formation to galaxy centers. We rely on sub-grid models of feedback to avoid the overcooling of gas and to mitigate the differences between the observed and simulated galaxies, but discrepancies still exist (Stinson et al., 2010; Bottrell et al., 2017; Furlong et al., 2017). This implies that $P_\delta(k)$ in the high k regime is still highly uncertain. Does the $P_\delta(k)$ ratio continue the trend of increasing monotonically? Or should it reach a saturation point at some high k regime? How to properly propagate the uncertainties of the poorly understood small scale $P_\delta(k)$ ratio into the errors of integrated $C^{ij}(\ell)$ which in turn affects the derived PCs? These questions require higher resolution hydrodynamical simulations to further address. Finally, we have briefly demonstrated in §4.5.5 that depending on the training simulation set, the derived PCs carry different abilities to mitigate baryonic effects, and differ in the final constraining power. It would be worthwhile to systematically investigate various possible combinations of the training simulations, to find a most effective set of PCs that are able to span a wide enough range of baryonic uncertainties but with less degradation on constraining power.

In future extensions of this work, we will apply the PCA framework to a configuration-space tomographic shear analysis on real data to constrain the baryonic feature of our Universe and compare it with hydrodynamical simulations. We aim to develop a consistent way of quantifying priors of PC amplitudes, which would provide us with more constraining power on cosmological parameters by shrinking the allowed range of baryonic physics modifications of the matter power spectrum. We will also develop a PCA tool for joint analysis of galaxy-galaxy lensing and galaxy clustering observables. The full 3×2-point analysis then can be self-consistently analyzed within the PCA framework to increase the constraining power on cosmology while safely marginalizing over baryonic physics.

Acknowledgments

We thank Alex Hall for reviewing this paper and providing useful suggestions to improve the manuscript. We thank Sukhdeep Singh, François Lanusse, Qirong Zhu, Arya Farahi, Hy Trac, Phil Bull, Tiziana Di Matteo, Alexander Mead, Irshad Mohammed, Ananth Tenneti for many constructive discussions and feedback. RM and HH are supported by the Department of Energy Cosmic Frontier program, grant DE-SC0010118. Part of the research was carried out at the Jet Propulsion Laboratory, California Institute of Technology, under a contract with the National Aeronautics and Space Administration and is supported by NASA ROSES ATP 16-ATP16-0084 grant.

4.A Power Spectrum Computation

Here we describe the practical implementation of our power spectrum computation from the simulation snapshots.

4.A.1 The power spectrum estimator

The matter density field in the Universe can be quantified via the overdensity $\delta(\mathbf{x})$, defined as $\delta(\mathbf{x}) = \frac{\rho(\mathbf{x})-\bar{\rho}}{\bar{\rho}}$, where $\rho(\mathbf{x})$ specifies the density function at position $\mathbf{x}$ and $\bar{\rho}$ is the global mean density. We first estimate $\delta(\mathbf{x})$ on a uniform grid of 1024 cells across a side of the simulation box with the particle deposition step carried out via Nearest Grid Point (NGP) assignment. Our estimator is

$$\hat{\delta}(\mathbf{x}) = \delta(\mathbf{x}) * W(\mathbf{x}) = \int_{\mathrm{V_{box}}} d\mathbf{x}' \delta(\mathbf{x}') W(\mathbf{x}-\mathbf{x}') \,. \tag{4.30}$$

Here the mass assignment function can be described by $W(\mathbf{x}) = \prod_i W(x_i)$, with

$$W(x_i) = \begin{cases} 1/\Delta L & \text{for} \quad |x_i| < \Delta L/2 \\ 0 & \text{else} \end{cases} \,, \tag{4.31}$$

where the grid cell side length $\Delta L = \mathrm{L_{box}}/1024$, and the index i is the axies label of the Cartesian coordinate system. We then perform a discrete Fourier transform on $\hat{\delta}(\mathbf{x})$ to derive its Fourier transformation pair $\hat{\delta}(\mathbf{k})$:

$$\hat{\delta}(\mathbf{k}) = \delta(\mathbf{k}) W(\mathbf{k}) \,. \tag{4.32}$$

After the Fourier transform, the convolution operation in Eq. (4.30) becomes a simple product, with $W(\mathbf{k})$ being the Fourier space mass assignment window function:

$$W(\mathbf{k}) = \prod_i W(k_i) = \prod_i \frac{\sin\left(\frac{k_i \Delta L}{2}\right)}{\left(\frac{k_i \Delta L}{2}\right)} \,, \tag{4.33}$$

where k_i $(i = x, y, z)$ is the i-th component of $\mathbf{k}$. The Fourier transformation pair of $\delta(\mathbf{x})$ then can be computed by

$$\delta(\mathbf{k}) = \frac{\hat{\delta}(\mathbf{k})}{W(\mathbf{k})} \,. \tag{4.34}$$

We choose the convention of Fourier transform as $\delta(\mathbf{k}) = \int d\mathbf{x}\, \delta(\mathbf{x}) e^{-i\mathbf{k}\cdot\mathbf{x}}$. Under this convention, the power spectrum can be estimated by averaging over all modes $\mathbf{k}$ with a length of k:

$$\hat{P}_\delta(k) = \frac{1}{\mathrm{V_{box}}} \left\langle |\delta(\mathbf{k})|^2 \right\rangle_{k=|\mathbf{k}|} \,, \tag{4.35}$$

with $\mathrm{V_{box}}$ being the box size of simulation.

The raw estimation of $\hat{P}_\delta(k)$ above is known to be affected by discreteness effects, which contributes into the power through a constant amplitude called shot noise

$$P_{\mathrm{shot}} = \mathrm{V_{box}}/N_{\mathrm{eff}} \,. \tag{4.36}$$

Here N_{eff} is the effective number of particles, which accounts for their difference in mass:

$$N_{\mathrm{eff}} = \frac{(\Sigma_i^N m_i)^2}{\Sigma_i^N m_i^2} \,, \tag{4.37}$$

where m_i is the individual particle mass, and N is the total number of particles. For DMO simulations where all tracer particles have equal mass, $N_{\mathrm{eff}} = N$. The final power spectrum $P_\delta(k)$ used throughout this work is derived after subtraction of the shot noise term:

$$P_\delta(k) = \hat{P}_\delta(k) - P_{\mathrm{shot}} \,. \tag{4.38}$$

4.A.2 The accuracy of power spectrum

On large scales, due to the limited size of simulation boxes, the statistical uncertainties of the estimated matter power spectra are dominated by cosmic variance. The contribution of cosmic variance on $P_\delta(k)$ can be estimated by (Takada & Hu, 2013):

$$\sigma^2(k) = 2\frac{P_\delta^2(k)}{N_{\rm modes}(k)} \ . \tag{4.39}$$

$N_{\rm modes}$ is total number of modes available in the bin range $[k - \Delta k/2, k + \Delta k/2]$:

$$\begin{aligned} N_{\rm modes}(k) &= \frac{1}{(2\pi)^3} V_{\rm box} \int_{k-\Delta k/2}^{k+\Delta k/2} 4\pi k^2 \, {\rm d}k \\ &\approx \frac{1}{2\pi^2} V_{\rm box} k^2 \Delta k \ . \end{aligned} \tag{4.40}$$

The small-scale error of power spectra is mostly caused by the simulation resolution. For DMO simulations, Heitmann et al. (2010) pointed out that the $P_\delta(k)$ values of different resolutions are within 1% agreement for $k < k_{\rm Ny}/2$, where the Nyquist wavenumber is set by the inter-particle separation on the initial grid:

$$k_{\rm Ny} = \frac{\pi N_{\rm p}}{{\rm L}_{\rm box}} \, , \tag{4.41}$$

with $N_{\rm p}$ being the cube-root of the total number of particles used in simulations. *For smaller scales at $k > k_{\rm Ny}/2$, we expect a suppression of power for scales around $k \sim k_{\rm Ny}$ followed by a steep rise of power at even larger k* (see Fig. 8 of Heitmann et al. 2010 and Fig. A3 of van Daalen et al. 2011). According to Heitmann et al. (2010), the suppression of power is due to discreteness effects in sampling small scale fluctuations. When fewer low-mass halos are resolved, $P_\delta(k)$ is suppressed at small scales. The steep rise of power is believed to be caused by incorrect shot noise subtraction. Shot noise should be scale-dependent at small scales rather than a simple constant as in Eq. (4.36).

For hydrodynamical simulations, the convergence properties are more difficult to systematically quantify due to the interplay between resolution effects and galaxy formation physics. For example, as the resolution increases, more lower mass halos are resolved, leading to an increased power of SN feedback. Subgrid parameters regulating SN feedback then must be modified to account for this effect in order to match the observables like galaxy stellar mass function. Typically subgrid prescriptions are designed to reach some level of convergence with the variation of resolution. However, the functionality of such self-regulation is rather limited. Eagle is currently the only hydro simulation with its subgrid model parameters re-calibrated to match observations when the resolution is changed (see Fig. 7 of Schaye et al. 2015). In the left-hand panel of Fig. A2 in van Daalen et al. (2011), they showed a convergence comparison between the power spectra of OWLS-REF hydro simulations with $k_{\rm Ny}$ of 16 (the current OWLS resolution used in this work) and 32 respectively. The two baryonic power spectra agree to within $\sim 10\%$ out to $k \approx 40 \ h{\rm Mpc}^{-1}$. We note that this statement only applies to OWLS-REF. There is no general rule on the behavior of convergence for hydro simulations, given that the galaxy observations are not yet converged, and that the subgrid prescriptions are all different.

4.B Power Spectrum Ratio

The power spectrum ratio between hydrodynamical and DMO simulations is an important quantity in this work. We rely on it in Eq. (4.1) to derive mock observables at different cosmology, as well as to build difference matrices to perform PCA. Here we discuss the validity of our estimates of this ratio over the range of scales used throughout this work, and describe how we perform extrapolation to smaller scales than those that are well-described in the simulation.

4.B.1 Discussion on the convergence of the power spectrum ratio

The ratios of matter power spectra that we use in this work are accurate to $k \lesssim 30\ h\mathrm{Mpc}^{-1}$ for Eagle/MB2/Illustris/Horizon-AGN and of $k \lesssim 10\ h\mathrm{Mpc}^{-1}$ for OWLS. Below we will justify this claim.

We have discussed the statistical uncertainty of $P_\delta(k)$ due to cosmic variance in §4.A.2. Based on the first order error propagation, $\mathrm{Var}[\frac{X}{Y}] = \frac{\overline{X}^2}{\overline{Y}^2}\left(\frac{\sigma_X^2}{\overline{X}^2} + \frac{\sigma_Y^2}{\overline{Y}^2} - 2\frac{\mathrm{Cov}[X,Y]}{\overline{X}\,\overline{Y}}\right)$, the cosmic variance contribution to the uncertainty in the power spectrum ratio is

$$\begin{aligned}\mathrm{Var}\left[\frac{P_{\delta,\mathrm{hydro}}(k)}{P_{\delta,\mathrm{DMO}}(k)}\right] = &\frac{1}{P^2_{\delta,\mathrm{DMO}}(k)}\sigma^2_{\mathrm{hydro}}(k)\\ &+\frac{P^2_{\delta,\mathrm{hydro}}(k)}{P^4_{\delta,\mathrm{DMO}}(k)}\sigma^2_{\mathrm{DMO}}(k)\\ &-2\frac{P_{\delta,\mathrm{hydro}}(k)}{P^3_{\delta,\mathrm{DMO}}(k)}\mathrm{Cov}\left[P_{\delta,\mathrm{hydro}}(k), P_{\delta,\mathrm{DMO}}(k)\right]\ ,\end{aligned} \tag{4.42}$$

where the variance of the power spectrum $\sigma^2_{\mathrm{hydro/DMO}}(k)$ is expressed in Eq. (4.39).

The hydrodynamical and DMO runs are set at exactly the same initial conditions, and baryonic effects are negligible on large scales. When $P_{\delta,\mathrm{hydro}}(k) \approx P_{\delta,\mathrm{DMO}}(k)$ and $\mathrm{Cov}\left[P_{\delta,\mathrm{hydro}}(k), P_{\delta,\mathrm{DMO}}(k)\right] \approx 1$, as is the case at small k, we expect the variance of the power spectrum ratio in Eq. (4.42) to approach zero.

On small scales, as discussed in §4.A.2, $P_\delta(k)$ would achieve 1% convergence out to $k \approx k_{\mathrm{Ny}}/2$. Hence, we expect the uncertainty in the power spectrum ratio due to limited simulation resolution to be $< 2\%$ to $k \approx k_{\mathrm{Ny}}/2$, where $k_{\mathrm{Ny}}/2$ is $\sim 30\ h\mathrm{Mpc}^{-1}$ for Eagle/MB2/Illustris/Horizon-AGN and $\sim 10\ h\mathrm{Mpc}^{-1}$ for OWLS.

For the cosmic variance contribution on small scales, we can derive an upper limit by setting $\mathrm{Cov}\left[P_{\delta,\mathrm{hydro}}(k), P_{\delta,\mathrm{DMO}}(k)\right]$ to zero in Eq. (4.42), and with the $\sigma^2_{\mathrm{hydro/DMO}}(k)$ estimated using Eqs. (4.39) and (4.40):

$$\mathrm{Var}\left[\frac{P_{\delta,\mathrm{hydro}}(k)}{P_{\delta,\mathrm{DMO}}(k)}\right]_{\mathrm{upper}} \to \frac{8\pi^2}{V_{\mathrm{box}}k^2\Delta k}\frac{P^2_{\delta,\mathrm{hydro}}(k)}{P^2_{\delta,\mathrm{DMO}}(k)}\ . \tag{4.43}$$

For $k \approx 10\ h\mathrm{Mpc}^{-1}$, $L_{\mathrm{box}} = 100\ h^{-1}\mathrm{Mpc}$, $\Delta k = 0.1$, and $\frac{P_{\delta,\mathrm{hydro}}}{P_{\delta,\mathrm{DMO}}} \approx 0.9$, the estimated variance of the power spectrum ratio is ~ 0.0005. Thus the 1σ uncertainty in the power spectrum ratio due to cosmic

variance is expected be $\lesssim 0.3\%$.[12]

If we naively derive the power spectrum ratio by using the raw data points of $P_{\delta,\mathrm{DMO}}(k)$ and $P_{\delta,\mathrm{hydro}}(k)$ at $k > k_{\mathrm{Ny}}/2$, the derived ratio will be overestimated due to the underestimation of the denominator of $P_{\delta,\mathrm{DMO}}(k)$ at scales of several times k_{Ny}, and underestimated toward even higher k due to the overestimation of $P_{\delta,\mathrm{DMO}}(k)$ (see §4.A.2). We will introduce our extrapolation scheme below to avoid the biases.

4.B.2 Power Spectrum Ratio Extrapolation Scheme

For scales below $k < 0.1\ h\mathrm{Mpc}^{-1}$, we simply let the ratio curve asymptotically approach one, which is a justifiable assumption since we know that baryons hardly modify the matter power spectrum on large scales. For small scales, as shown in Fig. 4.1, the power spectrum ratio between hydrodynamical and DMO simulations tends to increase after $k \gtrsim 20\ h\mathrm{Mpc}^{-1}$. This increase is caused by cooling effects in hydrodynamical simulation. In order to capture this physical effect, we make use of data points in $k \in [10, 30]\ h\mathrm{Mpc}^{-1}$, perform a smooth quadric spline fitting in $\log(k)$- $\log(P_{\delta,\mathrm{bary}}(k)/P_{\delta,\mathrm{DMO}}(k))$ space, and extrapolating the fitted trend out to $k > 30\ h\mathrm{Mpc}^{-1}$. Figure 4.1 shows the extrapolation curves for all baryonic scenarios.

The above extrapolation scheme holds for Eagle/MB2/IIIustris/Horizon-AGN simulations, where we have reliable power spectrum ratios in the range $k \in [10, 30]\ h\mathrm{Mpc}^{-1}$. For the OWLS simulation set, as discussed above, the ratio data is only well-determined to $k < 10\ h\mathrm{Mpc}^{-1}$. The black line in Fig. 4.16 indicates the naively derived power spectrum ratio from the raw data of OWLS-AGN and OWLS-DMO. In the case of OWLS-AGN, we do need data points slightly beyond k of $10\ h\mathrm{Mpc}^{-1}$ to capture the transition from suppression to enhancement of power. We therefore still make use of the raw data points in the range of $k \in [10, 30]\ h\mathrm{Mpc}^{-1}$, where the uncertainties may $> 2\%$ but not that worse, to perform extrapolation spline line fitting, and the resulting curve is indicated in the red-dashed curve of Fig. 4.16. The raw data curve is slightly higher than the extrapolating curve when k is large. This is resulting from the underestimation of the DMO power spectrum as discussed in §4.A.2 and §4.B. The extrapolation based on fitting data at $k \in [10, 30]\ h\mathrm{Mpc}^{-1}$ may exhibit uncertainties in the final extrapolation slope at high k. Therefore, we try to explore such uncertainties by setting slightly different extrapolating parameters that are shown as upper (yellow line) and lower (brown dot-dashed) bounds in Fig. 4.16. Finally, we also check the simplest constant extrapolation scheme as shown in the dark blue line. We will explore the effects of different extrapolation schemes on the resulting tomographic shear power spectra later.

If only using data points around $k < 10\ h\mathrm{Mpc}^{-1}$ to perform smooth extrapolation, one would fail to capture the cooling effect that typically exists in hydrodynamical simulations at high k. The light blue dash-dot-dotted line of Fig. 4.16 indicates such an extrapolation based on the data points for $k \in [3, 10]\ h\mathrm{Mpc}^{-1}$. This sets a very important requirement for our method. If we really want to use the PCA framework to achieve better cosmological parameter constraints by including more small scale information, the simulations that are used to build the PC basis must also have high enough resolution

[12] Chisari et al. (2018) have estimated the effect of cosmic variance on the power spectrum ratio (see their Fig. 5) by subsampling the Horizon-AGN simulation with a volume that is 8 times smaller then our setting here. So the expected 1σ error due to cosmic variance in their case should be on the order of 1% ($\sqrt{8}$ times larger then our setting). The total spread of their subsampled power spectra ratios is consistent with our derivation within 3σ.

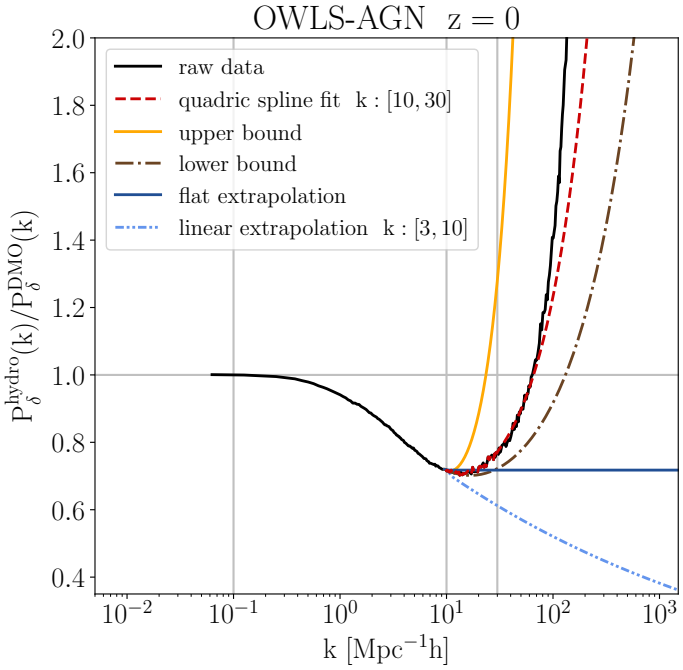

Figure 4.16: Power spectrum ratio between OWLS-AGN and OWLS-DMO at $z = 0$, assuming different extrapolation schemes above $k > 10\ h\text{Mpc}^{-1}$. The black line shows the raw data calculated by simply taking ratio from the raw OWLS power spectra from van Daalen et al. (2011). The red dashed line indicates the extrapolation scheme by extending a quadric spline fitted curve using the raw data points in $k \in [10, 30]\ h\text{Mpc}^{-1}$. The yellow and brown dot-dashed lines indicate the two possible upper and lower bounds one may derive, if there is some uncertainty in the raw data points $k \in [10, 30]\ h\text{Mpc}^{-1}$. The dark blue line plots a pure flat extrapolation. The light blue dash-dot-dotted line indicates the case of extrapolation when using data points in $k \in [3, 10]\ h\text{Mpc}^{-1}$, which are believed to be well-measured.

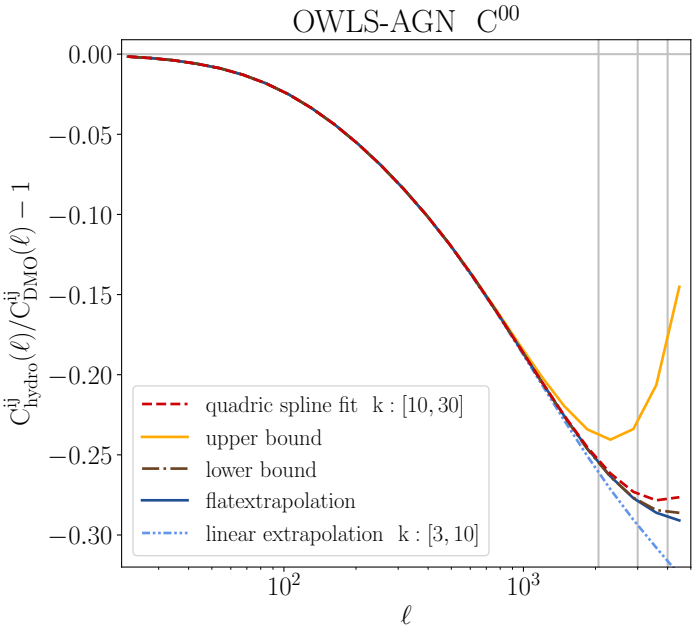

Figure 4.17: The ratio of tomographic shear power spectrum between OWLS-AGN and OWLS-DMO simulations for our lowest tomographic bin. Curves in different colors represent different $P_\delta(k)$ ratio extrapolation schemes as colored in Fig. 4.16. The vertical dashed line indicates the angular scale of $\ell = 2060$, where the cut is made for all of tomographic bins in our data vector. This cut is chosen such that the derived $C^{ij}(\ell)$ curve would not be too sensitive on different $P_\delta(k)$ ratio extrapolation schemes.

to construct a reasonable extrapolation down to the scale that goes into cosmological analysis. This is the reason why we avoid using the Rudd et al. (2008) and Gnedin et al. (2011) simulations to build our PC basis as in the previous work of E15. The half-Nyquist wavenumbers of these two simulations are too low to capture the up-turn in the power spectrum ratio, given the angular scales of $\ell \approx 2000$ used in this work.

We now justify how the choice of angular scale cut at $\ell \approx 2000$ is made. In Fig. 4.17 we present the computed tomographic shear power spectra in our lowest redshift bin, for various extrapolation schemes on the power spectra ratio shown in Fig. 4.16. The vertical gray line indicates the angular scale cut of $\ell = 2060$ we have adopted. One can see that the $C^{ij}(\ell)$ ratio only differs mildly at this scale. Therefore, although our current extrapolation scheme may lead to a considerable error in the $P_\delta(k)$ ratio, after the integration process, such error propagation in $C^{ij}(\ell)$ ratio is estimated to be within 10% when making an ℓ cut at ≈ 2000. We make a conservative choice of cutting in ℓ such that the final result is not too sensitive to our extrapolation scheme.

4.C Computing baryon-contaminated data vectors at varying cosmology

In this Appendix, we describe in detail how we compute baryon-contaminated data vectors as a function of cosmology. This procedure is needed to build the difference matrix (Eq. 4.8), weighted difference matrix (Eq. 4.20), or ratio matrix (Eq. 4.25) when doing PCA.

To produce a baryon-contaminated vector $\boldsymbol{B}_x$ at cosmology $\boldsymbol{p}_{\rm co}$, in principle we should rely on Eq. (4.1) to generate the matter power spectrum for that cosmology, and integrate it to derive the tomographic shear data vector

$$C^{ij}_{{\rm hydro},x}(\ell|\,\boldsymbol{p}_{\rm co}) = \frac{9H_0^4\Omega_m^2}{4c^4}\int_0^{\chi_{\rm h}} {\rm d}\chi \frac{g^i(\chi)g^j(\chi)}{a^2(\chi)} P_\delta^{{\rm hydro},x}\left(\frac{\ell}{f_K(\chi)}, \chi|\,\boldsymbol{p}_{\rm co}\right) . \tag{4.44}$$

However, to increase the computational speed, we approximate this step by

$$\boldsymbol{B}_x(\boldsymbol{p}_{\rm co}) = C^{ij}_{{\rm hydro},x}(\boldsymbol{p}_{\rm co}) = \frac{C^{ij}_{{\rm hydro},x}(\boldsymbol{p}_{\rm co,fid})}{C^{ij}_{\rm theory}(\boldsymbol{p}_{\rm co,fid})} C^{ij}_{\rm theory}(\boldsymbol{p}_{\rm co}) , \tag{4.45}$$

where $C^{ij}_{{\rm hydro},x}(\boldsymbol{p}_{\rm co,fid})$ is pre-computed using Eq. (4.44) setting at $\boldsymbol{p}_{\rm co,fid}$ and stored. $C^{ij}_{\rm theory}(\boldsymbol{p}_{\rm co})$ is our model vector $\boldsymbol{M}(\boldsymbol{p}_{\rm co})$ generated from HALOFIT. Approximating Eq. (4.44) by Eq. (4.45) avoids the need to integrate nine times when constructing the nine columns of $\boldsymbol{\Delta}(\boldsymbol{p}_{\rm co})/\boldsymbol{\Delta}_{\rm chy}(\boldsymbol{p}_{\rm co})/\boldsymbol{R}(\boldsymbol{p}_{\rm co})$ at each MCMC step. In using Eq. (4.45), we basically assume the quantity $[\frac{C^{00}_{\rm hydro}(\boldsymbol{p}_{\rm co})}{C^{00}_{\rm DMO}(\boldsymbol{p}_{\rm co})}]/[\frac{C^{00}_{\rm hydro}(\boldsymbol{p}_{\rm co,fid})}{C^{00}_{\rm DMO}(\boldsymbol{p}_{\rm co,fid})}] \approx 1$ at various $\boldsymbol{p}_{\rm co}$. To check the validity, we compute all the elements in this quantity using Eq. (4.44) and plot it in Fig. 4.18, with $\boldsymbol{p}_{\rm co}$ set at different values of Ω_m or σ_8, while keeping the rest of the cosmological parameters the same as $\boldsymbol{p}_{\rm co,fid}$. As shown, the C^{00} ratio curves are within 0.25% of 1 for various $\boldsymbol{p}_{\rm co}$ demonstrated here.

4.D Constraints on cosmological parameters of $\Omega_{\rm m}$, σ_8, and w_a

In this Appendix, we provide constraints on cosmological parameters of $\Omega_{\rm m}$, σ_8, and w_a after applying baryon mitigation techniques using HMCODE or various PCA methods. The solid markers indicate the amount of residual bias after mitigation, and the open markers indicate the 0.5σ errors on the marginalized 1D posteriors. We rely on this plot to check whether a mitigation method can successfully reduce the baryonic physics-induced bias to within 0.5σ for different cosmological parameters and baryonic scenarios. The results are briefly summarized in Tables 4.4 and 4.5. We refer readers back to discussions at §4.5.3 and §4.5.4 for details.

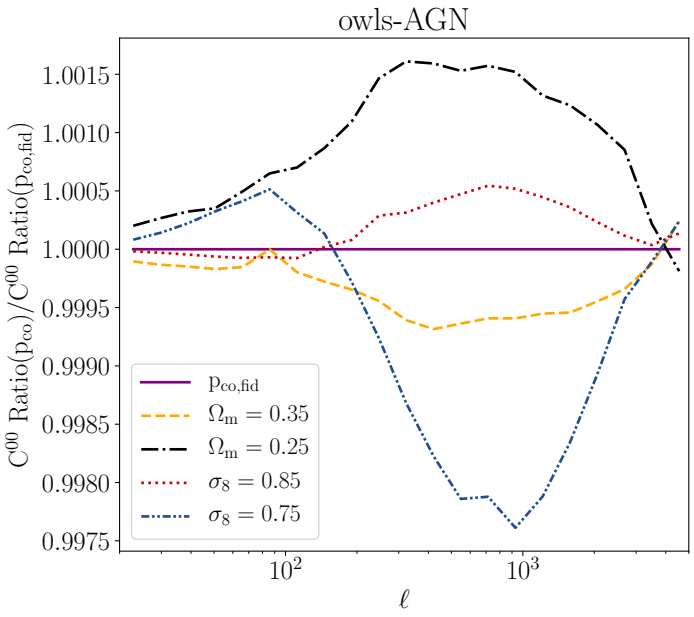

Figure 4.18: The ratio of tomographic power spectra ratio at bin C^{00} between hydrodynamical and DMO simulations evaluated at various $\boldsymbol{p}_{\rm co}$ v.s. $\boldsymbol{p}_{\rm co,fid}$, i.e, $[\frac{C^{00}_{\rm hydro}(\boldsymbol{p}_{\rm co})}{C^{00}_{\rm DMO}(\boldsymbol{p}_{\rm co})}]/[\frac{C^{00}_{\rm hydro}(\boldsymbol{p}_{\rm co,fid})}{C^{00}_{\rm DMO}(\boldsymbol{p}_{\rm co,fid})}]$. Here different curves indicate changes of Ω_m or σ_8 to values shown in the legend, while keeping the remaining cosmological parameters the same as $\boldsymbol{p}_{\rm co,fid}$. The fact that all ratio curves are ≈ 1 to within 0.25% indicates the validity of using Eq. (4.45) as our approximation.

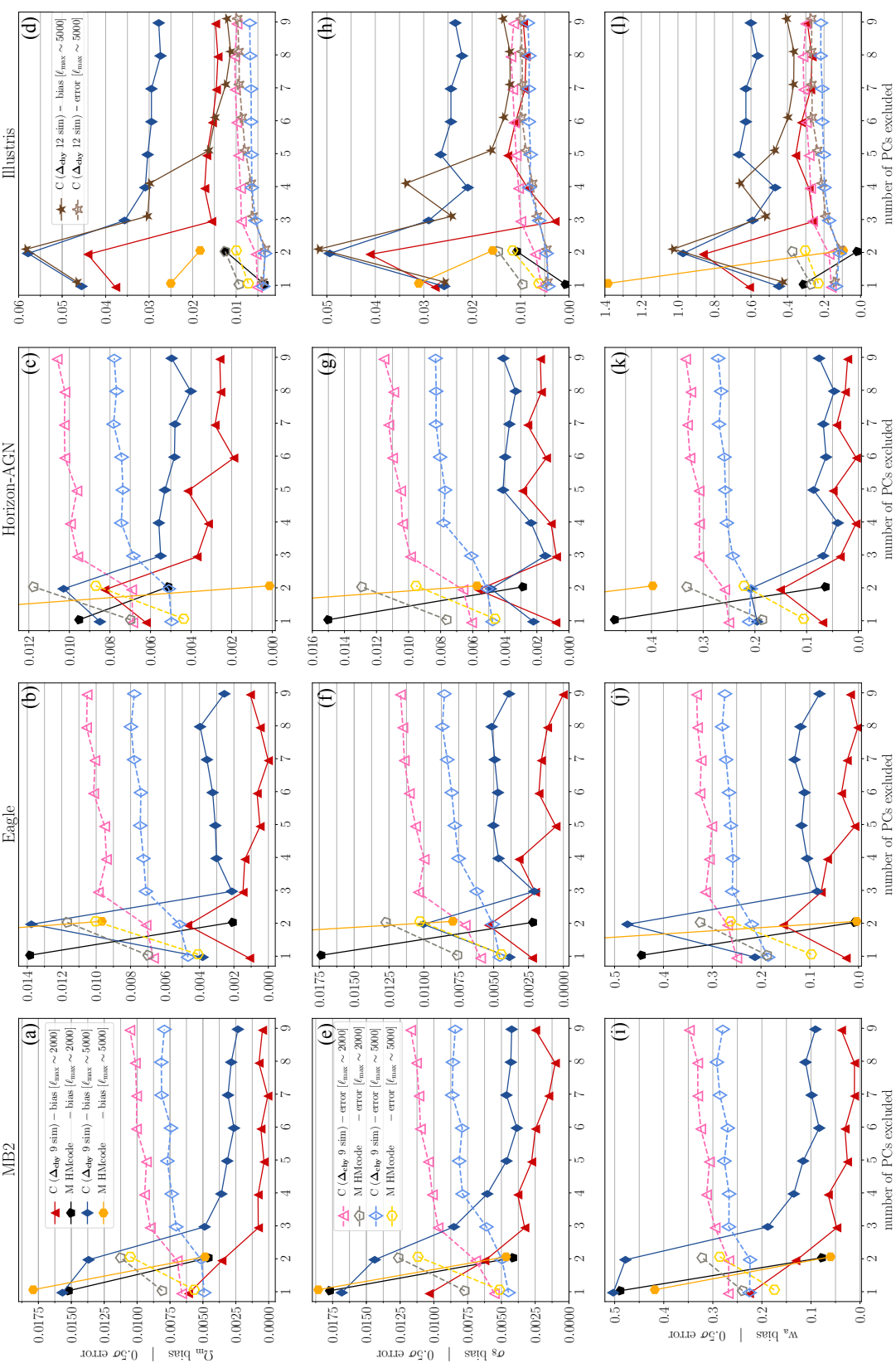

Figure 4.19: Similar to Fig. 4.15, but for cosmological parameters of $\Omega_{\rm m}$ (first row), σ_8 (second row) and w_a (third row), for various baryonic scenarios categorized in each different column.

Table 4.6: Goodness of fit for various baryon mitigation models.

	Eagle	MB2	Horizon-AGN	Illustris
no-mitigation at $\boldsymbol{p}_{\rm co,bestfit}$ ($\boldsymbol{p}_{\rm co,fid}$)	2.68 (30.92)	0.93 (5.71)	3.85 (103.2)	107.5 (3258)
HMCODE – A	2.09	0.74	2.34	4.84
HMCODE – A, η_0	0.91	0.29	1.69	4.80
PCA ex1 at $\boldsymbol{p}_{\rm co,bestfit}$ ($\boldsymbol{p}_{\rm co,fid}$)	1.39 (3.25)	0.70 (5.11)	0.75 (6.75)	11.91 (40.0)
PCA ex2	0.41 (0.39)	0.37 (0.81)	0.45 (2.72)	9.68 (34.2)
PCA ex3	0.28 (0.24)	0.28 (0.32)	0.26 (2.65)	3.08 (12.0)
PCA ex4	0.15 (0.07)	0.18 (0.30)	0.20 (1.38)	2.06 (4.89)
PCA ex5	0.13 (0.04)	0.14 (0.07)	0.16 (0.64)	1.65 (2.55)
PCA ex6	0.09 (0.03)	0.11 (0.06)	0.20 (0.59)	1.58 (2.18)
PCA ex7	0.11 (0.03)	0.12 (0.06)	0.19 (0.54)	1.50 (2.00)
PCA ex8	0.09 (0.03)	0.08 (0.06)	0.15 (0.53)	1.44 (2.00)
PCA ex9	0.07 (0.03)	0.10 (0.05)	0.15 (0.43)	1.37 (2.00)

4.E Goodness of fit for baryon mitigation models

In this Appendix, we summarize the fitting quality for various baryon mitigation methods. In Table 4.6, we provide the χ^2 values computed at the best-fitted (fiducial) cosmology for HMCODE and the PCA method C when applied on each baryonic scenario for the $\ell_{\rm max} \approx 2000$ likelihood simulations. Here we define our best-fitted parameters to be the median value at the marginalized 1D posterior distribution.

Notice that because our mock data vectors are noiseless, the χ^2 values cannot be used to make statements about overfitting or underfitting based on the reduced χ^2 criterion (i.e. we do not expect $\chi^2/({\rm d.o.f}) \approx 1$). However, using the information from the relative χ^2 values ($\Delta\chi^2$) and the relative degrees of freedom (Δ d.o.f) between two models, we can determine the model complexity needed from the data by performing the Chi-square difference test[13] .

For example, for the Illustris scenario, we see that when comparing the PCA results between excluding 1 PC mode to 5 PC modes, the $\Delta\chi^2 = 11.91 - 1.646 = 10.264$, and the Δ d.o.f = 4. The corresponding $p-$value is 0.036, which means that the improvement is marginally statistically significant ($p-$value < 0.05). Excluding 6 PC modes does not significantly improve the goodness of fit compared with the result when excluding 5 PC modes ($\Delta\chi^2 = 0.062$, Δ d.o.f = 1, $p-$value = 0.8).

After a few PC modes are excluded, we see that the χ^2 values computed at $\boldsymbol{p}_{\rm co,bestfit}$ is comparable to that computed at $\boldsymbol{p}_{\rm co,fid}$ for all baryonic scenarios. This means that excluding PC modes does not just reduce parameter bias in our simulated likelihood analysis, but the resulting best-fitting model also provides a good fit to the data.

[13] We refer readers to this link for more detail about Chi-square difference test.

5 Dark Energy Survey Year 1 Results: Constraints on Baryonic Effects

Abstract

In this work we develop a principal component (PC) based baryon mitigation pipeline in order to include the small scale cosmic shear data down to 2.5 arcmin into the original Dark Energy Survey (DES) Year 1 3×2 point analysis. We use the baryonic features from five sets of hydrodynamical simulations (OWLS-AGN, Eagle, Horizon-AGN, MB2, IllustrisTNG) to construct baryon-contaminated mock observable vectors, and perform principal component analysis (PCA) on them to derive PC modes with flexibility to span the uncertainties of baryonic physics. We validate our pipeline by running likelihood simulations to finalize pipeline settings and to understand expected performances before applying on real data. We find that marginalizing over one PC modes is sufficient to reduce systematic biases to the 1σ statistical error under the DES Y1 covariance, and we expect to have $\sim$10% smaller error bar on S_8 by including small scale cosmic shear data into analysis. For the expected constraining power on baryonic parameters, at most we would be able to differentiate two very distinct baryonic scenarios (e.g. Illustris v.s. MB2) by one sigma, given the DES Y1 statistical power. We also study the interplay of baryonic parameters with cosmology and nuisance parameters for other systematic effects. While there are some level of intrinsic correlation between the baryonic parameters and cosmology, we find that most of the degeneracies trends between the baryonic parameters and cosmology in our full analysis are driven by allowing the galaxy bias parameters to vary.

5.1 Theory and Analysis Setting

5.1.1 Data

Observational Data

We use the publicly released 3×2pt data vector from the Dark Energy Survey (DES) Y1 key project (Abbott et al., 2018) as our observational data vector[1]. Throughout the work, we adopt the METACALIBRATION (Huff & Mandelbaum, 2017; Sheldon & Huff, 2017) version shape catalog as our source sample for cosmic shear (Troxel et al., 2018), and the redMaGiC (Rozo et al., 2016) sample as the lens population for galaxy-galaxy lensing (Prat et al., 2018) and galaxy clustering (Elvin-Poole et al., 2018) measurements.

The DES Y1 source galaxies are divided into four tomographic bins ranging from $z = 0.2$ to 1.3, resulting in 10 auto- and cross-correlations of cosmic shear for ξ_+ and ξ_-, respectively. The

[1]The publicly released 3×2pt data vector and its associated covariance matrix, `2pt_NG_mcal_1110.fits`, can be downloaded at https://des.ncsa.illinois.edu/releases/y1a1/key-products

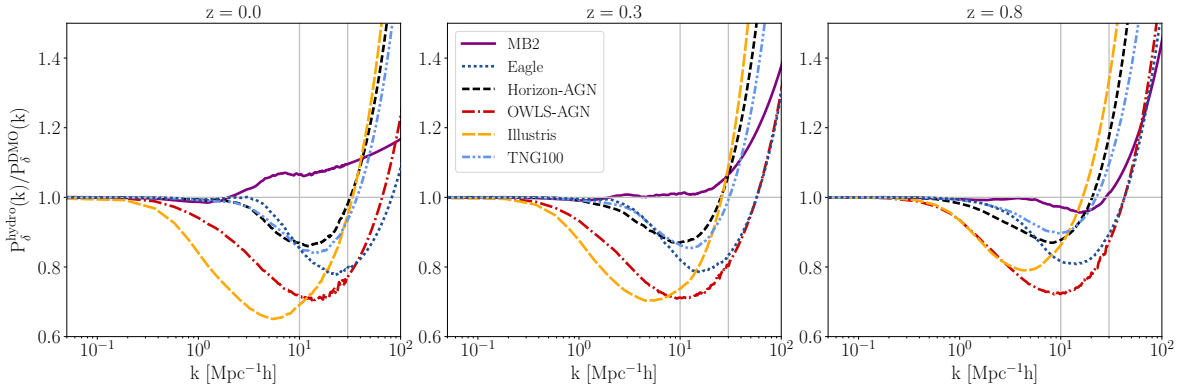

Figure 5.1: The effect of baryons on matter power spectrum. We plot the power spectrum ratio for hydrodynamical simulations of IllustrisTNG100, MB2, Eagle, Horizon-AGN, Illustris, and OWLS-AGN, with respect to their corresponding DMO simulation setting at the same initial condition, at redshifts 0, 0.3, 0.9 (within the redshift range that DES Y1 galaxy clustering and weak lensing observables is sensitive at).

lens galaxies are placed in five tomographic bins ranging from $z = 0.15$ to 0.9, resulting in 20 cross-correlations between lens and source samples for galaxy-galaxy lensing, and 5 auto-correlations for galaxy clustering. Each of the correlation statistics is measured using `treecorr`[2] in 20 log-spaced bins of angular separation $2.5' < \theta < 250'$. Conservative scale cuts are applied to the raw 3×2pt data vector to avoid modeling challenges on small scale (see Troxel et al. 2018; Krause et al. 2017 for the determination of scale cuts), resulting in a total of 457 elements for the fiducial DES Y1 3×2pt cosmological analysis (Abbott et al., 2018).

To extract the baryon information of our Universe, we extend the DES Y1 cosmic shear correlation function measurements to scales of 2.5 arcmin; together with the galaxy-galaxy lensing and galaxy clustering measurements (subjected to the original DES Y1 scale cuts), our extended 3×2pt data vectors have a total of 630 data points (400 elements for cosmic shear, 176 elements for galaxy-galaxy lensing and 54 elements for galaxy clustering).

Hydrodynamcial Simulation Data and Power Spectrum

To build our baryon mitigation models with sufficient flexibility and to validate our pipelines, a total of six hydrodynamical simulations is involved in this work: OWLS-AGN (Schaye et al., 2010; van Daalen et al., 2011), MassiveBlack-II (MB2, Khandai et al. 2015; Tenneti et al. 2015b), Horizon-AGN (Dubois et al., 2014), Eagle (Schaye et al., 2015), Illustris (Vogelsberger et al., 2014; Genel et al., 2014), IllustrisTNG (Springel et al., 2018; Pillepich et al., 2018b; Naiman et al., 2018; Marinacci et al., 2018; Nelson et al., 2018). We refer readers to §2 of Huang et al. 2019 (hereafter H19) for our brief summary on these simulations.

Figure 5.1 shows the effects of baryons for different hydrodynamical simulations in terms of their derived power spectrum ratios with respect to their corresponding dark matter only (DMO) simulations

[2]https://github.com/rmjarvis/TreeCorr

at the same initial condition. On small scale, the effects of baryons show large variations, and have different redshift evolution histories across simulations. On large scale, we expect the power spectrum ratios converge to unity because of the negligible baryonic effects there, and because of the cosmic variance fluctuations being canceled when taking ratios of power for pairs of simulations seeded at identical initial condition. In Appendix B of H19, we have discussed in detail on the convergence of power spectrum ratio and provide an upper limit estimation on its uncertainties due to cosmic variance.

We have computed the power spectrum ratio for MB2, Illustris, Eagle for the work of H19. The IllustrisTNG baryonic scenario is added into our power spectrum library using the publicly released TNG100 snapshot data (Nelson et al., 2019). The OWLS-AGN power spectra are computed by van Daalen et al. (2011). For Horizon-AGN, we use the power spectra data released by Chisari et al. (2018). We make a slight adjustment on the power spectrum ratios for Horizon-AGN, due to its $\sim 0.5\%$ excess above unity toward large scales, as shown in Fig. 5 of Chisari et al. (2018). According to van Daalen et al. (2019), this large-scale ($\lesssim 1\%$) excess of power is originating from details of simulation setup between pairs of hydrodynamical and DMO simulations, for which their transfer functions and the number of particles are often differ. Given that this sub-percent level offset is due to artifacts, we correct for this power mismatch by re-scaling the DMO power spectra using the linear growth factor, letting the ratio between $P_\delta^{\rm hydro}$ and $P_\delta^{\rm DMO}$ asymptotic to one toward large scales.

Mock Data Vectors

To validate our baryon mitigation pipeline, we generate three mock data vectors to conduct likelihood simulations: the pure theoretical data vector derived from CosmoLike with the fiducial parameters setting shown in Table 5.1 (we will label this mock data vector as the DMO scenario hereafter), and two baryon-contaminated mock data vectors with the Illustris and Eagle scenarios.

We derive the baryon-contaminated data vectors at specific cosmology $\boldsymbol{p}_{\rm co}$ using the underlying hydrodynamical power spectrum defined as

$$P_\delta^{\rm hydro}(k,z\mid \boldsymbol{p}_{\rm co}) = \frac{P_\delta^{\rm hydro,sim}(k,z\mid \boldsymbol{p}_{\rm co,sim})}{P_\delta^{\rm DMO,sim}(k,z\mid \boldsymbol{p}_{\rm co,sim})} P_\delta^{\rm theory}(k,z\mid \boldsymbol{p}_{\rm co})\,, \tag{5.1}$$

where the ratio term $\frac{P_\delta^{\rm hydro,sim}(k,z\mid \boldsymbol{p}_{\rm co,sim})}{P_\delta^{\rm DMO,sim}(k,z\mid \boldsymbol{p}_{\rm co,sim})}$ is visualized in Fig. 5.1. When using Eq. (5.1), we assume that baryonic effects and cosmology are independent, which is a fair assumption. According to van Daalen et al. (2019) the power spectrum ratio remains more or less the same when varying cosmologies (see their Fig. 6).

With the $P_\delta^{\rm hydro}(k,z\mid \boldsymbol{p}_{\rm co})$ being computed, we then pass it into the CosmoLike package to derive the baryon-contaminated data vectors, for which we detailed in §5.1.2.

5.1.2 Model

We use the CosmoLike package (Krause & Eifler, 2017), one of the parallel pipelines for DES cosmological inferences, to perform theatrical modeling on the 3×2pt data vectors. The linear DMO power spectrum is generated at each cosmology using CLASS (Blas et al., 2011), with nonlinear

correlations derived from the Takahashi et al. (2012) version of HALOFIT . Throughout the work, we consider a flat ΛCDMcosmological model with six free parameters, $\boldsymbol{p}_{\rm co} = \{\Omega_{\rm m},\ A_{\rm s},\ \Omega_{\rm b},\ n_{\rm s},\ \Omega_\nu h^2,\ h\}$.

Below we briefly summarize the theoretical modeling of the three types of two-point correlation functions and their associated systematic effects.

Cosmic Shear $\xi_\pm(\theta)$

The real-space cosmic shear correlation function in tomographic bins i, j is modeled as

$$\xi_\pm^{ij}(\theta) = (1+m^i)(1+m^j)\,\frac{1}{2\pi}\int {\rm d}\ell\ \ell J_{0/4}(\ell\theta) C_{\gamma\gamma}^{ij}(\ell)\ . \tag{5.2}$$

Here J_0 and J_4 are Bessel functions of the first kind. m^i is a constant multiplicative factor for each tomographic bin to account for shear calibration bias (Heymans et al., 2006). $C_{\gamma\gamma}^{ij}(\ell)$ is the detected shear-shear power spectrum, which contains the real lensing signal due to gravity (GG) as well as the contamination due to intrinsic alignment (II, GI, IG terms).

$$C_{\gamma\gamma}^{ij}(\ell) = C_{\rm GG}^{ij}(\ell) + C_{\rm II}^{ij}(\ell) + C_{\rm GI}^{ij}(\ell) + C_{\rm IG}^{ij}(\ell)\ . \tag{5.3}$$

For the real lensing contribution, under the Limber approximation and the flat Universe assumption,

$$C_{\rm GG}^{ij}(\ell) = \int_0^{\chi_{\rm h}} {\rm d}\chi_{\rm l} \frac{g^i(\chi_{\rm l}) g^j(\chi_{\rm l})}{\chi_{\rm l}^2} P_\delta(k=\frac{\ell}{\chi_{\rm l}}, \chi_{\rm l})\,, \tag{5.4}$$

where $\chi_{\rm l}$ is the comoving distance for the matter distribution (lens) along the line of sight, and $\chi_{\rm h}$ is the comoving horizon distance. The lensing kernel in the i-th tomographic interval is

$$g^i(\chi_{\rm l}) = \frac{3}{2}\frac{H_0^2\Omega_{\rm m}}{c^2}\frac{\chi_{\rm l}}{a(\chi_{\rm l})}\int_{\chi_{\rm l}}^{\chi_{\rm h}} {\rm d}\chi_{\rm s} n_{\rm s}^i(\chi_{\rm s})\frac{\chi_{\rm s}-\chi_{\rm l}}{\chi_{\rm s}}\,, \tag{5.5}$$

with $n_{\rm s}^i(\chi_{\rm s})$ being the probability density function (pdf) for the redshift distribution of source galaxies in tomographic bin i, defined such that $n_{\rm s}^i(\chi_{\rm s}){\rm d}\chi_{\rm s} = n_{\rm s}^i(z){\rm d}z$, and is normalized to unity.

For the intrinsic alignment (IA) contamination, we have the the intrinsic-intrinsic shape correlation due to the local gravity on pairs of source galaxies,

$$C_{\rm II}^{ij}(\ell) = \int_0^{\chi_{\rm h}} {\rm d}\chi_{\rm s} \frac{n_{\rm s}^i(\chi_{\rm s}) n_{\rm s}^j(\chi_{\rm s})}{\chi_{\rm s}^2} P_{\rm II}(k=\frac{\ell}{\chi_{\rm s}}, \chi_{\rm s})\,, \tag{5.6}$$

and the lensing shear-intrinsic shape correlations for pairs of galaxies with the foreground one being torqued and the background one being sheared under the effect of the same gravitational field,

$$C_{\rm GI}^{ij}(\ell) + C_{\rm IG}^{ij}(\ell) = \int_0^{\chi_{\rm h}} {\rm d}\chi \frac{g^i(\chi) n_{\rm s}^j(\chi) + n_{\rm s}^i(\chi) g^j(\chi)}{\chi^2} P_{\rm GI}(k=\frac{\ell}{\chi}, \chi)\ . \tag{5.7}$$

The $P_{\rm II}$ and $P_{\rm GI}$ are IA power spectra. Throughout the work, we adopt the commonly used non-linear alignment (NLA) model (Hirata & Seljak, 2004a) to mitigate IA uncertainties, i.e. assuming the amplitudes of IA power spectra are linearly related to the local density field:

$$\begin{aligned} P_{\rm II}(k,z) &= A^2(z) P_\delta(k,z) \\ P_{\rm GI}(k,z) &= A(z) P_\delta(k,z) \\ A(z) &= -A_{\rm IA} C_1 \frac{3H_0^2\Omega_{\rm m}}{8\pi G} D^{-1}(z)\,(\frac{1+z}{1+z_0})^{\eta_{\rm IA}}\ . \end{aligned} \tag{5.8}$$

Here $D(z)$ is the linear growth factor; C_1 is the normalization constant being set at $5\times10^{-14}\,\mathrm{M}_\odot^{-1}h^{-2}\mathrm{Mpc}^3$ (Brown et al., 2002); the pivot redshift z_0 is being set at 0.62. The nuisance parameters that go into the pipeline for IA marginalization are $A_{\rm IA}$ and $\eta_{\rm IA}$. For a more detailed IA analysis on DES Y1 data, see Samuroff et al. (2018).

Galaxy Clustering

The location galaxies traces the underlying matter density field, yet with some unknown bias factor which depends on the tracer galaxy properties. On large scale, under the simple scale-independent linear bias model, the theoretical prediction for galaxy-galaxy auto-correlation function in tomographic bin i is:

$$\begin{aligned} w^i(\theta) &= \frac{1}{2\pi}\int \mathrm{d}\ell J_0(\ell\theta) C^{ii}_{\delta_{\rm g}\delta_{\rm g}}(\ell) \\ C^{ii}_{\delta_{\rm g}\delta_{\rm g}}(\ell) &= (b^i_{\rm g})^2 \int_0^{\chi_{\rm h}} \mathrm{d}\chi_1 \frac{(n^i_1(\chi_1))^2}{\chi_1^2} P_\delta(k=\frac{\ell}{\chi_1},\chi_1)\,, \end{aligned} \tag{5.9}$$

where $n^i_1(\chi_1)$ is the pdf for the redshift distribution of lens galaxies, and $b^i_{\rm g}$ is the bias factor for each tomographic bin.

Galaxy-Galaxy Lensing

Galaxy-galaxy lensing, the cross correlation between the position of lens galaxies in bin i and their surrounding matter density field traced by the shear of source galaxies in bin j, is modeled as:

$$\gamma^{ij}_{\rm t}(\theta) = (1+m^j)\frac{1}{2\pi}\int \mathrm{d}\ell J_2(\ell\theta) C^{ij}_{\delta_{\rm g}\gamma}(\ell)\,, \tag{5.10}$$

where m^j is the multiplicative shear bias; J_2 is the second-order Bessel function. Similarity, the $C^{ij}_{\delta_{\rm g}\gamma}(\ell)$ term has contributions from both pure lensing and IA effects,

$$C^{ij}_{\delta_{\rm g}\gamma}(\ell) = C^{ij}_{\delta_{\rm g}{\rm G}}(\ell) + C^{ij}_{\delta_{\rm g}{\rm I}}(\ell)\,. \tag{5.11}$$

The the lensing term is

$$C^{ij}_{\delta_{\rm g}{\rm G}}(\ell) = b^i_{\rm g}\int_0^{\chi_{\rm h}} \mathrm{d}\chi_1 \frac{n^i_1(\chi_1) g^j(\chi_1)}{\chi_1^2} P_\delta(k=\frac{\ell}{\chi_1},\chi_1)\,. \tag{5.12}$$

The IA term is

$$C^{ij}_{\delta_{\rm g}{\rm I}}(\ell) = b^i_{\rm g}\int_0^{\chi_{\rm h}} \mathrm{d}\chi \frac{n^i_1(\chi) n^j_{\rm s}(\chi)}{\chi^2} P_{\rm GI}(k=\frac{\ell}{\chi},\chi)\,, \tag{5.13}$$

with the IA power spectrum $P_{\rm GI}$ being defined in Eq. (5.8).

Finally, throughout out the work, the uncertainty in the photometric redshifts are modeled as a constant shift from the initial pdf $n^i_{\rm pz}(z)$, for both source and lens galaxies, in each tomographic bin.

$$n^i_{\rm s}(z) = n^i_{\rm s,pz}\,(z-\Delta z^i_{\rm s}) \quad ; \quad n^i_1(z) = n^i_{\rm l,pz}\,(z-\Delta z^i_1) \tag{5.14}$$

Table 5.1: Parameters and priors used to run the likelihood analyses. *Flat* denotes a flat prior in the range given while *Gauss*(μ, σ) is a Gaussian prior with mean μ and width σ. The third column summarizes the fiducial parameter values we used to construct PCs. The cosmological, intrinsic alignment, and galaxy bias parameters are chosen to be in consistent with the posterior constraints from the fiducial ΛCDMmodel of DES Y1 3×2pt analyses (Abbott et al., 2018). The fiducial photo-z and shear calibration parameters are set at the peak of the gaussian prior for the purpose of running likelihood simulations.

Parameter	Prior	Fiducial Value
	Cosmology	
$\Omega_{\rm m}$	Flat (0.1, 0.9)	0.3
$A_{\rm s}$	Flat $(5 \times 10^{-10}, 5 \times 10^{-9})$	2.19×10^{-9}
$n_{\rm s}$	Flat (0.87, 1.07)	0.97
$\Omega_{\rm b}$	Flat (0.03, 0.07)	0.048
$\Omega_\nu h^2$	Flat $(5 \times 10^{-4}, 10^{-2})$	0.00083
h	Flat (0.55, 0.91)	0.69
	Lens Galaxy Bias	
$b_{\rm g}^1$	Flat (0.8, 3.0)	1.53
$b_{\rm g}^2$	Flat (0.8, 3.0)	1.71
$b_{\rm g}^3$	Flat (0.8, 3.0)	1.70
$b_{\rm g}^4$	Flat (0.8, 3.0)	2.05
$b_{\rm g}^5$	Flat (0.8, 3.0)	2.14
	Lens photo-z shift	
$\Delta z_{\rm l}^1$	Gauss (0.008, 0.007)	0.008
$\Delta z_{\rm l}^2$	Gauss (−0.005, 0.007)	-0.005
$\Delta z_{\rm l}^3$	Gauss (0.006, 0.006)	0.006
$\Delta z_{\rm l}^4$	Gauss (0.0, 0.01)	0.0
$\Delta z_{\rm l}^5$	Gauss (0.0, 0.01)	0.0
	Source photo-z shift	
$\Delta z_{\rm s}^1$	Gauss (−0.001, 0.016)	-0.001
$\Delta z_{\rm s}^2$	Gauss (−0.019, 0.013)	-0.019
$\Delta z_{\rm s}^3$	Gauss (+0.009, 0.011)	0.009
$\Delta z_{\rm s}^4$	Gauss (−0.018, 0.022)	-0.018
	Shear calibration (METACALIBRATION)	
m^1	Gauss (0.012, 0.023)	0.012
m^2	Gauss (0.012, 0.023)	0.012
m^3	Gauss (0.012, 0.023)	0.012
m^4	Gauss (0.012, 0.023)	0.012
	Intrinsic Alignment	
$A_{\rm IA}$	Flat (−5, 5)	0.45
$\eta_{\rm IA}$	Flat (−5, 5)	-1.0
	Baryon PC amplitude	
Q_i $(i = 1, 2, 3)$	Flat (−100, 100)	$\boldsymbol{Q}_{\rm DMO}$: [0.00 , 0.00 , 0.00] $\boldsymbol{Q}_{\rm illustris}$: [4.13 , −1.11 , 0.18] $\boldsymbol{Q}_{\rm eagle}$: [0.51 , 0.31 , −0.12]

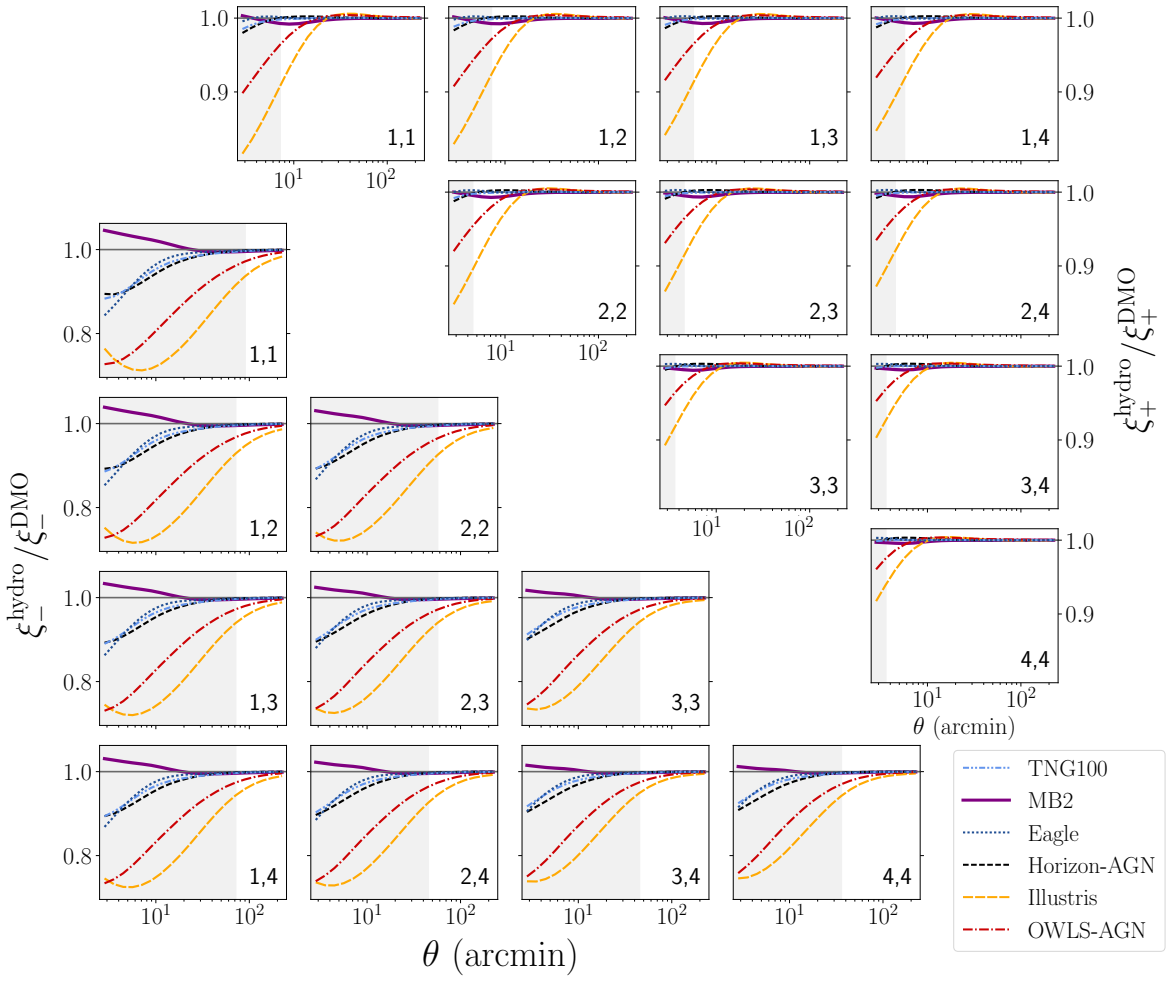

Figure 5.2: The effect of baryons on cosmic shear. Here we show the ratio of cosmic shear correlation functions for baryonic scenarios of IllustrisTNG100, MB2, Eagle, Horizon-AGN, Illustris, and OWLS-AGN, with respect to the theoretical (DMO) predictions. The gray bands highlight data points that were excluded in the fiducial DES Y1 analysis, but are now included in this work.

5.1.3 PC Decomposition to model baryonic effects

We adopt the principal component (PC) decomposition technique to model baryonic effects for small scale cosmic shear (Eifler et al., 2015). The basic idea of this technique is to perform principal component analysis (PCA) on the difference of the theoretical model vectors (the 3×2pt vectors for this work) between hydrodynamical and DMO simulations, for several baryonic scenarios. The resulting dominant PC modes then serve as a flexible bases set to account for possible baryonic effects of our Universe. In H19, we validate this method under an LSST-like cosmic shear experiment. We further improvement the efficiency of this method by applying some weighting when constructing PC modes. Throughout the work, we will apply the method C of H19 to mitigate uncertainties of baryons in DES Y1. Below briefly summarize the formalism of our method.

First, we build the difference matrix $\mathbf{\Delta}$ and weigh it by $\mathbf{L}^{-1}$ to derive the noise-weighted difference

matrix $\mathbf{\Delta}_{\rm ch}$.

$$\begin{aligned}\mathbf{\Delta}_{\rm ch} &= \mathbf{L}^{-1}\mathbf{\Delta} \\ &= \mathbf{L}^{-1}\left[\begin{array}{cccc} \boldsymbol{B}_1 - \boldsymbol{M} & \boldsymbol{B}_2 - \boldsymbol{M} & \dots & \boldsymbol{B}_{N_{\rm sim}} - \boldsymbol{M} \end{array}\right]_{N_{\rm data}\times N_{\rm sim}} \\ &= \mathbf{U}_{\rm ch}\,\mathbf{\Sigma}_{\rm ch}\,\mathbf{V}_{\rm ch}^{\rm t}\,.\end{aligned} \tag{5.15}$$

The weighting factor $\mathbf{L}^{-1}$ is derived from Cholesky Decomposition from covariance matrix $\mathbf{C}$ via

$$\mathbf{C} = \mathbf{L}\mathbf{L}^{\rm t}\,. \tag{5.16}$$

Each column of $\mathbf{\Delta}$ is a difference vector with 630 elements (§5.1.1), $\boldsymbol{B}_x - \boldsymbol{M}$, with $\boldsymbol{M}(\boldsymbol{p}_{\rm co,fid}, \boldsymbol{p}_{\rm nu,fid})$ being a DMO model vector setting at the fiducial parameters summarized in Table 5.1. $\boldsymbol{B}_x(\boldsymbol{p}_{\rm co,fid}, \boldsymbol{p}_{\rm nu,fid})$ represents for a model vector contaminated with baryonic scenario x.

In Fig. 5.2, we show the ratio of data vectors $\boldsymbol{B}_x/\boldsymbol{M}$ on cosmic shear for all the hydrodynamical scenarios involved in the analysis of this work. Notice that after integration, the variation of baryonic effects on ratios of $\xi_\pm$ is more monotonous to the θ range considered here, compared with their ratios in $P_\delta(k)$ as shown in Fig. 5.1. This feature makes it earlier to construct models to mitigate baryonic effects in observable spaces, but more challenging to constraint different baryonic scenarios via weak lensing observables.

Next, we apply the singular value decomposition (SVD) on $\mathbf{\Delta}_{\rm ch}$. The first $N_{\rm sim}$ columns of $\mathbf{U}_{\rm ch}$ matrix is a set of PC bases that can be used to fully span the baryonic features of our training simulations. For a given baryonic scenario x, we have

$$\mathbf{L}^{-1}(\boldsymbol{B}_x - \boldsymbol{M}) = \sum_{i=1}^{N_{\rm sim}} Q_i\,\mathbf{PC}_i\,. \tag{5.17}$$

Note that although we pass the full 3×2pt vector in Eq. (5.15) to perform PCA, for the galaxy-galaxy lensing and galaxy clustering parts, subjected to their conservative scale cuts, the resulting deviations from DMO scenario are extremely small in projection on these elements. Thus, the PCs mostly functions on accounting for baryonic effects in small-scale data points of cosmic shear.

With the PCs derived, we can then generate a baryonic model that utilizes PC amplitudes Q_i to simulate possible baryonic behaviors.

$$\boldsymbol{M}_{\rm bary}(\boldsymbol{p}_{\rm co}, \boldsymbol{p}_{\rm nu}, \boldsymbol{Q}) = \boldsymbol{M}(\boldsymbol{p}_{\rm co}, \boldsymbol{p}_{\rm nu}) + \sum_{i=1}^{n} Q_i\,\mathbf{L}\cdot\mathbf{PC}_i\,. \tag{5.18}$$

Here n specifies the number of PC amplitudes/PC modes used to model baryonic effect, and $n \leq N_{\rm sim}$. The operation of $\mathbf{L}\cdot\mathbf{PC}_i$ transforms the PC mode back to the same basis as $\boldsymbol{M}$.

Input hydrodynamical scenarios for PC construction

We construct two PC basis sets throughout this work for all the analyses. The first PC set is constructed with 5 hydrodynamical scenarios: OWLS-AGN, MB2, Horizon-AGN, TNG100, and Eagle. We will use this basis set to mitigate baryonic effects for our Illustris and DMO mock data vectors (see §5.1.1), and for the real DES Y1 observational data vector. The other PC basis set is constructed with

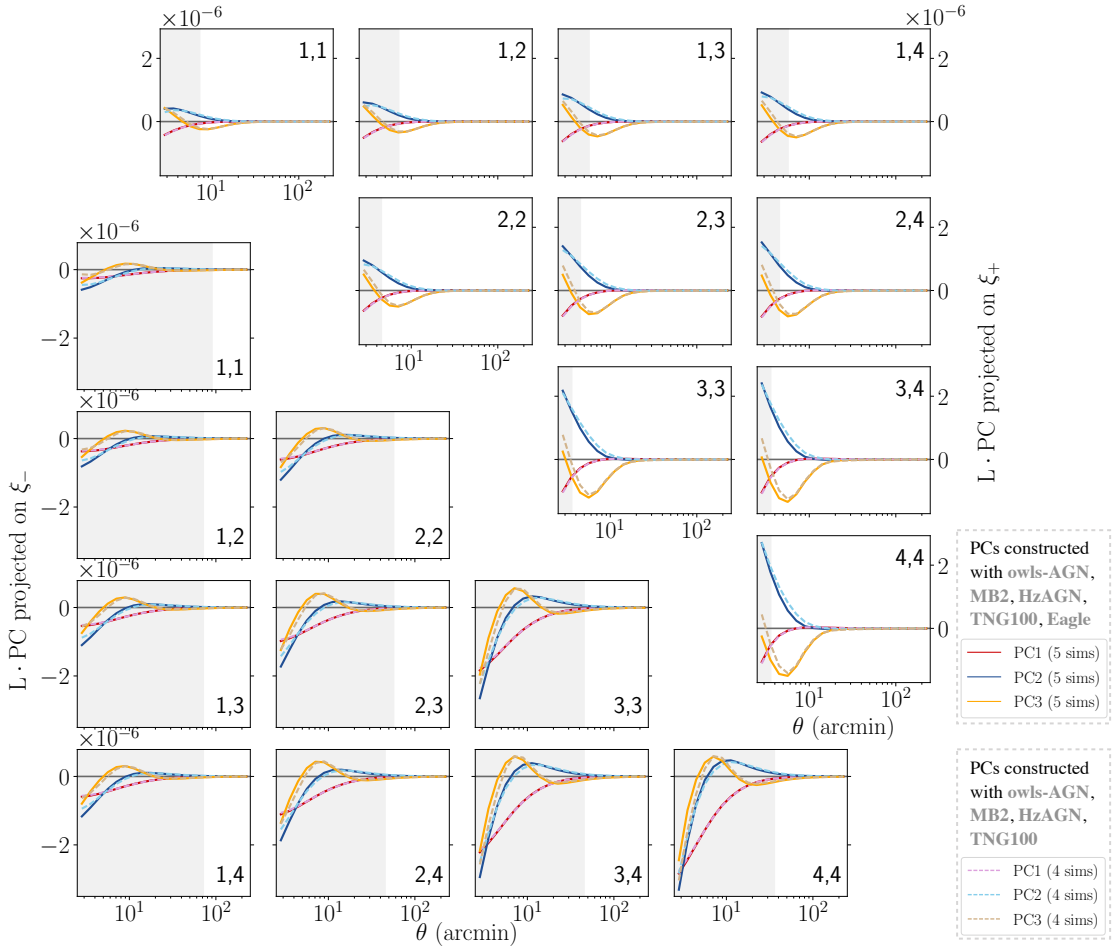

Figure 5.3: The principal bases used to model uncertainties of baryons. Here we show the first three $\mathbf{L} \cdot \mathbf{PC}$ components, as shown in Eq. (5.18), projected on the cosmic shear correlation functions.

hydrodynamical scenarios of OWLS-AGN, MB2, Horizon-AGN, and TNG100, for which the Eagle scenario is excluded, because we will use this PC set to perform mitigation for the Eagle mock data vector.

Figure 5.3 provides a visualization of $\mathbf{L} \cdot \mathbf{PC}_i$ in projection on $\xi_\pm$. One can see that most of variations are concentrating on small scales of ξ_-, where the baryonic effects have the largest variances across the baryonic scenarios that are used in PC construction, as shown in Fig. 5.2.

5.1.4 Likelihood Analysis

We infer the posterior probability distribution of cosmological ($\boldsymbol{p}_{\rm co}$) and nuisance parameters ($\boldsymbol{p}_{\rm nu}$) via Bayes' theorem:

$$P(\boldsymbol{p}_{\rm co}, \boldsymbol{p}_{\rm nu}|\boldsymbol{D}) \propto L(\boldsymbol{D}|\boldsymbol{p}_{\rm co}, \boldsymbol{p}_{\rm nu}) P_{\rm prior}(\boldsymbol{p}_{\rm co}, \boldsymbol{p}_{\rm nu})\,, \tag{5.19}$$

with the prior probability distribution or each of the parameter defined in Table 5.1. We assume the a simple Gaussian likelihood function:

$$L(\boldsymbol{D}|\boldsymbol{p}_{\rm co},\boldsymbol{p}_{\rm nu}) \propto \exp\left(-\frac{1}{2}\underbrace{\left[(\boldsymbol{D}-\boldsymbol{M})^t\,\mathbf{C}^{-1}\,(\boldsymbol{D}-\boldsymbol{M})\right]}_{\chi^2(\boldsymbol{p}_{\rm co},\boldsymbol{p}_{\rm nu})}\right), \tag{5.20}$$

where the $\mathbf{C}$ is the covariance matrix reflecting the statistical uncertainties of measurements. We use the publicly released covariance for DES Y1 computed from CosmoLike (Krause & Eifler, 2017). The calculation of covariance matrix and the associated validation tests is detailed in Krause et al. (2017).

We use the `emcee` package (Foreman-Mackey et al., 2013), which relies on the affine-invariant ensemble sampling algorithm (Goodman et al., 2010), to sample the parameter space. We run MCMC (Markov Chain Monte Carlo) chains to 2.5 million steps in length, and then discard the first 1.25 million steps as burn-in.

5.1.5 Blinding

We develop our baryon mitigation pipeline by running likelihood simulations on mock baryon-contaminated data vectors (§5.1.1), and use the information to determine the degrees of freedom (number of PC modes) needed to be opened to assure unbiased cosmological inferences, to learn what to expect in terms of the constraining power on baryonic parameters from the small-scale cosmic shear information, and to understand the expected improvement in cosmological constraint compared with the fiducial DES Y1 3×2pt scale cuts. After everything is fully understood among the authors, we then apply our pipeline on the real DES Y1 data (§5.1.1).

5.2 Likelihood Simulation Results

In this section we present our simulated likelihood results for the three mock data vectors of baryonic scenarios DMO, Eagle, and Illustris. The results shown here would stand as references for the designed and expected performances of our baryon mitigation pipeline.

5.2.1 Number of PC modes to be marginalized over given DES Y1 constraining power

The residual bias after marginalization

To determine how many PC modes are needed in Eq. (5.18) to safely marginalize over baryonic effects given DES Y1 covariance, we examine the posterior constraints on cosmological parameters for our likelihood simulation runs with increasing degrees of freedom opened until the bias on each of the cosmological parameters are within 1σ of the posterior distribution.

Figure 5.4 shows the marginalized 1D S_8 posterior constraints for our likelihood simulations. If the baryonic scenario of our Universe is like Eagle, even without marginalization the S_8 bias is still within 1σ for DES Y1, when extending cosmic shear to 2.5 arcmin. If using the Illustris scenario as a more conservative validation, we find that marginalizing over two PC modes should be enough to account for baryonic effects to within 1σ for DES Y1. We also note that subjected to the original Y1

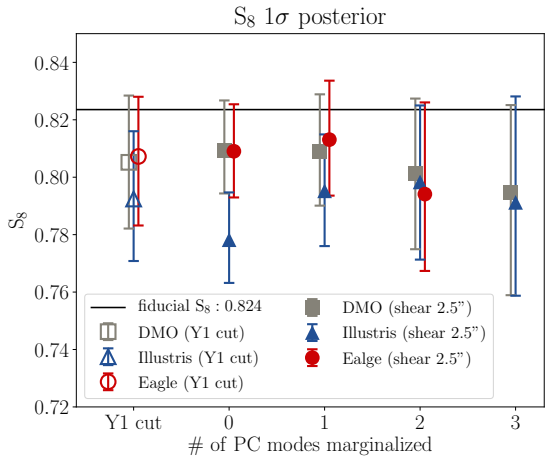

Figure 5.4: The marginalized 1D S_8 posterior constraints for our likelihood simulations with baryonic scenarios of DMO, Eagle and Illustris. The marker position, the lower and upper error bars indicate the median, the 16th and the 84th percentiles of marginalized 1D posteriors. The open symbols are results of 3×2 point mock data vectors subjected to the original DES Y1 scale cuts, while the filled symbols are results when extending the cosmic shear data points to 2.5 arcmin (§5.1.1), with different choices on the number of marginalizing PC amplitudes Q_i to account for baryonic effects.

scale cut, the bias on S_8 is expected to be $> 1\sigma$ (open blue triangle). This is because the original Y1 scale cut is designed and validated based on the OWLS-AGN scenario, which is less intense compared with Illustris (see Figs. 5.1 and 5.2).

The degradation on parameter constraint after marginalization

The small scale cosmic shear data points provide extra information in cosmology, while some of the information would lose after accounting for uncertainties of baryons. Here we try to understand the expected degradation on parameter constraints within the PCA framework, subjected to our choices on the number of marginalization parameters for baryons.

Figure 5.5 shows the marginalized 1σ error for S_8 for our likelihood analysis results on mock data vectors contaminated with baryonic scenarios of Illustris, Eagle and DMO. The gray bars are S_8 errors derived when applied the original Y1 scale cuts. The blue/red/orange/brown are the results with the cosmic shear data points extended to 2.5 arcmin, and with 0/1/2/3 PC mode(s) being marginalized when running analysis. The bar on the far left indicates the S_8 error when running the CosmoLike pipeline on real DES 3×2 pt data vector with original Y1 scale cuts. We find that when only marginalizing over one PC mode, we still have the advantage by relying on small scale cosmic shear data to obtain better cosmological constraint. However, when opening more than 2 PC modes to perform marginalization, we lose the benefit of adding extra data points due to our lack of knowledge to control uncertainties of baryonic effects.

To summarize, we find that, under the most conservative case for a Universe like Illustris, marginalizing over two PC modes should be sufficient for DES Y1 when including small scale cosmic shear into

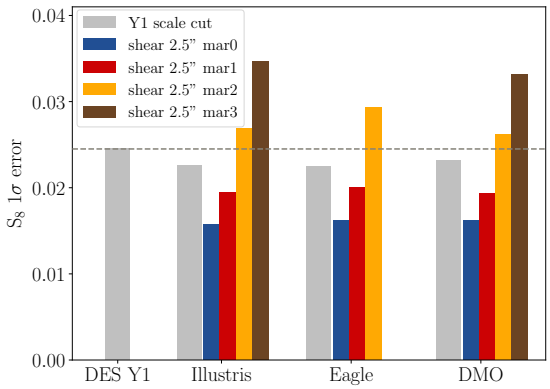

Figure 5.5: The marginalized 1σ error for S_8 for our likelihood analysis results on mock data vectors contaminated with baryonic scenarios of Illustris, Eagle and DMO, and on the real DES data subjected to original Y1 scale cuts (the bar on the far left). The gray bars are S_8 errors subjected to Y1 scale cuts. The blue/red/orange/brown are the results with the cosmic shear data points extended to 2.5 arcmin, and with 0/1/2/3 PC mode(s) being marginalized when doing analysis.

the 3×2 point analysis. However, this choice ends up with having less cosmological constraining power compared with the fiducial DES Y1 analysis subjected to conservative scale cuts. Luckily, it is believed that our Universe is not like Illustris, for which the radio-mode AGN feedback is known to be too violent such that too much gas are heated and ejected, leading to lack of baryons in galaxy groups (Haider et al., 2016). For the Eagle scenario, the expected biases are within 1σ even without applying any marginalization technique. *We therefore conclude that marginalizing over one PC mode is likely to be sufficient for DES Y1 covariance, for baryonic scenarios that are less intense compared with Illustris* (but we will still present the results with two PC modes coming into marginalization, when applied on real data). When marginalizing over only one baryonic parameter, we expect to have slightly better cosmological constraint after marginalization. As for the case of Eagle, we have $\sim$10% smaller error bar on S_8 when including small scale cosmic shear data compared with the result subjected to the original DES Y1 scale cut (Fig. 5.5).

Note that although throughout §5.2.1 we use the S_8 constraint to build our points, the conclusions would not change based on the results for Ω_m or σ_8.

The finding that we would only gain tighter cosmological constraint from small scale cosmic shear when marginalizing over one PC mode motivates the reasoning on our choice of baryonic scenarios when conducting PCA. With only a single PC mode involved, we hope that this PC mode could reflect the truth of our Universe as close as possible. Hence, we do not include the Illustris scenario in the PCA process, but only use it on validation. Unlike our previous PC construction in H19, we also exclude baryonic scenarios without AGN subgrid model in the OWLS simulation suit. Our final choice then being narrowed down to the remaining five hydrodynamical scenarios in our library (OWLS-AGN, Horizon-AGN, MB2, IllustrisTNG, Eagle), and use them as representatives on the range of uncertainties for baryonic physics.

5.2.2 The interplay among baryons, cosmology, and other systematic parameters

Here we investigate the correlations of the PC amplitudes (Q_i) with cosmological and other nuisance parameters as listed in Table 5.1. Since there are nearly 30 parameters involved in modeling the full 3×2 pt data vectors, it is challenging to draw a complete picture on the dependencies among parameters in such a high dimensional space. To approach this problem in a simpler way, we will use the likelihood simulation chains from the DMO scenario as demonstrations to construct potential interpretations.[3]

Figure 5.6 shows the posterior distributions for the likelihood analyses, with the DMO mock data vector as input. The numbers on the corner of the some selected panels are correlation coefficients of parameters derived from the MCMC chains as labeled in the legend. The correlation matrix is the inverse of parameter covariance matrix computed as

$$\mathbf{C}^{ij}_{\rm par} = \frac{1}{N-1}\sum_{k=1}^{N}(\boldsymbol{\theta}^{ik} - \langle\boldsymbol{\theta}^{i}\rangle)(\boldsymbol{\theta}^{jk} - \langle\boldsymbol{\theta}^{j}\rangle)\,, \tag{5.21}$$

with $\langle\boldsymbol{\theta}^{i}\rangle$ indicating the mean of the i-th parameter, and $k \in [1, N]$ being the index running over the first 90% higher likelihood steps in the MCMC chain. We discard 10% MCMC samples with low likelihood values when deriving parameter covariance in order to decrease the effects from samples distributed far away from high likelihood region.

The degeneracy of PC amplitudes with cosmology and systematic parameters can be found in panels of the last two raws of Fig. 5.6. We find that

- As highlighted in the yellow backgrounds, $Q_{1,2}$ have negative correlations with $\Omega_{\rm m}$ and positive correlations with σ_8, n_s. The tendency of degeneracy becomes stronger when opening two PC modes to perform marginalization.
- No apparent degeneracies for Q_i with neutrino and intrinsic alignment parameters.
- No apparent degeneracies for Q_i with systematic parameters subjected to informative priors (shear calibration and photo-z).[4]
- The PC amplitudes are found to have negative correlations with the galaxy bias parameters $b^i_{\rm g}$.
- As highlighted in the gray backgrounds, the parameter dependencies among $\Omega_{\rm m}$, σ_8, and $b^i_{\rm g}$ are really strong, with the absolute values of their correlation coefficients to be around 0.9.
- When allowing 2 PC amplitudes to vary, the correlation coefficient between Q_1 and Q_2 is -0.62.

To intuitively understand the parameter degeneracy derived from the MCMC black box in Fig. 5.6, we will use Figs. 5.7 and 5.8 to provide our explanation. In Fig. 5.7, we plot the fractional changes of model vectors ($\frac{\boldsymbol{M}-\boldsymbol{M}_{\rm fid}}{\boldsymbol{M}_{\rm fid}}$) when varying individual parameters to 1σ above (solid lines) or below (dash lines) from its fiducial value listed in Table 5.1. The 1σ value for each parameter adopted is derived from our DMO based likelihood simulation results when marginalizing over 2 PC modes (the blue contours shown in Fig. 5.6). To understand the posterior distribution with less complicated entanglement of parameters, in Fig. 5.8, we present results from a series of likelihood analyses for

[3]The main intuitions drawn would remain similar for the Eagle and Illustris MCMC chains.

[4]For clarity, in Fig. 5.6 we only select one or two representative tomographic bins for systematic parameters, but the degeneracy trends for bins that are not shown remain similar to the selected bins as demonstrated in the plot.

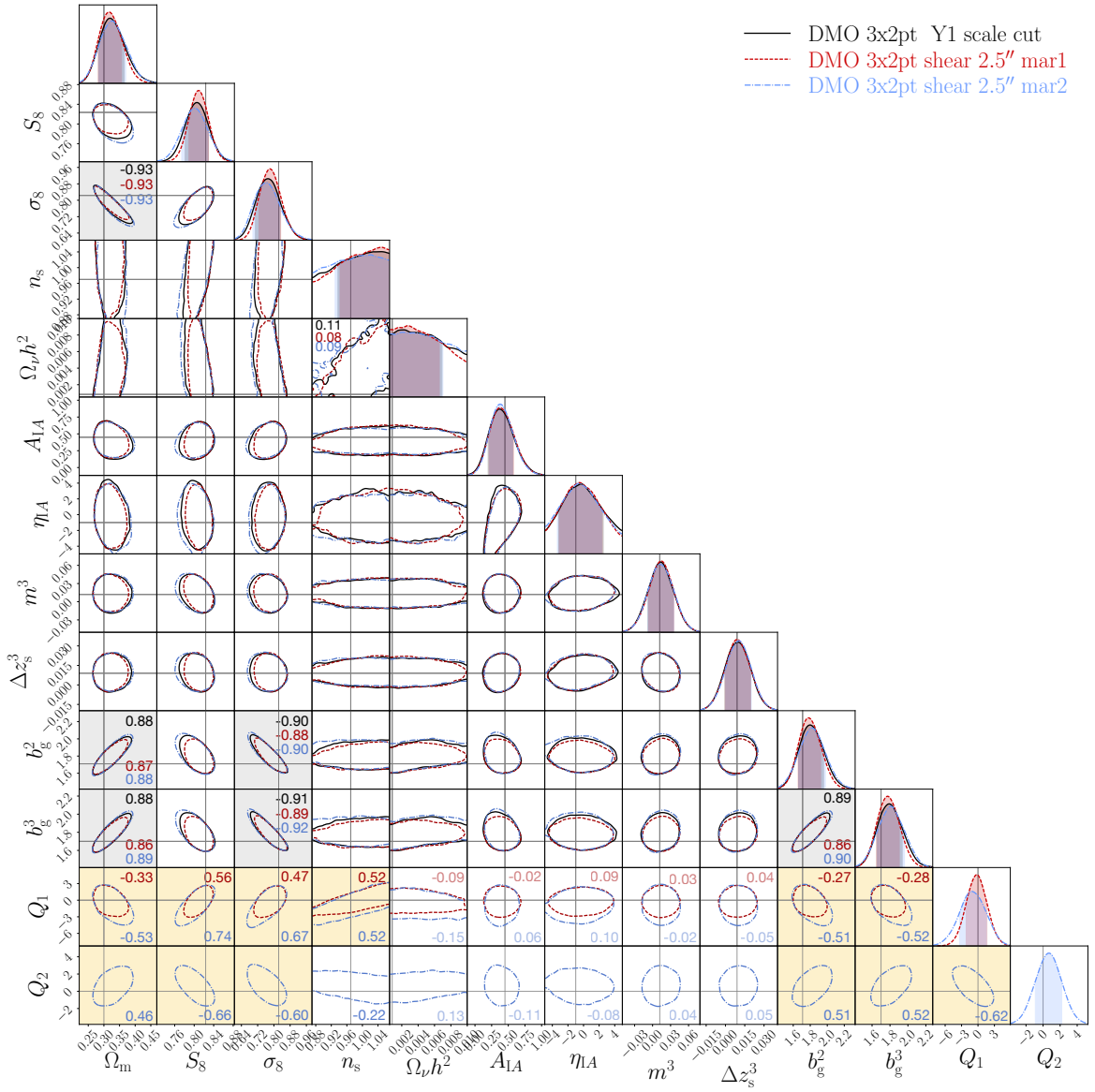

Figure 5.6: The posterior distributions for our likelihood analyses, with the DMO mock data vector as input. The fiducial parameter values are indicated in the cross lines (gray). The black contours indicate the 1σ level constraints with the original DES Y1 scale cuts applied on our mock data vector. The red / blue contours are results when extending cosmic shear down to 2.5 arcmin and with one / two PC amplitude(s) being marginalized. The colored numbers on the corner of the selected panels are correlation coefficients between two parameters derived from each of the corresponding MCMC chains.

the DMO 3×2 pt mock data vector with cosmic shear extended to 2.5 arcmin, but keep certain set of nuisance parameters fixed at their fiducial values. This experiment also allows us to investigate changes of degeneracy when different combinations of parameters are allowed to vary.

Below we provide our explanations on the correlation trends observed in Fig. 5.6 using evidences found in Figs. 5.7 and 5.8. From the dark blue chain shown in Fig. 5.8, when all other nuisance parameters are not allowed to vary, we derive slightly positive correlations between Q_1 with $\Omega_{\rm m}$ and σ_8 (correlation coefficient 0.17, and 0.51 respectively). This is supported from the upper panel of Fig. 5.7. When Q_1 increases, the power on $\xi_\pm$ decreases (mostly on small scale); one can boost the overall power of $\xi_\pm$ by increasing σ_8 ($\Omega_{\rm m}$), which leads to the positive correlation between Q_1 and σ_8 (Ω_m). The apparent differences in the angular scale variation of $\xi_\pm$ when varying Q_1 and σ_8 ($\Omega_{\rm m}$) further explains why the correlation exists but is weak.

From Fig. 5.8 we observe that opening degrees of freedom for systematic parameters subjected to tight priors barely disturb the original correlations among parameters (light blue vs dark blue contours). Adding IA parameters into the parameter pool also hardly changes the degeneracy directions of posteriors (gray vs dark blue contours). As shown in Fig. 5.7, although varying $A_{\rm IA}$ and $\eta_{\rm IA}$ results in an overall amplitude shifts on the data vectors, with the angular scale variation being similar as tuning σ_8, the degeneracies between IA and σ_8 can still be broken from the their distinction in the redshift direction. For example, in the bottom panel of Fig. 5.7, for galaxy-galaxy lensing, IA contamination only comes in correlations of lens and source pairs being affected by the same gravitational field (i.e. the (2,2) tomographic bins where there is an overlap in the lens-source redshift distribution); for tomographic bins that have little overlap in redshifts, there is almost no IA contamination, as shown in the (2,3) bin for $\gamma_{\rm t}$.

The galaxy bias parameters play an important role in varying the degeneracy of parameters, as shown in the dark blue v.s. yellow contours in Fig. 5.8. In fact, we can further conclude that the observed degeneracy trends in our full analysis (when opening all degrees of freedom) is driven by allowing $b_{\rm g}^i$ to vary, as shown from the high similarity between the yellow and red contours.

As shown in panels B and C, the correlation between Q_1 and σ_8 stays positive but is slightly boosted (0.51→0.67) when free galaxy bias parameters, while the correlation between Q_1 and $\Omega_{\rm m}$ changes from positive to negative direction (0.17→-0.5). We think this flipping of sign originates from the tight coupling among $b_{\rm g}^i$, $\Omega_{\rm m}$ and σ_8. When Q_1 increases, σ_8 tends to increase (panel C); because of the tight negative coupling between galaxy bias and σ_8 (panel E), $b_{\rm g}^i$ tends to decrease. Moreover, because of the significant positive correlation between $b_{\rm g}^i$ and $\Omega_{\rm m}$ (panel D), when $b_{\rm g}^i$ decreases, $\Omega_{\rm m}$ tends to decrease. This series of correlation eventually leads to the resulting negative between Q_1 and $\Omega_{\rm m}$ (i.e. Q_1 $\nearrow$, σ_8 $\nearrow$, $b_{\rm g}^i$ $\searrow$, $\Omega_{\rm m}$ $\searrow$), when galaxy bias parameters are allowed to vary. Although intrinsically Q_1 and $\Omega_{\rm m}$ tends to have slightly positive correlation, the much stronger degeneracy between $\Omega_{\rm m}$ and $b_{\rm g}^i$ erases this trend. One can go to the galaxy clustering column in Fig. 5.7 to find why the correlation between $\Omega_{\rm m}$ and $b_{\rm g}^i$ is positive. When increasing $\Omega_{\rm m}$, the amplitude of galaxy clustering decreases; this is because we have to adjust the A_s parameter accordingly in order to keep σ_8 fixed.[5]

[5]While the amplitude of galaxy clustering decreases when increasing $\Omega_{\rm m}$ at fixed σ_8, the overall amplitudes in cosmic shear and galaxy-galaxy lensing observables still increasing. This is because there are extra $\Omega_{\rm m}$ factors in their theoretical formulae coming from the lensing kernel shown in Eq. (5.5).

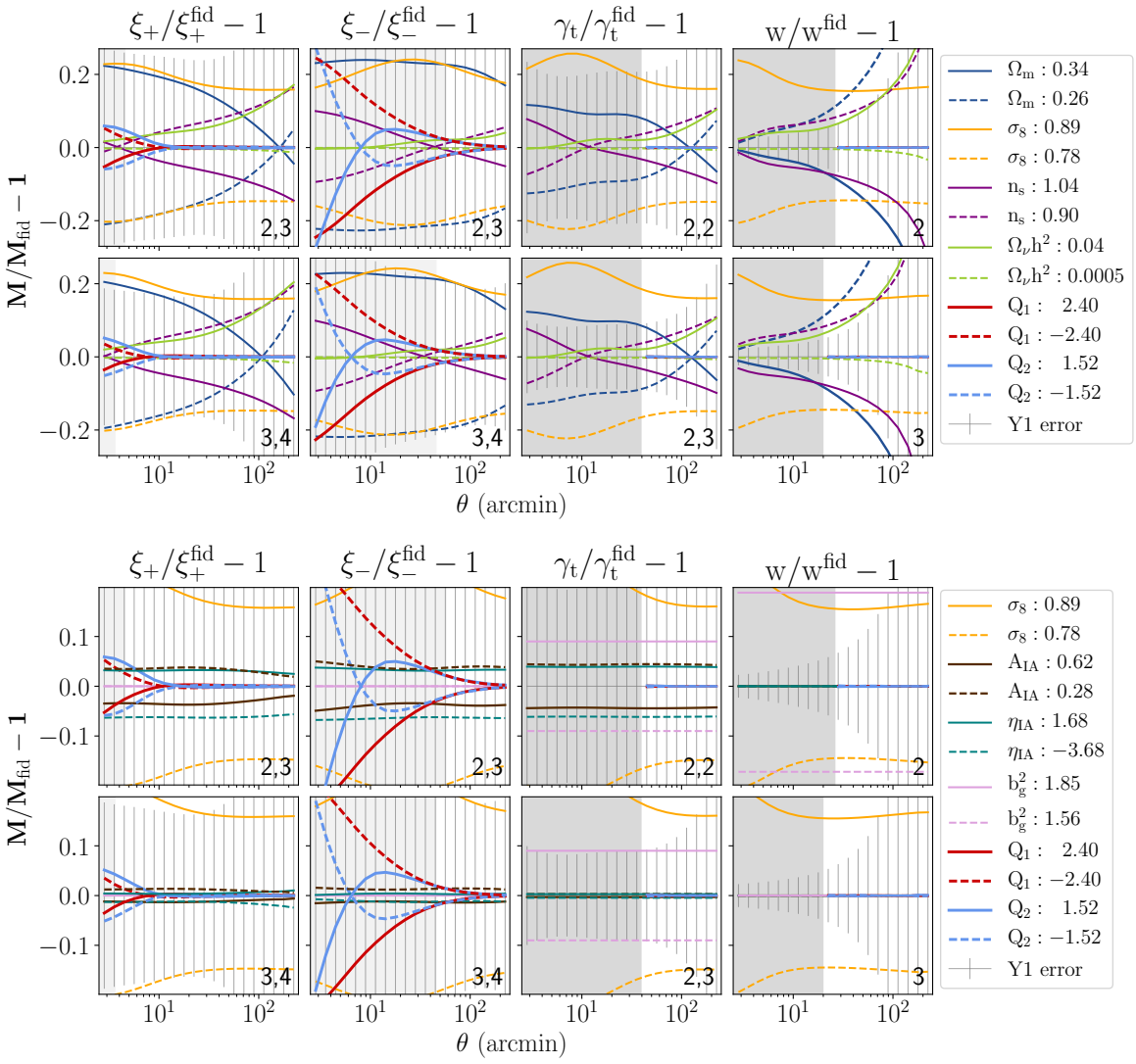

Figure 5.7: The fractional changes of model vectors when varying each of individual parameters to 1σ above (solid lines) or below (dash lines) its fiducial value listed in Table 5.1. We only select two tomographic bins for each of the observable as demonstration, with the bin information indicated on the bottom right corner of each panel (for galaxy-galaxy lensing, the first number is for lens tomographic bin; the second number for source). The darker gray bands covered in galaxy-galaxy lensing and clustering panels mark data points that are excluded throughout the work. The lighter gay bands in the cosmic shear observable highlight data points that are excluded in the original DES Y1 analysis, but are now included in this work. The error bars shown are the square root of the covariance matrix diagonal elements. For the neutrino parameter $\Omega_\nu h^2$, 0.0005 is the lowest value we can go with the choice of its prior range.

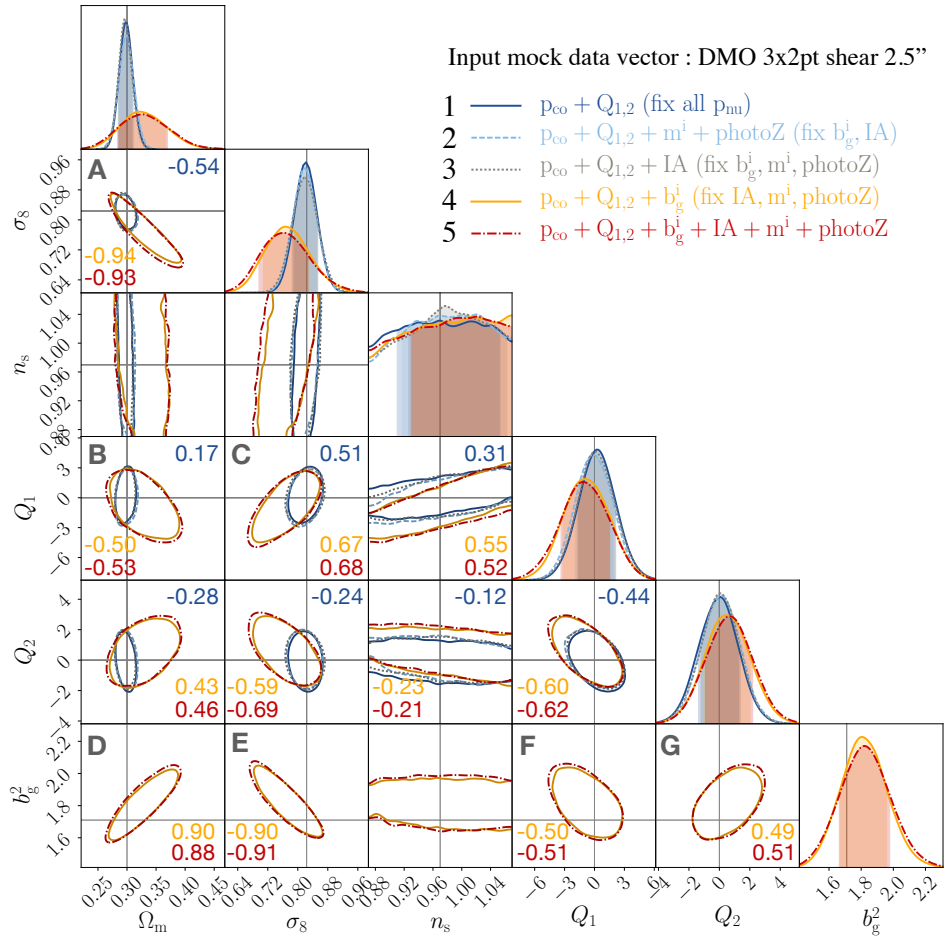

Figure 5.8: Posterior constraints from likelihood analyses with certain set of nuisance parameters fixed at their fiducial values. The input data vector is the DMO scenario with cosmic shear extended to 2.5 arcmin. We run five chains with the 6 cosmological and the two PC amplitudes always allowed to vary, but from top to bottom listed in the legend, we 1) fix all other systematic parameters (blue), 2) allow systematic parameters subjected to informative priors to vary (lightblue), 3) allow IA parameters to vary (gray), 4) allow galaxy bias parameters to vary (yellow), and finally the fifth chain plotted is the standard analysis with all nuisance parameters allowed to vary (red). The colored numbers on the corner of the selected panels are correlation coefficients between two parameters derived from chains No. 1, 4 and 5.

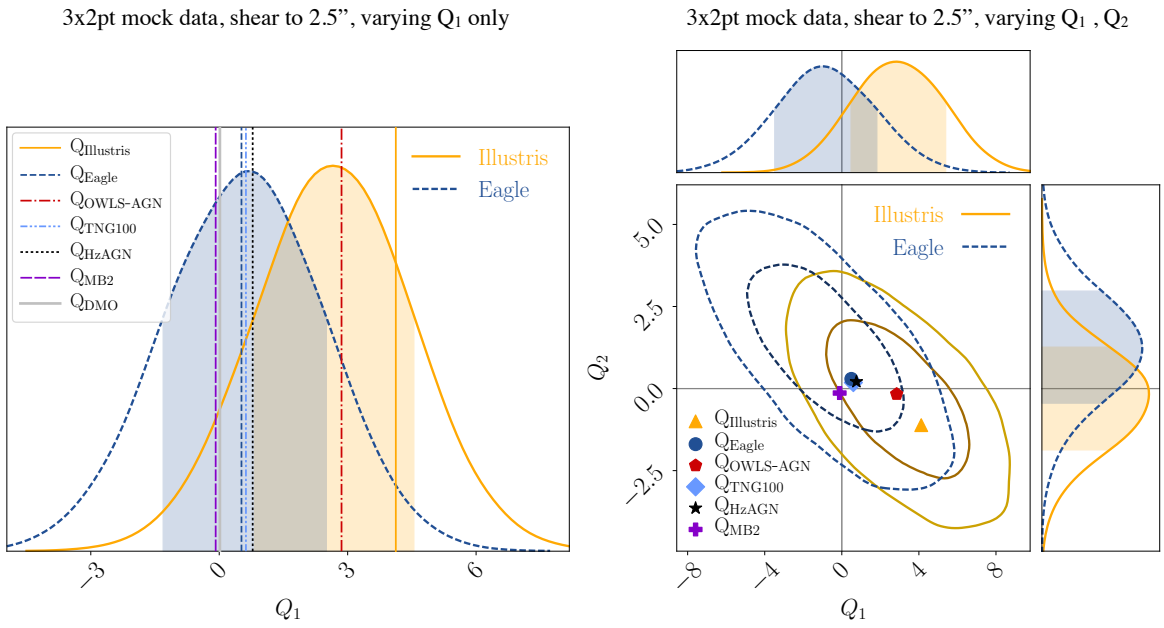

Figure 5.9: Posterior constraints of PC amplitudes for mock data vectors of Illustris and Eagle scenarios. The left panel shows the posterior of Q_1, when only marginalizing over 1 PC mode. The right panel shows the 2D posterior distribution of Q_1 and Q_2, for likelihood simulations when opening degrees of freedom for 2 PC amplitudes.

The degeneracies of $Q_{1,2}$ and galaxy bias parameters (panels F, G in Fig. 5.8) can also be explained through the coupling among b_g^i, Ω_m, σ_8. In principle, one may expect PC amplitudes being almost independent with galaxy bias parameters, because tuning $Q_{1,2}$ only affects the cosmic shear observable, while tuning b_g^i only affects the galaxy clustering part (see Fig. 5.7). However, due to the coupling of PC amplitudes with cosmology, $Q_{1,2}$ then are linked to galaxy bias parameters via the tight correlation among b_g^i with Ω_m or σ_8.

5.2.3 Expected constraints on baryonic parameters

Here we discuss the expected constraints on PC amplitude parameters, when including small-scale cosmic shear data points into analyses and given the DES Y1 covariance. We will use our likelihood simulation results with the Illustris and Eagle mock data vectors as input to demonstrate our points.

Figure 5.9 shows the posterior distributions of PC amplitudes, when marginalizing over only Q_1 on the left panel, and when varying both $Q_{1,2}$ parameters on the right panel. We also present the expected $Q_{1,2}$ values for various baryonic scenarios in various markers.

When only allowing one PC amplitude to vary, we are expected to exclude baryonic scenarios that are very different from the fiducial input by one sigma. For example, as shown in the left panel of Fig. 5.9, the Q_1 values for the OWLS-AGN and Illustris scenarios are falling outside the 1σ region of the posterior from the Eagle chain (blue). Similarly, when the input mock baryonic scenario is Illustris, the Q_1 values for MB2 and DMO scenarios can be ruled out by 1σ.

When allowing two PC amplitudes to vary, depending on the input mock data vector, the scatter

of PC amplitudes for all of the baryonic scenarios considered in this work may all fall within the 1σ region on the Q_1 and Q_2 projected plan, as shown in the right panel of Fig. 5.9, for the case of Illustris likelihood simulation result.

5.3 Future Works and Outlook

So far we have validated our pipeline using likelihood simulation analyses on several mock data vectors. Our pipeline is ready to be applied on real DES Y1 data once there is an agreement reached among the co-authors and the DES collaboration.

In real data analysis, many nuisance parameters are involved to account for various systematic effects. We find that there is only room for one extra PC parameter to account for baryonic effects in order to benefit from including small scale cosmic shear data into analysis, compared with the original Y1 conservative scale cut. Due to complex parameter degeneracies, the residual biases on cosmological constraints do not necessarily go down with increasing degrees of freedom opened, even in a noise free simulated analysis. It is thus important to reach better controls on prior information through improved understanding of baryonic physics in order to derive robust cosmological information from small scale data.

6 Conclusion and Outlook

Gravitational lensing provides a unique channel to directly probe dark matter, in contrast as relying on luminous galaxies as biased tracers on the large scale matter distribution. Even with this promising fact, we still need to deal with complex astrophysics related to galaxies in order to extract the pure lensing effect caused by gravity, and to relate the matter distribution information to cosmological models.

The complexity in astrophysics often requires high resolution data to fundamentally understand the triggering mechanism, spectroscopic information to extract required information, and large sample size to test possible hypotheses and establish arguments. As presented in **Chapters** 2 and 3, though with an attempt of understanding the physical origin of small-scale IA phenomenon, the best we could draw from data is concluded that small-scale IA is a complicated phenomenon potentially involving multiple relevant physical processes during galaxy and cluster formation and evolution. We also try to identify the evidence of tidal torquing effect on IA from various shape measurement methods with different weights on galaxy light profiles. Unfortunately, we are lack of galaxies to construct control sample to rule out systematic effects in shape measurement errors. On-going and future spectroscopic data from eBOSS and DESI will enlarge the sample size and push IA constraints to fainter galaxies and higher redshifts, enabling more stringent tests on theories of IA. Our IA analyses method will also be useful to build an empirically-motivated halo model for IA including parametric dependencies on galaxy and cluster properties.

While the science of cosmology is in the era of precision, many of the astrophysical quantifications are still in the phase of estimating errors in units of dex. Fortunately, in cosmological application the issue of astrophysics can be passively managed via quantifying their uncertainties and designing mitigation schemes to transport the current level of uncertainty constraints to marginalized error on cosmology. As demonstrated in **Chapters** 4 and 5, we design a modeling framework to deal with the systematic effect of baryons in cosmic shear measurements, with the flexibility to shrink the level of uncertainty opened in advance with next generation hydrodynamical simulations, which will continuously be tuned to match with novel observational constraints. Based on the assumption that current hydrodynamical simulations are well represented for the scatter of baryonic effects of our Universe, we have demonstrated that after mitigation, we could potentially benefit from involving small-scale information in cosmological analyses in certain circumstances. For future works, we can also quantify the diversity of IA power spectra from various hydrodynamical scenarios and construct small-scale IA mitigation models in a similar framework.

Building models based on hydrodynamical simulations is always a concern because currently no hydrodynamical simulation can well reproduce observational results in all aspects, and there is no guarantee that the parameter space can ever be fully explored, not to mention that different subgrid physics prescriptions are used in different hydrodynamical codes. Currently most of the hydrodynamical simulations are calibrated based on galaxy related quantities (e.g. the stellar mass function, stellar mass–black hole mass relation...). For the cosmology needs for weak lensing and cluster sciences, relatively larger scale effects ($\gtrsim$ few Mpc) of baryonic physics are more important given the limit of scale range we could potentially push down to constrain cosmology. At this regime,

the dominant baryonic effect is the suppression of power caused by baryonic feedback processes, which are closely related to the gas properties of halos. Additional observational data sets will soon be available to provide powerful constraints on the characteristics and the distributions of gas in our Universe. On-going Stage III thermal and kinetic Sunyaev-Zel'dovich measurements combined with future DESI spectroscopic galaxy samples will bring dramatic improvements on the sensitivity of signals, providing information on the thermodynamic properties of intergalactic medium (Battaglia et al., 2017). Over the next few years, the eROSITA mission, which was just successfully launched this summer, will create a deep full sky X-ray map of our Universe, and brining about 10^5 galaxy cluster samples for better understanding of halo gas profiles (Merloni et al., 2012). In the long run, the accumulated information from observed gas properties will play a crucial role in pinning down the parameter space allowed by baryonic feedback mechanisms, and provide more manageable calibration standards on hydrodynamical simulations for cosmological science.

Bibliography

Abazajian K. N., et al., 2009, ApJS, 182, 543

Abazajian K. N., et al., 2016, arXiv e-prints, p. arXiv:1610.02743

Abbott T. M. C., et al., 2018, Phys.Rev.D, 98, 043526

Adelman-McCarthy J. K., et al., 2006, ApJS, 162, 38

Agustsson I., Brainerd T. G., 2006, ApJ, 644, L25

Agustsson I., Brainerd T. G., 2010, ApJ, 709, 1321

Aihara H., et al., 2011, ApJS, 195, 26

Akaike H., 1998, in , Selected Papers of Hirotugu Akaike. Springer, pp 199–213

Allgood B., Flores R. A., Primack J. R., Kravtsov A. V., Wechsler R. H., Faltenbacher A., Bullock J. S., 2006, MNRAS, 367, 1781

Antilogus P., Astier P., Doherty P., Guyonnet A., Regnault N., 2014, Journal of Instrumentation, 9, C03048

Azzaro M., Patiri S. G., Prada F., Zentner A. R., 2007, MNRAS, 376, L43

Battaglia N., Ferraro S., Schaan E., Spergel D. N., 2017, J. Cosmology Astropart. Phys., 2017, 040

Baxter E. J., Rozo E., Jain B., Rykoff E., Wechsler R. H., 2016, MNRAS, 463, 205

Belokurov V., et al., 2006, ApJ, 642, L137

Bernardeau F., Colombi S., Gaztañaga E., Scoccimarro R., 2002, Phys.Rep., 367, 1

Bernardi M., Meert A., Vikram V., Huertas-Company M., Mei S., Shankar F., Sheth R. K., 2014, MNRAS, 443, 874

Bernstein G. M., Jarvis M., 2002, AJ, 123, 583

Binggeli B., 1982, A&A, 107, 338

Blanton M. R., Roweis S., 2007, AJ, 133, 734

Blas D., Lesgourgues J., Tram T., 2011, Journal of Cosmology and Astro-Particle Physics, 2011, 034

Blazek J., Mandelbaum R., Seljak U., Nakajima R., 2012, J. Cosmology Astropart. Phys., 5, 041

Blazek J., Vlah Z., Seljak U., 2015, J. Cosmology Astropart. Phys., 8, 15

Blazek J., MacCrann N., Troxel M. A., Fang X., 2017, preprint, (arXiv:1708.09247)

Blumenthal G. R., Faber S. M., Primack J. R., Rees M. J., 1984, Nature, 311, 517

Blumenthal G. R., Faber S. M., Flores R., Primack J. R., 1986, ApJ, 301, 27

Booth C. M., Schaye J., 2009, MNRAS, 398, 53

Bottrell C., Torrey P., Simard L., Ellison S. L., 2017, MNRAS, 467, 2879

Brainerd T. G., 2005, ApJ, 628, L101

Bridle S., King L., 2007, New Journal of Physics, 9, 444

Brown M. L., Taylor A. N., Hambly N. C., Dye S., 2002, MNRAS, 333, 501

Bruzual G., Charlot S., 2003, MNRAS, 344, 1000

Burnham K. P., Anderson D. R., 2003a, Model selection and multimodel inference: a practical information-theoretic approach. Springer Science & Business Media

Burnham K. P., Anderson D. R., 2003b, Model selection and multimodel inference: a practical information-theoretic approach. Springer Science & Business Media

Camelio G., Lombardi M., 2015, A&A, 575, A113

Catelan P., Kamionkowski M., Blandford R. D., 2001, MNRAS, 320, L7

Chabrier G., 2003, PASP, 115, 763

Chang C., et al., 2013, MNRAS, 434, 2121

Chen Y.-C., et al., 2015, MNRAS, 454, 3341

Chen Y.-C., Ho S., Brinkmann J., Freeman P. E., Genovese C. R., Schneider D. P., Wasserman L., 2016, MNRAS, 461, 3896

Chen Y.-C., et al., 2017, MNRAS, 466, 1880

Chisari N. E., Mandelbaum R., Strauss M. A., Huff E. M., Bahcall N. A., 2014, MNRAS, 445, 726

Chisari N., et al., 2015, MNRAS, 454, 2736

Chisari N. E., et al., 2018, MNRAS, 480, 3962

Ciotti L., Dutta S. N., 1994, MNRAS, 270, 390

Conroy C., Wechsler R. H., Kravtsov A. V., 2007, ApJ, 668, 826

Cooper A. P., D'Souza R., Kauffmann G., Wang J., Boylan-Kolchin M., Guo Q., Frenk C. S., White S. D. M., 2013, MNRAS, 434, 3348

Cooray A., Hu W., 2001, ApJ, 554, 56

Cooray A., Sheth R., 2002, Phys.Rep., 372, 1

Copeland D., Taylor A., Hall A., 2018, MNRAS, 480, 2247

Crain R. A., et al., 2015, MNRAS, 450, 1937

Cui W., Borgani S., Murante G., 2014, MNRAS, 441, 1769

DESI Collaboration et al., 2016, arXiv e-prints, p. arXiv:1611.00036

Dai B., Feng Y., Seljak U., 2018, J. Cosmology Astropart. Phys., 11, 009

Dalal N., White M., Bond J. R., Shirokov A., 2008, ApJ, 687, 12

Dark Energy Survey Collaboration et al., 2016, MNRAS, 460, 1270

Debattista V. P., van den Bosch F. C., Roškar R., Quinn T., Moore B., Cole D. R., 2015, MNRAS, 452, 4094

Di Matteo T., Springel V., Hernquist L., 2005, Nature, 433, 604

Dodelson S., 2017, Gravitational Lensing

Dong F., Pierpaoli E., Gunn J. E., Wechsler R. H., 2008, ApJ, 676, 868

Doré O., et al., 2018, arXiv e-prints, p. arXiv:1804.03628

Dubinski J., 1998, ApJ, 502, 141

Dubois Y., Devriendt J., Slyz A., Teyssier R., 2012, MNRAS, 420, 2662

Dubois Y., et al., 2014, MNRAS, 444, 1453

Eifler T., 2011, MNRAS, 418, 536

Eifler T., Schneider P., Hartlap J., 2009, A&A, 502, 721

Eifler T., Krause E., Schneider P., Honscheid K., 2014, MNRAS, 440, 1379

Eifler T., Krause E., Dodelson S., Zentner A. R., Hearin A. P., Gnedin N. Y., 2015, MNRAS, 454, 2451

Einasto J., Kaasik A., Saar E., 1974, Nature, 250, 309

Einstein A., de Sitter W., 1932, Proceedings of the National Academy of Sciences, 18, 213

Eisenstein D. J., et al., 2001, AJ, 122, 2267

Elvin-Poole J., et al., 2018, Phys.Rev.D, 98, 042006

Evans A. K. D., Bridle S., 2009, ApJ, 695, 1446

Faltenbacher A., Li C., Mao S., van den Bosch F. C., Yang X., Jing Y. P., Pasquali A., Mo H. J., 2007, ApJ, 662, L71

Faltenbacher A., Jing Y. P., Li C., Mao S., Mo H. J., Pasquali A., van den Bosch F. C., 2008, ApJ, 675, 146

Firth A. E., Lahav O., Somerville R. S., 2003, MNRAS, 339, 1195

Foreman-Mackey D., Hogg D. W., Lang D., Goodman J., 2013, PASP, 125, 306

Freedman W. L., 2017, Nature Astronomy, 1, 0169

Friedman J., Hastie T., Tibshirani R., 2001, The elements of statistical learning. Vol. 1, Springer series in statistics Springer, Berlin

Fukugita M., Ichikawa T., Gunn J. E., Doi M., Shimasaku K., Schneider D. P., 1996, AJ, 111, 1748

Furlong M., et al., 2017, MNRAS, 465, 722

Gao L., White S. D. M., 2007, MNRAS, 377, L5

Gao L., Springel V., White S. D. M., 2005, MNRAS, 363, L66

Genel S., et al., 2014, MNRAS, 445, 175

Giblin B., et al., 2018, MNRAS, 480, 5529

Gnedin N. Y., Kravtsov A. V., Rudd D. H., 2011, ApJS, 194, 46

Goodman J., Weare J., et al., 2010, Communications in applied mathematics and computational science, 5, 65

Grueber C., Nakagawa S., Laws R., Jamieson I., 2011, Journal of evolutionary biology, 24, 699

Gunn J. E., et al., 1998, AJ, 116, 3040

Haider M., Steinhauser D., Vogelsberger M., Genel S., Springel V., Torrey P., Hernquist L., 2016, MNRAS, 457, 3024

Hamana T., et al., 2019, arXiv e-prints, p. arXiv:1906.06041

Hao J., et al., 2010, ApJS, 191, 254

Hao J., Kubo J. M., Feldmann R., Annis J., Johnston D. E., Lin H., McKay T. A., 2011, ApJ, 740, 39

Harnois-Déraps J., van Waerbeke L., Viola M., Heymans C., 2015, MNRAS, 450, 1212

Hayashi E., Navarro J. F., Springel V., 2007, MNRAS, 377, 50

Hearin A. P., Zentner A. R., Ma Z., 2012, J. Cosmology Astropart. Phys., 4, 034

Heitmann K., White M., Wagner C., Habib S., Higdon D., 2010, ApJ, 715, 104

Heitmann K., Lawrence E., Kwan J., Habib S., Higdon D., 2014, ApJ, 780, 111

Heymans C., et al., 2006, MNRAS, 368, 1323

Hikage C., et al., 2019, PASJ, 71, 43

Hildebrandt H., et al., 2017, MNRAS, 465, 1454

Hirata C., Seljak U., 2003, MNRAS, 343, 459

Hirata C. M., Seljak U., 2004a, Phys.Rev.D, 70, 063526

Hirata C. M., Seljak U., 2004b, Phys.Rev.D, 70, 063526

Hirata C. M., Mandelbaum R., Ishak M., Seljak U., Nichol R., Pimbblet K. A., Ross N. P., Wake D., 2007, MNRAS, 381, 1197

Hogg D. W., Finkbeiner D. P., Schlegel D. J., Gunn J. E., 2001, AJ, 122, 2129

Hopkins P. F., Bahcall N. A., Bode P., 2005, ApJ, 618, 1

Hoshino H., et al., 2015, MNRAS, 452, 998

Hoyle B., et al., 2018, MNRAS, 478, 592

Hu W., 1999, ApJ, 522, L21

Hu W., Jain B., 2004, Phys.Rev.D, 70, 043009

Huang H.-J., Mandelbaum R., Freeman P. E., Chen Y.-C., Rozo E., Rykoff E., Baxter E. J., 2016, MNRAS, 463, 222

Huang H.-J., Mandelbaum R., Freeman P. E., Chen Y.-C., Rozo E., Rykoff E., 2018, MNRAS, 474, 4772

Huang H.-J., Eifler T., Mandelbaum R., Dodelson S., 2019, Monthly Notices of the Royal Astronomical Society, 488, 1652

Huff E., Mandelbaum R., 2017, arXiv e-prints, p. arXiv:1702.02600

Hung C.-L., Ebeling H., 2012, MNRAS, 421, 3229

Huterer D., Takada M., 2005, Astroparticle Physics, 23, 369

Ilbert O., et al., 2006, A&A, 457, 841

Ivezić Ž., et al., 2004, Astronomische Nachrichten, 325, 583

James G., Witten D., Hastie T., Tibshirani R., 2013, An Introduction to Statistical Learning with Applications in R. Springer-Verlag New York

Jing Y. P., Suto Y., 2002, ApJ, 574, 538

Joachimi B., Mandelbaum R., Abdalla F. B., Bridle S. L., 2011, A&A, 527, A26

Joachimi B., et al., 2015, Space Sci.Rev., 193, 1

Joudaki S., et al., 2017, MNRAS, 465, 2033

Joudaki S., et al., 2019, arXiv e-prints, p. arXiv:1906.09262

Kang X., van den Bosch F. C., Yang X., Mao S., Mo H. J., Li C., Jing Y. P., 2007, MNRAS, 378, 1531

Kasun S. F., Evrard A. E., 2005, ApJ, 629, 781

Kaviraj S., et al., 2017, MNRAS, 467, 4739

Khandai N., Di Matteo T., Croft R., Wilkins S., Feng Y., Tucker E., DeGraf C., Liu M.-S., 2015, MNRAS, 450, 1349

Kiessling A., et al., 2015, Space Sci.Rev., 193, 67

Kirk D., et al., 2015, Space Sci.Rev., 193, 139

Kitching T. D., Verde L., Heavens A. F., Jimenez R., 2016, MNRAS, 459, 971

Knebe A., Gill S. P. D., Gibson B. K., Lewis G. F., Ibata R. A., Dopita M. A., 2004, ApJ, 603, 7

Koester B. P., et al., 2007, ApJ, 660, 221

Köhlinger F., et al., 2017, MNRAS, 471, 4412

Komatsu E., et al., 2011, ApJS, 192, 18

Kormendy J., 1982, in Martinet L., Mayor M., eds, Saas-Fee Advanced Course 12: Morphology and Dynamics of Galaxies. pp 113–288

Krause E., Eifler T., 2017, MNRAS, 470, 2100

Krause E., Eifler T., Blazek J., 2016, MNRAS, 456, 207

Krause E., et al., 2017, preprint, (arXiv:1706.09359)

Kuehn F., Ryden B. S., 2005, ApJ, 634, 1032

Kuhlen M., Diemand J., Madau P., 2007, ApJ, 671, 1135

LSST Science Collaboration et al., 2009, arXiv e-prints, p. arXiv:0912.0201

Laigle C., et al., 2016, ApJS, 224, 24

Lauer T. R., et al., 2005, AJ, 129, 2138

Laureijs R., et al., 2011, preprint, (arXiv:1110.3193)

Lawrence E., et al., 2017, ApJ, 847, 50

Lee J., Evrard A. E., 2007, ApJ, 657, 30

Lee J., Pen U.-L., 2000, ApJ, 532, L5

Li Z., Wang Y., Yang X., Chen X., Xie L., Wang X., 2013, ApJ, 768, 20

Libeskind N. I., Frenk C. S., Cole S., Helly J. C., Jenkins A., Navarro J. F., Power C., 2005, MNRAS, 363, 146

Libeskind N. I., Hoffman Y., Tully R. B., Courtois H. M., Pomarède D., Gottlöber S., Steinmetz M., 2015, MNRAS, 452, 1052

Limber D. N., 1953, ApJ, 117, 134

Lin Y.-T., Mohr J. J., 2004, ApJ, 617, 879

Lin Y.-T., Mandelbaum R., Huang Y.-H., Huang H.-J., Dalal N., Diemer B., Jian H.-Y., Kravtsov A., 2016, ApJ, 819, 119

Lupton R. H., Gunn J. E., Ivezić Z., Knapp G. R., Kent S., Yasuda N., 2001, in ASP Conf. Ser. 238: Astronomical Data Analysis Software and Systems X. pp 269–278

MacCrann N., et al., 2017, MNRAS, 465, 2567

Mallows C. L., 1973, Technometrics, 15, 661

Mandelbaum R., 2018, ARA&A, 56, 393

Mandelbaum R., et al., 2005, MNRAS, 361, 1287

Mandelbaum R., Hirata C. M., Ishak M., Seljak U., Brinkmann J., 2006, MNRAS, 367, 611

Mandelbaum R., et al., 2011, MNRAS, 410, 844

Mandelbaum R., Slosar A., Baldauf T., Seljak U., Hirata C. M., Nakajima R., Reyes R., Smith R. E., 2013, MNRAS, 432, 1544

Marinacci F., et al., 2018, MNRAS, 480, 5113

Martínez H. J., Muriel H., Coenda V., 2016, MNRAS, 455, 127

Martizzi D., Teyssier R., Moore B., Wentz T., 2012, Monthly Notices of the Royal Astronomical Society, 422, 3081

Massey R., Kitching T., Richard J., 2010, Reports on Progress in Physics, 73, 086901

McCarthy I. G., Schaye J., Bower R. G., Ponman T. J., Booth C. M., Dalla Vecchia C., Springel V., 2011, MNRAS, 412, 1965

McCarthy I. G., Schaye J., Bird S., Le Brun A. M. C., 2017, MNRAS, 465, 2936

Mead A. J., Peacock J. A., Heymans C., Joudaki S., Heavens A. F., 2015, MNRAS, 454, 1958

Mead A. J., Heymans C., Lombriser L., Peacock J. A., Steele O. I., Winther H. A., 2016, MNRAS, 459, 1468

Merloni A., et al., 2012, arXiv e-prints, p. arXiv:1209.3114

Miyatake H., More S., Takada M., Spergel D. N., Mandelbaum R., Rykoff E. S., Rozo E., 2016, Physical Review Letters, 116, 041301

Miyazaki S., et al., 2012, Proc. SPIE, 8446, 84460Z

Mohammed I., Gnedin N. Y., 2018, ApJ, 863, 173

Mohammed I., Martizzi D., Teyssier R., Amara A., 2014, preprint, (arXiv:1410.6826)

More S., et al., 2016, ApJ, 825, 39

Morrison C. B., Schneider M. D., 2013, J. Cosmology Astropart. Phys., 11, 009

Mummery B. O., McCarthy I. G., Bird S., Schaye J., 2017, MNRAS, 471, 227

Naiman J. P., et al., 2018, MNRAS, 477, 1206

Navarro J. F., Frenk C. S., White S. D. M., 1996, ApJ, 462, 563

Nelson D., et al., 2015, Astronomy and Computing, 13, 12

Nelson D., et al., 2018, MNRAS, 475, 624

Nelson D., et al., 2019, Computational Astrophysics and Cosmology, 6, 2

Newman J. A., 2008, ApJ, 684, 88

Newman J. A., et al., 2015, Astroparticle Physics, 63, 81

Niederste-Ostholt M., Strauss M. A., Dong F., Koester B. P., McKay T. A., 2010, MNRAS, 405, 2023

Oemler Jr. A., 1976, ApJ, 209, 693

Oguri M., Takada M., Okabe N., Smith G. P., 2010, MNRAS, 405, 2215

Okumura T., Jing Y. P., Li C., 2009, ApJ, 694, 214

Onuora L. I., Thomas P. A., 2000, MNRAS, 319, 614

Osato K., Shirasaki M., Yoshida N., 2015, ApJ, 806, 186

Ostriker J. P., Peebles P. J. E., Yahil A., 1974, ApJ, 193, L1

Padmanabhan N., et al., 2008, ApJ, 674, 1217

Peacock J. A., Smith R. E., 2000, MNRAS, 318, 1144

Peng Y.-j., et al., 2010, ApJ, 721, 193

Peng Y.-j., Lilly S. J., Renzini A., Carollo M., 2012, ApJ, 757, 4

Penzias A. A., Wilson R. W., 1965, ApJ, 142, 419

Pereira M. J., Bryan G. L., 2010, ApJ, 721, 939

Pereira M. J., Kuhn J. R., 2005, ApJ, 627, L21

Pereira M. J., Bryan G. L., Gill S. P. D., 2008, ApJ, 672, 825

Perlmutter S., et al., 1999, ApJ, 517, 565

Pier J. R., Munn J. A., Hindsley R. B., Hennessy G. S., Kent S. M., Lupton R. H., Ivezić Ž., 2003, AJ, 125, 1559

Pillepich A., et al., 2018a, MNRAS, 473, 4077

Pillepich A., et al., 2018b, MNRAS, 475, 648

Planck Collaboration et al., 2014, A&A, 571, A16

Planck Collaboration et al., 2016, A&A, 594, A13

Planck Collaboration et al., 2018, arXiv e-prints, p. arXiv:1807.06209

Prat J., et al., 2018, Phys.Rev.D, 98, 042005

Ragone-Figueroa C., Plionis M., 2007, MNRAS, 377, 1785

Rasera Y., Teyssier R., 2006, A&A, 445, 1

Refregier A., Kacprzak T., Amara A., Bridle S., Rowe B., 2012, MNRAS, 425, 1951

Reyes R., Mandelbaum R., Gunn J. E., Nakajima R., Seljak U., Hirata C. M., 2012, MNRAS, 425, 2610

Richards G. T., et al., 2002, AJ, 123, 2945

Riess A. G., et al., 1998, AJ, 116, 1009

Rodríguez S., Padilla N. D., García Lambas D., 2016, MNRAS, 456, 571

Romanowsky A. J., Kochanek C. S., 1998, ApJ, 493, 641

Rong Y., Liu Y., Zhang S.-N., 2016, MNRAS, 455, 2267

Rozo E., Rykoff E. S., 2014, ApJ, 783, 80

Rozo E., Rykoff E. S., Bartlett J. G., Melin J.-B., 2015a, MNRAS, 450, 592

Rozo E., Rykoff E. S., Becker M., Reddick R. M., Wechsler R. H., 2015b, MNRAS, 453, 38

Rozo E., et al., 2016, MNRAS, 461, 1431

Rudd D. H., Zentner A. R., Kravtsov A. V., 2008, ApJ, 672, 19

Rykoff E. S., et al., 2012, ApJ, 746, 178

Rykoff E. S., et al., 2014, ApJ, 785, 104

Samuroff S., et al., 2018, arXiv e-prints, p. arXiv:1811.06989

Sastry G. N., 1968, PASP, 80, 252

Sato M., Hamana T., Takahashi R., Takada M., Yoshida N., Matsubara T., Sugiyama N., 2009, ApJ, 701, 945

Schaye J., et al., 2010, MNRAS, 402, 1536

Schaye J., et al., 2015, MNRAS, 446, 521

Schneider M. D., Bridle S., 2010, MNRAS, 402, 2127

Schneider A., Teyssier R., 2015, J. Cosmology Astropart. Phys., 12, 049

Schneider M. D., et al., 2013, MNRAS, 433, 2727

Schneider A., Teyssier R., Stadel J., Chisari N. E., Le Brun A. M. C., Amara A., Refregier A., 2019, Journal of Cosmology and Astro-Particle Physics, 2019, 020

Schwarz G., et al., 1978, The annals of statistics, 6, 461

Seljak U., 2000, MNRAS, 318, 203

Semboloni E., Hoekstra H., Schaye J., van Daalen M. P., McCarthy I. G., 2011, MNRAS, 417, 2020

Semboloni E., Hoekstra H., Schaye J., 2013, MNRAS, 434, 148

Shandarin S. F., Zeldovich Y. B., 1989, Reviews of Modern Physics, 61, 185

Sheldon E. S., Huff E. M., 2017, ApJ, 841, 24

Sifón C., Hoekstra H., Cacciato M., Viola M., Köhlinger F., van der Burg R. F. J., Sand D. J., Graham M. L., 2015, A&A, 575, A48

Simet M., McClintock T., Mandelbaum R., Rozo E., Rykoff E., Sheldon E., Wechsler R. H., 2017, MNRAS, 466, 3103

Simpson F., James J. B., Heavens A. F., Heymans C., 2011, Physical Review Letters, 107, 271301

Simpson F., Heavens A. F., Heymans C., 2013, Phys.Rev.D, 88, 083510

Singh S., Mandelbaum R., 2016, MNRAS, 457, 2301

Singh S., Mandelbaum R., More S., 2015, MNRAS, 450, 2195

Singh S., Alam S., Mandelbaum R., Seljak U., Rodriguez-Torres S., Ho S., 2019, MNRAS, 482, 785

Siverd R. J., Ryden B. S., Gaudi B. S., 2009, preprint, (arXiv:0903.2264)

Skibba R. A., van den Bosch F. C., Yang X., More S., Mo H., Fontanot F., 2011, MNRAS, 410, 417

Smargon A., Mandelbaum R., Bahcall N., Niederste-Ostholt M., 2012, MNRAS, 423, 856

Smith J. A., et al., 2002, AJ, 123, 2121

Smith R. E., et al., 2003, MNRAS, 341, 1311

Spergel D. N., et al., 2007, ApJS, 170, 377

Spergel D., et al., 2015, preprint, (arXiv:1503.03757)

Springel V., 2005, MNRAS, 364, 1105

Springel V., 2010, MNRAS, 401, 791

Springel V., Hernquist L., 2003, MNRAS, 339, 289

Springel V., Di Matteo T., Hernquist L., 2005, MNRAS, 361, 776

Springel V., et al., 2018, MNRAS, 475, 676

Stinson G. S., Bailin J., Couchman H., Wadsley J., Shen S., Nickerson S., Brook C., Quinn T., 2010, Monthly Notices of the Royal Astronomical Society, 408, 812

Stoughton C., et al., 2002, AJ, 123, 485

Strauss M. A., et al., 2002, AJ, 124, 1810

Sutherland R. S., Dopita M. A., 1993, ApJS, 88, 253

Takada M., Bridle S., 2007, New Journal of Physics, 9, 446

Takada M., Hu W., 2013, Phys. Rev. D, 87, 123504

Takada M., Jain B., 2009, MNRAS, 395, 2065

Takahashi R., Sato M., Nishimichi T., Taruya A., Oguri M., 2012, ApJ, 761, 152

Taylor P. L., Bernardeau F., Kitching T. D., 2018, Phys.Rev.D, 98, 083514

Tempel E., Guo Q., Kipper R., Libeskind N. I., 2015, MNRAS, 450, 2727

Tenneti A., Mandelbaum R., Di Matteo T., Feng Y., Khandai N., 2014, MNRAS, 441, 470

Tenneti A., Singh S., Mandelbaum R., Matteo T. D., Feng Y., Khandai N., 2015a, MNRAS, 448, 3522

Tenneti A., Mandelbaum R., Di Matteo T., Kiessling A., Khandai N., 2015b, MNRAS, 453, 469

Tenneti A., Mandelbaum R., Di Matteo T., 2016, MNRAS, 462, 2668

Tenneti A., Gnedin N. Y., Feng Y., 2017, ApJ, 834, 169

The EAGLE team 2017, preprint, (arXiv:1706.09899)

The LSST Dark Energy Science Collaboration et al., 2018, arXiv e-prints, p. arXiv:1809.01669

Tornatore L., Borgani S., Springel V., Matteucci F., Menci N., Murante G., 2003, MNRAS, 342, 1025

Tröster T., Ferguson C., Harnois-Déraps J., McCarthy I. G., 2019, MNRAS, 487, L24

Troxel M. A., et al., 2018, Phys.Rev.D, 98, 043528

Tucker D. L., et al., 2006, Astronomische Nachrichten, 327, 821

Velliscig M., van Daalen M. P., Schaye J., McCarthy I. G., Cacciato M., Le Brun A. M. C., Dalla Vecchia C., 2014, MNRAS, 442, 2641

Vogelsberger M., Genel S., Sijacki D., Torrey P., Springel V., Hernquist L., 2013, MNRAS, 436, 3031

Vogelsberger M., et al., 2014, MNRAS, 444, 1518

Wang Y., Yang X., Mo H. J., Li C., van den Bosch F. C., Fan Z., Chen X., 2008, MNRAS, 385, 1511

Wechsler R. H., Zentner A. R., Bullock J. S., Kravtsov A. V., Allgood B., 2006, ApJ, 652, 71

Weinberg D. H., Mortonson M. J., Eisenstein D. J., Hirata C., Riess A. G., Rozo E., 2013, Phys.Rep., 530, 87

Weinberger R., et al., 2018, MNRAS, 479, 4056

Weinmann S. M., van den Bosch F. C., Yang X., Mo H. J., 2006, MNRAS, 366, 2

Weisberg S., 2013, Applied Linear Regression, 4th Ed.. Wiley

Wen Z. L., Han J. L., 2013, MNRAS, 436, 275

White S. D. M., Rees M. J., 1978, MNRAS, 183, 341

Wong K. C., et al., 2019, arXiv e-prints, p. arXiv:1907.04869

Yang X., Mo H. J., van den Bosch F. C., Jing Y. P., 2005, MNRAS, 356, 1293

Yang X., van den Bosch F. C., Mo H. J., Mao S., Kang X., Weinmann S. M., Guo Y., Jing Y. P., 2006, MNRAS, 369, 1293

Yang X., Mo H. J., van den Bosch F. C., Pasquali A., Li C., Barden M., 2007, ApJ, 671, 153

York D. G., et al., 2000, AJ, 120, 1579

Zentner A. R., Rudd D. H., Hu W., 2008, Phys.Rev.D, 77, 043507

Zentner A. R., Semboloni E., Dodelson S., Eifler T., Krause E., Hearin A. P., 2013, Phys.Rev.D, 87, 043509

Zhang Y., Yang X., Wang H., Wang L., Mo H. J., van den Bosch F. C., 2013, ApJ, 779, 160

Zhao D., Aragón-Salamanca A., Conselice C. J., 2015, MNRAS, 448, 2530

Zu Y., Mandelbaum R., Simet M., Rozo E., Rykoff E. S., 2017, MNRAS, 470, 551

Zwicky F., 1933, Helvetica Physica Acta, 6, 110

de Jong J. T. A., et al., 2015, A&A, 582, A62

di Tullio G., 1978, A&A, 62, L17

di Tullio G. A., 1979, A&AS, 37, 591

van Daalen M. P., Schaye J., Booth C. M., Dalla Vecchia C., 2011, MNRAS, 415, 3649

van Daalen M. P., McCarthy I. G., Schaye J., 2019, arXiv e-prints, p. arXiv:1906.00968

van Dokkum P. G., et al., 2010, ApJ, 709, 1018

van Uitert E., Joachimi B., 2017, MNRAS, 468, 4502

van den Bosch F. C., Weinmann S. M., Yang X., Mo H. J., Li C., Jing Y. P., 2005, MNRAS, 361, 1203

van den Bosch F. C., Jiang F., Campbell D., Behroozi P., 2016, MNRAS, 455, 158